Politecnico di Torino
Department of Mechanical and Aerospace Engineering

In Collaboration with
Singapore Institute of Manufacturing Technology
Bio-Manufacturing Programme

DOCTORATE SCHOOL
PhD in Bioengineering and Medical-Surgical sciences
XXXI Cycle

PhD Dissertation

Design of innovative thermo- and photo-sensitive bioinks and printing setup for the fabrication of tissue engineered constructs

SUPERVISORS

Prof. Gianluca Ciardelli

Dr. May Win Naing

PhD CANDIDATE

Eng. Stefano Calzone

CO-SUPERVISOR

Dr. Monica Boffito

April 2019

Index

Acknowledgements

The author acknowledges:

- the FIRB Project -Fondo per gli Investimenti della Ricerca di Base- **"***Bioartificial materials and biomimetic scaffolds for a stem cell-based therapy for myocardial regeneration*"(Coordinator: Prof. Valeria Chiono, Politecnico di Torino, Italy).
- the IRMI Project - Italian Regenerative Medicine Infrastructure-.
- the ARAP Project -A*STAR Research Attachment Programme-"*Novel biomimetic scaffolds inducing stem cell fate: application in tissue engineering*" (Coordinator: Dr. May Win Naing, Singapore Institute of Manufacturing Technology, Singapore).

Short Curriculum Vitae

Eng. Stefano Calzone has a Master Degree in Biomedical Engineering from Politecnico di Torino, Italy (2014). After the degree he joined Prof. Gianluca Ciardelli's group with a scholarship. In November 2015 he started the PhD in Bioengineering and Medical-Surgical Sciences at Politecnico di Torino under the supervision of Prof. Gianluca Ciardelli. His research is focused on the synthesis and characterization of biodegradable polyurethanes for tissue engineering applications, with particular attention on the design of hydrogels. During his PhD, Stefano jointed Dr. May Win Naing group at Singapore Institute of Manufacturing Technology for 18 months, working on 3D bioprinting of custom-made bioinks with tunable properties.

He is author of 2 publications in international peer-reviewed journals, 2 contributions in book chapters, 11 conference proceedings.

Abstract

Tissue engineering approaches aim to the design of three-dimensional constructs that can support cell viability, growth and differentiation. Among the wide range of biomaterials available, hydrogels offer many advantages for different applications thanks to their watery nature and viscoelastic properties. Additive manufacturing has been massively investigated as tissue engineering approach because of its high technological versatility and the possibility to build three dimensional constructs with high resolution and printing fidelity as well as building speed.

Poloxamer 407 is a Food and Drug Administration approved triblock copolymer; its water solutions show a thermo-responsive behavior with micelle formation and packing with increasing temperature. Despite their reported advantages (e.g. ,non-toxic, able to form gels at room temperature at a concentration of 20 %w/v), such hydrogels are characterized by fast dissolution in aqueous environment and weak mechanical strength, limiting their *in vivo* application.

In this work, Poloxamer 407 (P407) were exploited as building block in the synthesis of amphiphilic copolymers suitable for the design of thermo-sensitive hydrogels for cell/drug carrier applications and bioprinting technology. In detail, P407 was chain extended to increase its molecular weight and enhance the hydrophobic interactions and hydrogen bonds of its chains in water environment, by exploiting polyurethane (PUR) versatile chemistry. An amphiphilic PUR (NHP407) was thus synthesized starting from P407, an aliphatic diisocyanate (1,6-hexanediisocyanate) and an amino acid derived diol (N-Boc serinol). NHP407-based solutions in water-based media were able to form biocompatible injectable thermo-sensitive hydrogels with faster and more efficient gelation kinetics, enhanced stability as well as mechanical properties, compared to P407-based ones. The application of such hydrogels as

biomolecule/drug carriers was evaluated by studying the encapsulation and the release of different hydrophobic antioxidant drugs (i.e., dexamethasone, curcumin, resveratrol.) and hydrophilic model proteins (i.e., bovine serum albumin, horseradish peroxidase). However, NHP407-hydrogels were not suitable for bioprinting approaches due to their relatively low stability in the shape of thin filaments. In order to overcome this drawback different strategies were explored in order to provide the designed PUR-based hydrogels with the potential to be chemically crosslinked. Among all the tested approaches, the addition of acrylate moieties within the hydrogels showed the best results in term of increase of stability in water environment Hence, three different families of thermo- and photo-sensitive hydrogels were designed and characterized. The first formulations involved the use of the previously designed PUR (NHP407) blended with a water-soluble acrylate polymer (e.g., poly(ethylene glycol) acrylate - PEGDA-) that upon UV/Vis irradiation forms a mesh entrapping the PUR-based micelles. The second approach, instead, dealt with the design of a new family of amphiphilic PURs exposing acrylate moieties (HHP407 and PHP407 synthesized by end-capping an isocyanate-terminated P407-based prepolymer with hydroxyethyl methyl acrylate or Pentaerythritol triacrylate, respectively) along their backbone, allowing the formation of a mesh of chemically cross-linked micelles upon light irradiation. Eventually, the last formulations involved the use of the latter PURs blended with an acrylate polymer (e.g., PEGDA) in order to obtain a double degree of crosslinking upon UV/Vis irradiation. The addition of chemical crosslinks within the hydrogel structure made it possible to design hydrogels with tunable stability in water environment as well as mechanical properties.

In order to select the best formulations to be applied in bioprinting approached, all the designed hydrogels were characterized in terms of thermo- and photo-sensitivity. Based rheological characterization, the NHP407/PEGDA- and HHP407/PEGDA-based formulations were

selected as bioinks. In order to 3D print PUR-based bioinks a commercially available bioprinter (Inkredible +, CELLINK) was modified and a custom-made printing process was designed.

Both the printing and photo-crosslinking procedures were studied separately in order to select the best paraments and conditions that allowed printing resolution and cell viability maximization. The best conditions of each procedure were finally combined to 3D print cellularized scaffolds in the shape of circular multi-layered constructs with a grid pattern showing prolonged stability and cell viability up to one month.

Moreover, the bicomponent nature of the designed bioinks allowed to finely tune both the bioink thermo- and photo-sensitivity in order to match different physico-chemical properties of soft tissues.

Thesis Goal and Outline

This thesis work will be carried out in the framework of two main projects: (i) the 2010 FIRB project “Bioartificial materials and biomimetic scaffolds for a stem cell-based therapy for myocardial regeneration” (founded by Ministero dell'Istruzione, dell'Università e della Ricerca, Italy), and (ii) the 2016 ARAP project “Novel Biomimetic Scaffold Inducing Stem Cell Fate: Application in Tissue Engineering” (founded by Agency for Science, Technology and Research -A*STAR-, Singapore). The first one faces the need of new alternative therapies to treat infarcted patients through the design of 3D printed hydrogel-based scaffolds loaded with growth factors, proteins and/or drugs to favor cell survival and induce their differentiation, with the final aim of stimulating cardiac tissue repair. The second project fits into a similar context and aims at the development of hydrogel-based scaffolds through 3D bioprinting with the goal to engineer scaffolds for human mesenchymal stem cell culture.

To achieve such goals, the chemical and technological versatility of polyurethane and extrusion-based bioprinting will combined to design a wide family of scaffolds differing in architecture, mechanical and physico-chemical properties.

More in detail, this thesis work will be initially focused on the synthesis and characterization of different polymers, mostly belonging to the polyurethane family, in order to design hydrogels with different physico-chemical and gelation properties. The use of custom-made polyurethanes will allow to finely control the hydrogel properties with the additional potential to bulk functionalize the hydrogels with biomimetic moieties. In detail, different polyurethane-based hydrogels will be designed showing photo- and/or thermo-sensitive behavior. Thorough physico-chemical, mechanical and biological characterization of the designed hydrogels will be performed in order to select the best formulations for the desired application. The use of hydrogels as printing materials offers the advantage to easily incorporate cells and

drugs/biomolecules in mild conditions. This possibility allows to fabricate cellularized scaffolds during the printing process, avoiding cell seeding after fabrication and allowing an efficient cell colonization within the constructs. On the other hand, the printing process needs to be carefully optimized in terms of applied shear stress to avoid or at least minimize cell damage during the bioink extrusion. To this aim, a through optimization of hydrogel composition as well as printing parameters will be carried out, by analyzing the effects of each contributor on cell viability and printing resolution and fidelity. The thermo-sensitive nature of the developed hydrogels will help cell dispersion, since cells can be added and homogeneously distributed within the hydrogel at a temperature lower than the gelation temperature (below 25 °C), i.e., in a sol or semi-gel phase. After being loaded in the syringe, the cellularized hydrogel will be subjected to a fast sol-to-gel transition prior to printing, modulating its viscosity acting on the temperature of the syringe in order to maximize the outcomes of the printing process and minimize cell suffering due to shear stress. To this aim, the possibility to print the hydrogels as biphasic sol/gel systems or a fully developed gels able to keep their shape upon printing will be exploited to balance the two concurrent needs of high resolution and poor cell suffering and death. Moreover, a faster sol-to-gel transition will be required to ensure a homogeneous cell distribution, avoiding cell sedimentation during the printing process. Eventually, by making the developed hydrogels photo-responsive, a further degree of freedom will be provided to the developed bioinks, allowing a fine modulation of the final mechanical properties and stability in aqueous environment of the scaffolds.

The use of the designed hydrogels as cell/drug/biomolecule carriers and as bioinks for 3D printing will be thoroughly assessed, and human mesenchymal stem cells will be finally printed upon encapsulation in the bioinks in view of a potential application of the developed constructs in tissue engineering/regenerative medicine. The plethora of hydrogels designed in this work

and the optimized printing protocols and parameters are expected to introduce significant improvements the biomedical field. In fact, new "LEGO"-like and customizable approaches will be developed, which could allow in the future the optimal and customized design and fabrication of bioengineered constructs replicating almost all tissues and organs of the human body for application in tissue engineering/regenerative medicine as *in vitro* models or reparative and regenerative devices.

The thesis will be divided in 6 chapters, whose content is summarized below.

Chapter 1: Introduction to tissue engineering concepts, polyurethane properties and additive manufacturing strategies.

Chapter 2: Literature overview on the application of polyurethanes in additive manufacturing for biomedical strategies.

Chapter 3: Design and characterization of thermo-sensitive hydrogels based on a custom-made amphiphilic polyurethane, and their application as cell/drug/biomolecule carriers.

Chapter 4: Design and characterization of thermo- and photo-sensitive hydrogels based on different custom-made polyurethanes and acrylate polymers.

Chapter 5: Application of the designed bioinks in extrusion-based bioprinting and design of the printing setup.

Chapter 1

Introduction

Abstract:

Tissue engineering approaches aims to design three dimensional constructs that can support cell viability, growth and differentiation. Among the wide range of biomaterials available, biodegradable polymers offer many advantages. However, polymers that are commercially available often own inappropriate mechanical properties and degradation kinetics. Polyurethanes are multi-block copolymers, usually based on a macrodiol, an isocyanate and a chain extender. The high versatility of polyurethane chemistry has been exploited in literature to design biomaterials showing a wide range of physico-chemical and mechanical properties, and additional features (e.g., shape-memory, stimuli-sensitivity). Moreover, because of this variety of exhibited properties, polyurethanes can be processed via both conventional and advanced fabrication technologies. Additive manufacturing has been massively investigated as tissue engineering approach because of its technological versatility and the possibility to build three dimensional constructs with high resolution and printing fidelity as well as building speed.

This chapter provides an overview of polyurethane chemical versatility and the different additive manufacturing technologies available for tissue engineering.

Keywords:

Tissue Engineering, Regenerative Medicine, Scaffold, Polyurethanes, Additive Manufacturing.

1.1. Background

Tissue engineering/regenerative medicine (TERM) aims to design functional constructs which are able to restore, maintain and improve the functionality of damaged tissues or whole organs.[1] In a recently emerging approach, TERM principles are also exploited to develop 3D tissue/organ models that could become useful devices in drug design and screening as well as in basic research.[2–4] The proper design of the three-dimensional (3D) matrix that provides the structural and mechanical support to the regeneration process is a key aspect to stimulate and control the formation of a new functional tissue as well as to guide the differentiation of stem cells.[5] By mimicking nature, the optimal 3D scaffold should finely replicate *in vitro* the physico-chemical and mechanical properties as well as the porous structure of the extracellular matrix (ECM) of the native tissue.[5,6] Moreover, the degradation of the scaffold should match the rate of the specific tissue growth, without releasing toxic products. In order to design scaffolds with these properties, the selection of the raw material and the scaffolding technology is a crucial issue.[7]

In this scenario, among the wide variety of available raw materials, polyurethanes (IUPAC abbreviation PURs, but commonly abbreviated PUs) are gaining increasing interest thanks to their high chemical versatility that opens the way to the possibility to design biomaterials with conveniently tuned physico-chemical and mechanical properties as well as optimal degradation rate. PURs have already found application in a lot of different production areas, such as clothing, automotive, footwear, furnishings, construction, paints and coatings.[8] In the 1970s, the broad variety of properties achievable with PUR chemistry also has drawn the attention of biomedical companies because of their distinctive mechanical properties. Hence, between the 1980s, non-degradable PURs have been used in clinics as long-term implants (e.g., cardiac pacemaker,[9] vascular grafts[10] and breast implant coatings[11,12]) collecting some catastrophic failures due to

the unsolicited degradation of the devices.[13,14] Later on, the knowledge in PUR chemistry has been translated to the design of a new class of biodegradable materials.[15] Over the last two decades, biodegradable PURs have been extensively investigated in TERM applications, in the form of injectable hydrogels or implantable scaffolds.[16–18] In hard tissue engineering, PUR-based constructs have been designed with the optimal flexibility and load bearing properties for orthopedic applications.[19,20] In this context, recent literature has explored the possibility of designing composite biomaterials based on PURs and ceramic particles, in order to combine the mechanical properties of PURs and the osteoconductive potential of ceramics, such as calcium phosphates.[21] Similarly, in soft tissue engineering, PUR-based constructs with proper mechanical and structural properties have found wide application in the repair and regeneration of cardiac tissue, blood vessels, peripheral nerves and skin.[22–29] Recently, PURs have been made antibacterial by (i) introducing antibacterial moieties along their backbone, (ii) loading antibacterial agents or (iii) treating construct surface to impart antibacterial potential.[7,8,29–33] PURs are also under extensive investigation in drug delivery, in the form of injectable hydrogels, including PUR-based thermosensitive sol-gel systems, or nano- and micro-particles with improved encapsulation efficiency and prolonged payload release over time.[24,29] The high potential of PURs in the biomedical field also lies in their high processability that allows to fabricate PUR-based constructs via both conventional and additive manufacturing (AM) fabrication technologies.[18] AM techniques, in particular, have been widely studied in the last ten years for TERM applications thanks to their high versatility and precision as well as the possibility to fabricate patient specific devices.[34]

1.2. Tissue Engineering

The field of tissue engineering (TE) has progressed massively in the last two decades, offering the potential for regenerating or modeling almost every biological tissue and organ.[1,35] The advances reported in the literature during this quite short time-lapse concern different disciplines, including biomaterials science, manufacturing technology, cell biology, surface functionalization, imaging and characterization of cell-biomaterial interactions (**Figure 1.1**).[6]

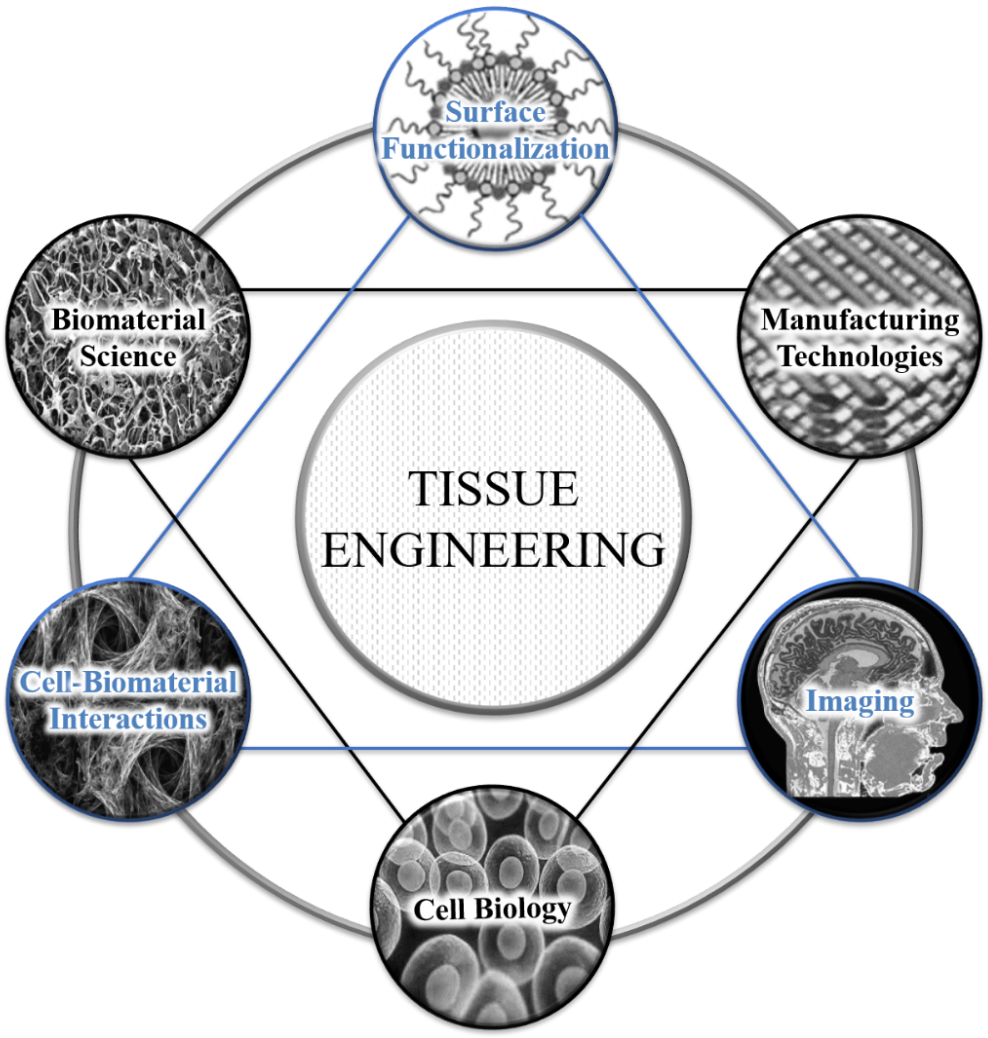

Figure 1.1 Multidisciplinary pillars in tissue engineering.

TE aims to develop bioengineered strategies with the potential to (i) stimulate or enhance the regeneration, or replace the functions of a damaged tissue/organ,[1] and (ii) engineer alternative

in vitro models that would replace to a certain extent animal models for drugs and therapies testing,[2–4] according to the 3Rs (Replacement, Reduction and Refinement) principles.[36] In order to reach this goal, TE follows different routes (**Figure 1.2**): (i) the use of biomimetic materials to simulate the physico-chemical and mechanical properties of the native microenvironment, thus providing a physical support for the cells (i.e., cell adhesion, proliferation and differentiation, and tissue growth); (ii) the processing of the latter in the form of a 3D scaffold in order to recapitulate *in vitro* the structural properties of the native ECM consisting of a variety of proteins and polysaccharides assembled into an highly organized network; (iii) the use of stem cells or differentiated cells as biological building blocks able to generate a functional tissue; and (iv) the addition of signaling cues that contribute to tissue development, such as biochemical (i.e., biomolecules such as proteins and growth factors) and biomechanical (i.e., bioreactors) stimuli.[1,6,37–39]

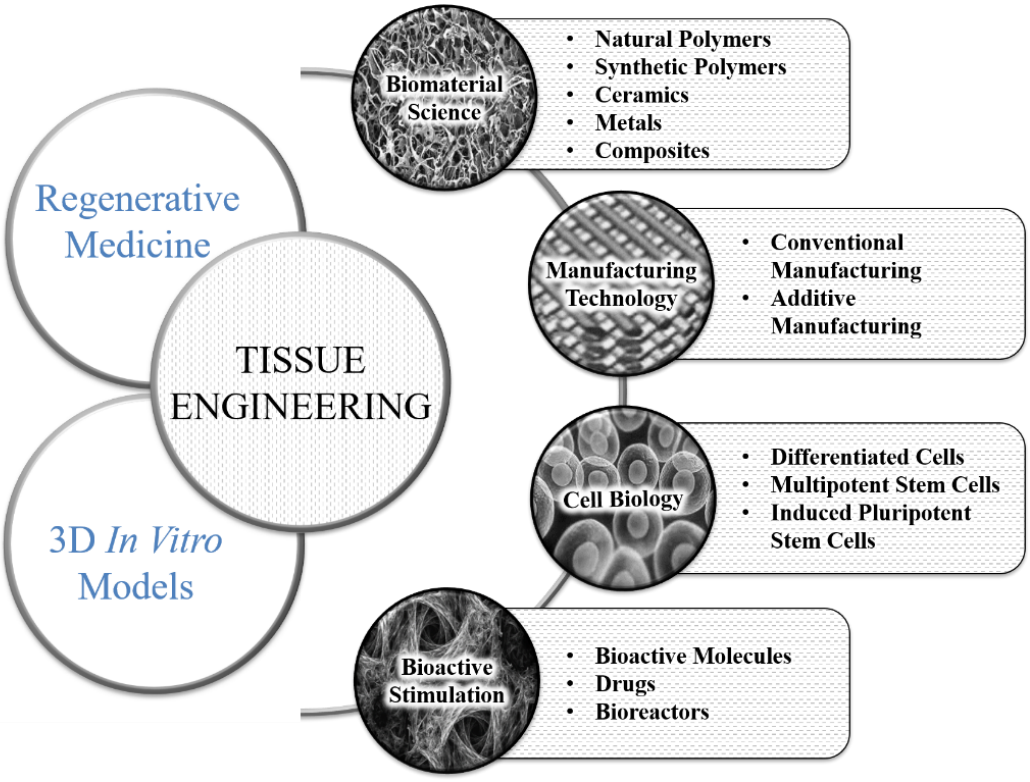

Figure 1.2 Tissue engineering principles and applications.

Thus, the ideal biomimetic scaffold is defined as a 3D porous matrix designed to (i) promote cell-scaffold cross-talk, cell adhesion, proliferation and differentiation, ECM deposition and tissue growth, (ii) allow sufficient supply of gases, nutrients, regulatory factors and biomolecules, (iii) biodegrade at a rate that matches the rate of tissue regeneration, and (iv) minimize inflammation and toxicity *in vivo*.[1,6,37,39] As previously mentioned, in order to enhance the biocompatibility of the scaffolds and improve cell growth, different biomolecules can be embedded into the designed 3D matrices through (i) bulk or surface functionalization procedures, or (ii) direct encapsulation in their free form or upon loading in carriers (e.g., nano- or micro-particles).[6] Eventually, the scaffold can be seeded with autologous cells (differentiated cells, multipotent or induced pluripotent stem cells) in order to develop cellularized matrices to replace the functionality of the targeted tissue or to simulate the native tissue for *in vitro* testing.[6] In a different regenerative approach, biomimetic and bioactive scaffolds can be designed as cell-free matrices that will recruit cells from the surrounding tissues and microenvironment upon implantation.[6]

A great number of different biomaterials has been proposed and processed for TE applications: natural and synthetic polymers, ceramics, composites and metals (**Figure 1.3**).[40,41] Natural and synthetic biodegradable polymers have been widely investigated as biomaterials for the fabrication of medical devices and TE scaffolds due to their easy processability and biocompatibility.[6] Researchers have optimized several techniques to process polymers into complex architectures according to certain designs for specific TE applications: conventional techniques (e.g., freeze-drying, phase separation, gas foaming and electrospinning) or additive manufacturing technologies (e.g., selective laser sintering -SLS-, fused filament fabrication -FFF-, liquid frozen deposition manufacturing -LFDM-, pressure assisted microsyringe -PAM-, stereolithography -SLA-, digital light processing -DLP- and Bio-printing).[6] Each method owns

distinct advantages and disadvantages; hence, the appropriate technique has to be selected for each specific application to match the requirements of a particular type of tissue/organ.

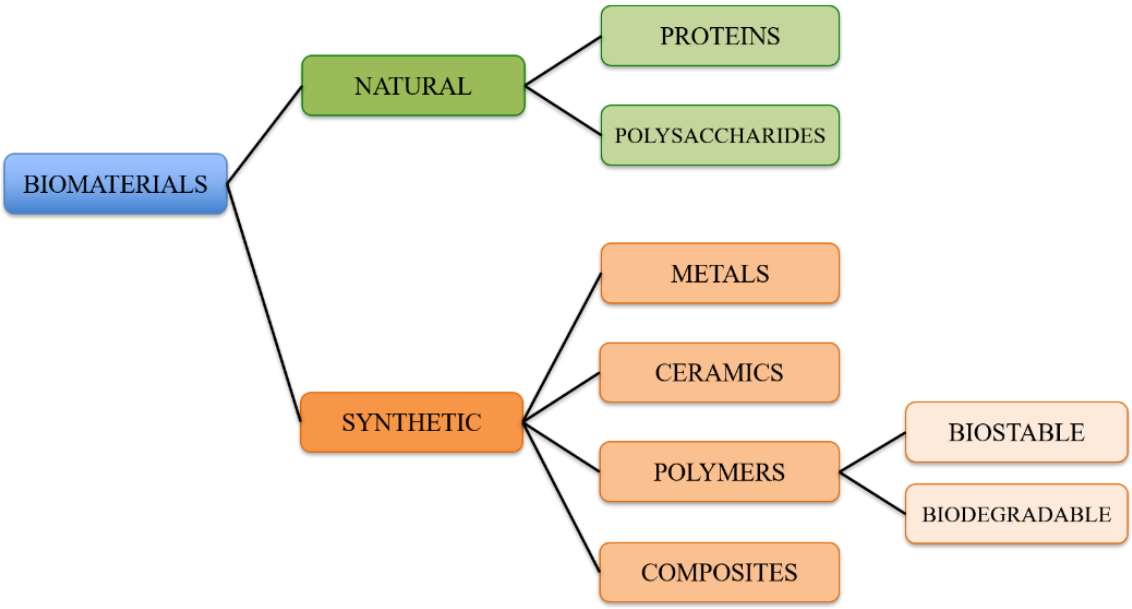

Figure 1.3 Biomaterials' classes for tissue engineering applications.

1.2.1. Regenerative Medicine

Regenerative medicine (RM) is a branch of TE that aims to maintain, improve or restore tissue functions that are deficient or have been lost as a consequence of pathological conditions, by designing biological substitutes or by stimulating tissue regeneration.[6] The general strategies applied in RM applications can be classified into three groups: (i) implantation of isolated cells into the body, (ii) delivering of biomolecules (e.g., growth factors) able to induce tissue formation and (iii) implantation of a cellularized 3D scaffold.[6,42] RM founds on the principle that living tissues are able to self-regenerate, and the supposition that the employment of biological components (e.g., cells and biomolecules) can enhance the potential for regeneration, thus further increasing the efficacy of these strategies.[43] Following this principle, RM is a technique based on the mimicking of nature. Natural tissues consist of three main components:

cells, ECM, and signaling factors. Therefore, RM seeks to create constructs that mimic the biological tissues' structures and functions by combining cells, biomaterials, and biomolecules (**Figure 1.4**).[38]

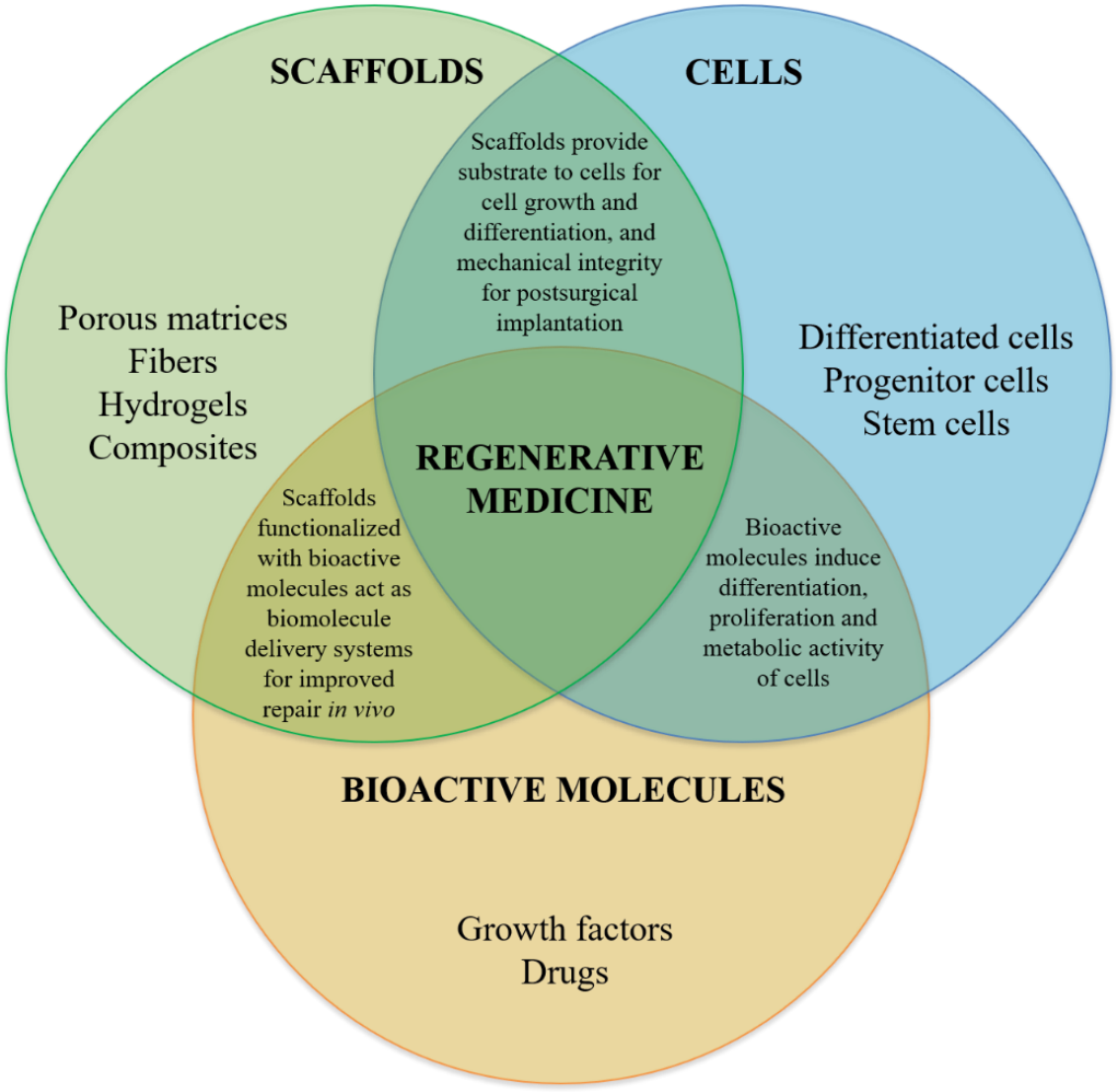

Figure 1.4 Triad of a classical regenerative medicine construct.

1.2.2. 3D *in* vitro Models

Animal models have strongly contributed to the establishment of modern medicine by increasing our knowledge of human biology. However, they cannot reproduce specific human

conditions and it has been showed that they usually are inefficient predictors in drug screening. On the other hand, two-dimensional (2D) *in vitro* models have intrinsic space and distribution limits that do not allow to finely mimic the 3D physiological environment.[2–4] In this context, TE strategies have been proposed to design alternative *in vitro* 3D models with the potential to partially replace animal models, in accordance with the 3Rs principles.[36] These models have been shown to be promising tools as new platforms for drug and therapy screening/testing, as well as for pathology onset/progression investigation.[2–4]

1.3. Design Considerations for Functional 3D Scaffold

Approaches in scaffold design should be able to produce structures with arbitrary or anatomical 3D shapes and create biocompatible hierarchical 3D matrices with high porosity and interconnected porous network, to achieve the desired mechanical properties (stiffness, elasticity), mass transport kinetics (permeability and diffusion) and degradation time (**Figure 1.5**).[5,40]

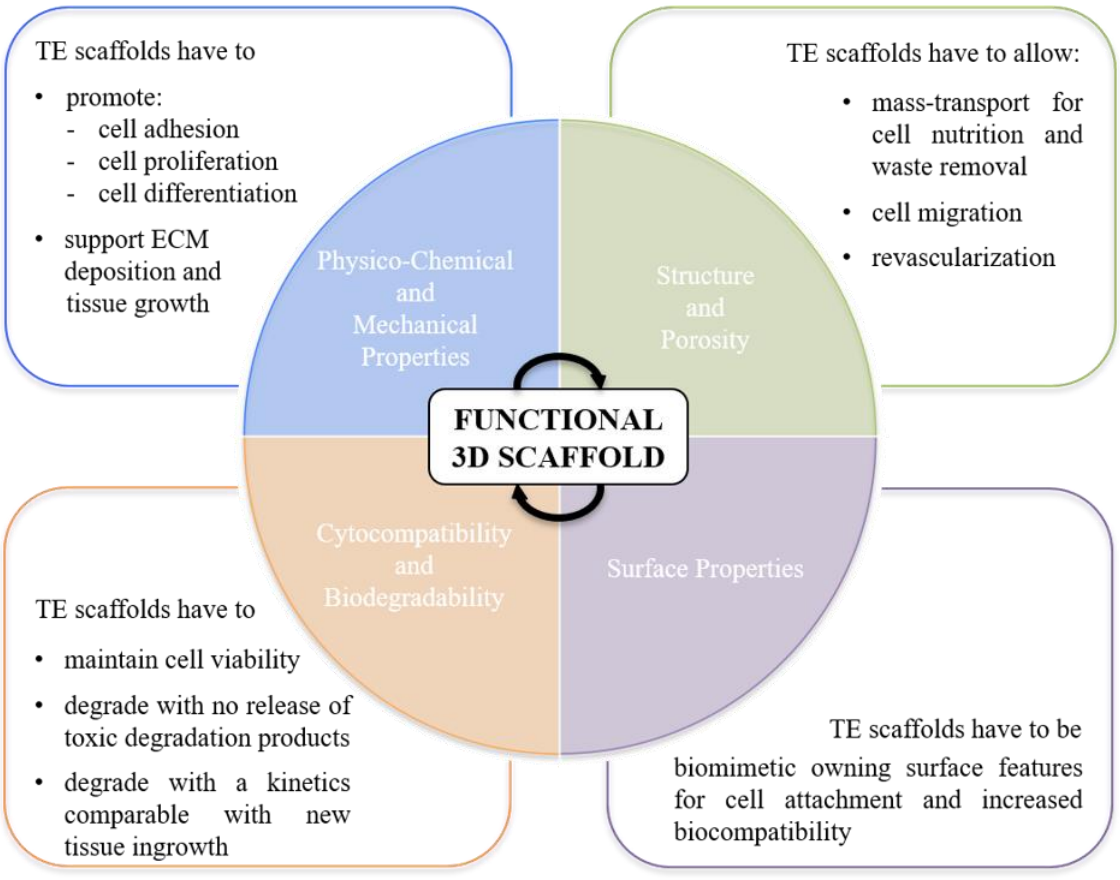

Figure 1.5 Functional 3D scaffolds' properties.

1.3.1. Cytocompatibility and Biocompatibility

Scaffolds for TE approaches must be cytocompatible to maintain cells' viability while mimicking the natural ECM environment to support their growth. As mentioned above, both

natural and synthetic polymers can be used as scaffold-forming materials to promote cell adhesion, proliferation and differentiation, and support/replace ECM functions. However, synthetic polymers generally have poor affinity with cells due to their low hydrophilicity and the absence of cell-recognition sites.[44]

Biodegradability is another important factor in the design of scaffolds. In fact, a scaffold for TE must be biodegradable in non-toxic degradation products, and degrade at a controllable rate that approximates the rate of tissue regeneration to ensure proper remodeling of the tissue, thus working as a temporary matrix that supports cell attachment, proliferation, and differentiation, and new-tissue formation.[6] Some synthetic biodegradable polymers, such as polyesters, degrade in acidic products that can induce inflammation, thus limiting their applicability in the biomedical field.[6] Functionalization or blending procedures with biomolecules or biopolymers can be carried out to enhance cell-scaffold interactions by improving hydrophilicity, incorporating cell-recognition domains and reducing the inflammatory response.[44]

1.3.2. Physico-Chemical and Mechanical Properties

Biomaterial science together with manufacturing determines the maximum functional properties (physico-chemical and mechanical properties) that a scaffold can achieve, as well as the previously mentioned cell-material interactions.[40] Scaffold porosity is a key aspect to ensure an adequate mass-transport of nutrients and oxygen, surface features for cell attachment, space for cell migration and expansion as well as revascularization. Accordingly, this porous structure imposes limitations on the achievable scaffold properties. Hence, the critical issue for scaffold design is to balance the mechanical (elastic modulus in the range of 0.4-350 and 10-1500 MPa for soft,[45] and hard[46] tissues, respectively) and mass-transport properties in order to create a biomimetic and functional structure.

1.3.3. Surface Properties

After scaffold/device implantation, the adsorption of plasma proteins onto biomaterial surfaces immediately occurs. As a result, the scaffold is covered with layers of host proteins resulting in its progressive degradation and the consequent recruitment of inflammatory immune cells (i.e. monocytes/macrophages and polymorphonuclear leukocytes). The biochemical cues released by these cells trigger angiogenesis and the deposition of collagen by fibroblasts leading to the formation of a collagenous fibrous capsule that isolates the implant from the surrounding biological tissues.[47] In order to avoid this phenomenon, surface modifications or functionalization can be applied to the scaffolds to enhance their biocompatibility and bioactivity.

1.4. Commercially Available Polymers: Pros & Cons

The term biodegradable polymers refers to a class of materials that can be degraded by microorganisms or by biological fluids *in vivo*.[48] The most frequently employed natural polymers in TE are proteins (e.g., collagen, silk, fibroin), glycosaminoglycans (e.g., hyaluronic acid), polysaccharides (e.g., chitosan, alginate, cellulose, agarose, starch) and their derivatives, due to their inherent biocompatibility (**Figure**).[6,49] The use of such polymers offers many advantages for TE applications, such as cell adhesion, biochemical signaling, cell responsive degradation and remodeling.[50] However, they often lack in the proper physical and mechanical properties required for engineering tissues and organs, as well as in the control of their degradation kinetics.[6] Moreover, natural polymers may subject patients to the risk of disease transmission and immuno-rejection,[50] which makes proper screening and purification mandatory, thus increasing their cost. On the other hand, synthetic biodegradable polymers usually exhibit controlled chemical structure, a higher degree of processing flexibility, no immunological concerns and higher uniformity compared to materials of natural origin.[6] Among synthetic biodegradable polymers, polyesters (e.g. poly(glycolic acid) -PGA-, poly(lactic acid) -PLA-, poly(lactic-co-glycolic acid) -PLGA-, poly(ε-caprolactone) -PCL-, poly(butylene succinate) -PBS-, poly(butylene adipate) -PBA-, poly(glycerol sebacate) -PGS-, poly(1,8-octanediol citrate) -POC-) have been widely used to produce TE scaffolds;[6] however, they usually lack the required elasticity to match that of living tissues (**Figure 1.6**).[51] Moreover, the hydrolysis of their ester bonds releases acidic products which can cause a strong inflammatory response.[18] Another drawback of polyesters related to TE applications is their hydrophobicity which can cause poor wetting and lack of cellular attachment and cell-surface interactions.[50] The processing of polyesters usually requires high temperature or toxic organic solvents, which make them not suitable for cell printing.[51] Natural polymers, on the other hand,

are hydrophilic and can be used for the design of bioinks for cell printing; however, they often need potentially cytotoxic cross-linkers to increase their stability in aqueous environment and enhance their mechanical properties. Bioinks for cell printing can also be designed by synthetic hydrophilic biomaterials in a water-based system.[6,51] In this context, different polymers such as poly(ethylene glycol) -PEG-, polyvinyls (e.g., poly(vinyl alcohol) -PVA-, poly(vinyl acetate) -PVAc- and poly(vinyl pyrrolidone) -PVP-), and some polyesters (e.g., PGA) have been widely investigated thanks to the possibility of tuning their physico-chemical and mechanical properties at a large extent (**Figure 1.6**).[52] Other synthetic polymer families have been also investigated such as polyanhydrides,[53] polyphosphazenes[54] and multi-blocks (e.g. polyurethanes -PURs-, poly(ether ester) block copolymers),[8,18,55] as well as polyesters extracted from micro-organisms (e.g., poly(hydroxy alkanoate)s -PHAs-, such as (poly(hydroxy butyrate) -PHB-, poly(hydroxy valerate) -PHV-, and their copolymers) (**Figure 1.6Figure**).[56]

In general, commercially available synthetic polymers are relatively poorly customizable: it is possible to select among different molecular weights and functionalization, but the intrinsic nature of the material does not change. In the case of multi-blocks, in addition to polymer molecular weight, modulation of their properties can be done by working on the molecular weight of each block and their weight ratio. Moreover, polymers functionalized with specific groups are commercially available, but they are much more expensive with respect to the original ones.

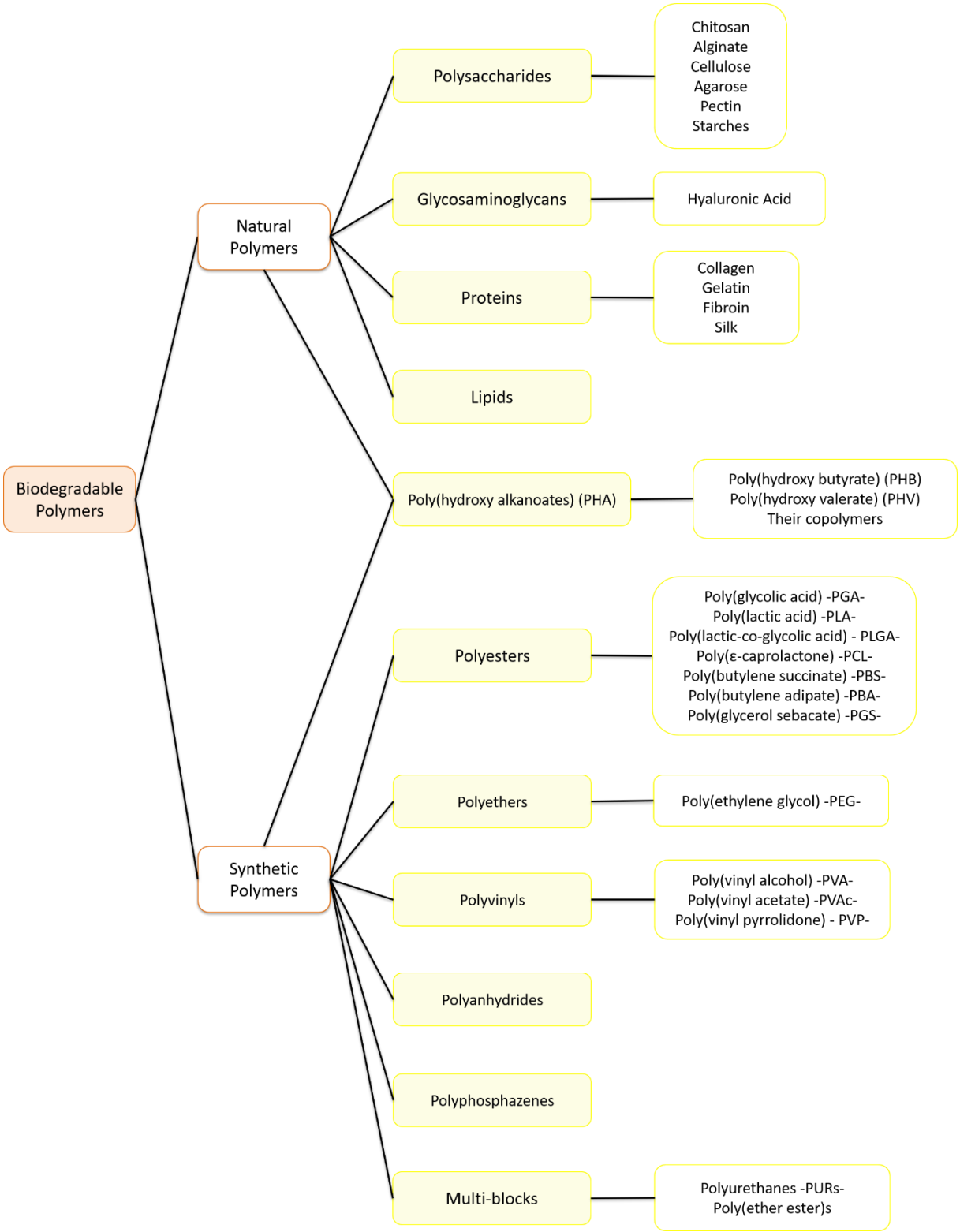

Figure 1.6 Biodegradable Polymers' classes for tissue engineering applications.

1.5. Can Polyurethanes Overcome the Drawbacks of Commercially Available Biomaterials?

PURs are a family of linearly segmented block copolymers characterized by the presence of urethane bonds, which result from the reaction of an isocyanate and an oxydrilic group.

The beginning of PUR history dates back to 1937 when Dr. Otto Bayer's research group discovered the diisocyanate polyaddition process. The first applications of PURs mainly involved soft foams and non-segmented semi-crystalline fibers. Due to the lack of rubber materials, intensive efforts were spent to develop polymeric elastomers during the Second World War. This new stimulus brought to the launch of the first PUR elastomer product by Bayer in 1950 (Vulkollan rubbers). Since then, PUR elastomers have been extensively applied in different fields such as textile, automotive, architectural and medical ones.[57,58]

Concerning the medical field, the use of non-degradable PURs in medical devices (e.g., cardiac pacemaker, vascular grafts and breast implant coatings) has been well documented since 1965.[59–65] More recently, researchers have also designed biodegradable PURs for TE scaffolds and other resorbable implants.[18,60,61,66,67] As synthetic polymers, PURs have gained attention for application in the biomedical field because of their excellent mechanical strength, flexibility, hemocompatibility and biocompatibility.[66]

1.5.1. Chemical Versatility of Polyurethanes

Depending on the chosen building blocks, PURs with linear or network structures can be designed. In particular, by using bifunctional reagents are used, the polymerization takes place linearly; on the other hand, when multifunctional reagents, PUR chains create crosslinking between them during the synthesis. Linear PURs usually are more widespread compared to

crosslinked ones due to their easier processability. Linear PURs are synthetized from the reaction of a diisocyanate, an oligodiol (macrodiol) and a chain extender (diol or diamine). Because of these three degrees of freedom, PURs form a large family of polymers with a wide range of chemical compositions and properties.[8,68]

Polyurethane polymerization reaction falls into the family of step growth or condensation polymerizations, but without the typical side-products (e.g., H_2O or CO_2).[8] PURs consist of soft and flexible segments with a low glass transition temperature (T_g), composed by the macrodiol, and a glassy or semicrystalline hard segment derived from the diisocyanate and the chain extender.[15,59,69] PURs can be synthesized via a one-step (all the reagents are reacted at once) or a two-step procedure (prepolymer method).[8]The prepolymer method consists of two steps: (i) the macrodiol is first reacted with an excess of diisocyanate to form an -N=C=O terminated prepolymer; (ii) the prepolymer is then reacted with a chain extender to form an $(AB)_n$ type copolymer characterized by an alternation of hard and soft segments (**Figure 1.7**). PUR structure, polydispersity and degree of branching are influenced by the synthesis method. Although the prepolymer method involves a longer reaction time, it allows greater control over the chemistry of the reaction leading to high molecular weight polymers, and, thus, influencing also the physical and mechanical properties, as well as the processability of the resulting material.[68]

PUR synthesis involves the formation of urethane or urea linkages by the reaction of the isocyanate group with an alcohol or an amine, respectively. Moreover, the nitrogen of urethane and urea groups can also form allophanates and biurets, respectively, creating heat-labile crosslinks and increasing the structural heterogeneity in PUR design.[59,65,68]

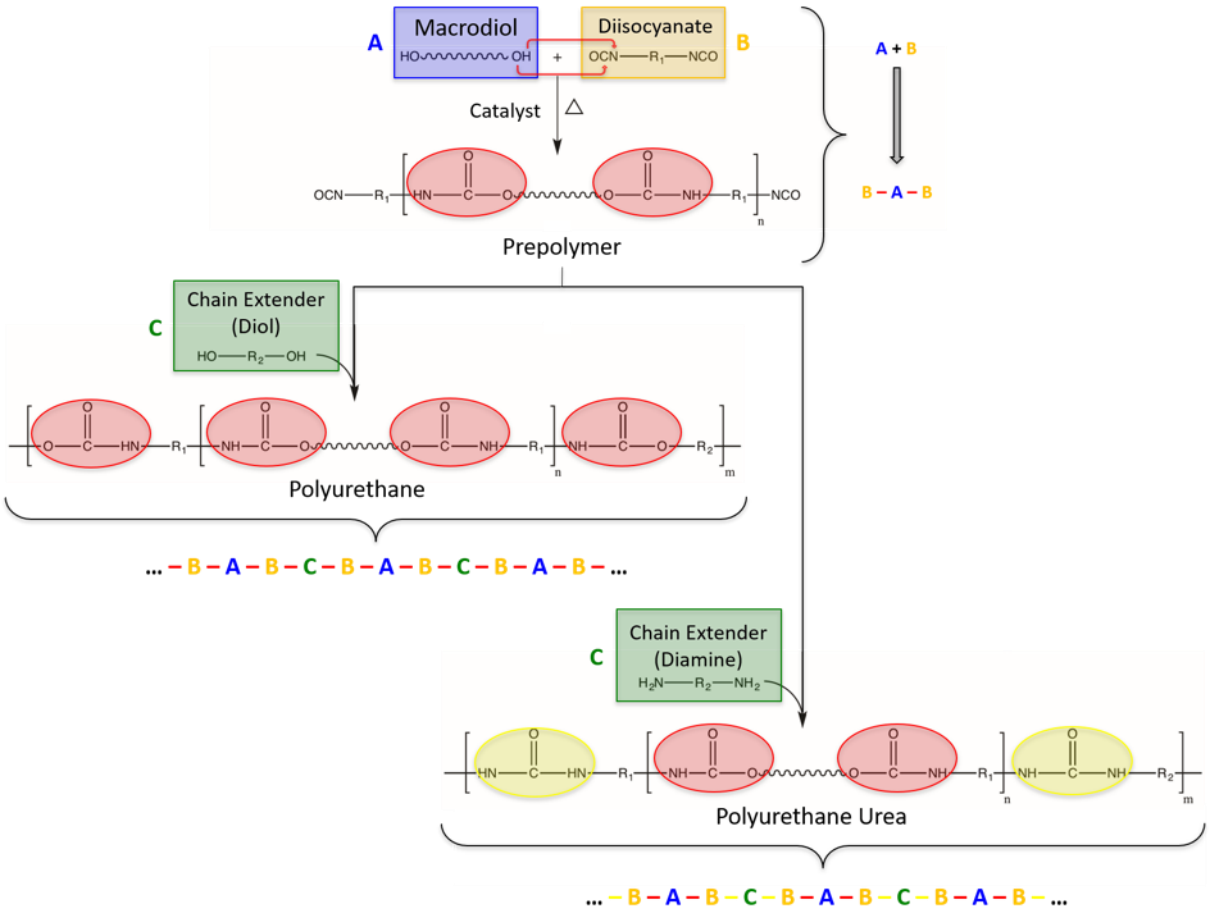

Figure 1.7 Polyurethane synthesis steps and structures.

1.5.1.1. Soft Segment Chemistry

Typically, the polyol (usually macrodiol) is an oligomeric macromonomer with low glass transition temperature and terminal hydroxyl (-OH) groups.[66]

Conventional polyols are polyesters (with repeating structure of -R-CO-O-R'-), polyethers (with repeating structure of -R-O-R'-), polycarbonates or their combinations in the form of diblock and triblock copolymers (**Table 1.1**).[15,59,69]

Polyol properties, in particular its molecular weight and flexibility, strongly influence the properties of the final PUR. In particular, long polyols give rise to elastomeric PUR with low-modulus, meanwhile short and/or multifunctional polyols produce stiff PURs.[70,71]

Table 1.1 PUR properties depending on macrodiol's composition.

Polyols	PUR Characteristics
Polyethers	Poly(ether urethane)s are flexible and resistant to hydrolytic degradation; however, they suffer from poor oxidative and thermal stability.[8,72,73]
Polyesters	Poly(ester urethane)s have good mechanical properties and heat resistance, but they are susceptible to hydrolytic degradation.[8,74,75]
Polycarbonates	Poly(carbonate urethane)s are more stable in terms of thermal and hydrolytic resistance. Moreover, they have superior mechanical properties.[8,76,77]

1.5.1.2. Hard Segment Chemistry

Diisocyanates are low molecular weight compounds containing two isocyanate groups that can react with either the polyol or the chain extender.[66] During PUR synthesis, these two functional groups linearly join together the polyol and the chain extender.

By using isocyanates with more than two functionalities, a 3D crosslinked network is formed. Both aliphatic and aromatic diisocyanates can be used to synthesize polyurethanes (**Table 1.2**). Chain extenders are diols or diamines, normally with low molecular weight, that react with isocyanate groups increasing the hard segment length.[65] These extended sequences increase the PUR mechanical strength acting as filler particles and physical crosslink sites. Moreover, chain extenders are used to increase hydrogen-bond density and the molecular weight of the PUR.[80] Furthermore, chain extenders with more than two functionalities also act as branching or crosslinking agents leading to PURs that are more resistant to high temperatures.[8]

The selection of a diamine or a diol determines whether urea or urethane groups are formed.

Table 1.2 PUR properties depending on isocyanates' chemical composition.

Isocyanates	PUR Characteristics
Aromatic isocyanate	Aromatic isocyanate-based PURs are characterized by higher mechanical properties and melting temperature due to their higher molecular weight deriving from the higher reactivity of aromatic isocyanates compared to aliphatic ones. Furthermore, their use increases the cohesion of hard domains leading to a slower degradation rate of the resulting PUR.[8,78] However, it has been showed that they could form aromatic amines after degradation *in vivo* causing toxic or carcinogenic effects.[79]
Aliphatic isocyanate	Aliphatic isocyanate-based PURs own lower mechanical properties, but they may be preferred in the synthesis of PURs for biomedical applications due to their increased biocompatibility.[8,79]

This finally influences polymer chain organization and, as a consequence, mechanical properties (**Table 1.3**). By incorporating degradable chain extenders based on amino acids or diesters (diol or diamine terminated), PURs with degradable hard segments can be designed.[65]

Table 1.3 PUR properties depending on chain extenders' chemical composition.[8]

Chain Extenders	PUR Characteristics
Diamine	PUR extended with a diamine usually have higher modulus and tensile strength, and lower elongation. In fact, diamine chain extenders quickly react with isocyanates to produce urea groups that can then produce biuret crosslinking. Poly(urethane urea)s are more difficult to process from the melt and have lower solubility in common solvents.[8,57]
Diol	Diol chain extenders bring to PURs with better elastic behavior and decreased modulus and tensile strength.[8,57]
Aromatic chain extender	Aromatic chain extenders increase PUR strength.[8]

Aliphatic chain extender	Aliphatic chain extenders produce softer PURs.[8]

1.5.2. Processability of Polyurethanes

As previously mentioned, molecular weight, and thus viscosity, sharply increases during PUR synthesis. Therefore, solvents are usually added to achieve better mixing, obtaining the so called solvent-borne PURs. In the solvent-based approach, polar organic solvents are used, such as dimethylacetamide (DMA), dimethylformamide (DMF), dimethylsulfoxide (DMSO), tetrahydrofuran (THF), 1,2-dichloroethane (DCE) and dichloromethane (DCM). The resulting thermoplastic PURs can be processed by melting or dissolving them in polar solvents.[8] Furthermore, they can be processed via different additive manufacturing techniques, exploiting heat or solvents.

More recently, eco-friendly waterborne PURs have received attention. Such PURs can be dispersed in water by incorporating hydrophilic groups into their chemical structure.

Waterborne PURs are usually characterized by low molecular weight, tensile strength and water resistance due to the low reactiveness of their chain extenders after dispersion.[81,82] In order to increase the mechanical properties of such PURs, monomers with high reactivity or containing free hydrogen atoms able to form hydrogen bond can be chosen to attain a greater extent of microphase separation.[83,84]

By exploiting the nanoscale dispersion of their particles and their self-assembly properties, waterborne PURs represents a versatile biomedical polymer platform for the design of drug/cell carriers. Additionally, waterborne PUR nanoparticles can be further processed in order to design thermo-sensitive hydrogels, electrospun fibers, elastic foams, and 3D printed scaffolds.

However, conventional waterborne PURs have often low viscosity, limiting their application as surface coatings and adhesives.[8]

1.5.3. Polyurethane Physico-Chemical and Mechanical Properties

The exceptional properties of PURs are strongly associated to their two-phase morphology: the presence of hard segments (which may be glassy or semi-crystalline) that are dispersed in a soft segment matrix (elastomeric).[85] This microphase separation occurs in polyurethanes due to the chemical incompatibility between hard and soft segments,[86,87] and it influences their physical characteristics, including their high tensile strength and modulus (**Figure 1.8**).

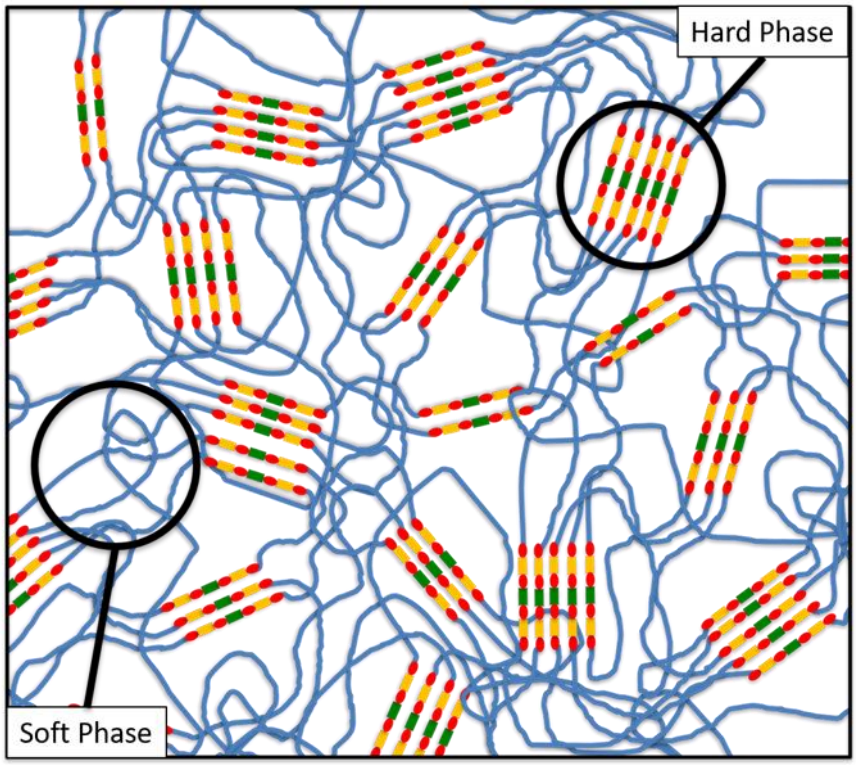

Figure 1.8 Polyurethane microphase separation.

PUR rubber-like behavior results from their hard domains that act as physical crosslinks by fixing the soft segments and preventing them to move when they are subjected to a stress. These

physical crosslinks are not thermally stable and the semi-crystalline hard phase can be melted upon heating. Consequently, linear PURs typically are thermoplastic elastomers that show rubber-like and thermoplastic behavior.[88]

The physico-chemical and mechanical properties of PURs are largely influenced by the aggregation state of their polymer chains as well as the properties of their building blocks. Thus, the PUR components (isocyanate, macrodiol and chain extender) can be selected in order to provide specific properties or functionalities. In particular, soft and hard segment chemical composition, molecular weight, content and degree of crystallinity, and crosslinking can influence PUR hydrophilicity, modulus, elongation, tensile and compressive strength.[57]

The relationships between PUR structure and properties can be generally divided into soft and hard segment effects (**Table 1.4**).

Table 1.4 PUR properties depending on chain extenders' chemical composition.

Soft segment effects	
Macrodiol Properties	**Effects**
By increasing soft segment molecular weight	Decrease in the initial modulus.[8,89]
	Reduction in modulus due to the increase of phase separation leading to increased soft segment mobility,[8,90]
	Reduction in permanent deformation due to the reduction in hard domain reorganization.[8,89]
By increasing soft segment crystallinity	Increase in modulus and tensile strength.[8,89,91]
	Reduction in elongation, percentage recovery and degradation rate.[8,89,91]

By combining different types of polyols	A combination of mechanical properties can be obtained.[8]

Hard segment effects

Isocyanate and Chain Extender Properties	Effects
By increasing hard segment content	Increase in modulus and tensile strength due to the increase in crosslinking.[8,91]
	Increase in modulus and tensile strength due to the increase in the size of the hard domains and phase separation.[8,91]
	Increase in permanent set.[8,91]
By using aromatic isocyanates (*vs* aliphatic isocyanates)	Increase in mechanical properties.[8]
By using aliphatic isocyanates (*vs* aromatic isocyanates)	Decrease in mechanical properties.[8]
By using symmetrical aliphatic isocyanates (*vs* asymmetrical isocyanates)	Increase in mechanical properties due to the increase in crystallization.[8]

PUR tensile strength is variable, with values ranging from a few MPa to tens MPa, while their elongation can exceed 1000%. Polyurethanes exhibit totally different mechanical characteristics with a higher elasticity than most of the other polymers usually considered for biomedical applications.[65] The unique elasticity of PURs derives from the formation of hydrogen bond between the hard segments, and the microphase separation of soft and hard segments, with hard segments acting as physical crosslinking.[8]

1.5.4. Polyurethane Degradation Kinetics

Polyurethanes have been initially evaluated for the fabrication of long term implants.[59–65] Despite their suitable mechanical strength, these polyurethanes failed due to their progressive degradation after implantation. Based on these evidences, in the 1990s intentionally degradable polyurethanes started to appear and find application in the emerging field of tissue engineering/regenerative medicine, beside the development of novel polyurethanes with improved biostability.

Living tissues constitute a very aggressive environment and polymers can be severely degraded after *in vivo* implantation. Polymer degradation in the biological environment results from the combination of different factors: enzymes, oxidizing agents and mechanical loads.[92]

Device degradation is generally attributed to a combination of several mechanisms, such as hydrolysis, oxidation, environmental stress cracking, enzymatic degradation and calcification. However, depending on PUR composition, some of these mechanisms can predominate over the others. Moreover, also white blood cells play an important role in *in vivo* degradation: neutrophils, monocytes and monocyte-derived macrophages attach to polymer surface after device implantation, leading to the presence of multinucleated giant cells and foreign body reaction.[92]

The available data indicate that PURs degrade faster *in vivo* compared to the *in vitro* test conditions developed to simulate biological environments.[93] Hydrolysis is one of the dominant mechanisms for PUR degradation in the aqueous environment of the body. Considering the characteristic two-phase morphology of PURs, it is possible to consider both soft and hard segment effects on degradation kinetics (**Table 1.5**).

Table 1.5 PUR degradation related to soft and hard segments.

Soft segment effects	
Macrodiol Properties	**Effects**
By decreasing the hydrophilic/hydrophobic balance of the components	Decrease in the rate of hydrolytic degradation by decreasing water diffusion through the PUR and restricting the access of water to the polymer chains in crystalline domains.[8,91,94]
By increasing crystallinity	
By incorporating non-degradable moieties into the soft segment	
Hard segment effects	
Isocyanate and Chain Extender Properties	**Effects**
By using biodegradable chain extender	Increase in degradation rate.[8,95]
By using peptide sequences as chain extenders	Addition of enzymatic degradation.[8,91]
By increasing hard segment content	Decrease in degradation rate.[47,96]

Hydrolysis is the main degradation mechanism of biodegradable PURs, due to the lysis of urethane bonds of hard segments and the ester bonds of soft segments (in the case of poly(ester urethane)s) in water environment.[8] Hydrolytic reactions can be catalyzed by a specific kind of enzyme (enzyme-catalyzed hydrolysis) or triggered by the presence of body fluids or water. The former usually has a faster degradation rate; moreover, it has been reported that some enzymes can degrade both aliphatic and aromatic polyesters (both soft and hard segment chemistries are implicated in enzymatic and oxidative degradation mechanisms). Moreover, since hard segments are less accessible by water and enzymes, soft segments usually degrade faster than hard segments.[8]

The mechanical properties and the degradation rate of PURs can be easily tuned by a proper selection of PUR building blocks, including changes in chemical structure, molecular weight, crystallinity, hydrogen bonding, and hydrophobicity of the monomers.

1.5.5. Polyurethane Biocompatibility

In vitro and *in vivo* PUR biological characterization has mainly focused on cellular, enzymatic, and tissue responses to the implanted material.[65] Cell/synthetic material interactions have been widely studied because of the role of biomaterials as cell supports to substitute and maintain organ or tissue functions. The first *in vitro* test to be performed is cytotoxicity, which investigates the effects of extracts from the biomaterial on cell morphology, viability or function. PUR biocompatibility has been assessed *in vitro* using various cell lines and assays. *In vivo* studies have also been conducted to assess body and tissue responses to polyurethane-based devices after implantation in the host environment.[65]

In general, PURs have been assessed to have good biocompatibility, maintaining sufficient cell adhesion and proliferation *in vitro*. However, normally the cytocompatibility is assessed only in the range of several days, without considering long-term efficacy and safety of PURs *in vivo* (weeks to months). PUR typical phase separated structure is accounted as a contributory factor to their biocompatibility. Takahara et al. demonstrated that platelet adherence and morphology on PUR films is significantly influenced by the size and characteristics of polymer microphase separation, surface heterogeneity and hydrophilicity.[97,98] Similarly, Hsu and Lin demonstrated that PURs with greater micro-phase separation result in superior biocompatibility.[99] Shah and Yun showed that L-tyrosine-based PUR ability to phase separate could be exploited to obtain heterogeneous surfaces with variable wettability that, in turn, influences cell adhesion, proliferation and distribution.[99] Attachment, growth and proliferation of different cell lines,

such as chondrocytes, osteoblasts, fibroblasts, stem cells, myoblasts and endothelial cells, on biodegradable polyurethanes with a wide variety of chemical compositions have been reported in the literature, demonstrating the favorable cell adhesion and growth characteristics of these polymers for several cell types.[93]

1.5.6. Polyurethane Functionalization

The heterogeneous morphology of polyurethanes is influenced by the environment the material interacts with. Therefore, PUR surface properties change in response to the nature of the surrounding environment: when the polymer is surrounded by a hydrophobic environment (e.g., PUR-air interface) the nonpolar components of the PUR (i.e. nonpolar macrodiol segments) preferentially segregate to the interphase. If the interphase is with a biological fluid, the PUR polar components preferentially adsorb to the interphase.[65]

In order to increase PUR biocompatibility and biostability, different strategies can be applied: surface modification by fluoropolymers, introduction of polysiloxane as soft segment, the addition of gold, silver nanoparticles, or nanosilica to form nanocomposites, blend with natural polymers.[8]

1.6. Technological Versatility of Additive Manufacturing Technologies

Additive manufacturing (AM), also known as 3D printing, fabricates objects layer-by-layer on an operating platform through computer-aided design (CAD).[100]

Conventional scaffold fabrication methods include solvent casting and particulate leaching, electro-spinning, emulsion freeze drying, phase separation and gas foaming. Using these methods, the physical properties of the resulting scaffolds have several limitations (i.e., poor control of pore size, shape and interconnectivity, scaffold geometry and dimensions).[101,102]

On the other hand, AM technologies allow the fabrication of customized design-dependent scaffolds with high precision and reproducibility, reduced waste, higher energy efficiency and lower time cost. As a consequence of its customizable nature, 3D printing technology is gaining more and more interest for application in the biomedical field where individual differences abound. In fact, geometry and architecture can be precisely controlled through the CAD in order to match the patient's specifications.[35,100,103–105]

Different additive manufacturing techniques have been applied in tissue engineering. They can be classified into two main groups according to the power source used during fabrication, namely temperature (nozzle based) or light (laser based) (**Figure 1.9**).[34,100,104,106]

All these techniques have their own disadvantages because most of them involve the application of heat, UV irradiation with the addition of a potentially toxic photo-initiator, and/or pressure to the polymer, or the solubilization of the material in an organic solvent to mold it into the desired shape.[103–105]

Because of these disadvantages, 3D printing technologies do not allow to use cells or biological molecules during the process.

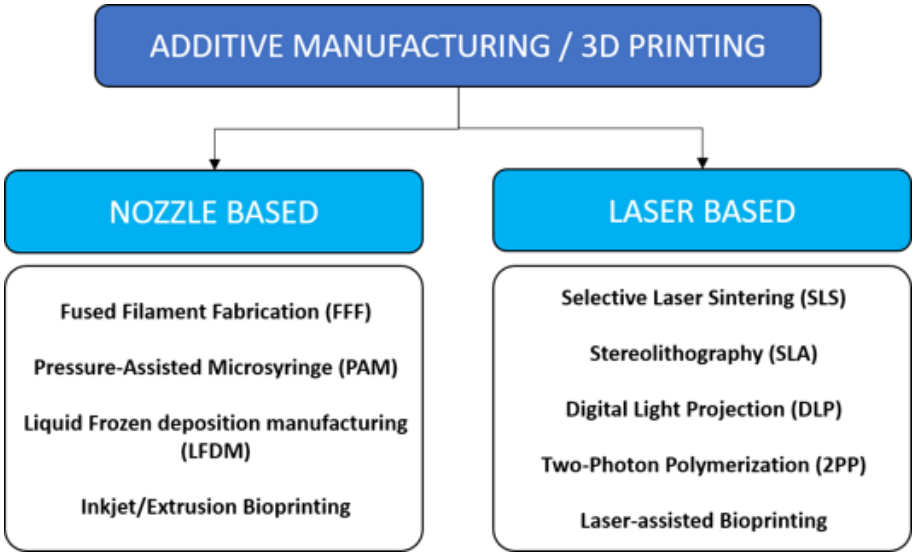

Figure 1.9 Additive manufacturing techniques.

The term bioprinting, instead, refers to a process that involves the use of a cellularized bioinks to design functional tissue constructs starting from 3D digital models.[107] Similarly to 3D printing, bioprinting can be classified depending on the involved process (**Figure 1.10**).[34,35,105,107]

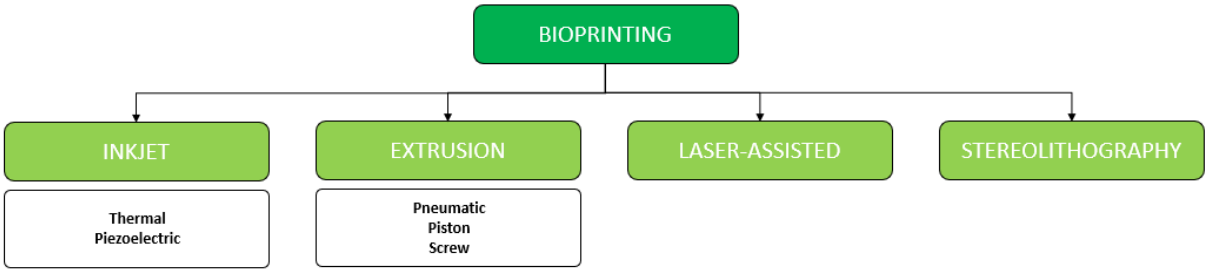

Figure 1.10 Bioprinting techniques.

Table 1.6 reports all the above-mentioned AM techniques with an outline of their specific characteristics and a schematic depiction of the main components.

Table 1.6 Additive manufacturing techniques' characteristics and pictures.

Melt-Extrusion-Based Techniques and Fused Filament Fabrication (FFF)

Description: Melt-extrusion techniques are based on the extrusion of a melted thermoplastic polymer through a heated nozzle and its deposition layer-by-layer on a construction platform according to a predefined pattern (computer-controlled motion). Among these techniques, the most common is the FFF, in which a filament of the desired material is fed through driving wheels and melted in a liquefier before extrusion from the nozzle (**Figure 1.11**). Usually, two separate extrusion nozzles can be used to deposit the building material and a supporting material which can be removed after the end of the printing process.[100,103,106]

Materials: Thermoplastic polymers, composites.

Resolution: 100-500 μm.[103,106]

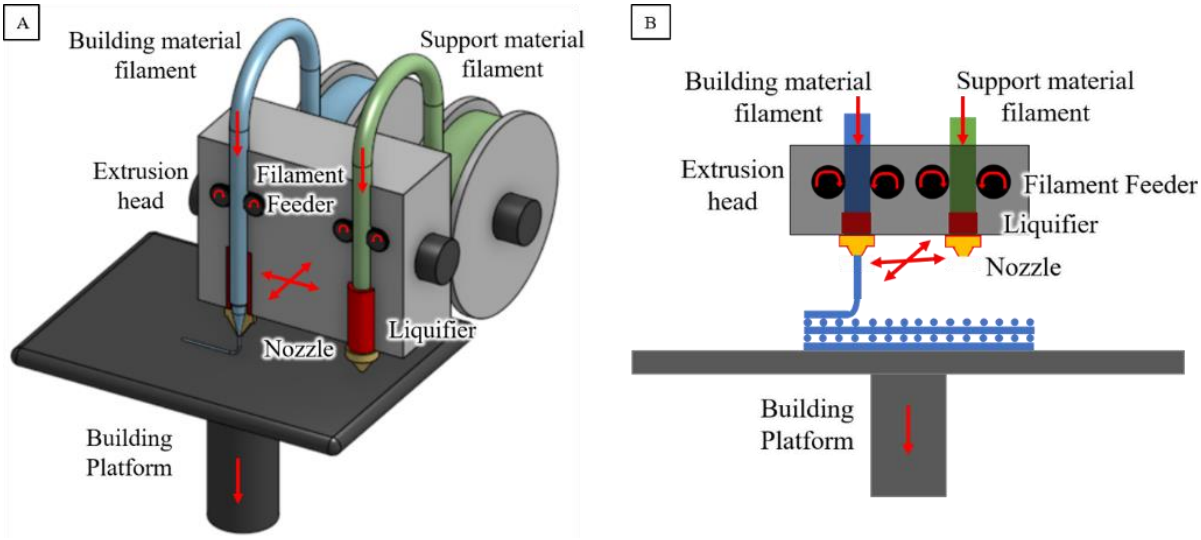

Figure 1.11 (A) 3D and **(B)** 2D schematics of Fused Filament Fabrication.

Pros:

- Fast and cheap technique, both considering equipment and raw material
- Good scaffold mechanical properties
- No material trapped within the scaffold
- Broad range of materials available

Cons:

- Possible thermal degradation of polymers
- Supports needed for structure overhangs
- Regular structure with high porosity
- Materials needed in shape of filaments
- Relatively low precision
- Too high temperature for cells and other biomolecules

Liquid Frozen Deposition Manufacturing (LFDM) and Pressure-Assisted Microsyringe (PAM)

Description: PAM and LFM are based on the pressure-assisted deposition of a polymeric solution in an organic solvent (**Figure 1.12**). Meanwhile PAM exploits the evaporation of a volatile solvent during the printing process in order to remove the solvent,[102] LFDM uses a low temperature chamber to allow the deposition process of a polymeric slurry followed by freeze-drying to remove the solvent.[100,103]

Materials: polymers, ceramics, composites, hydrogels.

Resolution: 5-600 µm for PAM,[102] 300-500 µm for LFDM.[103]

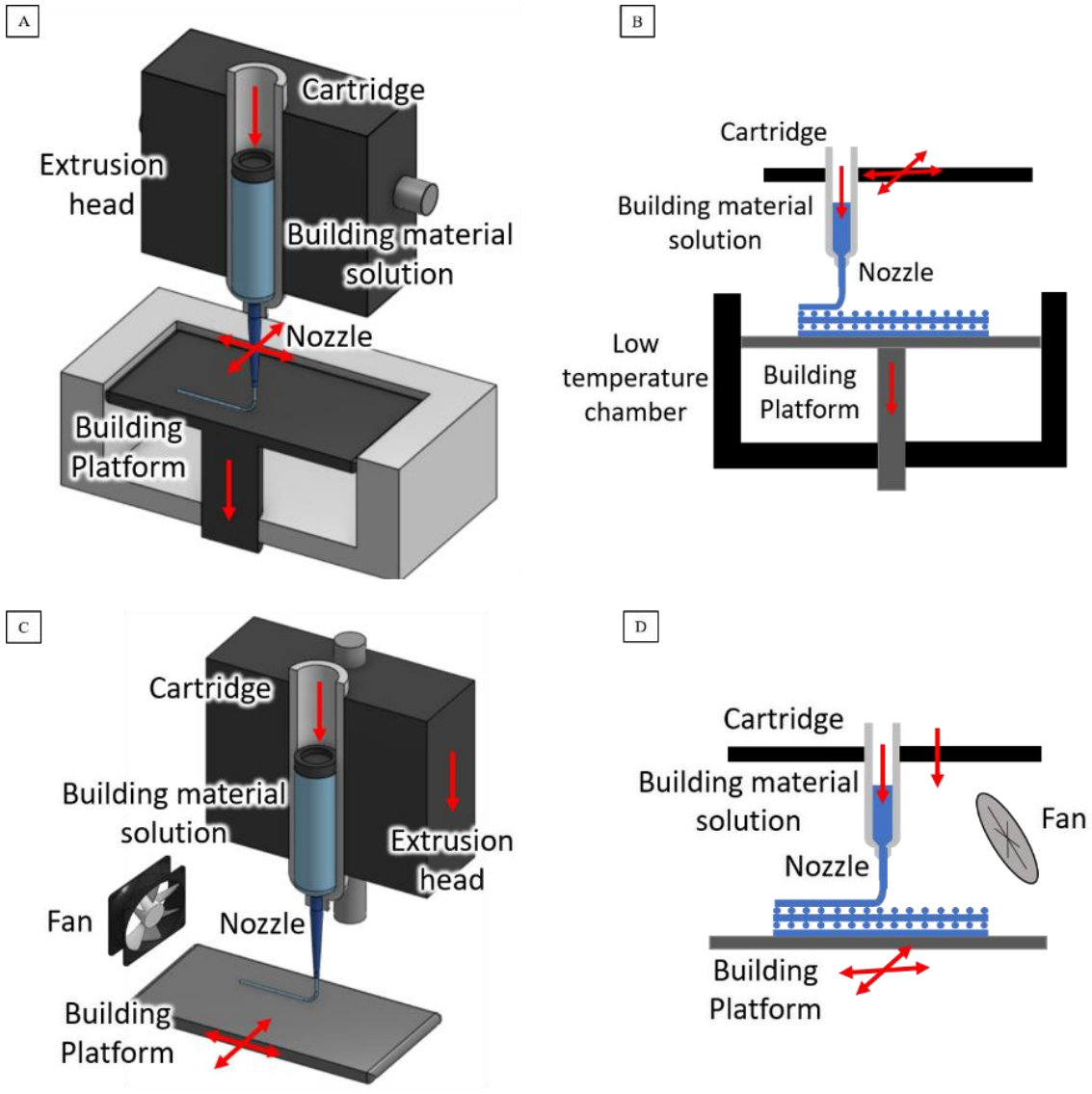

Figure 1.12 3D and 2D schematics of Liquid Frozen Deposition Manufacturing **(A**, **B)** and Pressure-Assisted Microsyringe **(C**, **D)**.

Pros:

- High accuracy on the deposition of polymeric solutions
- Possible micro-porosity due to freeze-drying
- Cheap technique

Cons:

- The need of organic solvents does not allow cell/biomolecule encapzulation during the printing
- Relatively low precision

Selective Laser Sintering (SLS)

Description: SLS is based on the application of high intensity laser beam (e.g. CO2 laser) to selectively sinter layers of polymer, ceramic or metal powder (**Figure 1.13**). After the generation of each layer, a new powder bed is spread by a roller to build up the 3D object layer-by-layer. The non-sintered materials serve as support for the subsequent layers.[100,103,106]

Materials: Polymers, ceramics, composites, metals.

Resolution: 50-1000 µm.[103,106]

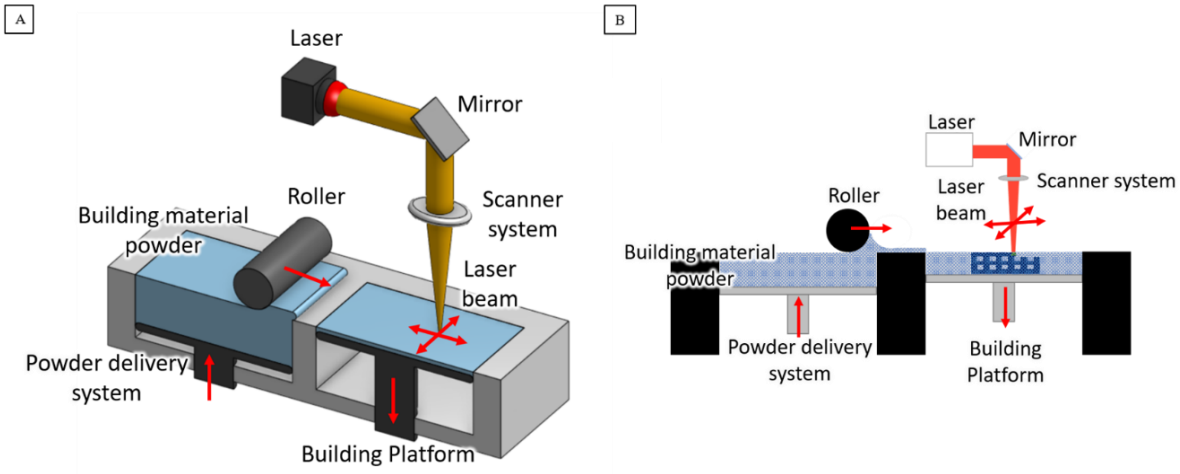

Figure 1.13 (A) 3D and **(B)** 2D schematics of Selective Laser Sintering.

Pros:

- No support materials needed (the bed of powders acts as support itself)
- Fast technique
- Broad range of materials available
- Creation of 3D scaffolds showing porosity at two different length-scales

Cons:

- Possible thermal degradation of polymers
- Limited and high-cost materials
- Trapped non-sintered material
- Rough scaffold surface (post treatment are often requested)
- Scaffolds generally present poor mechanical properties
- Complex technique

Stereolithography (SLA) and Digital Light Processing (DLP)

Description: SLA and DLP exploit ultraviolet (UV) light or laser to selectively polymerize layers of a photosensitive resin (**Figure 1.14**).

SLA is a bottom-up process in which a single beam laser is employed: after the polymerization of each layer, the printing platform is lowered in order to cover the previously built layer with a new layer of resin.[100,103,106] DLP, instead, is a top-down process that involves the use of a digital micromirror device (DMT) made of an array of mirrors that selectively diverts the light. Compared to conventional SLA, DLP is faster and a smaller amount of resin is necessary.[100] Further processing treatments are necessary to remove the non-polymerized resin and improve the polymerization between the layers (post-curing).

Materials: Polymers, composites, hydrogels.

Resolution: 15-150 µm or 0.5-10 µm depending on the systems.[103,106]

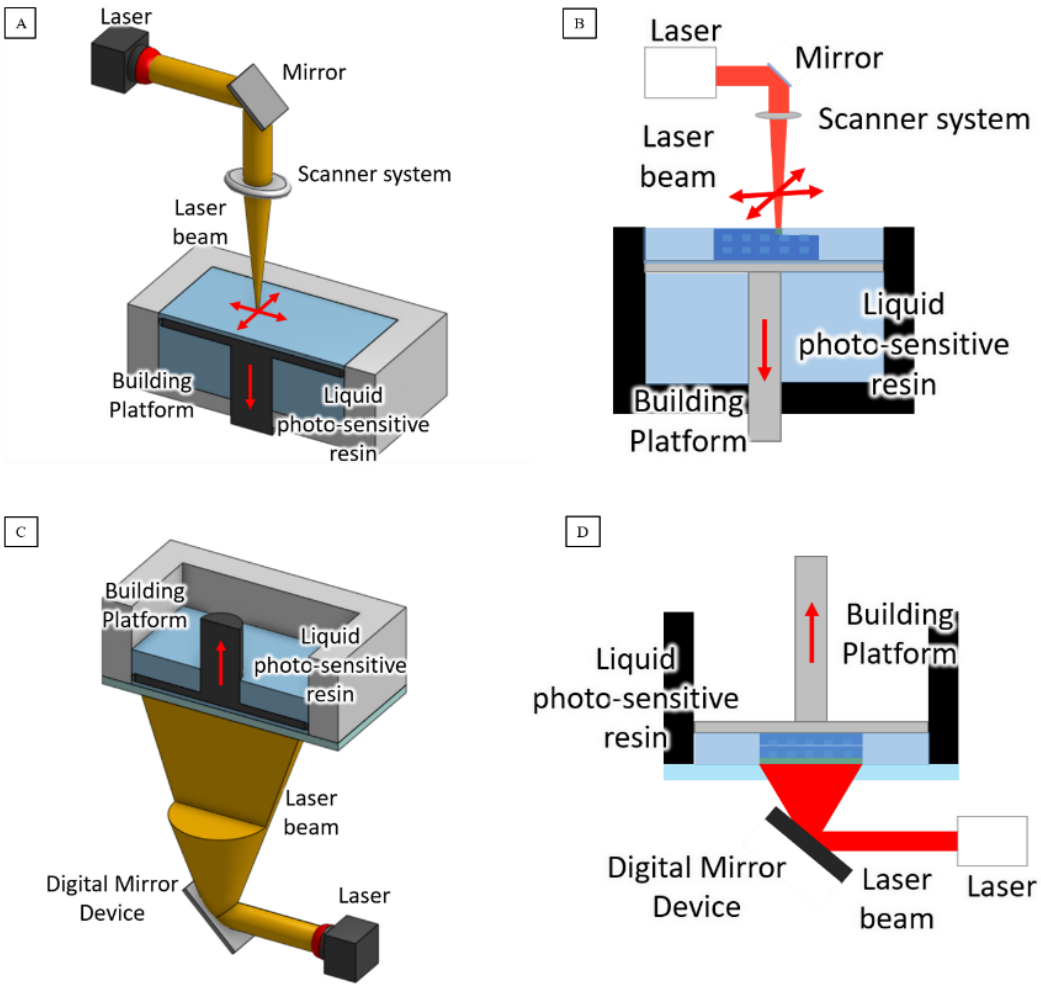

Figure 1.14 3D and 2D schematics of Stereolithography **(A**, B) and Digital Light Processing **(C**, **D)**.

Pros:

- Supports relatively easy to remove
- Possibility of encapsulating cells
- Good accuracy and surface finishing
- More complex geometries

Pros:

- Supports relatively easy to remove
- Possibility of encapsulating cells
- Good accuracy and surface finishing
- More complex geometries

DLP *vs* SLA

- Faster process
- Relatively smaller amount of photosensitive material required

SLA *vs* DLP

- Relatively higher amount of photosensitive material required
- Slower and more expensive technique

Two-Photon Polymerization (2PP)

Description: 2PP technique exploits a femtosecond laser radiation which results in highly localized temporal and spatial overlap of photons to induce chemical reactions between starter molecules and monomers of a photosensitive material (**Figure 1.15**).[108–110]

Materials: Polymers, composites, hydrogels.

Resolution: < 100 nm.[108]

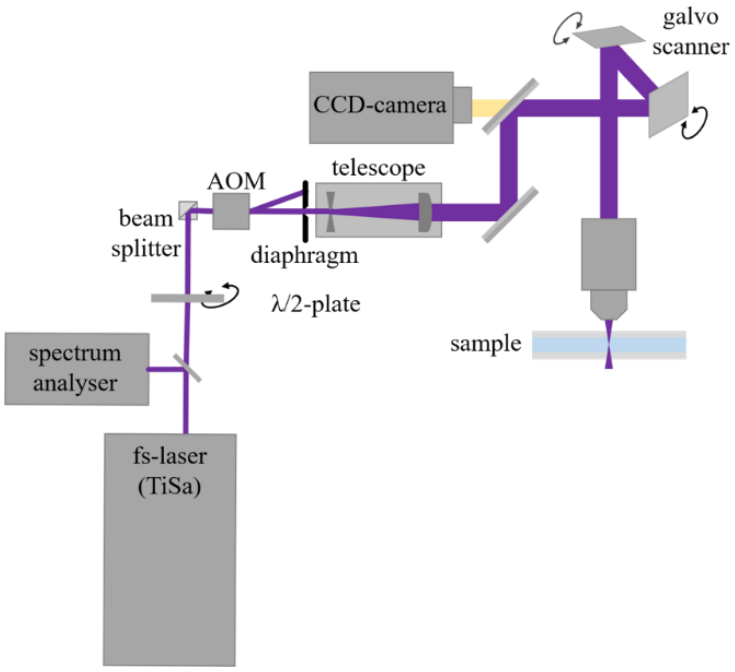

Figure 1.15 2D schematics of Two-Photons Polymerization.

Pros:

- Use of NIR as light source (*in vivo* application, higher depth of penetration)1
- High accuracy
- Small amount of photosensitive material required

Pros:

- Limited overall scaffold size
- Slow and very expensive technique
- Potentially toxic photoinitiators

Bioprinting

Description: 3D bioprinting is based on the use of bioinks to fabricate cellularized tissue constructs or organs with the use of 3D digital models.[35] Bioprinting includes different technologies that can be classified under four main categories: (i) inkjet-based (droplet based), (ii) extrusion-based, (iii) laser-based and (iv) stereolithography-based (**Figure 1.16**).

Inkjet bioprinting is a process adapted from the inkjet printing technology, based on the deposition of bioink droplets. Inkjet bioprinting can be further divided into subcategories depending on the type of trigger applied to form the droplet (e.g. thermal, piezoelectric).

Extrusion bioprinting is based on the squeezing out of the bioink from a nozzle forming a filament. The bioink can be extruded using pneumatic pressure or mechanical force by means of a piston or a screw.

Laser-assisted bioprinting includes different technologies based on the application of laser energy to pattern the bioink in a 3D structure. The most common approach involves the use of a laser energy absorbing layer (metal layer on which the bioink is attached) in order to generate a gas pressure and thus form a droplet of the bioink.[35]

Stereolithography bioprinting is a process based on classic SLA technology.[107]

Materials: Hydrogels and bioinks.

Resolution: 50 µm for inkjet-based, 100 µm for extrusion-based,

1-3 µm for laser-based[35],

1-150 µm for stereolithography-based.[103,106]

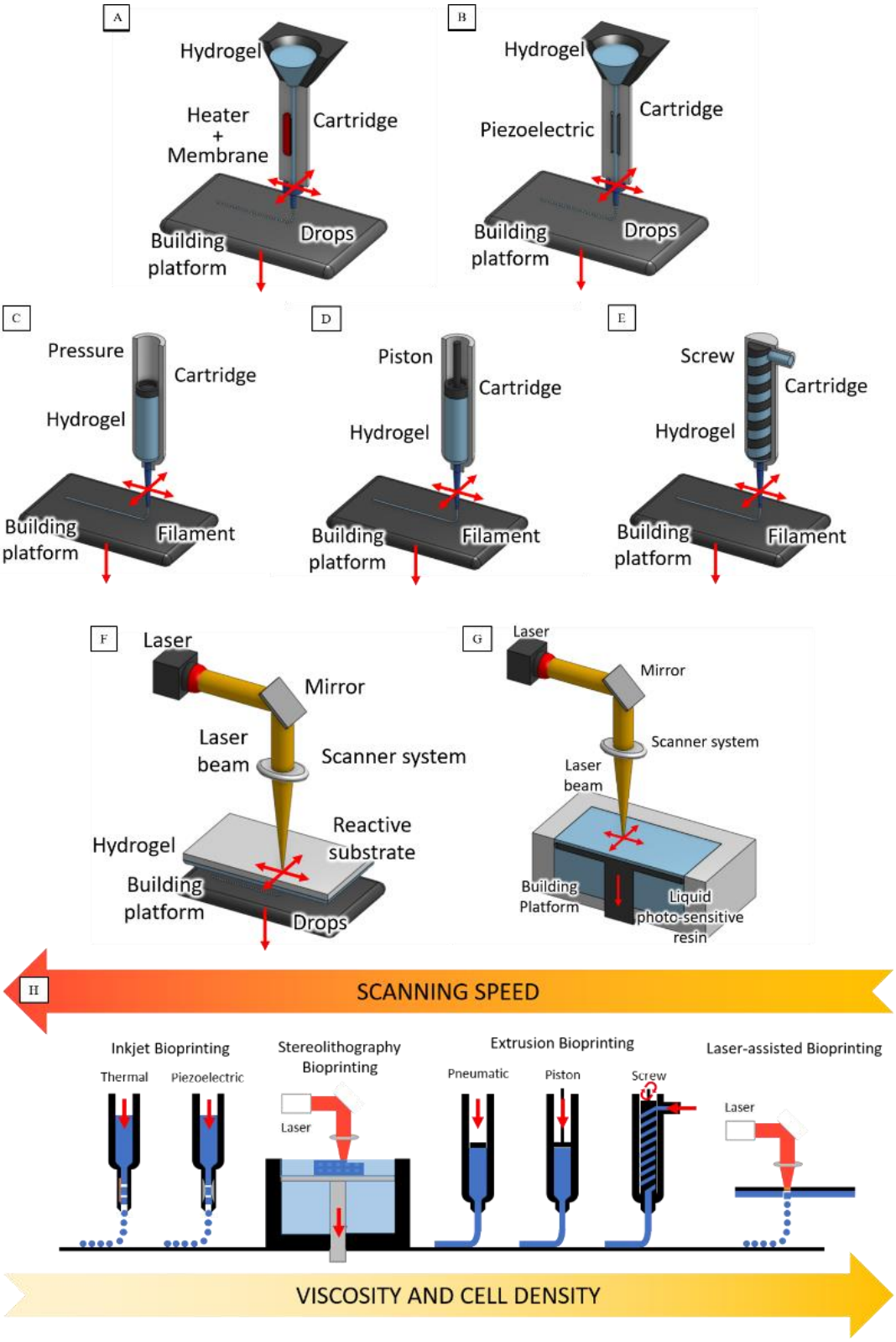

Figure 1.16 (**A-G**) 3D and (**H**) 2D schematics of 3D Bioprinting approaches (Inkjet-based, Extrusion-based, Laser-based and Stereolithography-based).

Pros:	Cons:
● Use of cells and biomolecules during the process leding to a homogeneus distribution	● Need to compromise on the resolution in order to guarantee cell viability
Inkjet Bioprinting	Inkjet Bioprinting
● High resolution and printing speed	● Low-viscosity bioinks (~ 3–12 mPa·s)
● Possibility to introduce cell concentration gradients	● Need of crosslinking step
	● Nozzle clogging
	● Limits on the cell concentration
Extrusion Bioprinting	Extrusion Bioprinting
● Scalability	● Low resolution
● Printability of high viscosity bioinks (~ 600 kPa·s)	● Risk of cell damaging by shearing force
● High cell concentration	● Nozzle-clogging
	● Need of bioinks with shearthinning property
Laser-assisted Bioprinting	Laser-assisted Bioprinting
● High resolution with the possibility to print a single cell per droplet	● Risk of photonic cell damage
● Non-contact and nozzle-free approach	● Risk of metallic nanoparticles induced cytotoxicity
● High cell viabilities and densities	● Complex and expensive technology
Sterolithography Bioprinting	Sterolithography Bioprinting
● High resolution and printing speed	● Low-viscosity bioinks
● Non-contact and nozzle-free approach	● Risk of photonic cell damage
	● Potentially toxic photoinitiators

Additive manufacturing has several advantages and it is currently considered a highly effective technology with the potential to revolutionize the tissue engineering/regenerative medicine field. However, many challenges still remain to be overcome.

References

[1] J. Vacanti, *J. Pediatr. Surg*. **2010**, *45*, 1.

[2] N.T. Elliott, F. Yuan, *J. Pharm. Sci*. **2011**, *100*, 1.

[3] G. Jensen, C. Morrill, Y. Huang, *Acta Pharm. Sin. B* **2018**, *8*, 5.

[4] K.M. Yamada, E. Cukierman, *Cell* **2007**, *130*, 4.

[5] S.J. Hollister, R.D. Maddox, J.M. Taboas, *Biomaterials* **2002**, *23*.

[6] B. Dhandayuthapani, Y. Yoshida, T. Maekawa, D.S. Kumar, *Int. J. Polym. Sci*. **2011**, *2011*, 2.

[7] S.C. Ligon, R. Liska, J. Stampf, M. Gurr, R. Mülhaup, *Chem. Rev*. **2017**, *117*.

[8] J. Stuart, L. Cooper, *Advances in Polyurethane BiomaterialsBiomaterials*, Woodhead Publishing, Duxford, UK **2016**.

[9] American Chemistry Council, www.polyurethane.americanchemistry.com/Applications/

[10] K. Hayashi, K. Takamizawa, T. Saito, K. Kira, K. Hiramatsu, K. Kondo, *J. Biomed. Mater. Res.* **1989**, *23*, 2.

[11] N. Handel, J. A. Jensen, Q. Black, J.R. Waisman, M.J. Silverstein, M. Gold, *Plast. Reconstr. Surg.* **1995**, *96*, 7.

[12] N. Handel, M.J. Silverstein, J.A. Jensen, A. Collins, K. Zierk, *Plast. Reconstr. Surg*. **1991**, *88*, 3.

[13] R.G. Hauser, D. Cannom, D.L. Hayes, V. Parsonnet, J. Hayes, N. Ratliff, G.F.O. Tyers, A.E. Epstein, S.C. Vlay, S. Furman, J. Gross, *Pacing Clin. Electrophysiol*. **2002**, *25*, 6.

[14] R.E. Phillips, M.C. Smith, R.J. Thoma, *J. Biomater. Appl.* **1988**, *3*, 2.

[15] S. A. Guelcher, *Tissue Eng. Part B Rev.* **2008**, *14*, 1.

[16] E. Caló, V.V. Khutoryanskiy, *Eur. Polym. J.* **2015**, *65*.

[17] P. Petrini, S. Farè, A. Piva, M.C. Tanzi, *J. Mater. Sci. Mater. Med*. **2003**, *14*, 8.

[18] H. Janik, M. Marzec, *Mater. Sci. Eng. C* **2015**, *48*.

[19] K. Gorna, S. Gogolewski, *J. Biomed. Mater. Res. Part A* **2003**, *67*, 3.

[20] S. Gogolewski, K. Gorna, A.S. Turner, *J. Biomed. Mater. Res*. **2001**, *77*.

[21] X. Miao, Y. Hu, J. Liu, A. P. Wong, *Mater. Lett*. **2004**, *58*, 3-4.

[22] V. Chiono, P. Mozetic, M. Boffito, S. Sartori, E. Gioffredi, A. Silvestri, A. Rainer, S.M. Giannitelli, M. Trombetta, D. Nurzynska, F. Di Meglio, C. Castaldo, R. Miraglia, S. Montagnani, G. Ciardelli, *Interface Focus* **2014**, *4*, 1.

[23] M. Boffito , F. Di Meglio , P. Mozetic , S.M. Giannitelli, I. Carmagnola, C. Castaldo, D. Nurzynska, A.M. Sacco, R. Miraglia, S. Montagnani, N. Vitale, M. Brancaccio, G. Tarone, F. Basoli, V. Chiono, *PLoS One* **2018**, *13*, 7.

[24] M. Boffito, E. Gioffredi, V. Chiono, S. Calzone, E. Ranzato, S. Martinotti, G. Ciardelli, *Polym. Int.* **2016**, *65*, 7.

[25] S. Sartori, M. Boffito, P. Serafini, A. Caporale, A. Silvestri, E. Bernardi, M.P. Sassi, F. Boccafoschi, G. Ciardelli, *React. Funct. Polym*. **2013**, *73*, 10.

[26] A. Silvestri, S. Sartori, M. Boffito, C. Mattu, A.M. Di Rienzo, F. Boccafoschi, G. Ciardelli, *J. Biomed. Mater. Res. Part B: Appl. Biomater.* **2013**, *102*, 5.

[27] C. Tonda-Turo, M. Boffito, C. Cassino, P. Gentile, G. Ciardelli, *Mater. Lett*. **2016**, *167*.

[28] V. Chiono, S. Sartori, S. Calzone, M. Boffito, C. Tonda-Turo, C. Mattu, P. Gentile, G. Ciardelli, in *Science and Principles of Biodegradable and Bioresorbable Medical Polymers* (Ed: Xiang Zhang), Woodhead Publishing, Duxford, UK **2017**, pp. 189-216.

[29] M. Boffito, S. Sartori, C. Mattu, G. Ciardelli, in *Advances in Polyurethane Biomaterials* (Ed: J. Stuart, L. Cooper), Woodhead Publishing, Duxford, UK **2017**, pp. 387–416.

[30] C. Pontremoli, M. Boffito, S. Fiorilli, R. Laurano, A. Torchio, A. Bari, C. Tonda-Turo, G. Ciardelli, C. Vitale-Brovarone, *Chem. Eng. J.* **2018**, *340*.

[31] C. Mattu, M. Boffito, S. Sartori, E. Ranzato, E. Bernardi, M. P. Sassi, A. M. Di Rienzo, G. Ciardelli *J. Nanoparticle Res*. **2012**, *14*.

[32] C. Mattu, R.M. Pabari, M. Boffito, S. Sartori, G. Ciardelli, Z. Ramtoola, *Eur J Pharm Biopharm* **2013**, *85*, 3.

[33] C. Mattu, A. Silvestri, T.R. Wang, M. Boffito, E. Ranzato, C. Cassino, G. Ciofani, G. Ciardelli, *Polym. Int*. **2016**, *65*, 7.

[34] J. Lee, J. An, C.K. Chua, *Appl. Mater. Today* **2017**, *7*.

[35] S. Vijayavenkataraman, W. C. Yan, W. F. Lu, C. H. Wang, J. Y. H. Fuh, *Adv. Drug Deliv. Rev.* **2018**.

[36] L. U. Sneddon, L. G. Halsey, N. R. Bury, *J. Exp. Biol.* **2017**, *220*, 3007.

[37] R. Langer, D. A. Tirrell, *Nature* **2004**, *428*, 487.

[38] T. K. Merceron, M. Burt, Y. Seol, H. Kang, S. J. Lee, J. J. Yoo, *Biofabrication* **2015**, *7*.

[39] R. L. R. L. J. Vacanti, Ed., *Principles of Tissue Engineering*, **2014**.

[40] S. J. Hollister, *Nat. Mater.* **2005**, *4*, 518.

[41] Q. L. Loh, C. Choong, *Tissue Eng. Part B Rev.* **2013**, *19*, 485.

[42] R. L. and J. P. Vacanti, *Science (80-.).* **2014**, *31*, 920.

[43] Q.Z. Chen, S.E. Harding, N. N. Ali, A.R. Lyon, A.R. Boccaccini, *Mater. Sci. Eng. R Reports* **2008**, *59*, 1.

[44] Y. E. Kim, Y. J. Kim, *Polym. J.* **2013**, *45*, 845.

[45] G.A. Holzapfel, R.W. Ogden, *Biomechanics of Soft Tissue in Cardiovascular Systems*, Springer, Berlin, DE **2003**.

[46] A. Arbor, F.M. Company, S. A. Goldstein, *J. Biomech* **1994**, *21*, 4.

[47] A. Nair, L. Tang, *Semin. Immunol.* **2017**, *29*, 62.

[48] K. Hung, C. Tseng, S. Hsu, *Adv. Healthc. Mater.* **2014**, *3*, 1578.

[49] D. Choudhury, H.W. Tun, T. Wang, M.W. Naing, *Trends Biotechnol*. **2018**, *36*, 8.

[50] D. Puppi, F. Chiellini, A.M. Piras, E. Chiellini, *Prog. Polym. Sci*. **2010**, *35*, 4.

[51] F. Hsieh, H. Lin, S. Hsu, *Biomaterials* **2015**, *71*.

[52] S. Pyo, P. Wang, H.H. Hwang, W. Zhu, J. Warner, S. Chen, *Appl. Mater. Interfaces* **2016**, *9*, 1.

[53] N. Kumar, R.S. Langer, A.J. Domb, *Adv. Drug Deliv. Rev*. **2002**, *54*, 7.

[54] I. Teasdale, O. Brüggemann, *Polymers* **2013**, *5*, 1.

[55] S. Kim, S. Liu, *Biomater. Sci. Eng*. **2018**, *4*, 5.

[56] K.P. Luefa, F. Stelzera, F. Wiesbrock, *Chem. Biochem. Eng.* **2015**, *29*, 2.

[57] S. Ramesh, P. Rajalingam, G. Radhakrishnan, *Polym. Int*. **1991**, *25*, 4.

[58] N.M.K. Lamba, K.A. Woodhouse, S.L. Cooper, *Polyurethanes in Biomedical Applications*, CRC Press, Boca Raton, USA **1998**.

[59] A. Burke, N. Hasirci, in *Biomaterials: From Molecules to Engineered Tissue* (Ed. N. Hasirci, V. Hasirci), CRC Press, Boca Raton, USA **2004**, pp. 83-101.

[60] J.M. Anderson, A. Hiltner, M.J. Wiggins, M.A. Schubert, T.O. Collier, W.J. Kao, A.B. Mathur, *Polym. Int*. **1998**, *46*, 3.

[61] R. S. Bezwada, *Polym. Mater. Sci. Eng*. **2009**, *101*.

[62] J. W. Boretos, W. S. Pierce, *J. Biomed. Mater. Res*. **1968**, *2*, 1.

[63] S. Gogolewski, *Colloid Polym. Sci.* **1989**, *267*, 9.

[64] P.A. Gunatillake, D.J. Martin, G.F. Meijs, S.J. McCarthy, R. Adhikari, *Aust. J. Chem*. **2003**, *56*, 6.

[65] P. Vermette, H. J. Griesser, G. Laroche, R. Guidoin, *Landes Biosci*. **2001**, *6*.

[66] J. P. Santerre, K. Woodhouse, G. Laroche, R. S. Labow, *Biomaterials* **2005**, *26*.

[67] G.T. Howard, *Int. Biodeterior. Biodegradation* **2002**, *49*.

[68] M. Szycher, *Szycher's Handbook of Polyurethanes*, CRC Press, Boca Raton, USA **2013**.

[69] A. Hafeman, J. Davidson, S. Guelcher, *PMSE Prepr* **2007**, *97*.

[70] D.J. Martin, G.F. Meijs, P.A. Gunatillake, S.P. Yozghatlian, G.M. Renwick, *J. Appl. Poymer Sci.* **1999**, *71*.

[71] K. Gisselfält, B. Helgee, *Macromol. Mater. Eng.* **2003**, *288*, 3.

[72] J. Rychlý, A. Lattuati-Derieux, B. Lavédrine, L. Matisová-Rychlá, M. Malíková, K. Csomorová, *Polym. Degrad. Stab*. **2011**, *96*, 4.

[73] E. Yilgör, E. Burgaz, E. Yurtsever, İ. Yilgör, *Polymer* **2000**, *41*, 3.

[74] D.G. Thompson, J.C. Osborn, E.M. Kober, J.R. Schoonover, *Polym. Degrad. Stab*. **2006**, *91*, 12.

[75] S. Awasthi, D. Agarwal, *Pigment. Resin. Technol.* **2010**, *39*, 4.

[76] M. Špírková, J. Pavličević, A. Strachota, R. Poreba, O. Bera, L. Kaprálková, *Eur. Polym. J*. **2011**, *47*, 5.

[77] M.C. Tanzi, D. Mantovani, P. Petrini, R. Guidoin, G. Laroche, *J. Biomed. Mater. Res*. **1997**, *36*, 4.

[78] D.K. Chattopadhyay, K.V.S.N. Raju, *Prog. Polym. Sci*. **2007**, *32*, 3.

[79] H.K. Lindberg, A. Korpi, T. Santonen, K. Säkkinen, M. Järvelä, J. Tornaeus, Mutat. Res. **2011**, *723*, 1.

[80] J. Datta, *Ind. Crops Prod*. **2014**, *61*.

[81] L. Hou, Y. Ding, Z. Zhang, Z. Sun, Z. Shan, *Colloids Surf. A Physicochem. Eng. Asp*. **2015**, *467*.

[82] M.S. Yen, P.Y. Tsai, P.D. Hong, *Colloids Surf. A Physicochem. Eng. Asp*. **2006**, *279*, 1-3.

[83] M.M. Rahman, H.D. Kim, *J. Appl. Polym. Sci*. **2016**, *102*, 6.

[84] S.H. Park, I.D. Chung, A. Hartwig, B.K. Kim, *Colloids Surf. A Physicochem. Eng. Asp*. **2007**, *305*, 1-3.

[85] S.L. Cooper, A.V. Tobolsky, *J. Appl. Polym. Sci*. **1966**, *10*, 12.

[86] M.H. Hansen, *Ind. Eng. Chem. Prod. Res. Dev*. **1969**, *8*, 1.

[87] C.M. Hansen, *Prog. Org. Coat*. **2004**, *51*.

[88] Q. Chen, L. Shuling, G.A. Thouas, *Prog. Polym. Sci*. **2013**, *38*, 3-4.

[89] Z. Ma, Y. Hong, D.M. Nelson, J.E. Pichamuthu, C.E. Leeson, W.R. Wagner, *Biomacromolecules* **2011**, *12*, 9.

[90] K. Gisselfalt, B. Helgee, *Macromol. Mater. Eng*. **2003**, *288*, 3.

[91] G.A. Skarja, K.A. Woodhouse, J. Appl. Polym. Sci. **2000**, *75*, 12.

[92] J.V. Cauich-Rodríguez, L.H. Chan-Chan, F. Hernandez-Sánchez, J.M. Cervantes-Uc, in *Biomaterials Sciences and Biomedical Applications* (Ed: R. Pignatello), InTech, London, UK **2013**.

[93] A. Pathiraja, R. Gunatillake, R. Adhikari, in *Biodegradable Polymers: Processing, Degradation and Applications* (Ed: G.P. Felton), Nova Science Publishers, New York, USA **2011**.

[94] D. Cohn, T. Stern, M.F. González, J. Epstein, *J. Biomed. Mater. Res*. **2002**, *59*, 2.

[95] L. Tatai, T.G. Moore, R. Adhikari, F. Malherbe, R. Jayasekara, I. Griffiths, P.A. Gunatillake, *Biomaterials* **2007**, *28*.

[96] A. Lendlein, R. Langer, *Science* **2002**, *296*, 5573.

[97] A.T.J.I. Takahara, T. Kajiyama, M. Takayanagi, W.J. MacKnight, *Polymer* **1985**, *26*.

[98] A.O.A. Takahara, S.L. Cooper, A.J. Coury, *Biomaterials* **1991**, *12*.

[99] S.H. Hsu, Z.C. Lin, *Colloids Surfaces B Biointerfaces* **2004**, *36*, 1.

[100] G.H. Wu, S. Hsu, *J. Med. Biol. Eng*. **2015**, *35*, 3.

[101] X. Wei, X. Wang, Y. Yan, R. Zhang, *J. Bioact. Compat. Polym*. **2008**, *223*.

[102] L. Cheng, L. Changyong, *International Conference on Information Sciences, Machinery, Materials and Energy* **2015**.

[103] C. Mota, D. Puppi, F. Chiellini, E. Chiellini, *J. Tissue Eng. Regen. Med*. **2015**, *9*.

[104] X. Wang, Q. Ao, X. Tian, J. Fan, Y. Wei, W. Hou, H. Tong, S. Bai, *Materials* **2016**, *9*, 10.

[105] W. Aljohani, M.W. Ullah, X. Zhang, G. Yang, *Int. J. Biol. Macromol*. **2018**, *107*, A.

[106] B. Bhushan, M. Caspers, *Microsyst. Technol*. **2017**, *23*, 4.

[107] D. Choudhury, S. Anand, M.W. Naing, *Int. J. Bioprinting* **2018**, *4*, 2.

[108] X. Zhou, Y. Hou, J. Lin, *AIP Adv*. **2015**, *5*, 3.

[109] T. Weiß, G. Hildebrand, R. Schade, R., K. Liefeith, *Eng. Life Sci*. **2009**, *9.*

[110] A. Doraiswamy, C. Jin, R.J. Narayan, P. Mageswaran, P. Mente, R. Modi, R. Auyeung, D.B. Chrisey, A. Ovsianikov, B. Chichkov, *Acta Biomater*. **2006**, *2*, 3.

Chapter 2

Literaure Review

Abstract:

The concurrent exploitation of the chemical and technological versatility of polyurethanes and additive manufacturing, respectively, could realistically advance the biomedical field, contributing to the definition of a new material/technology platform which, in principle, could answer to every specific need of researchers, patients, surgeons and medical doctors.

This chapter provides a critical literature overview on the application of polyurethanes in additive manufacturing for biomedical strategies, showing that their combination could effectively lead in the future to the fabrication of the optimal scaffolds for the regeneration of almost all tissues/organs.

Keywords:

Tissue Engineering, Regenerative Medicine, Scaffold, Polyurethanes, Additive Manufacturing.

2.1. Polyurethane in Additive Manufacturing

By combining AM and PURs, multifunctional and smart products can be finely designed and customized to be applied to each damaged part of the body.

Their excellent processability and versatility allow PURs to be fabricated by various 3D printing procedures for different medical applications (e.g., fabrication of scaffolds for regenerative medicine applications, 3D in vitro models, and lab-on-chips). PURs have been also exploited as substrates for 3D printed biological sensors and as molding or forming materials in indirect additive manufacturing techniques, where they are casted in 3D printed molds as infills or used to form the molds. Different custom-made and commercially available PURs (e.g. thermoplastic PURs, water-bone dispersions and stimuli sensitive PUR-based solutions) have been studied for additive manufacturing approaches.

2.1.1. Regenerative Medicine

Thermoplastic PURs,[1–5] water-bone PUR-based dispersions and stimuli sensitive PUR solutions[6–10] have been applied in different AM techniques, such as SLS,[5] melt-extrusion technologies and FFF,[1–4,11–14] LFDM[9,10,15–19] and PAM,[20] inkjet printing,[21–23], DLP[24–26] and bioprinting, [6–8] with the aim of designing 3D matrices for regenerative medicine applications.

2.1.1.1. Thermoplastic Polyurethanes in Selective Laser Sintering, Melt Extrusion Deposition & Fused Filament Fabrication

Polymer powder and filament are processed under high temperature in SLS and FFF, respectively. The exposure to a high temperature (≥ melt temperature) for a prolonged period of

time exposes the materials to the risk of thermal degradation with a consequent reduction of the molecular weight and tensile strength. In the case of PURs, biodegradable polyesters, often incorporated as soft segments in PUR synthesis, are subjected to degradation at high temperatures (pyrohydrolysis), which leads to a detrimental loss in mechanical properties and workability, and the release of acidic components. Therefore, the modulation of the temperature and the printing time are crucial parameters in the set-up of both FFF and SLS protocols. Moreover, the high temperature does not allow to use cells during the printing process. Thus, cells have to be seeded on the printed scaffolds with all the consequent drawbacks (e.g., poor cell distribution and penetration within the 3D scaffold).

Nevertheless, despite these drawbacks, the use of biodegradable thermoplastic PURs has been thoroughly investigated in both the mentioned techniques. There are some commercially available biocompatible PURs for SLS (Desmosint®, Bayer - Elastollan®, BASF) and FFF (Desmopan®, Bayer - ECO TPU, Falshforge) applications. In other works, instead, researchers preliminary processed commercial or custom-made PURs to make them suitable for AM techniques (e.g., by extruding them in the form of filaments of appropriate diameters for FFF applications). [2,3,12–14]

Vasquez et al.[5] applied SLS to 3D print a commercial biocompatible PUR (Elastollan, BASF) and studied the correlation between the merging of PUR powder (granulometry: 58 ± 22 μm) and the resultant mechanical properties by changing the sintering energy and the laser scanning rate. They demonstrated that by increasing temperature and laser scanning rate, the mechanical properties of the resulting construct increase due to the greater extent to which the PUR powder merge.

Some research groups exploited PUR chemical versatility in AM techniques based on extrusion fused deposition, including FFF.[1–4,11] In this context different families of PURs were studied

(biodegradable,[1–4] non-degradable[11] and shape memory[12–14]) for different applications (cardiac tissue,[1] trachea,[2] muscle-tendon unit[4] and cartilage tissue regeneration[11]).

For instance, Chiono et al.[1], Tsai et al.[2] and Chen et al.[3] applied biodegradable thermoplastic PURs for printing 3D elastic matrices. In the first two works, custom-made PURs have been exploited to modulate the final scaffold's properties. Chiono et al.[1] designed a biocompatible PUR with high molecular weight, starting from PCL diol, 1,4-butane diisocyanate (BDI) and L-lysine ethyl ester as chain extender, while Tsai and colleagues[2] synthesized two different PURs starting from a polyester polyol (PCL diol) and a polyether polyol, an aromatic diisocyanate (4,4-methylenebis(phenyl isocyanate)) and a short linear diol chain extender (1,4-butane diol). In the last work, instead, Chen et al.[3] used a commercially available PUR (Pearlthane) in combination with PLA and graphene oxide (GO). In Chiono's work,[1] a custom-designed melt extrusion system was used to fabricate bi-layered scaffolds with a 0°/90° lay-down pattern, showing high reproducible quality. The printed scaffolds showed the elastomeric behavior typical of PURs and biocompatibility with human cardiac progenitor cells (hCPCs), showing that the cells adhere, spread and proliferate (**Figure 2.1 A** and **B**). In this work, PUR powders were directly used to feed the custom-made AM instrument. In Tsai's and Chen's works,[2,3] instead, the PURs were first extruded to obtain 1.75 mm filaments, suitable for commercial FFF instruments. With the aim of mimicking adult trachea structural and mechanical properties, Tsai and coworkers[2] printed scaffolds consisting of tubular elastic structures with different diameter and thickness, showing structural heterogeneity, material anisotropy and biomechanical versatility (**Figure 2.1 C** and **D**). The authors showed the possibility to design elastic matrices mimicking the structure and the mechanical properties of a heterogeneous tissue such as the trachea. Moreover, they demonstrated the possibility to control the porosity and the biocompatibility with bronchial epithelial cells. The scaffolds printed by Chen and colleagues[3]

exhibited good biocompatibility with NIH/3T3 fibroblast cells, and showed that the mechanical response of the construct is highly dependent on printing orientation (**Figure 2.1 E-G**).

In 2015, Merceron et al.[4] presented a new method for the fabrication of complex structures based on different synthetic biomaterials and cell types to mimic a muscle-tendon unit (MTU). Two synthetic polymeric materials were used as scaffolding components (a PUR and PCL) and two cellularized bioinks as the biological components (hyaluronic acid / gelatin / fibrinogen containing C2C12 myoblasts and NIH/3T3 fibroblasts). The MTU construct was designed using a commercial thermoplastic PUR (Tecoflex LM-95A, Lubrizol, Wickliffe, USA) with C2C12 myoblasts for the muscle side, and PCL with NIH/3T3 fibroblasts for the tendon side. Both the polymers were melted and printed, followed by the appropriate cell-laden bioink, that was eventually cross-linked using a thrombin solution obtaining a 20×5×1 mm (LxWxH) structure. Tensile test and cell viability test showed the success of the approach of mimicking a MTU. Wang et al.[11], instead, exploited a commercial non-degradable elastic PUR (2103-80A, Upjohn Co, US) to make a porous scaffold for cartilage tissue regeneration through melted extrusion forming technique based on AM. The obtained scaffolds showed interconnected pores, good biocompatibility and mechanical properties. Moreover, cellularized platelet-rich plasma gel was added and crosslinked on the PUR mesh in order to improve cell distribution and density, thus promoting chondrocyte proliferation and inducing expressions of aggrecan and type II collagen genes.

2.1.1.2. Thermoplastic Shape Memory Polyurethanes in Fused Filament Fabrication

The high chemical versatility of PURs makes it possible to design smart materials with particular features, such as shape memory.

Raasch et al.[12], Kashyap et al.[13] and Hendrikson et al.[14] investigated the use of commercial shape memory PURs (MM4520[12] and MM3520[13,14] -SMP Technologies Inc., Nagoya, Japan) in AM. As already seen previously, also in these works the PURs were first extruded in shape of a filament in order to feed a FFF instrument.

Raasch et al.[12] printed scaffolds with +45°/−45° pattern, showing that thermal post-treatment (annealing) can be exploited to increase the speed of the shape recovery process, thus changing the mechanical properties of the 3D printed constructs.

Kashyap et al.[13] designed a radiopaque shape memory PUR for the fabrication of endovascular embolization devices, by combining extrusion, FFF and salt leaching. In this approach, NaCl and Tungsten were added as porogen and radiopacity enhancer, respectively. The final scaffolds showed high porosity (around 36%), forming an interconnected network after the leaching process.

By exploiting the shape recovery property, it would be possible to implant the construct in a patient by minimally invasive surgery. Furthermore, the shape memory effect could be exploited to mechanically stimulate the cells seeded onto the scaffolds, as an alternative to bioreactors for tissue regeneration. Concerning this aspect, Hendrikson's results[14] showed that the cells (human mesenchymal stromal cells) seeded onto a 3D printed scaffold in the temporary shape were significantly more elongated after the shape recovery.

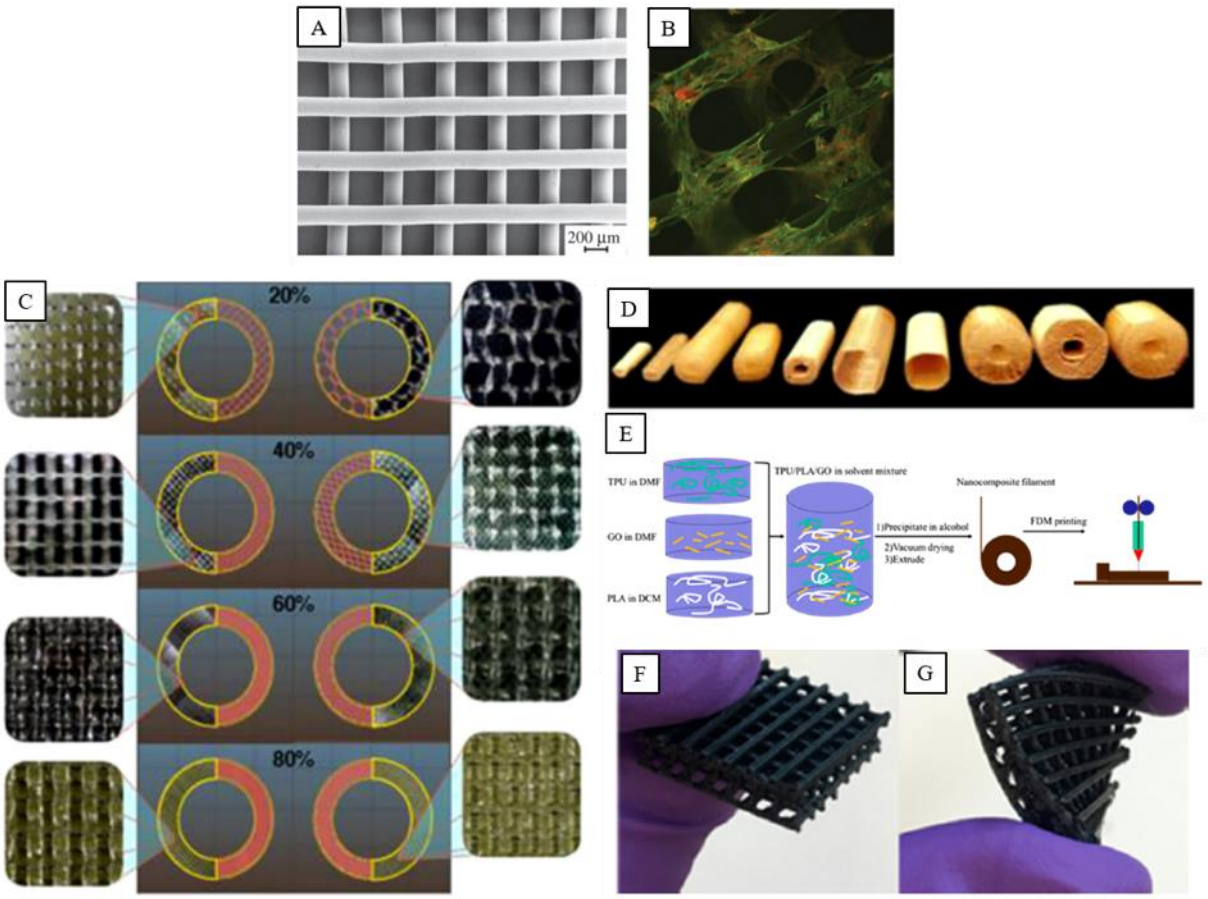

Figure 2.1 Chiono et al.[1] 3D printed PUR scaffolds: **(A)** scanning electron microscope (SEM) image; **(B)** fluorescent microscope images of cardiac progenitor cells seeded onto the PUR scaffold (green: actin; red: cell nuclei). Adapted with permission.[1] 2014, Royal society publishing. Tsai et al.[2] 3D printed PUR scaffolds: **(C)** CAD models and corresponding 3D printed patterns; **(D)** pictures of 3D printed scaffolds. Adapted with permission.[2] 2017, Nature partner journals. Chen et al.[3] 3D printed constructs: **(E)** Scheme of the PUR/PLA/GO filament preparation and FDM printing process, **(F, G)** photos of 3D printed grid scaffolds. Adapted with permission.[3] 2016, American Chemical Society.

2.1.1.3. Thermoplastic Polyurethanes in Liquid Frozen Deposition Manufacturing and Pressure Assisted Microsyringe

Efforts have been also spent to study other approaches based on LFDM and PAM techniques.[15–20] In this case, the PURs have to be solubilized in solvents in order to be extruded through a

nozzle. This is the main disadvantage of these techniques since toxic organic solvents are usually needed to dissolve PURs. Besides, PUR must be dissolved in a solvent that can be freeze-dried, for LFDM, or a volatile solvent that can evaporate quickly, for PAM. For these reasons, the choices of chemical compositions for the PURs are limited for LFDM and PAM applications. Even in these cases, it is not possible to cellularize the forming constructs directly during the printing process because of the presence of organic solvents.

Jung et al.[15] microfabricated a commercial PUR (Medical-grade, Tecoflex, Lubrizol Co., Wickliffe, OH) using a LFDM technique to develop a trachea. The scaffold was printed in the shape of half-pipe (1.8 x 0.18 x 2 cm HxTxD) by solubilizing the PUR in chloroform, and showed a micro-scale architecture allowing cellular infiltration for the biological integration with the host tracheal tissue. Jung and coworkers[15] showed the potential of the 3D printed PUR scaffolds to maintain trachea biomechanical function *in vivo* (rabbit tracheal defect model).

Xu et al.[16] designed and fabricated a complex 3D vascular system with interconnected channels in order to mimic human liver. An elastomeric PUR was synthetized starting from PCL, PEG and 1,6-hexamethylene diisocyanate (HDI) and processed using a LFDM system upon solubilization in 1,4-dioxane.Yan et al.[17] also dissolved a biodegradable custom-made PUR (synthesized starting from PEG -M_w 1000 Da-, PCL -M_w 2000 Da- and HDI) and heparin in 1,4-dioxane to print biodegradable vascular stents on a LFDM system showing good elasticity and anticoagulation properties. In another approach, Cui et al.[18] employed LFDM to print nerve conduits from inks based on a PUR (synthesized starting from PCL, PEG and HDI) solubilized in 1,4-dioxane and type I collagen solubilized in acetic acid, respectively. Cui and coworkers[18] showed the possibility to promote nerve repair by adding type I collagen as the internal layer of the conduit, meanwhile the PUR provided mechanical support as external layer. In a similar way, but adding a cellularized hydrogel to the structure, Huang et al.[19] demonstrated the rapid

manufacturing of a hybrid hierarchical PUR-cell/hydrogel construct by a LFDM system. Similarly to the previous work, the same synthetic PUR (based on PCL, PEG and HDI) was used to provide mechanical support, while a gelatin/alginate/fibrinogen hydrogel was used for adipose-derived stem cell encapsulation. The process consisted of the extrusion of the PUR solution (solubilized in tetraglycol) followed by the deposition of the cellularized ink, within the PUR layers. The obtained cellularized scaffold preserved cell viability and proliferation both *in vitro* and *in vivo*.

Whatley et al.[27] reported the application of a custom made PUR (synthetized starting from PCL diol and methyl-2,6-diisocyanatohexane -LDI-) dissolved in DMF (15 %w/v) in LFDM for the fabrication of intervertebral disk structures -IVD-. The polymer solution was extruded on the freezing stage kept at -4 °C, in the shape of concentric lamellae to mimic the native IVD. The fabricated scaffolds exhibited excellent control over macro- and micro-structure as well as mechanical properties comparable to those of native IVD tissue. The authors showed the possibility to influence seeded cells (bovine IVD cells) behavior by aligning them along the concentric lamellae, thus leading to a final cell morphology similar to the native IVD tissue.

On the other hand, Vozzi et al.[20] used a custom-made PUR (synthetized starting from PCL diol -M_w 1250 Da-, LDI and 1,4-cyclohexane dimethanol -CDM- as chain extender) dissolved in chloroform to print structures with square, hexagonal and octagonal grids through a custom-made PAM system (**Figure 2.2 A-C**). The authors showed the possibility to tune the line width and the mechanical properties of the deposited structures by varying solution viscosity, deposition speed, nozzle diameter or applied pressure. The printed structures showed good cytocompatibility and enhanced cell adhesion. *In vivo* implantation of PUR scaffolds demonstrated their complete degradation after three months with a slight inflammatory response.

2.1.1.4. Water-bone Polyurethanes in Liquid Frozen Deposition Manufacturing and Pressure Assisted Microsyringe

As previously mentioned for scaffolds made by LFDM, PURs are often dissolved in toxic organic solvents prior to process them. Thus, the final products may contain residues of solvents, compromising their biocompatibility.

Adopting water-bone biodegradable PURs can overcome the above issue; however the viscosity of such PURs is often too low to be directly 3D printed. Hence, the printing process is usually conducted on a low-temperature platform (around -4/-20 °C) to allow the printed construct to keep its shape. Viscosity enhancers, such as PEO, are usually added at different concentrations to favor printability. The low-temperature printing process of water-bone PURs also opens the way to the encapsulation of biomolecules sensitive to temperature or organic solvents. As for waterborne 3D printing, the medium for polymer solubilization is water, it is thus convenient to encapsulate bioactive factors in the constructs.

Hung et al.[9] designed a novel biodegradable water-bone PUR for cartilage tissue engineering, starting from PCL diol and polyethylene butylene adipate diol (40/60%), and 2,2-bis(hydroxymethyl) propionic acid as chain extender. In this work, the PUR solution was employed through a liquid-frozen deposition manufacturing LFDM technique to fabricate elastic scaffolds using PEO as a viscosity enhancer (**Figure 2.2 D-E**). The authors demonstrated that the viscosity of the ink drastically influences the printing process. If the viscosity is too low, the ink cannot maintain the shape, causing the construct to collapse. On the other hand, when the viscosity of ink becomes too high, it is not able to pass continuously through the nozzle, causing deficiencies in the final constructs. The same PUR was also blended with hyaluronic acid (HA) to print scaffolds with controlled release of chondrogenic induction factors (Y27632 or TGFb3).[10] The authors showed the ability of such scaffolds to promote the self-aggregation

of mesenchymal stem cells (MSCs) and to induce their chondrogenic differentiation. Moreover, the application of PUR/HA scaffold in rabbit chondral defects showed significantly improved cartilage regeneration.

By exploiting the same LFDM technique, Wang et al.[28] designed PUR-based scaffolds for bone tissue regeneration. Even in this case, a water-bone PUR was synthetized starting from PCL diol and PLLA diol, isophorone diisocyanate, and 2,2-bis(hydroxymethyl)propionic acid and ethylenediamine as chain extenders. To enhance viscosity, PEO or gelatin type A were mixed with the PUR, while superparamagnetic iron oxide nanoparticles (SPIO NPs) were added to promote osteogenic induction and shape fixation. hMSCs were seeded onto the printed scaffolds to evaluate bone regeneration. PUR-PEO scaffolds showed better shape memory properties, while PUR-gelatin scaffolds exhibited better cell viability (**Figure 2.2 F-G**). The addition of SPIO NPs enhanced the crystallinity of both PCL and PLLA segments, thus increasing the shape fixity ratio. Moreover, SPIO NPs release from the PUR-based 3D printed scaffolds promoted osteogenesis of hMSCs and the secretion and deposition of collagen and calcium.

2.1.1.5. Polyurethanes in Inkjet Printing and Other Techniques

The literature also reports on the use of PURs to successfully print objects through inkjet printing[21–23] or other similar techniques, such as bioplotting or powder-bed technologies.[29]

For instance, Krober et al.[21] designed a reactive inkjet printing technology to create micro PUR dots, lines and pyramids. These structures were fabricated *in situ* by inkjet printing two separate inks containing isophorone diisocyanate and an oligomer of poly(propylene glycol), and a catalyst and a cross-linking agent, respectively. The droplets merged on the substrate and polymerized *in situ* within five minutes to form a solid micron-sized PUR structure.

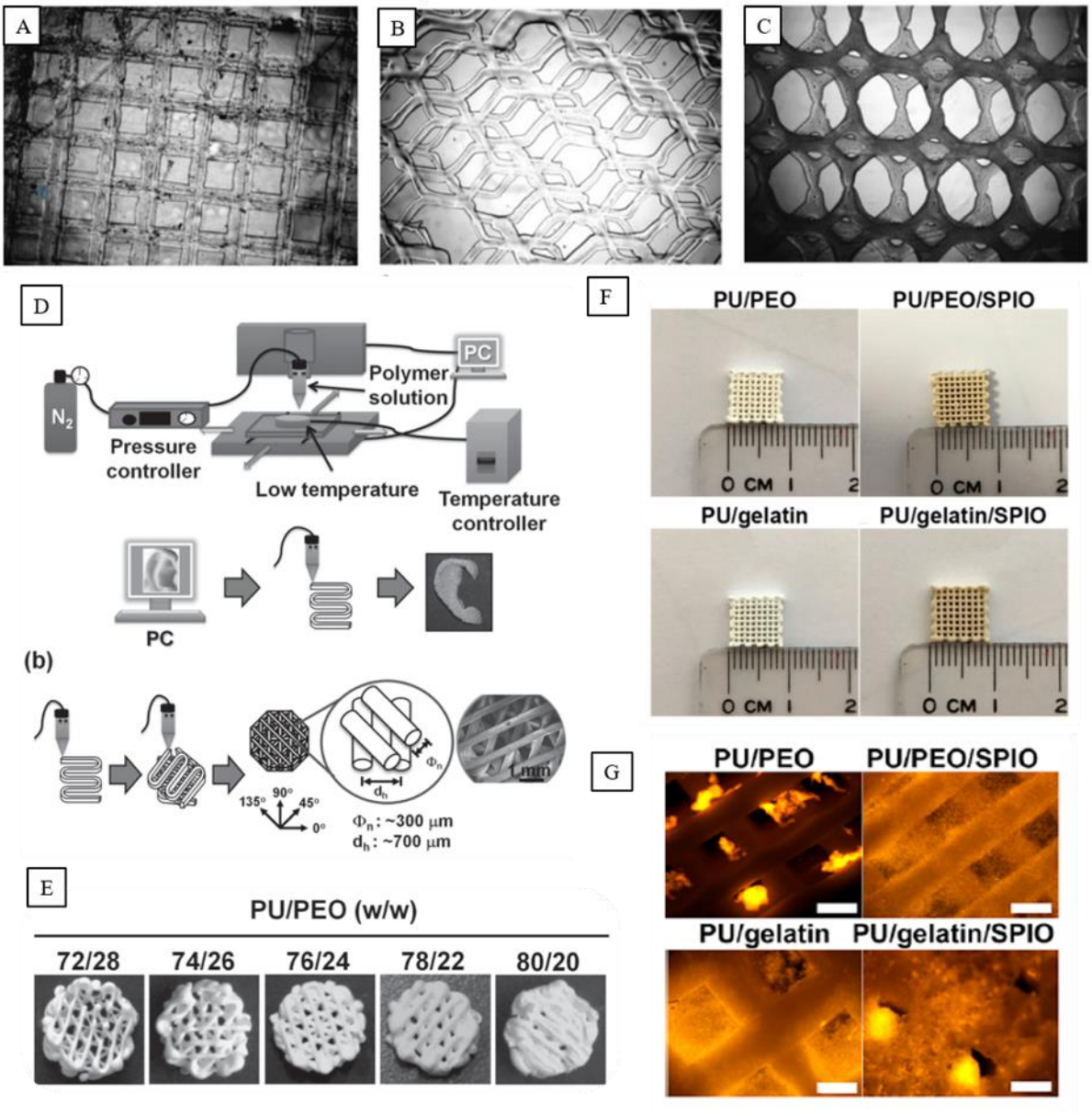

Figure 2.2 Vozzi et al.[20] 3D printed PUR scaffolds: **(A-**C) microscope images of the scaffolds with different geometries. Adapted with permission.[20] 2008, Wiley. Hung et al.[9,10] 3D printed scaffolds: **(D)** schematics of the LFDM system and printing parameters, **(E)** pictures of the 3D printed scaffolds. Reproduced with permission.[9] 2014, Wiley. Wang et al.[28] 3D printed scaffolds: **(F)** pictures of the 3D printed scaffolds with different compositions, **(G)** fluorescence microscope images of MSCs seeded on the 3D printed scaffolds (labeled with PKH26 red fluorescent membrane dye). Adapted with permission.[28] 2018, American Chemical Society.

Müller et al.[22] adopted this concept to design an ink for 3D printing based on an oligodiol (polypropyleneglycol - Lupranol 1100, BASF, Germany), methylene di-p-phenyl-diisocyanate

(MDI) and a trifunctional polyol (glycerine-based polyether - Lupranol 3300, BASF, Germany). They showed the possibility to tune scaffold mechanical properties by changing the relative ratios of the reagents.

Zhang et al.[23] synthesized a biodegradable anionic water-bone PUR from MDI, PCL diol and N,N-bis (2-hydorxyethyl)-2-aminoethane-sulfonic acid (BES) as chain extender. Due to the presence of sulfonic acid groups, the PUR turned out to be pH sensitive, being water soluble in basic conditions and insoluble in acidic conditions. Scaffolds were fabricated by inkjet printing acetic acid onto a PUR solution leading to the precipitation of the inkjet-printed areas. However, this method only resulted in 2D final products due to the low viscosity of acetic acid.

Agrawal et al.[29] developed a new class of fiber-reinforced hydrogels using an AM technique to form PUR based scaffolds impregnated with an epoxy-based hydrogel. Two commercially available PURs (poly[4,4'-methylenebis(phenyl isocyanate)-alt-1,4-butanediol/ di(propyleneglycol)/polycaprolactone] -Sigma Aldrich- and Texin DP7-1205 -Bayer Material Science LLC-) were blended and solubilized in DMF to form fiber through a pressure-driven syringe mounted on a dispensing system. The entire writing process was carried out under water so that the polymer fiber rapidly formed via solvent exchange, forming 1 cm thick scaffolds with 400 layers of 25 μm/layer and a 0°/90° pattern.

In a different approach, Pfister et al.[30] applied a commercial adhesive made ofa mixture of starch and cellulose (ZP11) to 3D print a biodegradable PUR (synthetized starting from lysine ethyl ester diisocyanate and isophorone diisocyanate). However, the stability of the final products was quickly lost in aqueous environment due to the water-solubility of the adhesive. To overcome this drawback, an isocyanate was mixed with the ZP11 adhesive to react with the PUR. Although the authors succeeded in increasing both water-resistance and tensile strength,

the 3D printed structures were subjected to uncontrolled swelling when implanted, with a consequence decrease in geometry accuracy.

2.1.1.6. Polyurethane-based Photo-sensitive Inks in Digital Light Processing

Different research groups exploited the mentioned PUR chemical versatility to design photo-sensitive hydrogels suitable for AM techniques based on UV-Vis light irradiation.[24–26] In this context, different tissues have been targeted due to the possibility to easily modulate the mechanical properties of the final PUR-based scaffolds by controlling the PUR chemistry and the printing parameters (e.g., exposure time and power density).

Kim et al.[31] applied a commercial acrylated PUR resin added with inorganic substances to increase the viscosity of the ink in SLA 3D printing; gel composition was modulated so that viscosity was high enough to allow the ink to be extruded before the light-induced polymerization.

Shie et al.[25] and Pyo et al.[26] reported continuous optical 3D printing of water-based photo-sensitive PURs through DLP technology. (**Figure 2.3 A-C**). While Shie et al.[25] blended two different commercial PURs (a water-based light-cured PUR and a water-based thermoplastic PUR -LUX 260 and U2101, Alberdingk Boley, Krefeld, Germany-) with hyaluronic acid (HA), Pyo et al.[26] synthesized green chemistry-derived isocyanate-free aliphatic PURs starting from different polyamines and six-membered cyclic carbonates functionalized with methacrylate groups. In the first approach,[25] the mechanical properties of the final specimens were tuned to mimic the ones of articular cartilage by blending different concentrations of the two PURs. Moreover, the addition of hyaluronic acid (HA) allowed to increase cell compatibility and promote cell adhesion, proliferation, and chondrogenic differentiation of human Wharton's jelly

mesenchymal stem cells (hWJMSCs). In the second approach,[26] instead, the authors showed the possibility to tune the scaffold stiffness by changing UV exposure time and polyamines used during the PUR synthesis. Eventually, the cytocompatibility of C3H 10T1/2 cells (mouse fibroblast cell line) seeded on the printed structures was assessed.

The main drawback of all these methods regards the need for toxic photoinitiators to bring about the reaction.

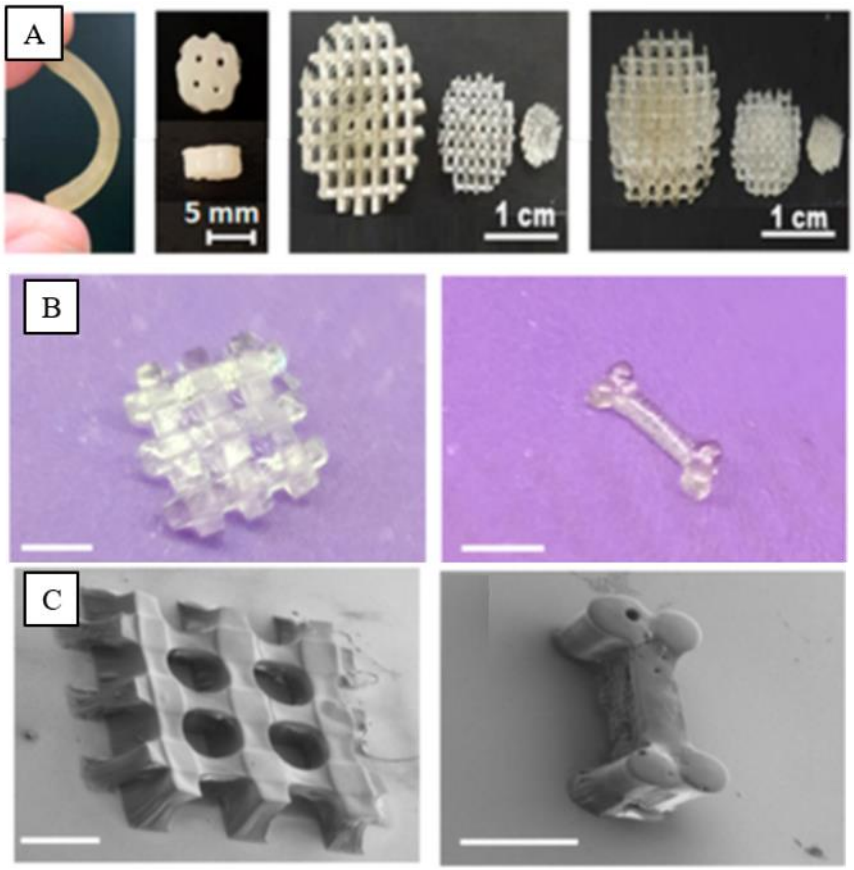

Figure 2.3 (A) Shie et al.[25] 3D printed scaffolds (circular scaffolds with a grid pattern 90/90°, 100 µm layer thickness and 20 s of irradiation). Adapted with permission.[25] 2017, MDPI. Pictures **(B)** and SEM images **(C)** of Pyo et al.[42] 3D printed constructs. Adapted with permission.[42] 2018, American Chemical Society.

2.1.1.7. Polyurethane-based Thermo-sensitive Inks in Bioprinting

Similarly to photo-sensitive gels, also polyurethane-based thermosensitive inks have been employed in AM techniques.

For instance, Hsieh et al.[6,7] and Tsai et al.[8] showed the application of cellularized PUR-based thermo-sensitive solutions in nozzle-based extrusion bio-printer. In all these works, thermo-sensitive cell-printing inks based on an aqueous dispersion of biodegradable PUR nanoparticles, which may form gel near 37 °C without any crosslinker, were designed. By controlling PUR chemistry and its solid content in the water dispersion, the mechanical properties of the resulting 3D scaffolds can be finely tuned to match the requirements for the investigated application.

Hsieh et al. [6] developed two different water-bone biodegradable PURs based on PCL diol (M_n ~ 2000 Da) and PLLA diol or PDLLA diol (M_n ~ 2000 Da). The properties and the modulus of the PUR dispersion were adjusted by working on the chemistry and the ratio of the two polyesters in the soft segment, and by tuning the PUR solid content (25-30 %w/v, in order to match the stiffness of neural tissue) in the ink, respectively. Cellularized inks encapsulating murine neural stem cells (NSCs, $4x10^6$ cells/mL) were subsequently 3D printed by a custom-made inkjet system equipped with a 250 μm nozzle and using 55 kPa constant pressure (**Figure 2.4**). Cellularized scaffolds with 8 layers (~1.5 mm thickness) and a 0°/90° pattern were printed showing that the PUR based on PCL-PDLLA was more suitable for the growth of NSCs, and that low stiffness (achieved by low solid content) facilitated NSC survival and growth. Moreover, the two PURs showed to be able to promote glial and neuronal differentiation of NSCs. Eventually, by using a zebrafish neural injury model, PUR/NSCs hydrogels showed the potential to increase function recovery of damaged nervous system related to neurodegenerative diseases.[7]

Tsai et al.[8], instead, synthesized three different water-bone PURs starting from PCL diol and oligodiol of amphiphilic blocks (PLLA−PEO diblock or PDLLA−PEO diblock) or PDLLA-PEO-PLLA triblock oligodiol. Dispersions (25-30 %w/v) prepared starting from the PCL/PLLA−PEO (90/10 %w/w) PUR were mixed with human umbilical cord derived MSCs (2×10^6 cells/mL) and printed in the form of 3×3 cm^2 squares with 2 mm thickness and a 0°/90° pattern, using a 260 μm nozzle, a pressure of 241-275 kPa and a volume flow rate of 1.67 μL/sec. The biological results showed that MSCs proliferated in the deposited layers. The viability and proliferation of MSCs cultured in a 25 %w/v concentrated PUR gel turned out to be higher than those of MSCs cultured in a PUR gel with 30 %w/v concentration due to the differences in stiffness and in nutrient/waste diffusivity.

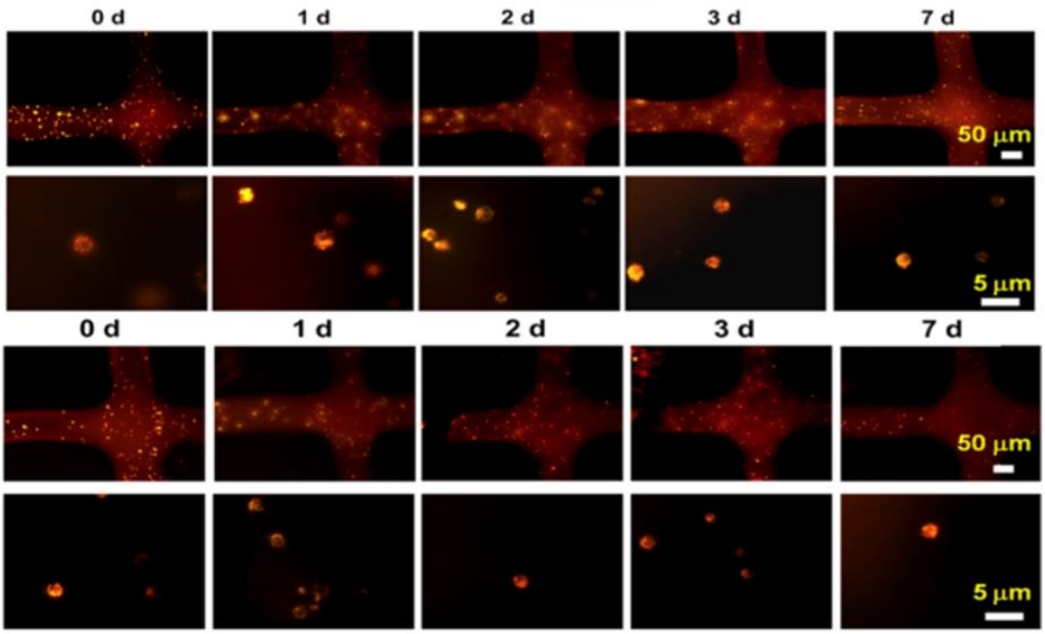

Figure 2.4 Tsai et al.[8] 3D printed cellularized scaffolds: fluorescence microscopy images of MSCs (labeled with PKH26 red fluorescent membrane dye) encapsulated within the scaffolds with 30% and 25% solid content, respectively. Adapted with permission.[8] 2015, American Chemical Society.

2.1.2. 3D Models

In the field of 3D models few research groups reported the use of PURs with AM technologies. Mizutani et al.[32] and Noecker et al.[33] exploited PURs' elasticity for the production of 3D models of organs for preoperative surgery planning. In detail, Mizutani and colleagues[32] applied PUR resins in SLA for the fabrication of 3D full-sized models of occipitocervical or upper cervical spines, while Noecker et al.[33] did not use PURs as 3D printed materials, but as elastic cover to give flexibility to the models.

Buijis et al.[34] fabricated PUR-based scaffolds combining 3D printing and injection molding technique to quantify solute transport in cyclically deformed tissues using an optical imaging method. Similarly to Noecker et al., also in this case PURs were chosen to simulate the elasticity of native biological tissues.

2.1.3. Microfluidic Devices and Sensors

Some literature works involve the use of PUR for the production of microfluidics devices through AM techniques. In this field SLA is mainly used and thus photosensitive PURs have been exploited for this purpose.

Meanwhile Alvankarian et al.[35] directly used a methacrylated PUR as a resin for lithography, Piccin et al.[36] and Qin et al.[37] applied a mold fabricated by standard photolithography to cast PUR resins and fabricate micro-channels. In particular, Alvankarian et al.[35] proposed a two-step exposure lithography technique that allowed the rapid fabrication of microstructures with high resolution and reproducibility by exploiting the crosslinking of a PUR methacrylate resin. Piccin et al.[36] used an elastomeric biosource-derived PUR for the fabrication of microfluidic devices by additive manufacturing. Following an indirect approach, PUR resin was casted

directly on the positive high-relief mold and crosslinked. This approach was applied to fabricate miniaturized capillary electrophoresis to study the electroosmotic flow as a function of pH and perform separation of catecholamines. In a similar way, Quin et al.[37] showed the applicability of SLA techniques for the fabrication of PUR nanostructures. A UV-curable PUR was cured inside a polydimethylsiloxane (PDMS) mold obtained by replica molding of a patterned master. Different research groups applied PURs as an elastic substrate on which sensitive materials were printed to produce wearable sensors. Wang et al.[38], Vuorinen et al.[39], Vatani et al.[40] and Bandodkar et al.[41] combined conductive nanocomposites and PURs for the layer-by-layer fabrication of sensors with arbitrary geometries. Wang et al.[38] developed a spraying-evaporation deposition modeling process to incorporate carbon nanotube layers into a shape memory thermoplastic PUR to fabricate nano-composites. Vuorinen et al.[39] fabricated epidermal temperature sensors by inkjet-printing a conductive polymer ink containing graphene and a screen printed silver flake ink on a PUR substrate, showing good adhesion to skin. Bandodkar et al.[41] combined the mechanical and electrical properties of PUR and carbon nanotubes to design a tailored screen printable stretchable ink to produce electrochemical sensors and biofuel cell arrays. Elastomeric PUR addition turned out to enhance the intrinsic stretchability of the printed carbon nanotube-based ink, thus adding a second degree of stretching. Vatani et al.[40] developed a mechanically compliant tactile sensor through the deposition of a photo-curable ink containing carbon nanotubes, embedded into a flexible PUR. Tartarisco et al.[42] mixed a commercial PUR resin (Polytek 74-20) with crosslinking agents, and extruded the material layer-by-layer, showing the possibility to tune printing resolution by changing pressure and nozzle speed. However, the potential presence of residual unreacted crosslinking agents represents an issue to the application of this approach in TE.

2.1.4. Indirect Additive Manufacturing

In indirect manufacturing processes, the final parts are produced by exploiting 3D printed molds, patterns or tools, via traditional manufacturing processes.

Koo et al.[43] investigated the design of custom-shaped PUR-based grafts starting from magnetic resonance imaging data using a custom-made mold fabricated through rapid-prototyping methods. Hernàndez-Còrdova et al.[44] demonstrated the potential of combining indirect additive manufacturing and PURs for the fabrication of soft scaffolds with controlled 3D micro-architecture and pore size for cardiac tissue engineering. The process was carried out by first printing poly(vinyl alcohol) following a wood-stack model. Successively, the PUR solution was pressure injected inside the 3D printed mold and the poly(vinyl alcohol) was eventually washed out by water. The so produced scaffolds showed regular tubular pores with excellent mechanical properties and good biocompatibility with cardiac myocytes.. By using a similar indirect approach, Sarles et al.[45] designed solidified biomolecular networks based on liquid-supported lipid bilayers and water-swollen hydrogels. PUR substrates were produced using a 3D printed mold in order to encapsulate the solidified biomolecular networks. Shestopalov et al.[46] applied a PUR in indirect additive manufacturing as a molding material. They reported a new inkless catalytic micro-contact printing technique able to reproduce patterns on self-assembled monolayers of Boc- and TBS-protected thiols through a PUR-acrylate stamp functionalized with sulfonic acids.

Verstraete et al.[47] and Claeys et al.[48] applied thermoplastic PURs in hot melt extrusion/injection molding to design tablets for drugs sustained oral release. Verstraete and coworkers[47] tested both commercial PURs (aliphatic extrusion-grade PURs, solution-processable PURs and PUR-based hydrogel) and custom-made PURs (based on PEO, HDI and 1,4-butanediol). Commercial PURs with low processing temperatures (approx. 80-110°C)

showed high potential for the manufacturing of high drug loaded (up to 70%, w/w) tablets. Moreover, they demonstrated the possibility to exploit PUR chemistry to finely control the release of different types of drugs (e.g., diprophylline, theophylline and acetaminophen) by changing the length of the PEO soft segment in custom-made PURs. Similarly, Claeys et al.[48] tested different PURs (differing in the composition of their hard and soft segments) for the release of metoprolol tartrate, theophylline and diprophylline. Drug/polymer mixtures were first extruded and then processed in the shape of biconvex tablets showing the possibility to produce solid dispersions with no drug degradation phenomena, a drug content up to 65%wt and a controlled release capacity. Moreover, their results showed that the oral administration of PUR-based tablets did not affect the gastrointestinal ecosystem (pH, bacterial count, short chain fatty acids).

Stevenson et al.[49] demonstrated the fabrication of near infrared (NIR) polymer composites catheters by combining a medical grade PUR with a fluorescent dye (IRDye 800CW). To fabricate the catheters the PUR/dye mixture was extruded to produce hollow tubes. The authors demonstrated that the PUR surface and mechanical properties were not affected by adding fluorescent contrast agent. Furthermore, the PUR prevented the IRDye 800CW to photobleach and degrade when exposed to bright light and warmer temperatures.

2.2. Can Polyurethane in Additive Manufacturing Launch a New Era in the Biomedical Fields?

As already mentioned and thoroughly overviewed in the previous sections of this review, PUR chemical versatility can be exploited to design different biomaterials with a wide plethora of physico-chemical, mechanical, surface and biological properties. The specific characteristics (i.e., chemical composition, molecular weight, crystallinity, polarity and hydrophilicity) of each PUR building block (i.e., macrodiol, diisocyanate and chain extender) significantly affect the physico-chemical, surface, biological and mechanical properties of the resulting PURs as well as the technologies that can be used to process them in the desired form (i.e., porous scaffolds for tissue engineering and regenerative medicine, tissue/organ models, organ on chips and sensors). Furthermore, by exploiting the relatively easy chemistry of PURs biomaterials with additional features (e.g., stimuli-sensitivity, shape memory) or functionalities (e.g., specific chemical groups such as acrylates, thiols, amino groups or peptide sequences) can be synthesized.

Scaffold mechanical properties represent a key aspect in TERM approaches, as the implanted constructs must be functionally integrated in the host tissue and provide a suitable mechanical support to the repair and regenerative processes. In this context, PURs may represent a valuable and promising alternative to commercially available polymers and many researchers have already reported different strategies to tune the mechanical properties of PUR-based scaffolds over the last few decades. Some of them modulated scaffold mechanics by simply working on the selection of appropriate building blocks to match the stiffness of a specific tissue/organ.[1,2,4,11,15,16,22,27] For instance, Müller et al.[22] reported on the possibility to modulate the mechanical properties of the final construct by changing reagent ratio f during the synthesis,

while Sartori and coworkers[50] demonstrated that PUR mechanical properties can be finely tuned by simply changing the chain extender. In addition, a proper selection of PUR building blocks can open the way to the possibility to provide the resulting polymer with shape memory behavior which could be exploited in the biomedical field for a variety of applications.[12–14] Moreover, by optimizing the shape recovery behavior, multiple mechano-transductive cues could be delivered to the cells to direct their activity and differentiation. Most of the reported works have highlighted the advantage of using PURs in terms of elasticity of the final products, compared to commercial polymers, such as polyesters and polyethers. In this regard, Merceron et al.[4] combined PUR elasticity with PCL stiffness to engineer a multicomponent muscle-tendon unit.

Another approach to tune material physico-chemical, biological and mechanical properties consists in blending PURs with other natural or synthetic polymers, or adding fillers to them. For instance, Chen et al.[3] blended a PUR with PLA and graphene oxide (GO) as filler to further enhance scaffold final properties, such as mechanical properties, thermal stability and cell viability. Similarly, Kashyap et al.[13] combined a shape memory PUR with NaCl and Tungsten to modulate radiopacity and mechanical and structural properties. Wang and coworkers,[28] instead, added superparamagnetic iron oxide nanoparticles to a water-bone PUR to promote osteogenic induction and shape fixity.

By adding a natural polymer to the PUR-based formulation, a further increase in scaffold cytocompatibility and cell/construct crosstalk could be obtained. Merceron and coworkers[4] and Wang et al.[11] showed the possibility to increase the cell seeding efficiency and efficacy by exploiting natural hydrogels as cell carriers. Yan et al.[17] mixed PUR with heparin to enhance anticoagulation properties of the final vascular graft. Cui et al.[18] combined PUR mechanical properties with the intrinsic biocompatibility of a natural polymer (type I collagen) to enhance

tissue regeneration. Huang et al.[19] applied a PUR in combination with a cellularized natural hydrogel working as mechanical support and cell carrier, respectively. Hung and coworkers[10] also combined a PUR with HA to release chondrogenic induction factors and promote both self-aggregation of mesenchymal stem cells and their chondrogenic differentiation. Shie et al.[25] blended two different PURs to modulate the mechanical properties of the final construct printed through a DLP system. Moreover, they added hyaluronic acid in order to increase the cytocompatibility of the scaffolds. Boffito, Di Meglio, Mozetic et al.[51] have recently demonstrated that surface grafting of laminin on melt-extruded PUR scaffolds promotes adhesion, expansion and differentiation of cardiac progenitor cells towards the cardiac, endothelial and smooth muscle cell phenotypes. In another work, the same group has investigated PUR mechanical properties change in response to microfabrication through a conventional scaffolding technology (i.e., thermally induced phase separation).[52] The authors showed that, in addition to the expected effects observed at the macro-scale and induced by the presence of an interconnected porosity, the distribution of PUR stiffness values at the nano-scale, as assessed by atomic force spectroscopy, changes in response to the thermal and mechanical stress applied to the material during its processing.

Researchers sometimes reported the use of fillers, such as PEO, to tune the viscosity of a PUR-based formulation in order to make it suitable for a specific AM technology.[9,28,31] For instance, Hung et al.[9] and Wang et al.[28] combined a water-bone PUR with PEO or a mixture of PEO and gelatin as viscosity enhancers in LFDM, reporting on the key role exerted by viscosity in this technique: when viscosity is too low the shape cannot be maintained, but, if viscosity becomes too high, the solution cannot pass continuously through the nozzle. Kim et al.[31] combined an acrylated PUR resin with inorganic fillers to control the viscosity of the ink and modulate the mechanical properties.

Other research groups mainly focused their attention of tuning scaffold properties working on printing parameters. For instance, Pyo et al.[26] applied a custom-made PUR in DLP technique and modulated the properties of the resulting scaffolds by controlling the UV exposure time. Vasquez et al.[5], Chen et al.[3] and Vozzi et al.[20] studied the effects of SLS (i.e., powder granulometry, powder delivery system temperature, laser power and beam speed), FFF (i.e., temperature, feed rate and printing speed) and PAM (i.e., pressure, printing speed and solution viscosity) printing parameters on the mechanical properties of PUR 3D printed scaffolds. Chen and coworkers[3] also showed the dependence of mechanical properties from the printing orientation.

PURs can be designed in the form of thermoplastic powder, pellets or filament for SLS and melt extrusion technologies, photo-sensitive resins for laser-based techniques based on photo-crosslinking (e.g., SLA, DLP), and stimuli-sensitive hydrogels (e.g., thermo-sensitive, photo-sensitive and pH-sensitive) for inkjet printing and bioprinting technologies. The variety of PUR chemical compositions suitable for FFF, LFDM and PAM applications is limited because of the need for high temperature and organic solvents, respectively. For the same reasons, these technologies do not allow the encapsulation of cells and biomolecules during the printing process. Water-born PURs have been applied in LFDM, but viscosity enhancers are usually required to make the formulation extrudable. Also in this case, the technique does not allow cell/biomolecule loading during the printing process because of the low temperature and the freeze drying process that usually is needed to dry the scaffold. In the field of water-born PUR-based ink formulations there is still room for improvement in terms of viscosity enhancer and technological limitations coming from the impossibility of cell encapsulation due to the low-temperature platform used for solidification. In order to improve this aspect, PUR chemical

structure can be exploited to design stimuli-responsive materials leading to temperature-responsive, photo-curable or pH-sensitive systems.

The wide range of properties achievable combining PUR and AM allows the researchers to target different tissues (i.e. heart tissue,[1] tracheal tissue,[2,15] muscle tissue,[4] cartilage tissue,[9–11,25] vascular tissue,[13,19] nerve tissue,[17] intervertebral disk,[27] skin[20] and bone tissue[28]), while their cytocompatibility has been demonstrated with different cell lines (human cardiac progenitor cells,[1] NIH/3T3 fibroblast cells,[3,4,20] human dermal fibroblasts and bronchial epithelial cells,[2] chondrocyte cells,[11] human mesenchymal stromal cells,[14] adipose-derived stem cell,[19] bovine IVD cells,[27] mesenchymal stem cells,[10,28] human osteosarcoma cell,[30] Wharton's jelly mesenchymal stem cells,[25] and mouse fibroblast cell C3H 10T1/2[26]). Many research groups have also reported the ability of PUR to promote cell infiltration *in vivo* with poor foreign body reaction.[15,17]

Different commercial purs are already available (Vasquez et al.[5], Chen et al.[3], Merceron et al.[4], Wang et al.[11], Raasch et al.[12], Kashyap et al.[13], Hendrikson et al.[14], Jung et al.[15], Agrawal et al.[29], Kim et al.[31], Shie et al.[25]), but the three degrees of freedom given by PUR chemistry still allow researchers to set up new materials with finely tuned properties and additional features to fully meet the specific requirements of each application. This aspect explains the wide variety of *ad-hoc* synthesized custom-made PURs reported in the literature (Chiono et al.[1], Tsai et al.[2], Xu et al.[16], Yan et al.[17], Cui et al.[18], Huang et al.[19], Whatley et al.[27], Vozzi et al.[20], Hung et al.[9,10], Wang et al.[28], Krober et al.[21], Müller et al.[22], Zhang et al.[23], Pfister et al.[30], Pyo et al.[26], Hsieh et al.[6,7], Tsai et al.[8]). In addition, the existence of many PURs on the market represents an advantage in view of a potential scale-up of a lab-scale PUR synthesis protocol as starting knowledge and grounds already exist. Moreover, many PUR formulations have already gained approval for use in the biomedical field and the effects of

sterilization protocols on different PURs have been thoroughly investigated.[53–57] On the other side, AM techniques represent a promising technological platform for industrialization as they allow a mass-production of highly reproducible and precise constructs. In addition, in a different approach, AM technology opens the way to the possibility to adapt the CAD model to specific requirements, thus answering to the increasing need of patient-specific devices and implantables scaffolds. Hence, the summary reported in this work clearly highlights the potential coming from the combination of high versatile materials and technologies in opening the way to the possibility to design and fabricate the optimal scaffolds for the repair and regeneration of almost all tissues in the human body. In this regards, the suitability of both the biomaterials and the scaffolding technologies to industrialization, sterilization and large-scale production is essential in view of the commercialization of the designed products. PUR chemical versatility can thus be effectively combined with the technological versatility of AM technologies in order to efficiently tune scaffold final properties to a large extent, by exploiting either PUR chemistry and formulation, the printing parameters or both.

2.3. Conclusions

Over the last decades, PURs have been shown to be a family of polymers with many advantages in terms of versatility and intrinsic properties coming from their particular micro-structure (i.e., mechanical properties, biocompatibility and cell response). Thanks to the progression in PUR chemistry as well as the understanding of their microphase separation and degradation mechanisms, PURs have the potential to open a new era in the biomedical field, both in TERM applications and in the design of biomedical devices (e.g., sensors, lab-on-chip). To these aims, PURs have found widespread application in basic and applied research as stand-alone or support materials as well as in combination with other commonly used natural and synthetic polymers. PURs can be designed to have various physico-chemical and mechanical properties as well as proper biodegradation rates, by selecting specific building blocks during the synthesis. Moreover, PURs versatility also lies on the possibility to match the demands of different fabrication technologies: they can be 3D printed from polymer melts, solutions or dispersions. Waterborne PUR dispersions have been remarkably showing high potential for the design of novel bioinks for tissue/organ printing with the possibility to 3D print elastic cellularized scaffolds.

Hence, smart PUR materials and 3D printing combination can result to massive advances of 3D bioprinting for large-scale and customized biomedical applications.

References

[1] V. Chiono, P. Mozetic, M. Boffito, S. Sartori, E. Gioffredi, A. Silvestri, A. Rainer, S.M. Giannitelli, M. Trombetta, D. Nurzynska, F. Di Meglio, C. Castaldo, R. Miraglia, S. Montagnani, G. Ciardelli, *Interface Focus* **2013**, *4*.

[2] K.J. Tsai, S. Dixon, L.R. Hale, A. Darbyshire, D. Martin, A. De Mel, *npj Regen. Med*. **2017**, *16*.

[3] Q. Chen, J. D. Mangadlao, J. Wallat, A. De Leon, J. K. Pokorski, R. C. Advincula, *ACS Appl. Mater. Interfaces* **2017**, *9*.

[4] T.K. Merceron, M. Burt, Y. Seol, H. Kang, S.J. Lee, J.J. Yoo, *Biofabrication* **2015**, *7*.

[5] G.M. Vasquez, C.E. Majewski, B. Haworth, N. Hopkinson, *Addit. Manuf*. **2014**, *1–4*.

[6] F. Hsieh, H. Lin, S. Hsu, *Biomaterials* **2015**, *71*, 48.

[7] F. Hsieh, S. Hsu, *Organogenesis* **2015**, *11*.

[8] Y. Tsai, S. Li, S. Hu, W. Chang, U. Jeng, S. Hsu, *ACS Appl. Mater. Interfaces* **2015**, *7*.

[9] K. Hung, C. Tseng, S. Hsu, *Adv. Healthc. Mater*. **2014**, *3*.

[10] K. Hung, C. Tseng, L. Dai, S. Hsu, *Biomaterials* **2016**, *83*.

[11] Z. Wang, H. Qin, Z. Feng, Y. Zhao, *J. Biomater. Appl.* **2016**, *30*, 7.

[12] J. Raasch, M. Ivey, D. Aldrich, D.S. Nobes, C. Ayranci, *Addit. Manuf*. **2015**, *8*.

[13] D. Kashyap, P. K. Kumar, S. Kanagaraj, *Addit. Manuf*. **2018**.

[14] W.J. Hendrikson, J. Rouwkema, F. Clementi, C.A. Van Blitterswijk, S. Farè, L. Moroni, *Biofabrication* **2017**, *9*, 3.

[15] S.Y. Jung, S.J. Lee, H.Y. Kim, H.S. Park, Z. Wang, H.J. Kim, J.J. Yoo, *Biofabrication* **2016**, *8*.

[16] Wei Xu, Xiao Wang, *J. Bioact. Compat. Polym.* **2008**, *223*, 103.

[17] Y. Yan, X. Hong Wang, D. Yin, R. Zhang, J. *Bioact. Compat. Polym*. **2007**, *22*, 3.

[18] T. Cui, Y. Yan, R. Zhang, L. Liu, W. Xu, X. Wang, *Tissue Eng. Part C Methods* **2009**, *15*, 1.

[19] Y. Huang, K. He, X. Wang, *Mater. Sci. Eng. C* **2013**, *33*, 6.

[20] G. Vozzi, A. Rechichi, F. Dini, C. Salvadori, F. Vozzi, S. Burchielli, F. Carlucci, M. Arispici, G. Ciardelli, P. Giusti, A. Ahluwalia, *Macromol. Biosci*. **2008**, *8*, 1.

[21] P. Kröber, J. T. Delaney, J. Perelaer, U.S. Schubert, *J. Mater. Chem*. **2009**, *19*, 29.

[22] M. Müller, Q.U. Huynh, E. Uhlmann, M.H. Wagner, *Prod. Eng*. **2014**, *8*, 1-2.

[23] C. Zhang, X. Wen, N.R. Vyavahare, T. Boland, *Biomaterials* **2008**, *29*, 28.

[24] J.H. Kim, K.B. Kim, W.C. Kim, J.H. Kim, H.Y. Kim, *Korean J. Orthod*. **2014**, *44*, 2.

[25] M. Y. Shie, W. C. Chang, L. J. Wei, Y. H. Huang, C. H. Chen, C. T. Shih, Y. W. Chen, Y. F. Shen, Materials **2017**, *10*, 2.

[26] S. Pyo, P. Wang, H. H. Hwang, W. Zhu, J. Warner, S. Chen, *Appl. Mater. interfaces* **2016**

[27] B.R. Whatley, J. Kuo, C. Shuai, B.J. Damon, X. Wen, *Biofabrication* **2011**, *3*.

[28] Y. Wang, U. Jeng, S. Hsu, *ACS Biomater. Sci. Eng*. **2018**, *4*.

[29] A. Agrawal, N. Rahbar, P.D. Calvert, *Acta Biomater*. **2013**, *9*, 2.

[30] A. Pfister, R. Landers, A. Laib, U. Hübner, R. Schmelzeisen, R. Mülhaupt, *J. Polym. Sci. Part A Polym. Chem.* **2004**, *42*, 3.

[31] S.G. Kim, W.S. Chu, W.K. Jung, S.H. Ahn, *J. Mater. Process Technol*. **2007**, *187-188*.

[32] J. Mizutani, T. Matsubara, M. Fukuoka, N. Tanaka, H. Iguchi, A. Furuya, H. Okamoto, I. Wada, T. Otsuka, *Eur. Spine J*. **2008**, *17*, 5.

[33] A.M. Noecker, J. Chen, Q. Zhou, R.D. White, M.W. Kopcak, M.J. Arruda, B.W. Duncan, *Pediatr. Circ. Support Perfus. ASAIO* **2006**, *52*.

[34] J. Op Den Buijs, D. Dragomir-Daescu, E.L. Ritman, *Ann. Biomed. Eng*. **2009**, *37*, 8.

[35] J. Alvankarian, B.Y. Majlis, *PLoS One* **2015**, *10*, 3.

[36] E. Piccin, W. Karlos, T. Coltro, S. Claro, L. Henrique, E. Carrilho, *J. Chromatogr*. **2007**, *1173*.

[37] D. Qin, Y. Xia, G.M. Whitesides, *Nat. Protoc*. **2010**, *5*, 3.

[38] X. Wang, J. Sparkman, J. Gou, *Compos. Sci. Technol*. **2017**, *141*.

[39] T. Vuorinen, J. Niittynen, T. Kankkunen, T. M. Kraft, M. Mäntysalo, *Nature Scientific Reports* **2016**, *6*.

[40] M. Vatani, E.D. Engeberg, J. Choi, *Sensors Actuators A. Phys*. **2013**, *195*.

[41] A.J. Bandodkar, I. Jeerapan, J. You, J. Wang, *Nano Lett*. **2016**, *16*.

[42] G. Tartarisco, G. Gallone, F. Carpi, G. Vozzi, *Mater. Sci. Eng. C* **2009**, *29*, 6.

[43] S. Koo, B.A. Hargreaves, G.E. Gold, J.L. Dragoo, *Magn. Reson. Imaging*. **2013**, *31*, 3.

[44] D.A. Mathew, R. Balint, R. Hern, *J. Biomed. Mat. Res. A* **2016**, *104A*, 8.

[45] S.A. Sarles, L.J. Stiltner, C.B. Williams, D.J. Leo, *ACS Appl. Mater. Interfaces* **2010**, *2*, 12.

[46] T. Thiols, A.A. Shestopalov, R.L. Clark, E. J. Toone, *Nano Lett*. **2010**, *10*.

[47] G. Verstraete, J. Van Renterghem, P.J. Van Bockstal, S. Kasmi, B.G. De Geest, T. De Beer, J.P. Remon, C. Vervaet, *Int. J. Pharm*. **2016**, *506*, 1-2.

[48] B. Claeys, A. Vervaeck, X.K.D. Hillewaere, S. Possemiers, L. Hansen, T. De Beer, J. Paul, C. Vervaet, *Eur. J. Pharm. Biopharm*. **2015**, *90*.

[49] A.T. Stevenson, L.M. Reese, T.K. Hill, J. Mcguire, A.M. Mohs, R. Shekhar, L.R. Bickford, A.R. Whittington, *Biomaterials* **2015**, *54*.

[50] S. Sartori, M. Boffito, P. Serafini, A. Caporale, A. Silvestri, E. Bernardi, M.P. Sassi, F. Boccafoschi, G. Ciardelli.*React. Funct. Polym.* **2013**, *73*, 1366.

[51] M. Boffito, E. Bernardi, S. Sartori, G. Ciardelli, M. P. Sassi, V. Chiono. *J. Biomed. Mater. Res.* **2014**, 103, 162.

[52] V. Chiono, P. Mozetic, M. Boffito, S. Sartori, E. Gioffredi, A. Silvestri, A. Rainer, S.M. Giannitelli, M. Trombetta, D. Nurzynska, F. Di Meglio, C. Castaldo, R. Miraglia, S. Montagnani, G. Ciardelli. *Interface Focus*. **2014**, *4*, 1.

[53] N. Hirata, K.I. Matsumoto, T. Inishita, Y. Takenaka, Y. Suma, H. Shintani, *Radiat. Phys. Chem*. **1995**, *46*, 3.

[54] N. Ma, A. Petit, O.L. Huk, L. Yahia, M. Tabrizian, *J. Biomater. Sci. Polym. Ed.* **2003**, *14*, 3.

[55] S. Bertoldi, S. Farè, H.J. Haugen, M.C. Tanzi, *J. Mater. Sci. Mater. Med*. **2015**, *26*, 5.

[56] R. Muschalek, L. Nash, R. Jones, S.M. Hasan, B.K. Keller, M.B.B. Monroe, D.J. Maitland, *J. Med. Device* **2017**, *11*, 3.

[57] M. Griffin, N. Naderi, D.M. Kalaskar, E. Malins, R. Becer, C.A. Thornton, I.S. Whitaker, A. Mosahebi, P.E.M. Butler, A.M. Seifalian, *Int. J. Biomater*. **2018**, *2018*.

Chapter 3
Thermo-sensitive Polyurethane-based Hydrogels

Abstract:

This chapter includes the works carried out within the 2010 FIRB project "*Bioartificial materials and biomimetic scaffolds for a stem cell-based therapy for myocardial regeneration*" and deals with the design of rapid prototyped cellularized hydrogel-based scaffolds loaded with growth factors, proteins and/or drugs to favor cell survival and induce their differentiation, with the final aim of stimulating cardiac tissue repair.

To this aim, the polyurethane chemistry was chosen to chain extend the Poloxamer P407. Poloxamer, is a low cost, FDA approved, amphiphilic triblock copolymer, whose aqueous solutions undergo a sol-gel transition with increasing temperature. However, such physical hydrogels suffer of short residence time, low mechanical properties and high permeability. By increasing the molecular weight of the Poloxamer it was possible to design hydrogels with increased thermo-responsive properties and stability in water environment as well as mechanical properties. Therefore, the polyurethane-based hydrogels partly overcome Poloxamer-based gel drawbacks, having also the potential to be functionalized with peptide sequences or proteins. The polyurethane based hydrogels were fully characterized in term of physico-chemical properties and eventually two concentrations were chosen to be tested as injectable cell/biomolecule carrier.

Keywords: Polyurethane, Thermo-sensitive Hydrogel, Drug Release.

3.1. Introduction

Hydrogels have received considerable attention in TERM applications thank to their characteristic mechanical properties, the possibility to easily encapsulate cells and biomolecules as well as the amenability to physico-chemical modifications. In particular, compared to solid form biomaterials (i.e. scaffolds), hydrogels allow less invasive regenerative strategies due to their injectability.

Hydrogels are 3D, hydrophilic, polymeric networks characterized by the ability to absorb and retain an extensive amount of water causing the swelling of such networks with the consequent increase in dimensions while maintaining their shape. This property leads to their characteristic soft and rubbery consistence, that enables them to mimic specific aspects of tissue microenvironments, in particular those related with soft tissues.[1-5] Moreover, their watery interiors and viscoelastic properties, provide a conducive microenvironment for cells, and their porosity allows free diffusion of oxygen, nutrients and water/soluble metabolites as well as biomolecules and drugs.[2,5-9] For these reasons, hydrogels have been thoroughly investigated for cell and biomolecules/drugs encapsulation and delivery.[4,5,10]

The hydrogels' gelation process take place by chemical or physical crosslinking of water-soluble precursors, homopolymers or copolymers, of natural or synthetic origin.[11] The swelling/deswelling properties of a hydrogel can be tuned through their precursor chemical composition as well as surface modification (i.e. incorporation of responsive functionalities), to respond to specific stimuli such as pH, temperature, ionic strength, molecules, electric or magnetic signals.[12]

The capability of a hydrogel to induce tissue regeneration largely relies on the biomaterial selected to produce it, as it guides the cellular growth, differentiation and organization providing physical support for cells as well as topographical, chemical and biological cues.[11]

3.1.1. Thermo-sensitive Hydrogel

Thermo-sensitive hydrogels are a class of hydrogels that are considered particularly interesting because of their ability to undergo reversible sol-gel transitions in response to temperature changes. The gelation is driven exclusively by temperature and does not require the supplement of other potentially toxic chemical reagents, such as cross-linkers, catalysts or organic solvents. Thermo-sensitive hydrogels can be categorized into positive-sensitive hydrogels with an upper critical gelation temperature (UCGT) and negative-sensitive hydrogels with a lower critical gelation temperature (LCGT). While the former gel upon cooling below the UCGT, the latter undergo a sol-gel transition with increasing temperature above LCGT (**Figure 3.1**), when polymer water solution concentration is above critical gelation concentration (CGC). Hydrogels based on LCGT polymers are receiving increasing attention as cell, bioactive molecule and drug carriers due to many advantages, such as (i) the possibility to easily encapsulate cells and biomolecules in mild conditions by dispersing them at temperatures lower than LCGT, when the polymer solution is in a sol state, followed by gelation in physiological conditions, (ii) the convenience of application (possibility to minimally invasive injection in the sol state followed by gelation *in situ*) and (iii) easy formation in any desired shape (capability to completely fill any body cavities or defects prior to complete gelation).[4,8,13-15]

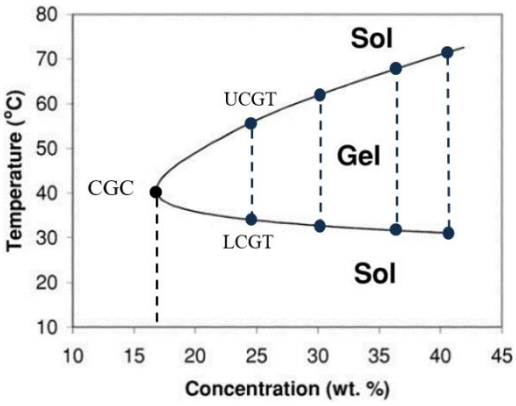

Figure 3.1 Example of sol-gel and gel-sol transitions of thermo-sensitive hydrogels.

3.1.2. Poloxamers

The Poloxamers, also known by the trademark Pluronic, Synperonic and Tetronic, are non-toxic FDA approved triblock copolymers of poly(ethylene oxide) (PEO) and poly(propylene oxide) (PPO) available in different molecular weights and PPO/PEO ratios. The presence of PEO and PPO blocks with an ABA-type triblock structure in a single polymer chain gives rise to amphiphilic molecules that self-assemble undergoing to a sol-gel transition with a LCGT behavior (**Figure 3.1**). Like many other thermo-sensitive hydrogels, the P407-based one gels by micelles formation and packing with increasing temperature (**Figure 3.2**).

Poloxamer P407 (M_n=12600 g/mol, PEO_{99}–PPO_{67}–PEO_{99}), is one of the most widely studied temperature-sensitive polymers and has been applied as drug and/or cell carriers.[16-18] In fact, P407-based hydrogels have been showed to be non-toxic and able to form gels at 25 °C at a concentration of 20 %w/v.[19-22] However, its applications are greatly limited by its poor mechanical properties as well as its fast dissolution and high permeability in aqueous environment, resulting from the purely physical crosslinking (i.e. hydrophobic interactions and hydrogen bonds).[23-25] P407 drawbacks also derives from its triblock chemical structure with terminal hydrophilic groups that does not allowed the micelles to form bridges between them. On the other hand, triblock-based hydrogels with terminal hydrophobic groups promote the linking between micelles due to the possibility of the triblock to work as a bridge.

Moreover, concerning the drug release applications, low solubilization of extremely hydrophobic drugs results in low drug-loading, and hydrophobic drugs can easily form a partial suspension, which may result in thermo-dynamic instability of the gel system.

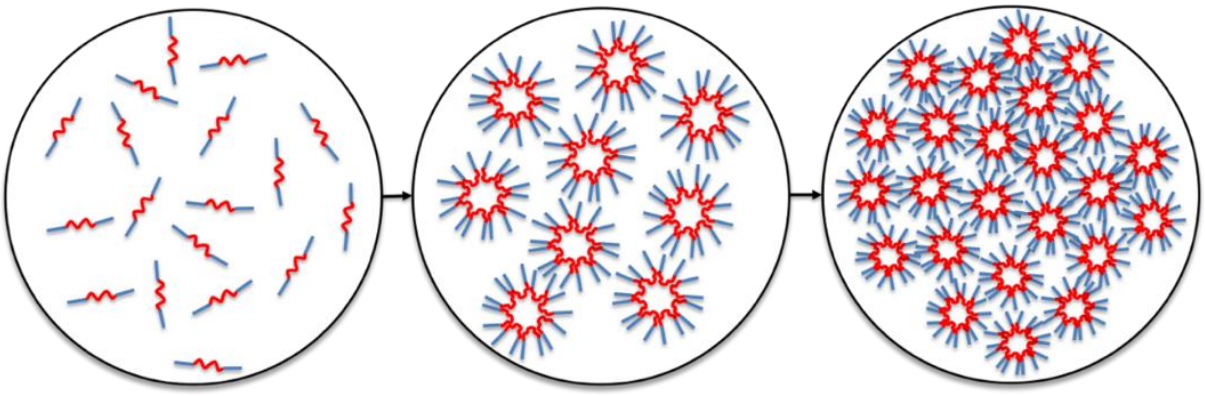

Figure 3.2 Representation of the gelation process by micelles formation and packing. The micelles are characterized by a hydrophobic core and a hydrophilic shell.

Increasing poloxamer molecular weight or providing it with functional groups for chemical crosslinking during sol-gel transition are valid strategies to enhance hydrogel stability in water environment.[23-28] Moreover, fabricating a larger hydrophobic domain in a biomaterial may result in higher drug loading and extend drug release.

In 2006, Sun et al.[23] reported a poloxamer-based disulfide multiblock copolymer with enhanced and thiol-concentration-dependent stability and drug release kinetics. Similarly, Niu and colleagues[24] synthesized an acrylate/thiol modified Poloxamer P407, which solutions were able to undergo physical and chemical gelation in physiological conditions as a consequence of the hydrophobic interactions and the spontaneous reaction between thiol and acrylate. In order to decrease the polymer concentration necessary to induce the sol-gel transition at 37 °C, Volkmer et al.[25] successfully chain extended Pluronic P123 with 1,6-hexanediisocyanate (HDI), 1,4-butane diisocyanate and hydrogenated diphenylmethane diisocyanate. Similarly, Cohn and colleagues[26, 27] chain extended Pluronic F127 with HDI, demonstrating the effectiveness of such strategy in increasing hydrogel viscosity and decrease critical gelation concentration (CGC, the minimal concentration required to observe a sol-gel transition) compared to F127-based hydrogels. Similar results were reported in 2014 by Loh et al.[28] who

synthesized a poly(ether carbonate urethane) from Pluronic F127 and poly(polytetrahydrofuran carbonate) diol, using HDI as coupling agent.

In this chapter, the chain extension strategy, to improves the P407-based hydrogels properties, was improved through the PUR chemistry. In order to demonstrate the enhanced properties of the designed hydrogels, aqueous solutions of the synthesized PUR (acronym NHP407) and poloxamer P407 were both characterized in terms of micellization potential, gelation temperature, time and kinetics, and stability in water environment. In addition, hydrogel injectability, cytotoxicity and permeability to nutrients were tested from the perspective of their application in the biomedical field as injectable *in situ* sol-gel systems or bioinks in bioprinting technology. Moreover, PUR-based hydrogels capability to load and deliver drugs/biomolecules was assessed by encapsulating hydrophobic antioxidant drugs (curcumin, dexamethasone and resveratrol) and two hydrophilic proteins, used as models for growth factor and protein release (horseradish peroxidase, bovine serum albumin).

3.1.3. Antioxidant Drugs

Oxidative stress is one of the major symptoms connected to physiological functions and numerous diseases such as cancer, diabetes, infectious, cardiovascular and neurodegenerative diseases as well as in the aging process.[29,30] A free radical is any species capable of independent existence that contains one or more unpaired electrons. Such highly reactive oxidizing molecules are endogenously produced in the human body, both by deliberate synthesis (e.g., by activated phagocytes) and by chemical side-reactions (e.g., oxidases and oxygenases). Other exogenous factors (e.g., UV radiation) can produce oxidant as well.

Among these reactive molecules, those deriving from reactive oxygen species (ROS) have the main biological impact because they are endogenously produced at the highest concentration.

Oxidative stress, occurring when there is an imbalance between oxidants and anti-oxidants in favor of the oxidants,[31] has been showed to act as the converging point of stimuli leading to autophagy.[32] ROS have the ability to potentially damage cell structure by taking electrons from cellular biomolecules (e.g. DNA, proteins) and generating chain reactions.[32]

Several antioxidants are available for therapeutic use, coming from natural or synthetic sources.[33] However, biological barriers limit the efficiency of such drugs, preventing their accumulation in specific diseased sites. Moreover, due to the diffusion of the drug molecules, undesirable side effects are common.[34]

Drug delivery platforms such as injectable hydrogels and nanoparticles have emerged as suitable vehicles for overcoming pharmacokinetic limitations associated with conventional drug formulations.

3.2. Materials and Methods

3.2.1. Amphiphilic Poloxamer-based Polyurethane Synthesis

In order to increase the stability of P407-based hydrogels, the P407 chains were extended through the PUR chemistry. To this aim, a PUR was synthetized through a two-step procedure based on (i) a first reaction of Poloxamer P407 and HDI, followed by (ii) a second reaction between the formed prepolymer and an amino acid derived diol (N-Boc serinol). The Boc-protected amino groups are available for further functionalization with proteins or peptides after deprotection in acidic conditions.[35]

3.1.1.1. Reagents and Solvents

Poloxamer P407, 1,6-diisocyanatoexane (HDI), dibutyltindilaurate (DBTDL) and N-Boc serinol were purchased from Sigma Aldrich, Italy.

Poloxamer P407 and N-Boc Serinol were dried overnight under reduced pressure at room temperature in a desiccator to remove residual water before use. HDI was periodically distilled at low pressure and stored in a flask with flat bottom in a desiccator. All solvents were purchased from Sigma Aldrich (Italy) in the analytical grade. Anhydrous 1,2 dichloroethane (DCE) was prepared using molecular sieves for at least 8 hours before use. Molecular sieves were activated in an oven at 120 °C for at least 8 hours. Glassware required for the synthesis, magnets, spatulas and tweezers were dried overnight in an oven at 120 °C.

3.1.1.2. Synthesis Steps

Poloxamer-based amphiphilic PUR was synthesized through a two-step procedure in inert atmosphere using anhydrous DCE as solvent and starting from P407 as macrodiol, HDI and N-Boc serinol as chain extender.[36]

Briefly, Poloxamer P407 (20 %w/v in DCE) was first reacted with HDI (1:2 molar ratio with respect to the P407) for 2.5 h at 80 °C, in the presence of the catalyst DBTDL (0.1 %w/w with respect to the P407) to form the prepolymer. In the second step, N-Boc serinol was added (3 %w/v in DCE, 1:1 molar ratio with respect to P407) and the reaction was stopped with methanol after 1.5 h at 60 °C. The polymer was collected by precipitation in petroleum ether (4:1 volume ratio with respect to DCE), purified by dissolution in DCE (20 %w/v) followed by precipitation in diethyl ether and methanol (98:2, 5:1 volume ratio with respect to DCE). The polymer was collected by centrifugation at 6000 rpm and 5 °C and dried overnight at room temperature. Eventually, the obtained polymer was grinded and washed in diethyl ether (50 mg/ml) overnight. The purified polymer was dried overnight under vacuum at room temperature and stored in nitrogen atmosphere at 5 °C to prevent the oxidative degradation.

3.1.1.3. Polyurethane Nomenclature

The synthesized PUR has acronym NHP407, where the first letter (N) indicates the chain extender, H corresponds to HDI, while P407 refers to Poloxamer P407.

3.1.2. Physico-Chemical Characterization

Attenuated Total Reflectance Fourier Transform Infrared (ATR-FTIR) spectroscopy and Size Exclusion Chromatography (SEC) were exploited to assess the success of PUR synthesis.

3.1.2.1. Infrared Spectroscopy

ATR-FTIR spectra of the synthesized NHP407 and its precursor (P407) were obtained in the spectral range from 4000 to 600 cm^{-1} at room temperature using a Perkin Elmer Spectrum 100 equipped with an ATR accessory (UATR KRS5) with diamond crystal. Each spectrum was obtained as a result of 16 scans with a resolution of 4 cm^{-1} and analyzed using the Perkin Elmer Spectrum Software.

3.1.2.2. Size Exclusion Chromatography

Number average and weight average molecular weights (M_n and M_w), and molecular weight distribution ($\alpha = M_w/M_n$) of NHP407 and P407 were estimated by SEC. The instrument was equipped with a Refractive Index (RI) detector and two Waters Styragel columns (HT2 and HT4) conditioned at 35 °C. Tetrahydrofuran (inhibitor-free, for HPLC, ≥99.9%) was used as mobile phase at a flow rate of 0.4 ml/min. M_n and M_w were determined by the Agilent ChemStation Software relative to the universal calibration curve. The latter was constructed based on 10 narrow polystyrene standards ranging in M_n from 740 to $18 \cdot 10^4$ g/mol. The polymers were dissolved in tetrahydrofuran (2 mg/ml) and filtered through a 0.45 µm syringe filter before analysis.

3.1.3. Hydrogel Preparation

Thermo-sensitive hydrogels were prepared by NHP407 and P407 powder solubilization in aqueous media at 5 °C to avoid micellization and/or gelation during solution preparation. In detail, each sample at a given concentration was prepared by dissolving a known amount of

polymer in phosphate buffered saline (PBS, pH 7.4) or Dulbecco's Modified Eagle Medium (DMEM) with low glucose content, depending on the applications.

3.1.4. Thermo-sensitive Hydrogel Characterization

In order to evaluate the use of NHP407-based solutions as injectable drugs/biomolecules/cells carriers and as bioinks for extrusion-based bioprinting, the thermo-sensitive behavior and the gelation properties were first studied. Moreover, hydrogels injectability and cytotoxicity was assessed and the release of drugs/biomolecules was studied.

3.1.4.1. Dynamic Light Scattering

The average hydrodynamic diameter of the micellar structures present in NHP407- and P407-based solutions (0.5, 1, 3, 5 and 6 %w/v in PBS) was estimated by dynamic light scattering (Zetasizer Nano S90, Malvern Instruments, UK) at different temperatures (25, 30, 37 and 45 °C, equilibration time 5 minutes), according to the method reported by Pradal et al.[37] Micelle size was taken as the mean value of three measurements. Due to the turbidity of the gel forming samples, only non-gelling systems were studied to investigate the mechanism of structure formation.

3.1.4.2. Critical Micellar Temperature Estimation

Hydrogel critical micellar temperature (CMT) was studied by adding the fluorescent dye 1,6-diphenly-1,3,5-hexatriene (DPH, $4 \cdot 10^{-4}$ M in methanol) to NHP407- and P407-based solutions (0.1, 0.5, 1, 3, 5and 6 %w/v in PBS) as a contrast marker for micellization. UV-Vis absorption spectroscopy (PerkinElmer Lambda 25 UV/VIS Spectrometer) was used to evaluate

micellization since DPH absorbance (DPH main absorption peak at 350-360 nm) increases as it distributes from the hydrophilic into the hydrophobic regions, in this case micelle core. The analyses were conducted in the temperature range from 5 to 40 °C at a rate of 1 °C/step (equilibration time 5 minutes). CMT was estimated starting from the recorded spectra according to the protocol reported by Alexandridis et al.[38]

3.1.4.3. Tube Inverting Test

Sol-gel-sol phase transition and gelation time in physiological conditions of NHP407- and P407-based solutions were investigated by using the tube-inverting method. The volume of each solution was kept at 1 ml in total regardless of the concentration and was put in a Bijoux sample container with an inner diameter of 17 mm.

Concerning the sol-gel-sol phase transition, each sample was subjected to a controlled temperature increase from 5 °C to 70 °C, at a rate of 1 °C/step. Each step consisted of a 1 °C temperature increase, followed by temperature maintenance for 5 minutes and tube inversion, that allowed the visual inspection of the sol-gel-sol transition. Conditions of sol and gel were defined as “flow liquid sol” and “no flow solid gel” in 60 s, respectively.

Concerning the gelation time in physiological conditions, instead, the samples were incubated at 37 °C and sol-gel transition was verified by inverting the vials for 60 seconds at predefined time points (1, 2, 3, 4, 5, 6, 7, 8, 9, 10, 11, 12, 13, 14, 15, 30 minutes) upon samples acclimatization at 5°C for 10 minutes. Conditions of sol and gel were defined as previously reported.

3.1.4.4. Rheological Characterization

Specimens for rheological analysis were prepared according to the protocol previously described (paragraph 3.1.3). Rheological measurements were carried out on a stress-controlled rheometer (MCR302, Anton Paar GmbH) using a 50 mm parallel plates geometry with a gap of 0,8 mm. The rheometer was equipped with a Peltier system for temperature control.

Rheological characterization provides useful insight in order to investigate the gelation processes under isothermal and non-isothermal conditions.

Under isothermal conditions, small amplitude oscillatory shear (SAOS) tests was used to assess linear rheological properties, and large amplitude oscillatory shear (LAOS) test (nonlinear) was exploited to detect structural information. In particular, complex fluids are classified to four types depending on LAOS behavior (storage modulus -G'- and loss modulus -G''- trends): (Type I) strain thinning: G′ and G″ decrease; (Type II) strain hardening: G′ and G″ increase; (Type III) weak strain overshoot: G′ decrease and G″ first increase and eventually decrease); (Type IV) strong strain overshoot: G′ and G″ first increase and eventually decrease.

Temperature ramp test (non-isothermal) was used to determine the viscosity trend by changing the temperature.[39]

SAOS tests were performed in the frequency range from 0.1 to 100 rad/s, at 0.1 % strain and 25, 30 and 37 °C. LAOS tests were performed in the strain range from 0.01 to 100 %, at 1 Hz frequency and 37 °C. For each analysis, the sample was put on the lower plate of the rheometer at 0 °C, heated at the desired temperature, maintained in quiescent conditions for 10 minutes to reach the thermal stability and finally isothermally tested. Temperature ramp tests were performed in the temperature range from 5 to 40 °C, at constant shear rate (10 Hz) and a slope of 1 °C/min.

3.1.5. Swelling and Stability to Dissolution Test

Stability and swelling tests were carried out on NHP407-based (15 and 20 %w/v) and Poloxamer P407-based (20 %w/v) hydrogels, prepared according to the previously described protocol. Before starting the tests, all the prepared samples were weighted (W_{gel_i}). The prepared hydrogels (1 ml in Bijou sample container) were then incubated at 37 °C (IKA KS-4000i control) to induce gelation prior to test beginning. After approx. 15 minutes, 2 ml of PBS (pH 7.4, 37 °C) were added to each vial. At predefined time points (3 h, 6 h, 1 d, 3 d, 5 d, 7 d, 15 d, 25 d, 35 d), 3 samples were taken and weighted (W_{gel_f}) after removal of the residual PBS. The gels were then freeze dried (Martin Christ ALPHA 2-4 LSC) and again weighted ($W_{freeze\ dried\ gel\_f}$). A control gel (non-incubated sample) was also freeze dried and weighted ($W_{freeze\ dried\ gel\_i}$). PBS absorption (%) and hydrogel weight loss (%) were calculated according to the following equations (**Equation 1**and **Equation 2**):

$$PBS\ absorption\ (\%) = \frac{W_{gel\_f} - W_{gel\_i}}{W_{gel\_i}} \cdot 100 \qquad \textbf{(Equation 1)}$$

$$\text{Hydrogel weight loss } (\%) = \frac{W_{freeze\ dried\ gel\_i} - W_{freeze\ dried\ gel\_f}}{W_{freeze\ dried\ gel\_i}} \cdot 100 \qquad \textbf{(Equation 2)}$$

Results are reported as mean ± standard deviation.

3.1.6. Permeability Test

Permeability studies were performed to model the transport of nutrients to the cells encapsulated in the bioinks. Fluorescein isothiocyanate-dextran (FD4, M_w 3000-5000 g/mol) is generally used as a model of nutrients,[40] since its Stokes radius (14 Å) is higher than that of nutrients (glucose and NaCl show a Stokes radius of 3.8 and 1.4 Å, respectively).

NHP407-based bioinks (15 and 20 %w/v, 1 ml) were prepared according to the protocol previously reported and subjected to gelation at 37 °C for 15 minutes. 1 mL of a FD4 solution in PBS (1 mg/ml) was then added to each vial and the samples was incubated at 37 °C. At predefined time steps (1, 7, 24, 48, 72,168 h), 3 samples were taken and the residual absorbance of the FD4 solution was measured by UV-VIS spectroscopy in the 350-600 nm range, since the main absorption intensity peak of FD4 is expected at 493 nm. Therefore, the amount of FD4 absorbed by the hydrogel was indirectly defined as the difference between the starting and the residual FD4 content in the solution incubated with the samples. The test was conducted in triplicate. Results are reported as mean ± standard deviation.

3.1.7. Hydrogel Injectability and Diffusivity

Hydrogel injectability and potential applicability in additive manufacturing technologies was preliminarily evaluated using a volumetric pump equipped with a traditional 2.5 ml plastic syringe. 10, 15 and 20 %w/v concentrated NHP407-based hydrogels were characterized. To make the hydrogels easily noticeable, PBS was colored with Toluidine Blue (0.1 w/v, Sigma Aldrich, Italy) before sample preparation. Injectability was tested using two needles (6.3 mm length) differing in internal diameter (200 and 250 μm). The tests were conducted at four different flow rates (3, 5, 8 and 10 ml/h) and three hydrogel temperatures (5, 25 and 37 °C).

The capability of the bioinks to gel *in situ* was evaluated as previously reported by Ma et al.[41] Both P407-based and NHP407-based solutions equilibrated at 5 °C were injected into a backer containing 37 °C water. As in injectability tests, Toluidine Blue was added to PBS before solution preparation to clearly see the gel. The capability of the hydrogel to diffuse in a tissue was assessed by injecting it in a bovine heart. The heart was first sectioned in squares, equilibrated at 37 °C in an incubator (IKA KS-4000i control) and then injected with a 15 %w/v

concentrated NHP407 hydrogel (400 µL) previously conditioned at 5 and 25 °C. The injected heart was again equilibrated at 37 °C for 5 minutes prior to dissection. All the tests carried out to assess gel injectability, *in situ* formation and potential diffusion in a tissue were thoroughly recorded and photographed.

Qualitative dissolution study was also performed on the hydrogels in the form of thin filaments. For this purpose, the hydrogels were extruded through a syringe equipped with nozzle (200 and 250 µm diameters) and incubated at 37 °C. The progressive filament dissolution was assessed by visual inspection.

3.1.8. Cytotoxicity Test

Cytotoxicity of hydrogel eluates was evaluated on three different cell lines: keratinocytes (HaCaT), myoblasts (C2C12) and fibroblasts.

HaCaT cells are immortalized human skin keratinocytes that mimic many properties of normal epidermal keratinocytes. They are not invasive and can differentiate under appropriate experimental conditions. C2C12 is an immortalized mouse myoblast cell line. Human fibroblast cell line (46 BR.1N) was obtained from European Collection of Cell Cultures (ECACC). Cells were maintained at 37 °C, 5% CO_2, in DMEM supplemented with 10% fetal bovine serum (FBS) and 1% antibiotic mixture.

Hydrogel cytotoxicity was assessed on extracts of biomaterial in complete medium. Briefly, extracts were obtained by incubating the hydrogel in DMEM (supplemented with 10% fetal bovine serum, 290 µg/mL glutamine, 100 U/mL penicillin and 100 µg/mL streptomycin) at a concentration of 0.1 g/mL for 24 h at 37 °C. The obtained hydrogel extracts were added to subconfluent cell cultures (20000 cells/well, 96-well plates) on conventional tissue culture plates. After 24 h, the medium was removed and cells were gently washed with PBS, stained

for 10 min with 0.5% crystal violet in 145 mmol/L NaCl, 0.5% formal saline, 50% ethanol, and washed three times with water. Crystal violet was eluted from the cells with 33% acetic acid and the absorbance of the supernatants was measured at 540 nm in a microplate reader (Infinite 200 Pro, Tecan, Wien, Austria).

3.1.9. Biomolecules and Drugs Incorporation and Release

NHP407-based hydrogels with a PUR concentrations of 15 and 20 %w/v were tested as potential drug and biomolecule carriers. To this aim, hydrophobic drugs (dexamethasone -DEXA, M_w=392 Da-, curcumin -CUR, M_w=368 Da- and resveratrol -RES, M_w=228 Da-) and hydrophilic model proteins (bovine serum albumin -BSA, M_w=66000 Da- and horseradish peroxidase -HRP, M_w=40000 Da-) were encapsulated within the hydrogels at a final concentration of 1 mg/ml and their release profile was studied. Thermo-sensitive properties of the obtained carriers were also evaluated to assess the effects of molecule loading on the sol to gel transition.

3.1.9.1. Hydrogel Preparation

Bovine serum albumin and horseradish peroxidase were first dissolved (1 mg/ml) in PBS and the resulting solution was used for NHP407 powder solubilization according to the previously described protocol. For hydrophobic drug encapsulation, NHP407 powder was first dissolved in pure PBS and the drugs (1 mg/ml) were added after solubilization in EtOH (10 mg/ml for DEXA and RES, 20 mg/ml for CUR). EtOH was then evaporated under stirring at 5 °C overnight.

3.1.9.2. Characterization of Hydrogel Thermo-sensitive Behavior

Gelation time and sol-gel phase transition of drug/protein-loaded NHP407 solutions were investigated to assess the effects of drug/biomolecule encapsulation on the gelation properties of PUR-based hydrogels. Tests to estimate gelation time in physiological condition and the sol-gel-sol phase transition were performed according to the protocols previously described (paragraph 3.1.4.3).

Rheological characterization of drug/protein-loaded NHP407 solutions was also performed according to the protocols reported in paragraph 3.1.4.4.

3.1.9.3. *In vitro* Release Test

Drug/protein-loaded hydrogels (1 ml) were prepared in Bijou sample containers according to the previously described protocol and incubated at 37 °C for 15 minutes to form a gel. Then 1 ml of PBS was added to each gel and the vials were kept at 37 °C in incubator (IKA KS-4000i control). At predetermined time points (1 h, 5 h, 1 d, 2 d, 3 d, 7 d, 10 d, 14 d, 21 d and 28 d) PBS was removed from the vials and the same volume of PBS at 37 °C was added. The collected solutions were analyzed to determine the total amount of released drug by High Pressure Liquid Chromatography (HPLC, Thermo Scientific Dionex UltiMate 3000), UV-Vis spectroscopy (PerkinElmer Lambda 25 UV/VIS Spectrometer) or Bicinchoninic Acid (BCA) Protein Assay, depending on the analyzed molecule. In detail, the amount of released DEXA was determined by HPLC, setting the detection wavelength at 238 nm and using a mobile phase at 25 °C composed of acetonitrile and water (60:40, v:v), an injection volume and flow rate of 20 µl and 1 ml/min, respectively.[42] The amount of released RES and CUR, instead, was measured by UV-Vis spectroscopy by collecting absorbance spectra in the 200-400 nm and 350-600 nm range (resolution 1 nm); since the main absorption intensity peak of RES and CUR appears at 306 and

431 nm, respectively.[43,44] The amount of released proteins (BSA and HRP) was evaluated by using a BCA Protein Assay according to the kit instructions, by measuring the absorbance at 540 nm in a microplate reader (Sirio S, SEAC, Florence, Italy). All tests were conducted in triplicate. Results are reported as mean ± standard deviation.

To further explain the nature of drug and protein release behavior from the studied formulations, Peppas equations[45] were used (**Equation 3** and **Equation 4**), written as:

$$\frac{M_t}{M_\infty} = k \cdot t^n \qquad \textbf{(Equation 3)}$$

$$log\left(\frac{M_t}{M_\infty}\right) = n \cdot log(t) + log(k) \qquad \textbf{(Equation 4)}$$

Where M_t and M_∞ are the absolute cumulative amounts of drug released at time t and infinite time, respectively, k is a constant related to the structural and geometric characteristics of the device, and n is the release exponent, indicative of the mechanism of drug release. According to Peppas equation there are distinct physical meanings of n: (i) n=0.45 indicates diffusion-controlled drug release, termed Fickian diffusion, (ii) n=0.89 indicates relaxation or swelling-controlled drug release, which is termed case II transport. When n is between the two values the drug release behavior can be regarded as a superimposition of both the cases, which is named anomalous transport.

3.1.9.4. Sodium dodecyl sulfate-polyacrylamide gel electrophoresis

Sodium dodecyl sulfate-polyacrylamide gel electrophoresis (SDS-PAGE) was performed at the Department of Applied Science and Technology (DISAT) of Politecnico di Torino (Biosolar Lab, Alessandria, Italy). SDS-PAGE analysis was performed to experimentally confirm the electrophoretic properties and integrity of the released BSA. An aliquot of release solutions

containing released BSA and an aliquot of stock BSA solutions were analyzed. The protein molecular weight standard used was the low molecular weight calibration kit for SDS electrophoresis: phosphorylase b (97.0 kDa), albumin (66.0 kDa), egg albumin (40.0 kDa) and carbonic anhydrase (30.0 kDa), trypsin inhibitor (20.0 kDa), lactalbumin (14.0 kDa). Protein bands were visualized by staining with Coomassie Blue Colloidal Blue Staining Kit. The gel was developed using the protocol supplied by manufacturer and images acquired by using a BioDoc-IT Gel Documentation System (UVP, Inc.,Upland,CA).

3.1.9.5. Enzymatic Activity Quantification

HRP enzymatic activity was calculated by quantification of oxidative 3,3′,5,5′-Tetramethylbenzidine (TMB) substrate in a peroxidase solution using a TMB Substrate Kit (Santa Cruz Biothecnology, Germany).

TMB (3, 20, 5, 50-tetramethylbenzidine) is a chromogenic substrate for HRP. Once oxidized by the enzyme, this substrate yields a blue product that absorbs at 370 nm and 652 nm. The addition of 2M sulfuric acid to stop the reaction changes the product to yellow that absorbs at 450 and 405 nm. End-point assay (incubation at 25 °C followed by addition of 2M sulfuric acid to stop the reaction) was carried out according to the kit instructions. Absorbance was measured at 450 nm in a micro plate reader (SirioS, SEAC, Florence, Italy).

3.1.10. Functionalization Potential Study

The possibility to functionalize the PUR by BOC de-protection by exposing the amino groups was studied.

3.1.10.1. BOC de-protection of NHP407

In order to expose free amino groups along NHP407 polymeric chains, the PUR was dissolved in chloroform (1 %w/v) and trifluoroacetic acid (TFA) was then added according to Park et al. procedure.[46]

BOC de-protection process was optimized in order to minimize the amount of TFA used, while maintaining the de-protection efficiency and minimizing the risk of polymer chemical degradation. Several chloroform/TFA ratios were tested (50:50, 60:40, 70:30, 80:20, 90:10, 95:5, 100:0 v:v).

BOC de-protection was performed for 1 h at room temperature and rotary evaporation was applied to remove both TFA and chloroform. Subsequently, the de-protected polymer was again solubilized in chloroform (1 %w/v, 100 ml) for a second rotary evaporation in order to completely remove all the TFA traces. This process was performed twice. Eventually, the polymer was solubilized in demineralized water overnight and dialyzed (10-12 kDa cut-off) against water at 6 °C for 3 days to completely remove BOC groups and residual solvent traces. The dialyzed solution was finally freeze-dried (Martin Christ ALPHA 2-4 LSC, Osterode am Harz, Germany) to collect the polymer (yield: 83%). In addition, de-protected PUR powder were washed in diethyl ether overnight at room temperature to remove any residues of TFA. The collected material was finally dried at room temperature and stored in nitrogen atmosphere at 5 °C.

The obtained PUR has acronym SHP407, where the first letter (S) indicates the de-protected amino groups, H corresponds to HDI, while P407 refers to Poloxamer P407.

3.1.10.2. Physico-Chemical Characterization

In order to assess the chemical integrity of the PUR upon BOC de-protection in acid conditions, the FTIR and SEC analyses were performed following the previously reported protocols (paragraph 3.1.2.1 and 3.1.2.2).

Moreover, the success of the BOC de-protection was assessed by means of Proton Nuclear Magnetic Resonance (^{1}H-NMR). ^{1}H-NMR analyses were performed in anhydrous deuterated dimethyl sulfoxide (DMSO-d6, 99.8% D with 0.03% TMS) by means of Avance III Bruker spectrometer equipped with a 11.75 T superconductor magnet (500 MHz ^{1}H Larmor frequency). The ^{1}H-NMR spectra were recorded by averaging 12 runs, with 10 sec relaxation time. The signals were referenced to TMS at 0 ppm.

3.1.10.3. Ninhydrin assay (Kaiser test)

The amount of exposed amino groups after de-protection reaction was quantified by ninhydrin assay (Kaiser test kit, Sigma Aldrich, Italy) following supplier's instructions. Both NHP407and SHP407 were weighted (10 mg) and the testing reagents were added according to the manufacturer's protocol. Samples were incubated at 120 °C for 5 minutes and absorbance was measured through a UV-Vis spectrometer (PerkinElmer Lambda 365 UV/VIS Spectrometer) at 570 nm to finally determine the molar concentration of NH_2 groups.

3.1.11. Statistical analysis

Results are reported as mean ± standard deviation. Statistical analysis was performed using GraphPad Prism version 7.00 for Windows (GraphPad Software, La Jolla, CA, USA; www.graphpad.com). Two-way ANOVA analysis followed by Bonferroni's multiple

comparison test was used to compare results. The statistical significance of each comparison was assessed according to **Table 3.1**.

Table 3.1 Values of levels of statistical significance

P	Wording	Summary
<0.0001	Extremely significant	****
0.0001 to 0.001	Extremely significant	***
0.001 to 0.01	Very significant	**
0.01 to 0.05	Significant	*
<0.05	Not significant	ns

3.2. Results and Discussion

3.2.1. Polyurethane Chemical Characterization

ATR-FTIR spectroscopy was exploited to assess the success of PUR synthesis. **Figure 3.3** shows the ATR-FTIR spectra of Poloxamer 407 (the macrodiol used during the synthesis) and polyurethane NHP407, after its synthesis.

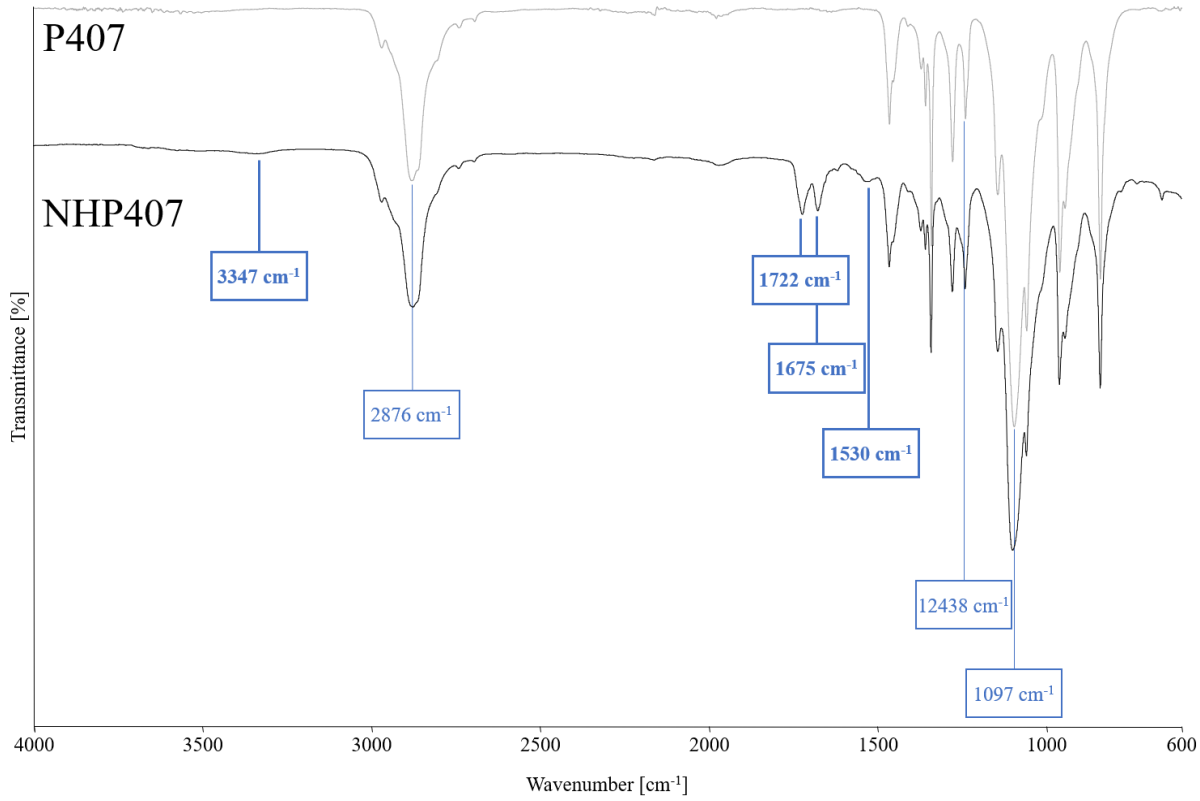

Figure 3.3 ATR FTIR spectra of P407 (grey) and NHP407 (black). Differences between the two spectra, proving successful NHP407 synthesis, are highlighted at 3347, 1722, 1675 and 1530 cm^{-1}. The peaks at 2876, 1238 and 1097 cm^{-1} are typical of P407.

P407 spectrum presents the characteristic absorption peaks of CH_2 stretching vibrations (2876 cm^{-1}) and CH_2 rocking and C-O-C stretching vibrations (1097 cm^{-1}) due to the repeated $–OCH_2CH_2$ units of PEO. PUR spectrum demonstrated synthesis success: two new bands

appeared at 1722 cm^{-1} and 1675 cm^{-1}, which are attributed to the stretching vibration (amide I) of free and bounded carbonyl group (C=O), respectively, while the peak at 1530 cm^{-1} represents N-H bending vibrations (amide II), indicating the formation of urethane linkages. The urethane and amide groups also showed absorption at 3347 cm^{-1}, ascribed to N-H stretching. The complete conversion of the monomers was proved by the absence of unreacted diisocyanate absorption peak at 2200 cm^{-1}.

Polyurethanes average numeral molecular weight (M_n) obtained by SEC was in the range of 50000-58000 Da, with a polydispersity index of 1.4, indicating a narrow distribution of the molecular weight as a consequence of the good control on the polymerization process.

3.2.2. Micelle hydrodynamic diameter

NHP407 and P407 solubilized in aqueous media are expected to organize into micelles with a hydrophobic core and a hydrophilic shell due to their amphiphilic properties.[38,47]

DLS analysis showed that unimers, micelles and aggregates were present in the solutions depending on the solubilized polymer, solution concentration and temperature.[37,48] **Figure 3.4** reports light scattering patterns for a 1 %w/v concentrated solution of P407 and NHP407 at four different temperatures (25, 30, 37 and 45 °C). Both the size distribution by intensity and by volume are reported. The size distribution among unimers, micelles and aggregates is temperature-sensitive.

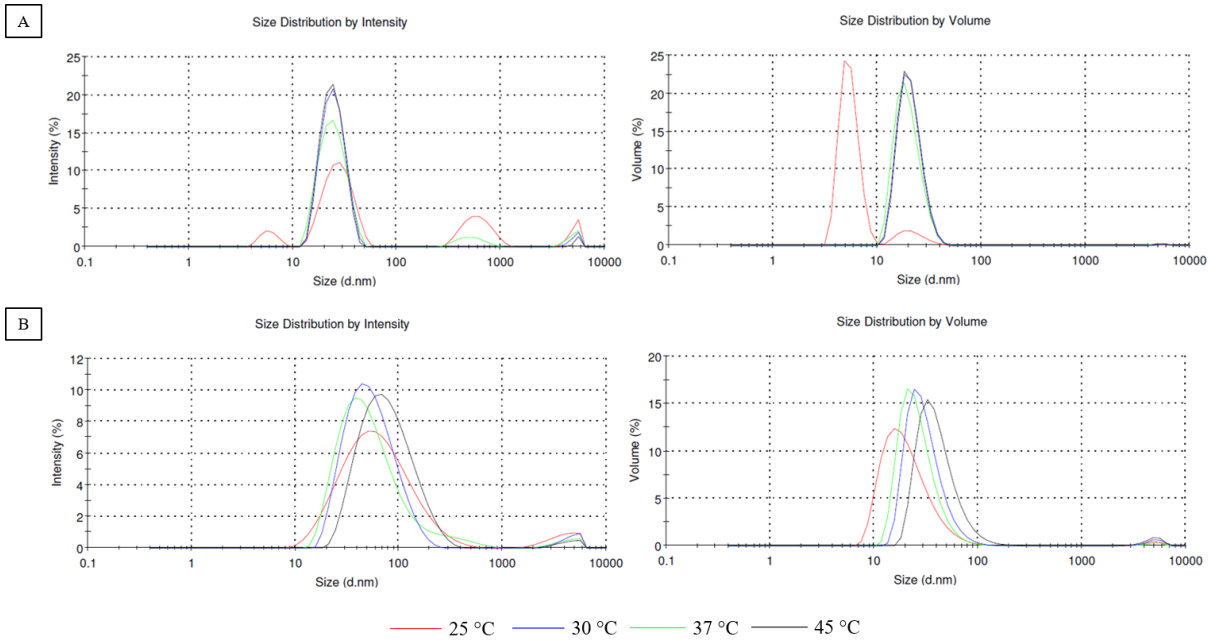

Figure 3.4 DLS patterns for **(A)** P407- and **(B)** NHP407-based solutions with 1 %w/v concentration. Unimers (about 6nm in diameter), micelles (about 30 nm in diameter) and aggregates (about 650nm in diameter) are present in P407-based sample at 25 °C. With increasing temperature unimers form micelles. In contrast, NHP407-based solution with the same concentration is already completely organized into micelles at 25 °C (about 90 nm in diameter).

Concerning the size distribution by intensity of the P407-based solution with 1 %w/v concentration, unimers (6.4±0.4 nm), micelles (28.2±0.3 nm) and aggregates (652.5±44.7 nm) were observed at 25 °C in the size distribution by intensity. However, in the size distribution by volume only unimers and micelles were visible. The reason of this phenomenon can be attributed to the fact the aggregates are bigger than the other structures and thus they scatter more light, however they are less numerous.

With increasing temperature, the micellar structure became progressively prevalent. Moreover, P407 micelle size has been reported to decrease with increasing temperature, due to PEO unit dehydration.[37,48] For the P407-based solution with 1 %w/v concentration, the average micelle size slightly decreased from 28.2±0.3 nm at 25 °C to 24.5±0.1 nm at 45 °C. In contrast, NHP407-

based solution with the same concentration was already completely organized in micelles at 25 °C. The average micelle diameter decreased from 88.9±10.3 nm at 25 °C to 57.3±4.0 nm at 37 °C and then increased to 70.7±17.1 nm at 45 °C. The different behavior of P407- and NHP407-based micelles was probably due to the strong attractive intermicellar interactions in NHP407-based solution, leading to micellar clustering, dominating over PEO dehydration phenomena.[49] The presence of larger micellar structures due to aggregation phenomena was also suggested by the wide distribution of the average micelle size in the case of the NHP407-based solution compared to P407-based one.[50]

In agreement with data reported by Cohn et al.,[20] P407 micelle size was not dependent on solution concentration: at 25 °C the micelles of P407-based solutions with 0.5 and 1 %w/v concentration were of 24.0±0.8 and 28.2±0.3 nm average size, respectively. In contrast, NHP407 micelle dimension increased with increasing solution concentration: at 25 °C the micelles of NHP407-based solutions with 0.5 and 1 %w/v concentration were of 46.0±6.9 and 88.9±10.3 nm average size, respectively. The different behavior of NHP407 and P407 solutions at the same concentration was probably due to aggregation phenomena of NHP407 micelles, due to the higher molecular weight of NHP407 compared to P407.

3.2.3. Critical Micellar Temperature Estimation

UV-visible spectroscopy was performed on diluted P407- and NHP407-based solutions at different temperatures in the presence of DPH, to measure their CMT, which is the temperature at which micellar structures start to form in the polymer solutions. At low temperatures, NHP407 and P407 polymeric chains in solution did not arrange into micelles, as demonstrated

by the negligible UV-visible absorption at 356 nm, which was indicative of the non-solubilization of DPH in a hydrophobic environment (**Figure 3.5 A**).

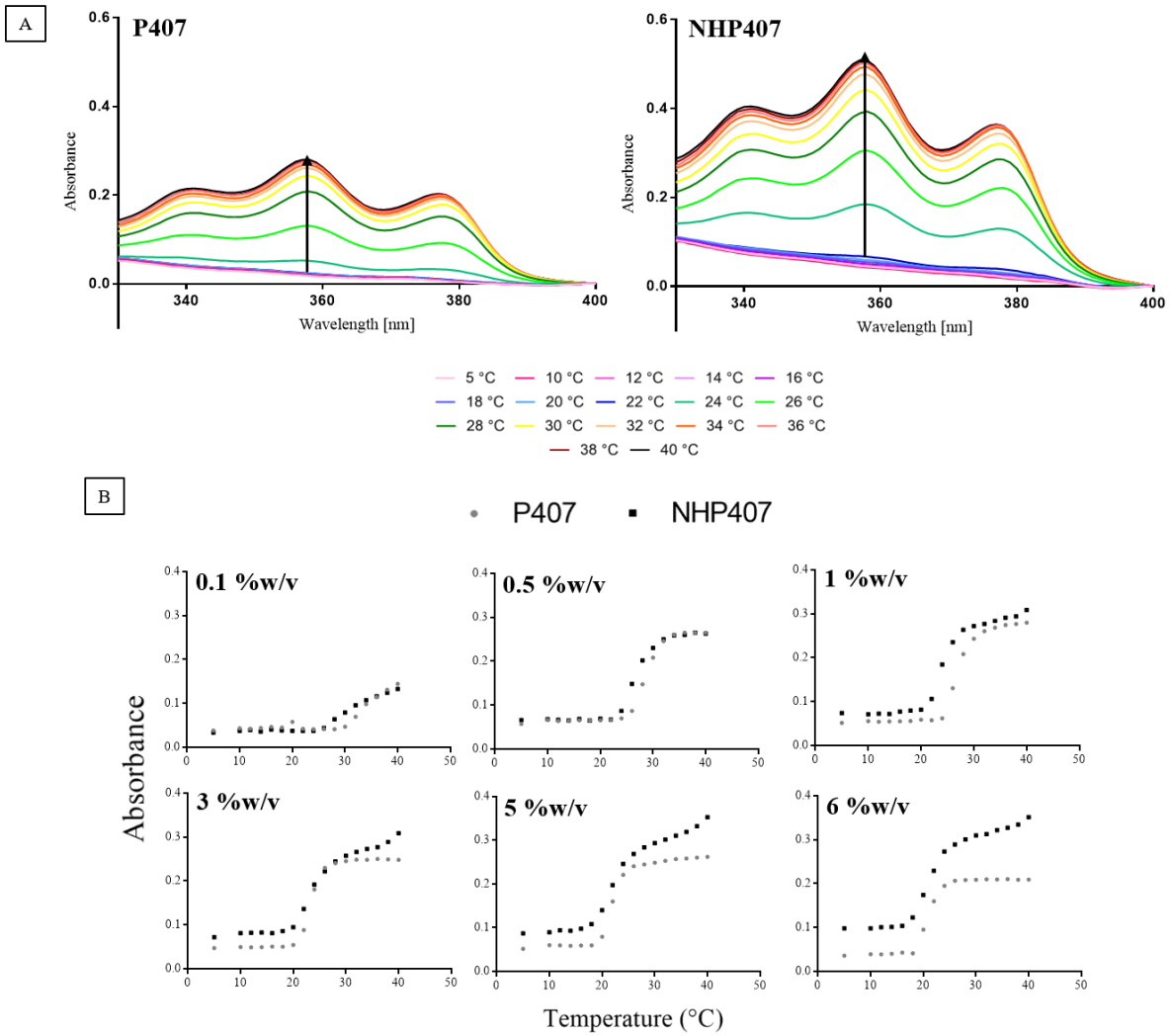

Figure 3.5 (A) UV-visible absorption spectra of DPH/P407- and DPH/NHP407-based solutions (1 %w/v) at different temperatures (5-40 °C). The appearance of an absorption peak at 356nm (due to DPH solubilization into the hydrophobic micelle core) proves micelle formation. **(B)** Absorption intensity of DPH/P407- and DPH/NHP407-based solutions at 356 nm as a function of temperature.

With increasing temperature, the UV-visible spectrum of both P407- and NHP407-based solutions showed a strong absorption at 356 nm, attributed to DPH solubilization into the hydrophobic micelle core, thus proving micelle formation. Moreover, the intensity of such

absorbance band increased with increasing temperature, indicating the progressive formation of micelle and a higher level of organization among the micelles forming aggregates (**Figure 3.5 A**). The CMT of the analyzed samples was estimated from the first inflection of the sigmoidal curve of the absorption intensity at 356 nm *versus* temperature, as it was caused by the formation of hydrophobic domains (**Figure 3.5 B**).

For both P407- and NHP407-based solutions, the CMT decreased with increasing the polymer concentration. At the same polymer concentration, NHP407-based solutions showed a slightly lower CMT compared to P407-based ones (around 1-2 °C). CMT values obtained for P407- and NHP407-based solutions are listed in **Table 3.2** as a function of copolymer concentration.

Table 3.2 CMT values obtained for P407- and NHP407-based solutions.

Concentration (%w/v)	**Critical Micellar Temperature (°C)***	
	P407	**NHP407**
0.1	29	24
0.5	25	23
1	23	22
3	21	20
5	19	18
6	18	17

* Error ±1 °C

3.2.4. Thermo-sensitive Behavior Characterization

3.2.4.1. Tube Inverting Test

Figure 3.6 reports the sol-gel transition curves for P407- and NHP407-based solutions in PBS, while the critical gelation concentrations and the sol-gel transition (gelation) temperatures are reported in **Table 3.3** and **Table 3.4**, respectively.

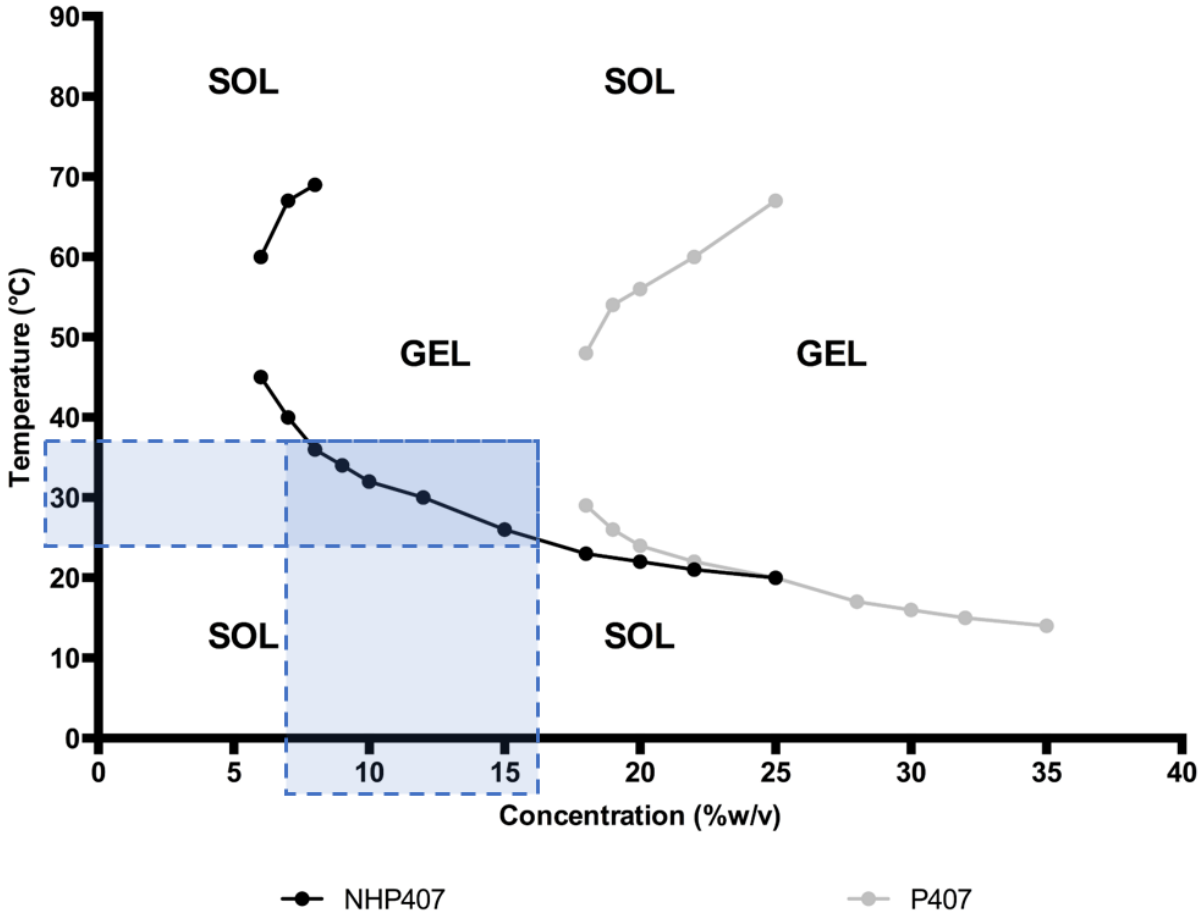

Figure 3.6 Sol-gel-sol transition curves for P407- and NHP407-based solutions in PBS.

NHP407-based solutions exhibited substantially different sol-gel transition behavior with respect to P407-based ones. In particular, NHP407 aqueous solutions underwent gelation at lower temperatures (between room temperature and body temperature) and the range of

concentration that showed gelation in the interested temperature range was wider, allowing a better tuning of the hydrogel properties.

Table 3.3 Critical Gelation Concentration for P407- and NHP407-based solutions in PBS.

Formulation	Critical Gelation Concentration (°C)
NHP407	6±1 °C
P407	18±1 °C

Table 3.4 Gelation Temperature for P407- and NHP407-based solutions in PBS.

Polymer Concentration (%w/v)	Gelation Temperature of NHP407-based solutions (°C)	Gelation Temperature of P407-based solutions (°C)
7.5 %w/v	37±1 °C	*
10 %w/v	32±1 °C	*
12.5 %w/v	30±1 °C	*
15 %w/v	26±1 °C	*
17.5 %w/v	24±1 °C	31±1 °C
20 %w/v	22±1 °C	26±1 °C

* the samples did not gel

No differences were observed between PBS- and DMEM-based solutions in terms of gelation temperature (**Figure 3.7**); thus, the two media were indiscriminately used depending on the applications. Therefore, although DMEM and PBS composition is different, the overall salting out effect of the corresponding hydrogels was approximately the same.

On the other hand, the polymers solubilized in water showed a slightly different behavior: the resultant hydrogels underwent gelation at higher temperature compared to those solubilized in PBS and DMEM. The reason of this phenomenon lies on the absence of salting out salts that are reported to induce a decrease of few degrees in gelation temperature.

Moreover, water is not suitable for biological applications and thus it was initially excluded from the hydrogel formulation.

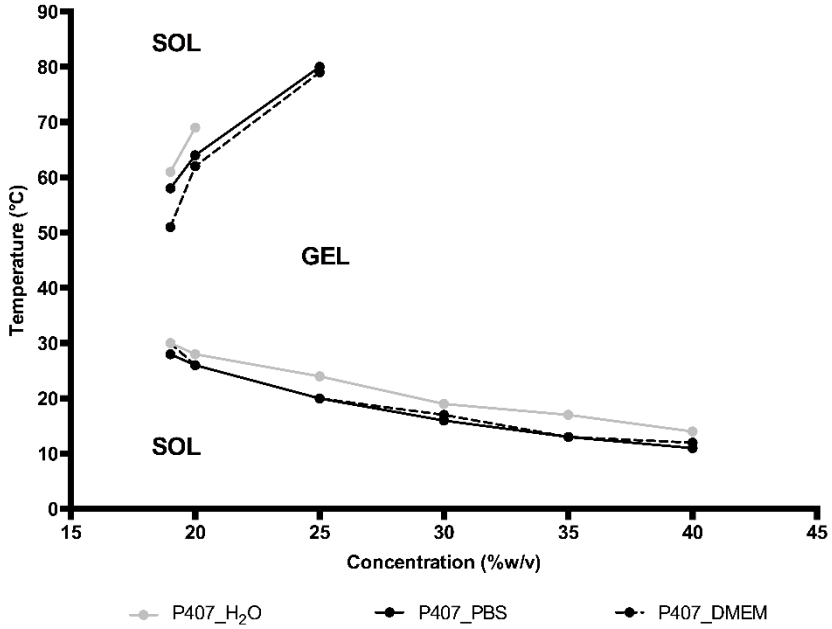

Figure 3.7 Sol-gel-sol transition curves for P407-based solutions in different media.

In addition, gelation time at 37 °C of various P407- and NHP407-based solutions was studied to evaluate hydrogel gelation potential in physiological conditions (**Figure 3.8**)

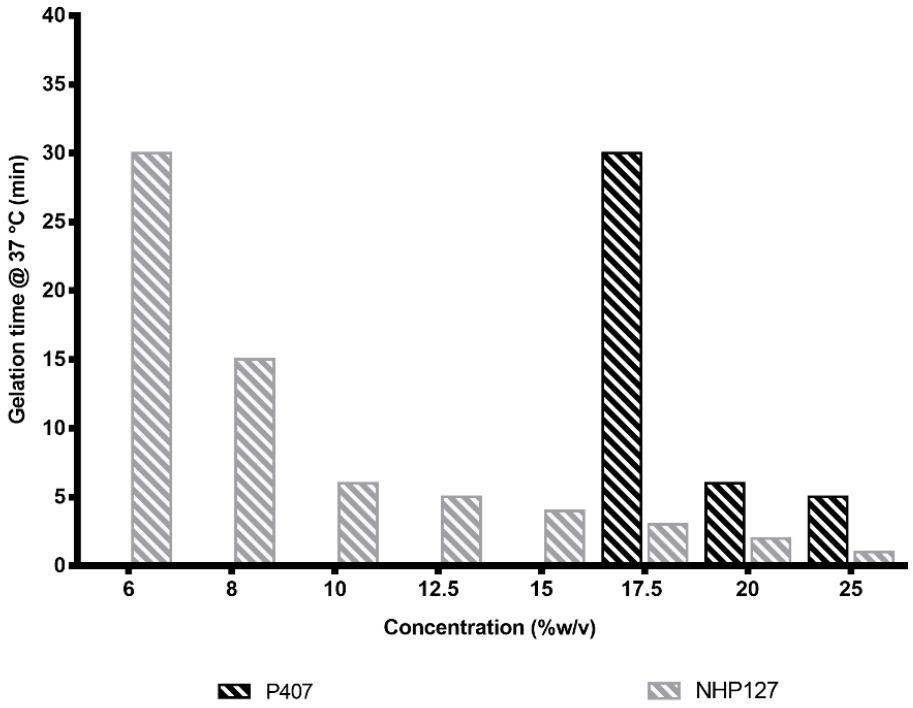

Figure 3.8 Gelation time at 37 °C of P407- and NHP407-based solutions prepared in PBS.

The NHP407-based solutions substantially show faster gelation in physiological conditions compared to P407-based samples with the same polymer concentration (1 and 5 minutes for required for gelation of NHP407 and P407 aqueous solution with 25 %w/v concentration).

3.2.4.2. Rheology

Information about the different gelation properties of P407- and NHP407-based solutions was obtained by means of LAOS and temperature ramp tests.

The trends of storage (G') and loss (G'') moduli, and shear stress (τ) as a function of applied strain (γ) for P407-based and NHP407-based solutions at 20 %w/v and 37 °C are reported in **Figure 3.9**.

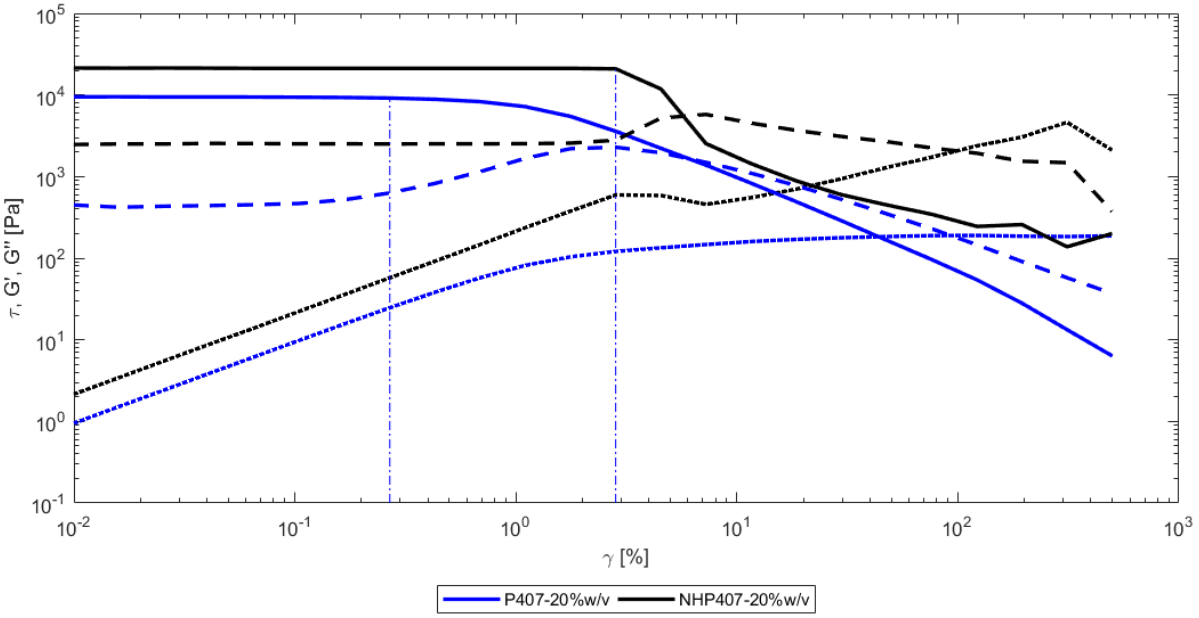

Figure 3.9 LAOS test: G', G'' and shear stress (τ) versus strain (γ) at 37 °C. Comparison between P407- and NHP407-based hydrogels at 20 %w/v (solid line: G', dashed lines: G'', dotted lines: τ; P407: blue, NHP407: black). The blue dash-dotted lines identify the linear viscoelastic region.

LAOS tests displayed the typical response of an associative polymer structure, where G' and G'' are depicted as a function of strain. With increasing γ above the linear viscoelastic region (LVE), G' decreases but G'' first increases and then decreases like a weak strain overshoot phenomenon (i.e., Type III behavior).

Figure 3.10 reports the characteristic parameters extracted from LAOS tests (i.e., maximum strain and shear within the linear viscoelastic (LVE) region, initial G' and G'' values and their offset, maximum G'' value, its offset compared to the initial value and yield stress).

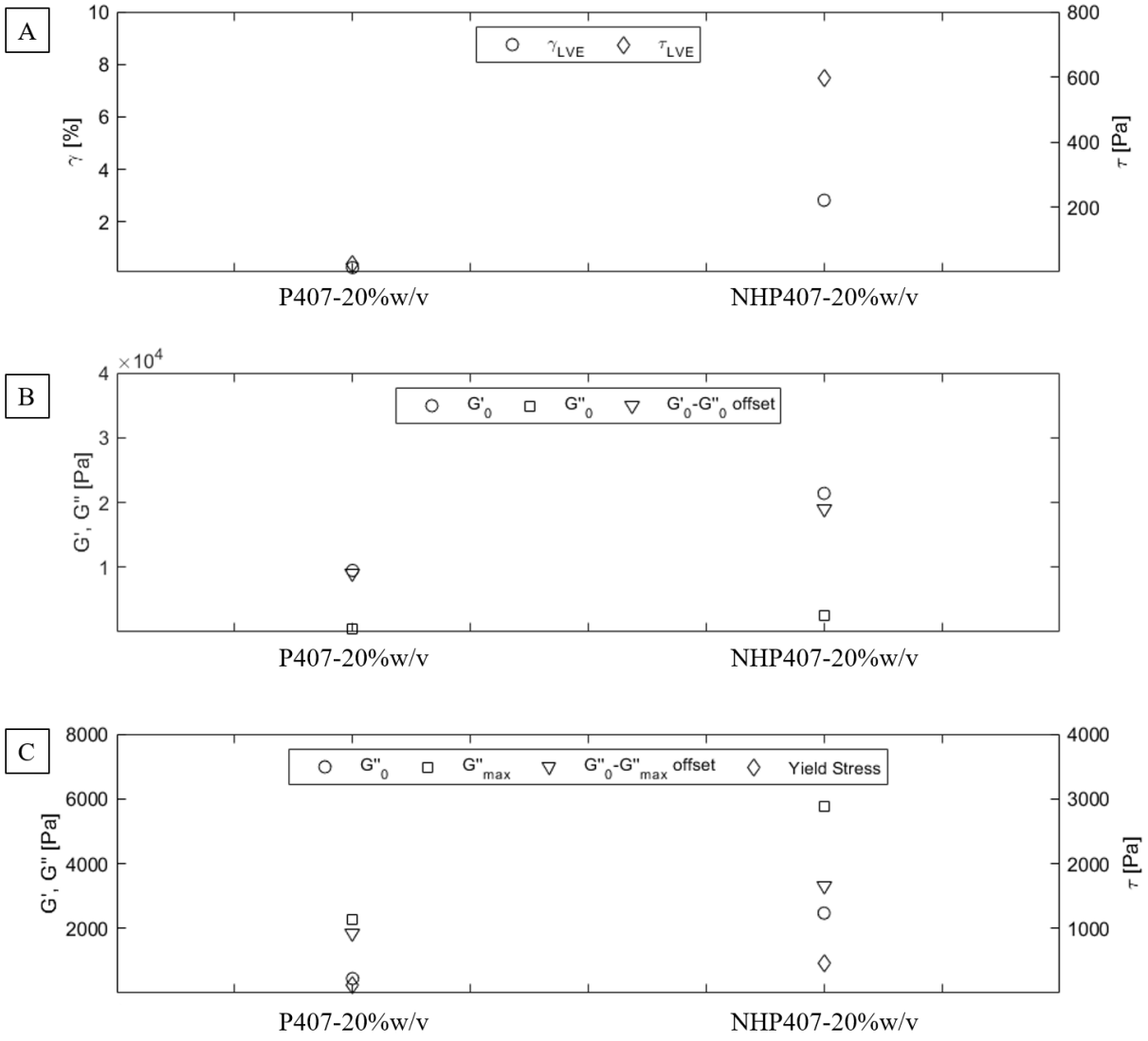

Figure 3.10 LAOS main parameters for P407-based and NHP407-based hydrogels at 20 %w/v. **(A)** Maximum strain and shear within the LVE region. **(B)** Initial G' and G'' values and their offset. **(C)** Initial and maximum G'' values, their offset and yield stress.

NHP407-based solutions show higher resistance to deformation (LVE region) compared to P407-based ones with the same composition (**Figure 3.9** and **Figure 3.10 A**). This result highlighted the higher viscoelastic properties of PUR hydrogels compared to P407-based ones, resulting from its higher molecular weight that leads to more stable and packed micelles. NHP407-based samples also showed higher initial G' and G'' values as well as their offset compared to P407-based ones (**Figure 3.9** and **Figure 3.10 B**), meaning that in PUR-based gels

the elastic contribution to their behavior was dominant over viscous components. Moreover, NHP407-based systems showed higher G'' maximum value and higher offset between it and its initial value as well as greater yield stress (**Figure 3.9** and **Figure 3.10 C**). Hence, both P407- and NHP407-based hydrogels underwent a structural damage characterized by the appearance of small cracks that progressively propagate in bigger cracks; however, this behavior was more pronounced in NHP407-based gels compared to P407-based ones with the same composition, probably because of a different micelle and network morphology.

The trend of viscosity (η) as a function of temperature during the temperature-driven sol-to-gel transition of P407- and NHP407-based solutions at 20 %w/v is reported in **Figure 3.11**.

Initially, viscosity decreased as a function of temperature, as typical of fluid systems (sol phase). Then, a minimum value of viscosity was reached (at the gelation onset temperature -T_{onset}-), followed by an increase in viscosity, due to micelle nucleation and packing. P407-based solutions, after reaching the T_{onset}, showed a monotonic increase in viscosity, followed by a sharp increase as a function of temperature during the growth of micelles with the conversion of the homogeneous fluid into a biphasic system. Finally, viscosity reached a plateau value, suggesting the complete transition of the system in the gel state. On the other hand, NHP407-based solutions only showed a sharp increase in viscosity and the final plateau, suggesting the achievement of a complete gelation, was not visible. Instead, an apparent reduction in viscosity appeared after a maximum value was reached. This effect was not due to some transition within the material, but rather to melt fracture of the system (the gel, subjected to a continuous strain rate, slide out of the plates and crumbled) (**Figure 3.11**). For this reason, a precise estimation of gelation temperature (T_{gel}, temperature at viscosity plateau) for PUR-based sol-gel systems was not possible.

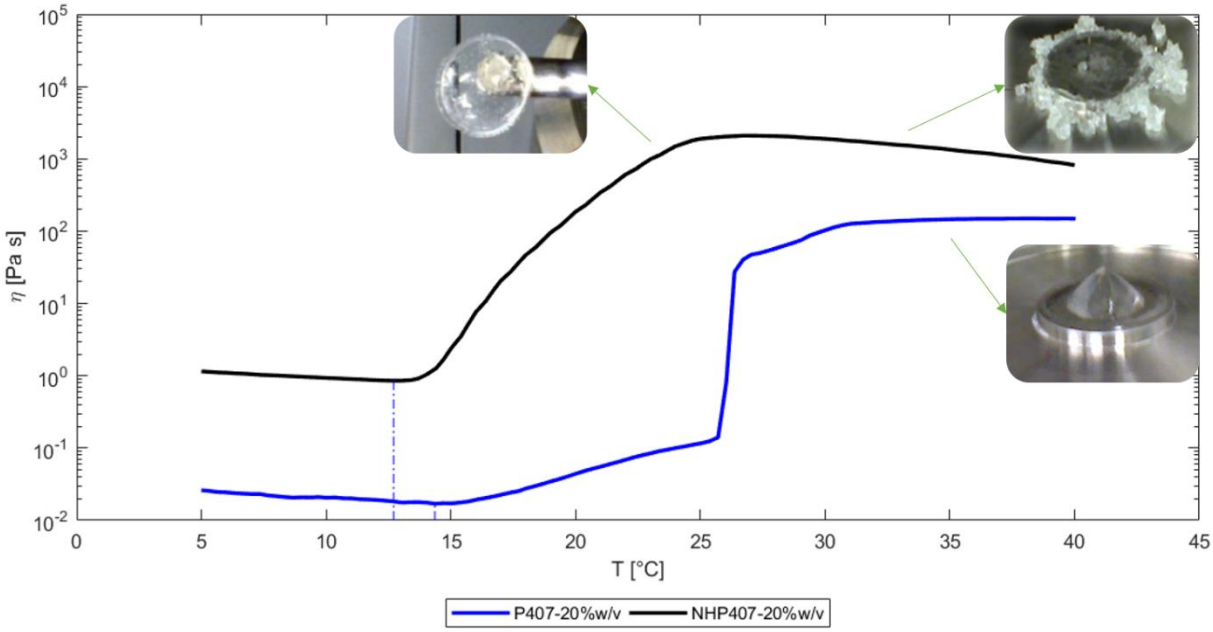

Figure 3.11 Temperature ramp test: viscosity *versus* temperature during the sol-to-gel transition. Comparison between P407- and NHP407-based solutions at 20 %w/v (P407: blue, NHP407: black). The blue dash-dotted lines identify T_{onset} (temperature at the minimum value of viscosity).

Figure 3.12 shows the main significative parameters extracted from the non-isothermal results (i.e. T_{onset} and viscosities at different temperature -5, 10, 15, 20, 25, 30, 35 °C-).

Compared to P407-based solutions, NHP407-based hydrogels exhibit lower T_{onset}, meaning that PUR-based micellar structures formed faster and the overall gelation process turned out to be quicker (**Figure 3.11** and **Figure 3.12 A**). Additionally, NHP407-based hydrogels showed higher viscosity compared to P407-based one with the same concentration at all the considered temperatures (**Figure 3.11** and **Figure 3.12 B**).

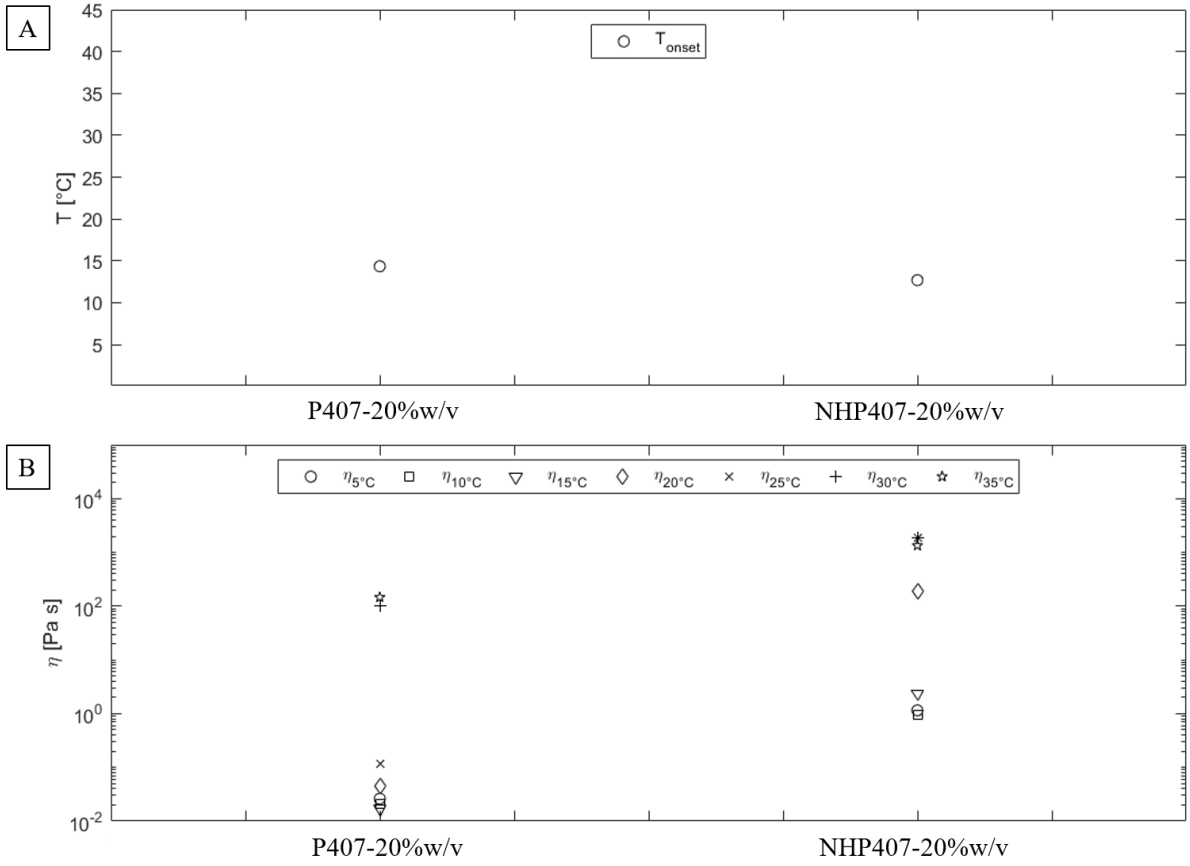

Figure 3.12 Main parameters characterizing temperature ramp test results for P407-based and NHP407-based solutions at 20 %w/v. **(A)** T_{onset}, **(B)** viscosity at different temperatures (5, 10, 15, 20, 25, 30, 35 °C).

Information about the different gelation properties of NHP407-based solutions with different PUR concentrations (10, 15 and 20 %w/v) was obtained by means of LAOS, SAOS and temperature ramp tests.

Results of LAOS analysis carried out on NHP407-based gel with different concentration are reported in **Figure 3.13**. As previously mentioned, LAOS results displayed the typical response of associative polymer structures, where G' and G'' are depicted as a function of strain with a Type III behavior.

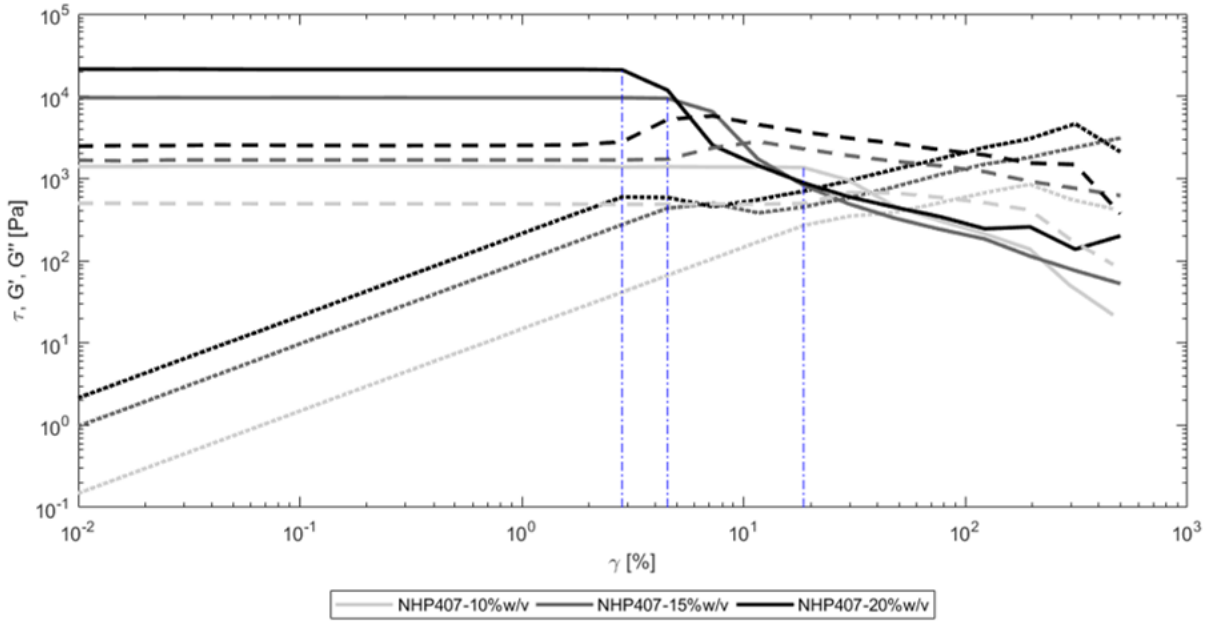

Figure 3.13 LAOS test: G', G'' and τ *versus* strain at 37 °C. Comparison among NHP407-based sol-gel systems at 10, 15 and 20 %w/v (solid line: G', dashed lines: G'', dotted lines: τ) (NHP407_10%w/v: light grey, NHP407_15%w/v: grey, NHP407_20%w/v: black). The blue dash-dotted lines identify the linear viscoelastic region.

Figure 3.14 shows the characterizing parameters of LAOS test results (i.e., maximum strain and shear within the linear viscoelastic (LVE) region, initial G' and G'' values and their offset, maximum G'' value, its offset compared to the initial value and yield stress).

NHP407-based formulations showed lower resistance to deformation (LVE region) with increasing concentration (**Figure 3.13** and **Figure 3.14 A**), meaning that higher PUR-concentrations form stiffer structures. A similar trend was observed in G' and G'' values as well as in their offset (**Figure 3.13** and **Figure 3.14 B**), suggesting that the elastic contribution to gel mechanical properties becomes more and more dominant with respect the viscous component with increasing PUR concentration. Moreover, NHP407-based samples showed higher G'' maximum value and higher offset between it and its initial value as well as greater yield stress (**Figure 3.13** and **Figure 3.14 C**). Hence, PUR concentration in the sol-gel systems plays a key

role in determining gelation onset and kinetics, as well as the mechanical strength of the resulting micellar network.

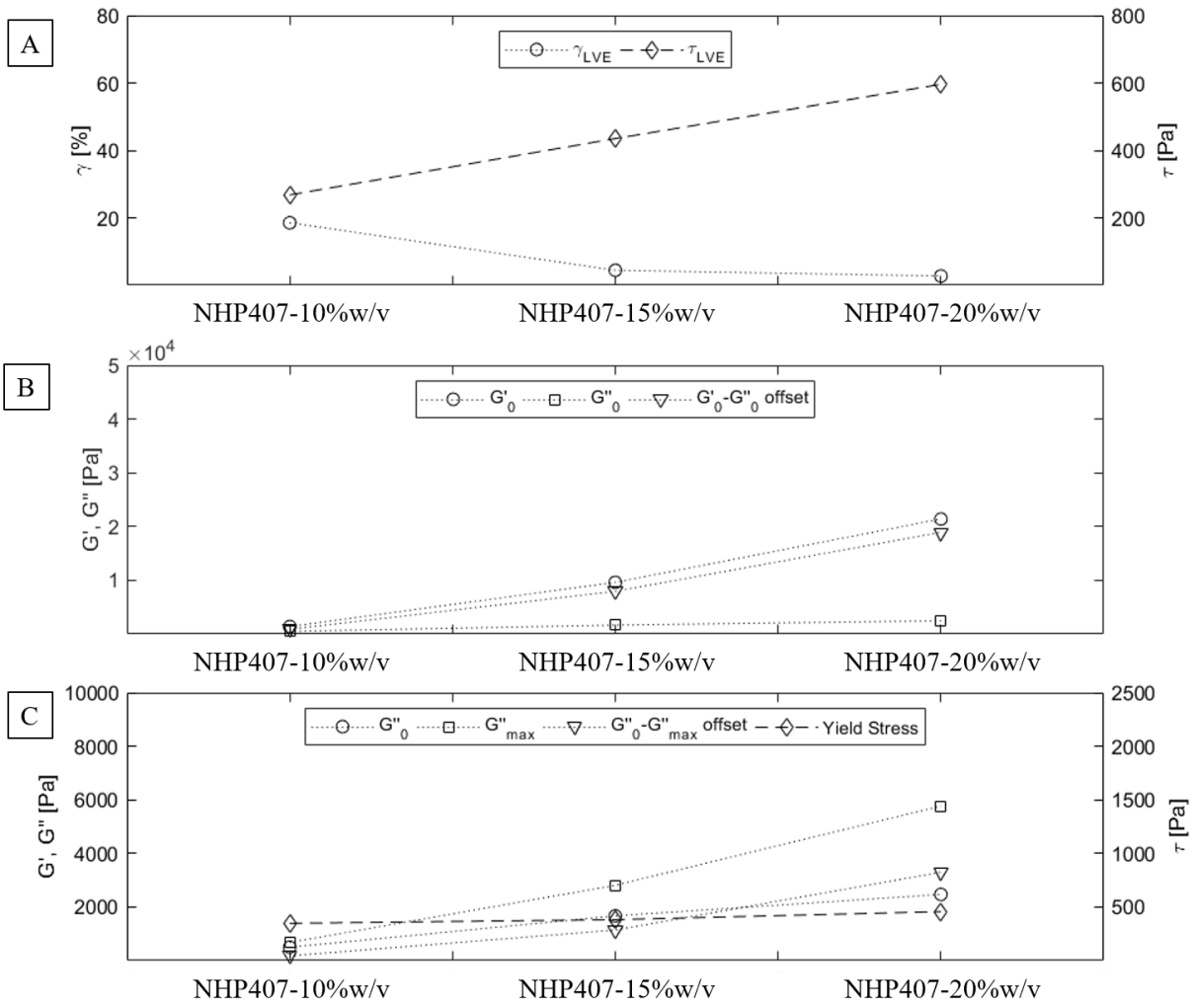

Figure 3.14 LAOS main parameters for NHP407-based samples at 10, 15 and 20 %w/v. **(A)** Maximum strain and shear within the LVE region. **(B)** Initial G' and G'' values and their offset. **(C)** Initial and maximum G'' values, their offset and yield stress.

Concerning SAOS tests, the behaviors of G' and G'' as a function of the frequency of NHP407-based solutions at 10, 15 and 20 %w/v and different temperatures (25, 30 and 37 °C) are reported in **Figure 3.15.**

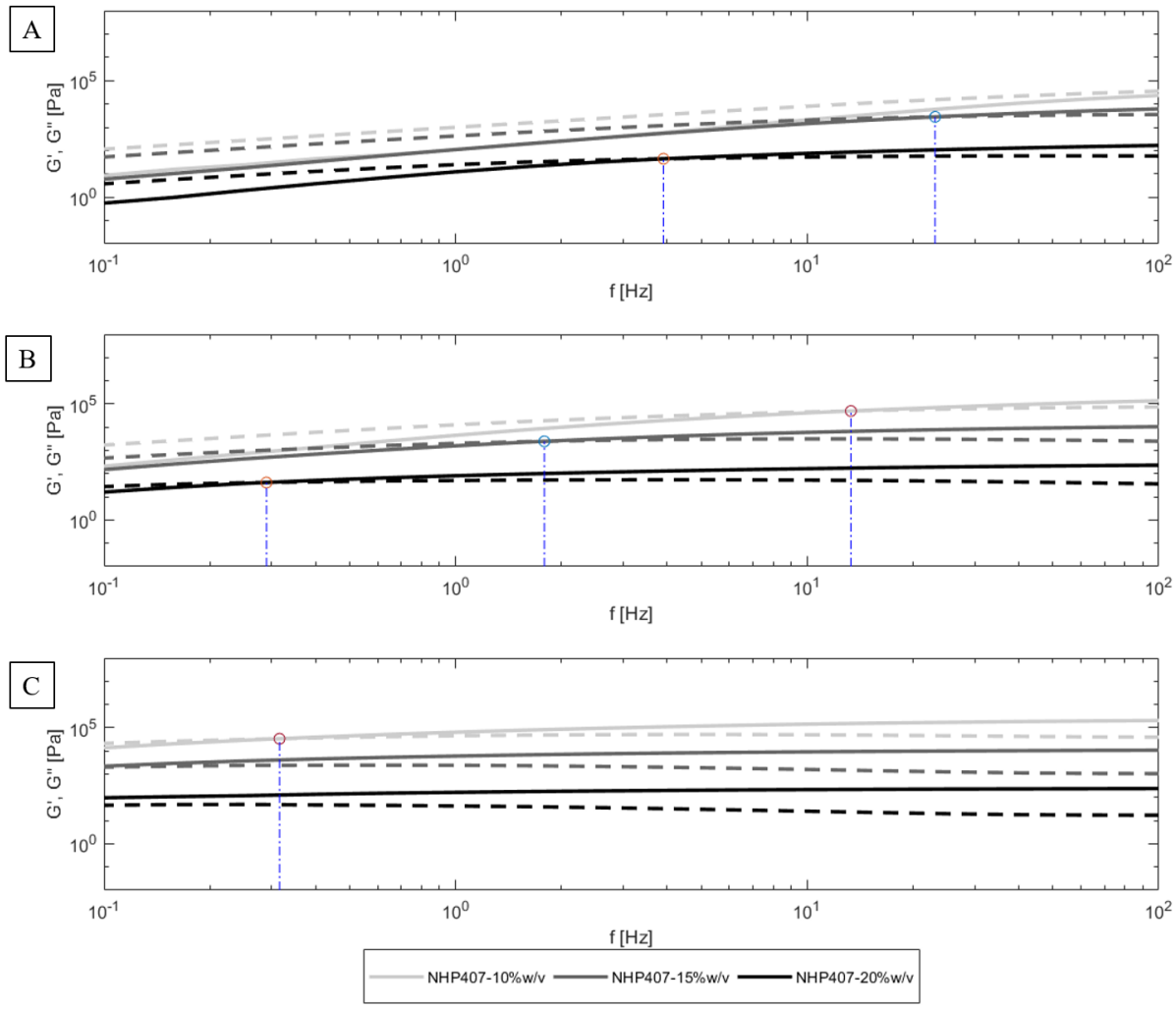

Figure 3.15 SAOS test: G' and G'' *versus* angular frequency at **(A)** 25, **(B)** 30, **(C)** 37 °C. Comparison between NHP407-based sol-gel systems at 10, 15 and 20 %w/v (solid line: G', dashed lines: G'', NHP407_10%w/v: light grey -shifted $x10^{2}$-, NHP407_15%w/v: grey, NHP407_20%w/v: black -shifted $x10^{-2}$-). The blue dash-dotted lines identify G'-G'' crossover.

Fully developed gels are known to have G' higher than G'' and G′ independent over angular frequency. The frequency at the crossover between G' and G'' ($f_{crossover}$) gives important information about the gelation process: the lower the $f_{crossover}$ is, the lower the $f_{crossover}$ is, the more the biphasic sol-gel systems can be consider similar to a gel rather than to a sol; hence when two or more formulations are compared, those with lower $f_{crossover}$ can be assumed to show a more efficient and faster gelation process.

G′ trend of NHP407 hydrogel with 10% w/v concentration turned out to be frequency-dependent at all the tested temperatures, with the typical behavior of fluid systems at 25 °C (**Figure 3.15**). At 30 and 37 °C the system acted like a biphasic sol-gel system: at frequency lower than $f_{crossover}$ it behaved like a fluid, while at frequency higher than $f_{crossover}$ it behaved like a gel. By increasing temperature, $f_{crossover}$ decreases, suggesting the progressive transition of the system from the sol to the gel state. For more highly concentrated hydrogels, at 37 °C, G′ was always higher than G'', even if it was still dependent over frequency, suggesting that the systems were in the gel phase, but they still lacked a fully developed gel network. Similarly to hydrogels with 10 %w/v polymer concentration, at lower temperatures the 15 and the 20 %w/v concentrated samples acted as biphasic sol-gel systems (**Figure 3.15**). As expected, $f_{crossover}$ values turned out to be also dependent over polymer concentration in the sol-gel systems (**Figure 3.16**), with lower values for hydrogels with higher PUR content, as a consequence of their capability to start their transition from the sol to the gel state at lower temperatures, as assessed by tube inverting tests. **Figure 3.16** shows the main significative parameters extracted from the SAOS tests (i.e. angular frequencies at G'-G'' crossover at different temperature and PUR concentration, G'-G'' offset at different angular frequencies).

NHP407-based sol-gel systems also showed higher G'-G'' offset with increasing concentration and temperature (**Figure 3.16 B, Figure 3.16 C** and **Figure 3.16 D**), as already observed in LAOS tests. On the other hand, G'-G'' offset increased with increasing angular frequency (**Figure 3.16 B, Figure 3.16 C** and **Figure 3.16 D**) due to the biphasic nature of the analyzed sol-gel systems.

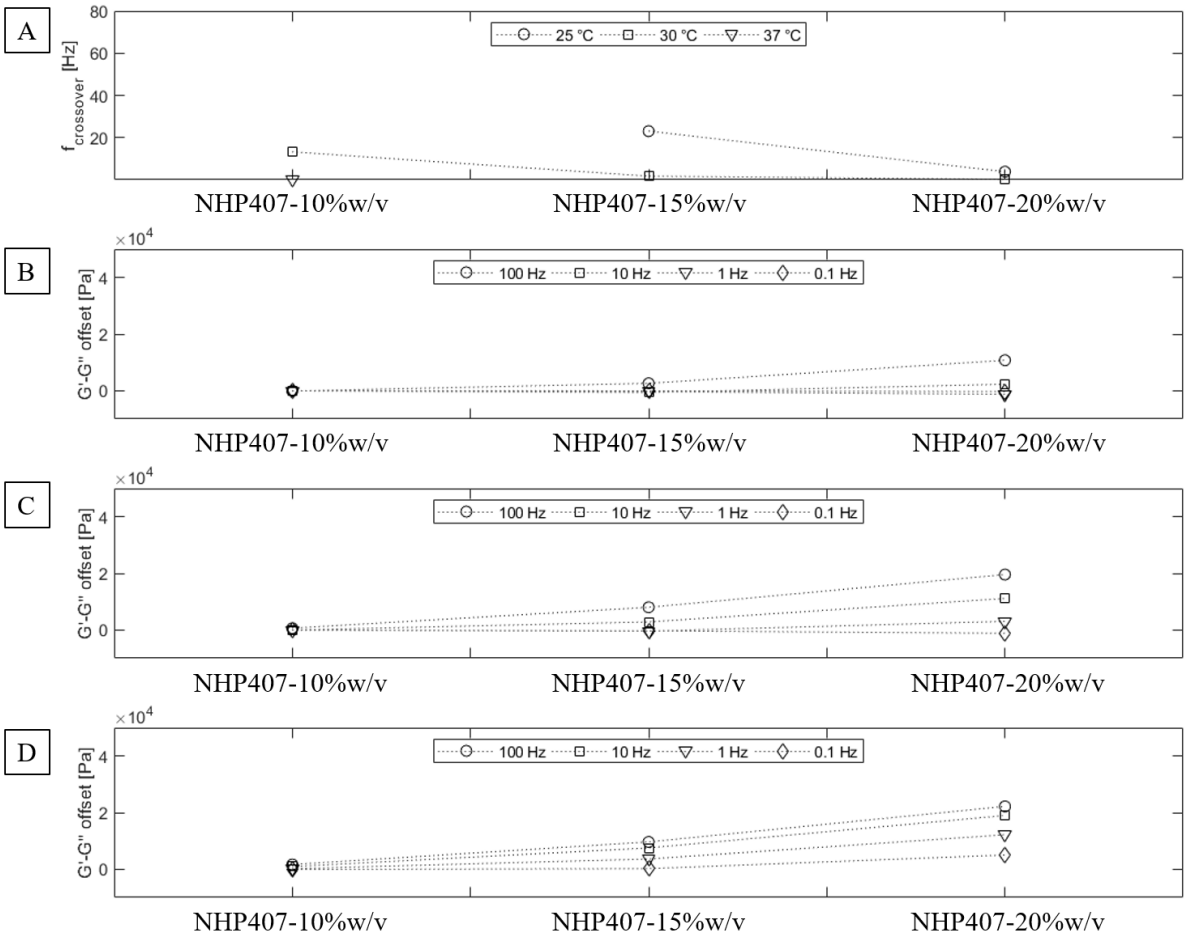

Figure 3.16 SAOS main parameters for NHP407-based solutions at 10, 15 and 20 %w/v, and 25, 30 and 37 °C. **(A)** f at G'-G'' crossover. G'-G'' offset of the different concentrated solutions at **(B)** 25 °C, **(C)** 30 °C and **(D)** 37 °C.

SAOS tests also allowed to assess the shear thinning behavior of the developed hydrogels, (**Figure 3.17**) with complex viscosity (η*) decreasing with increasing shear rate.

The shear thinning behavior was more evident for sol-gel systems with higher PUR concentration and the dependence of complex viscosity over shear rate increased with increasing temperature.

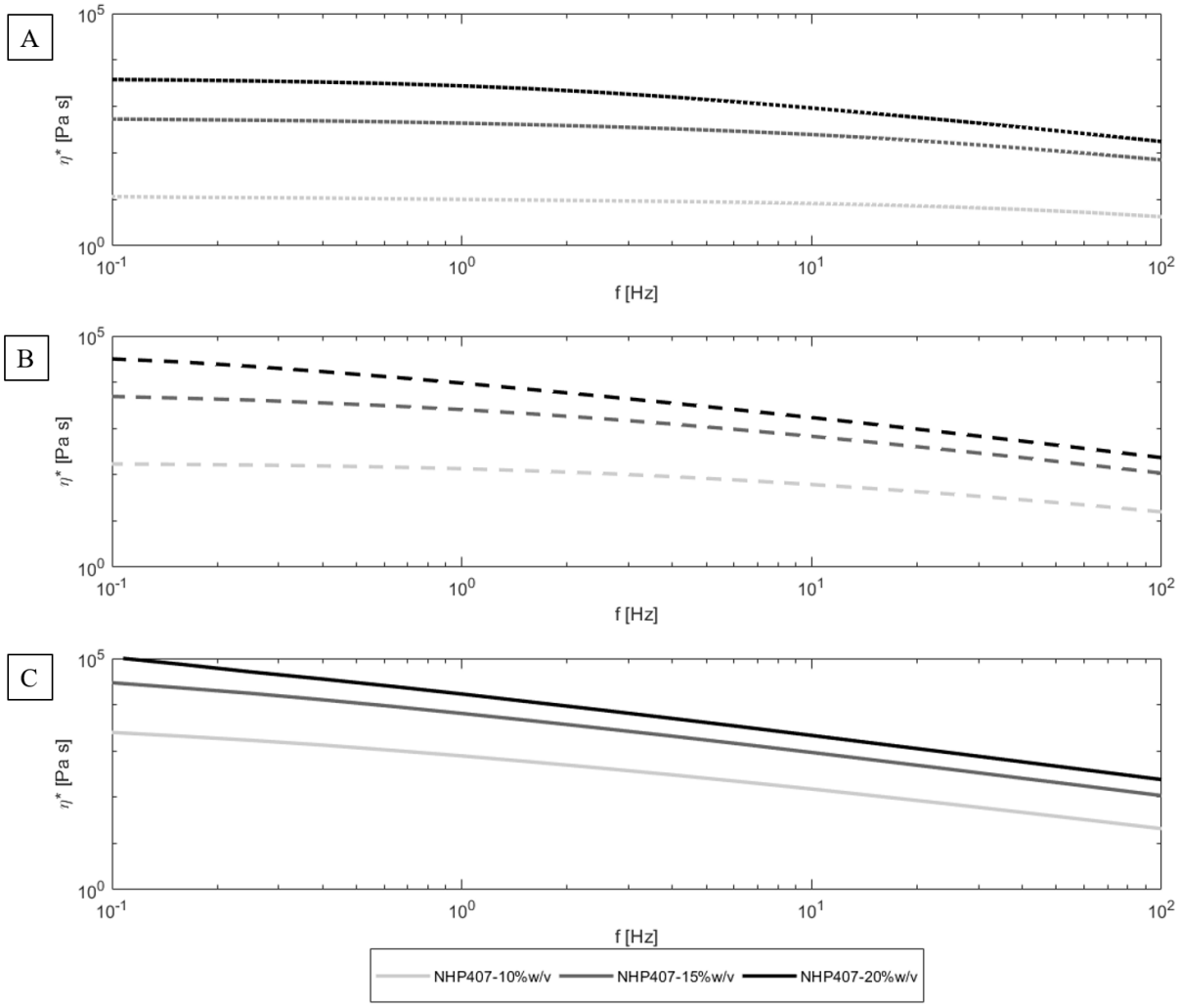

Figure 3.17 SAOS test: complex viscosity versus angular frequency. Shear thinning behavior of NHP407-based hydrogels at different concentrations and temperatures: **(A)** 25 °C, **(B)** 30 °C and **(C)** 37 °C.

The trend of viscosity (η) as a function of temperature during the temperature-driven sol-to-gel transition of NHP407-based solutions at 10, 15 and 20 %w/v PUR concentration is reported in **Figure 3.18.**

All the analyzed samples showed a similar trend of viscosity: viscosity initially decreased as a function of temperature (sol state) until a minimum value (at T_{onset}) was reached; then, it started to increase until a maximum before decreasing again (due to melt fracture phenomena).

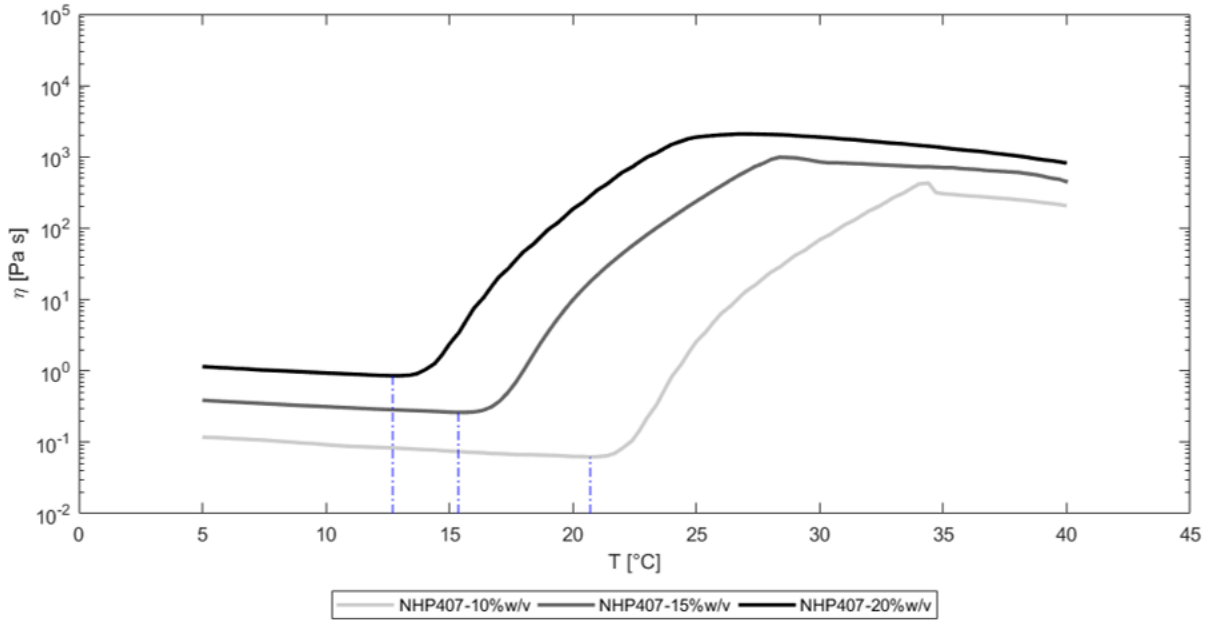

Figure 3.18 Temperature ramp test: viscosity *versus* temperature during sol-to-gel transition. Comparison between NHP407-based formulations at 10, 15 and 20 %w/v concentration. The blue dash-dotted lines identify T_{onset} values.

Figure 3.19 reports the main parameters extracted from temperature ramp tests results (i.e., T_{onset} and viscosities at different temperatures -5, 10, 15, 20, 25, 30, 35 °C-).

NHP407-based hydrogels exhibited lower T_{onset} with increasing PUR concentration, suggesting that the critical micellar volume required for the onset of gelation can be reached at lower temperatures for hydrogels with higher polymer content (**Figure 3.18** and **Figure 3.19 A**). Moreover, the analyzed formulations showed higher viscosity with increasing PUR concentration (**Figure 3.18** and **Figure 3.19 B**), as expected.

All the analyzed NHP407-based compositions showed a sharp increase in viscosity after reaching the T_{onset}; however, by decreasing PUR-concentration the trend of the viscosity became bimodal. Moreover, the slope of second part of the curve decreases with decreasing PUR concentration. This behavior suggested that the gelation process was slower for the hydrogel with lower PUR concentration.

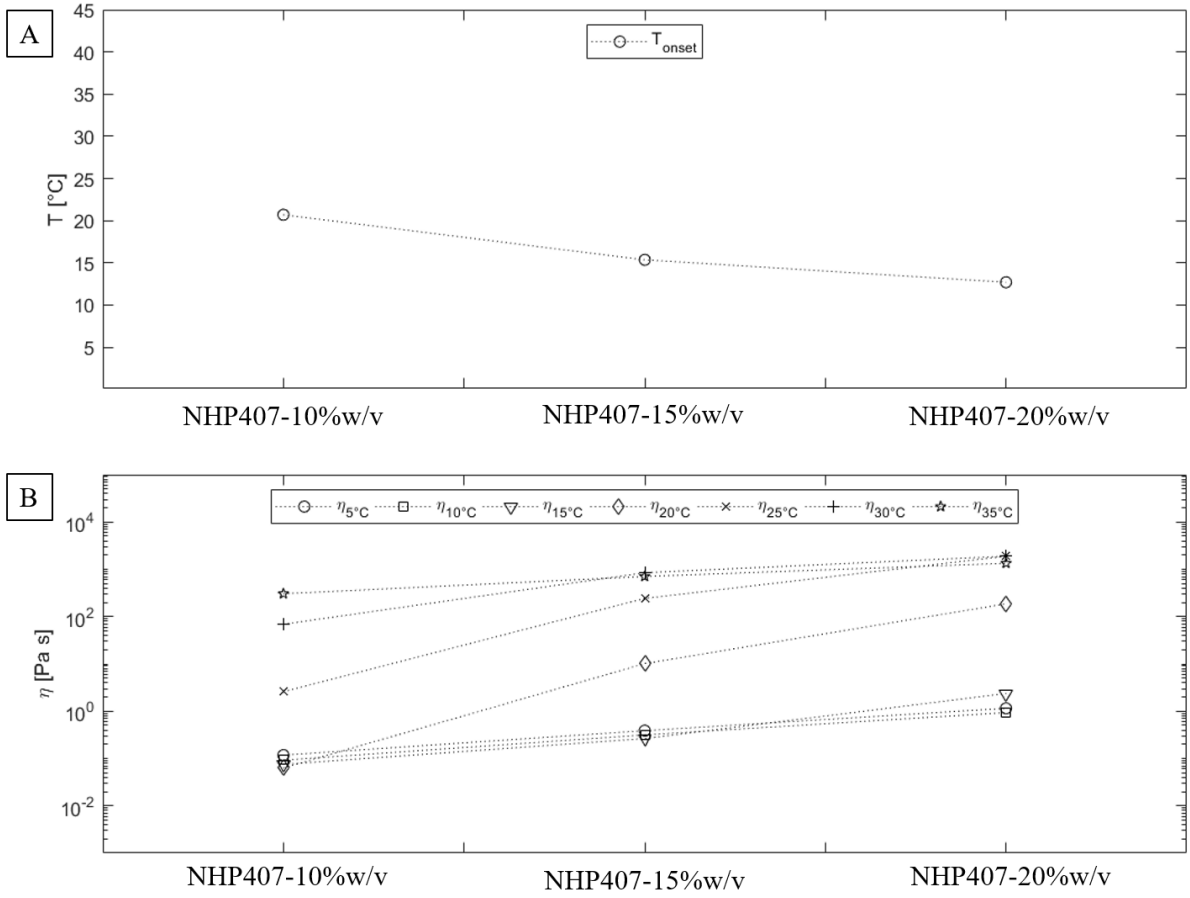

Figure 3.19 Main parameters extracted from temperature-ramp test results carried out on NHP407-based sol-gel systems at 10, 15 and 20 %w/v PUR concentration. **(A)** T_{onset}, **(B)** viscosities at different temperatures (5, 10, 15, 20, 25, 30, 35 °C).

3.2.5. Hydrogel Swelling and Stability to Dissolution in Aqueous Environment

Stability tests of P407- and NHP407-based gels at 20 %w/v concentration were carried out to assess gel dissolution/degradation time (**Figure 3.20**).

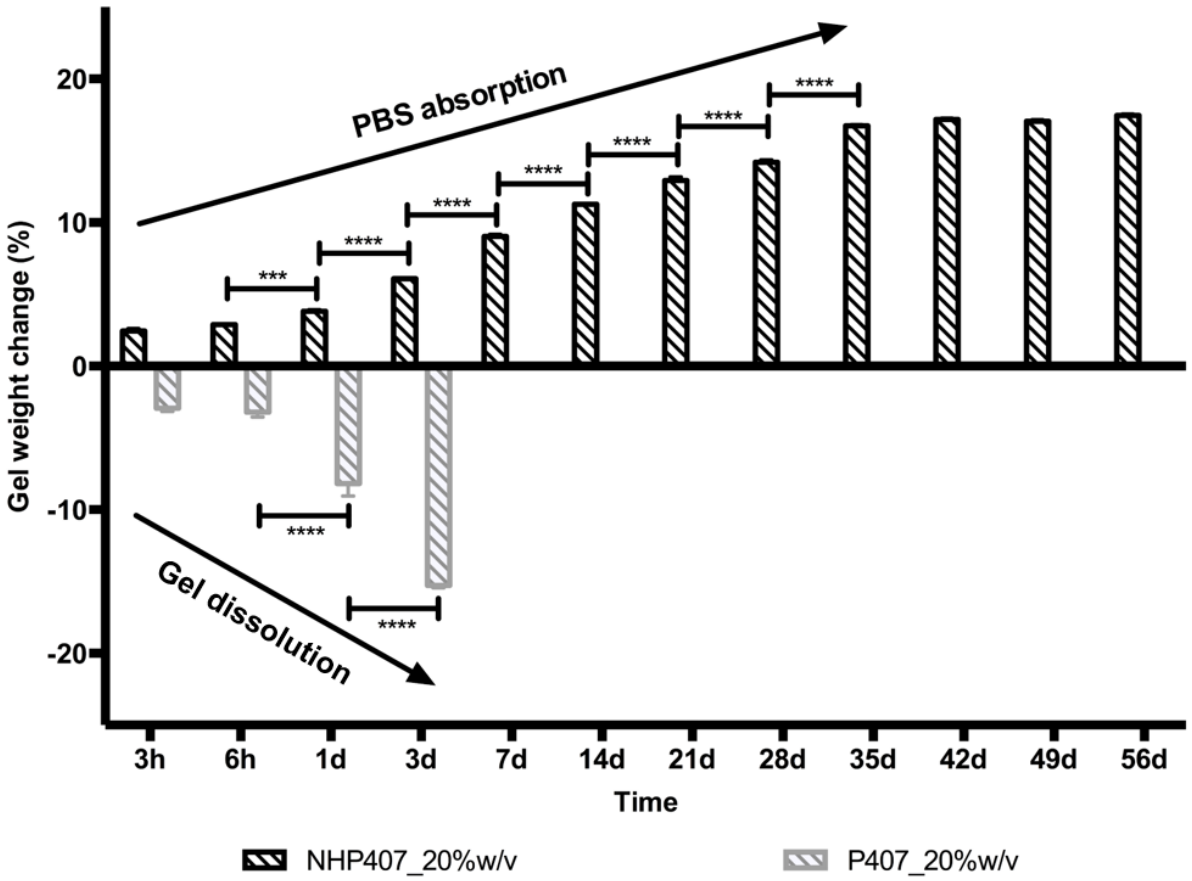

Figure 3.20 Gel weight change (%) as a function of time for P407- and NHP407-based hydrogels at 20 %w/v.

NHP407-based gels with 20% w/v concentration progressively increased their weight as a function of time due to PBS absorption. In contrast, P407-based hydrogels, with the same polymer content, progressively lost their weight with increasing incubation time and completely dissolved after 5 days.

NHP407-based hydrogels with different concentrations (10, 15, 20 %w/v) were also characterized in terms of PBS absorption (**Figure 3.21 A**) and dissolution (**Figure 3.21 B**) overtime. For NHP407-based hydrogels with 15% and 20% w/v concentration, PBS absorption (**Figure 3.21 A**) increased as a function of time. At each analyzed time interval, PBS absorption was the highest for the hydrogel with 20% w/v concentration compared to the other two compositions (significant difference at each time point except for 3h).

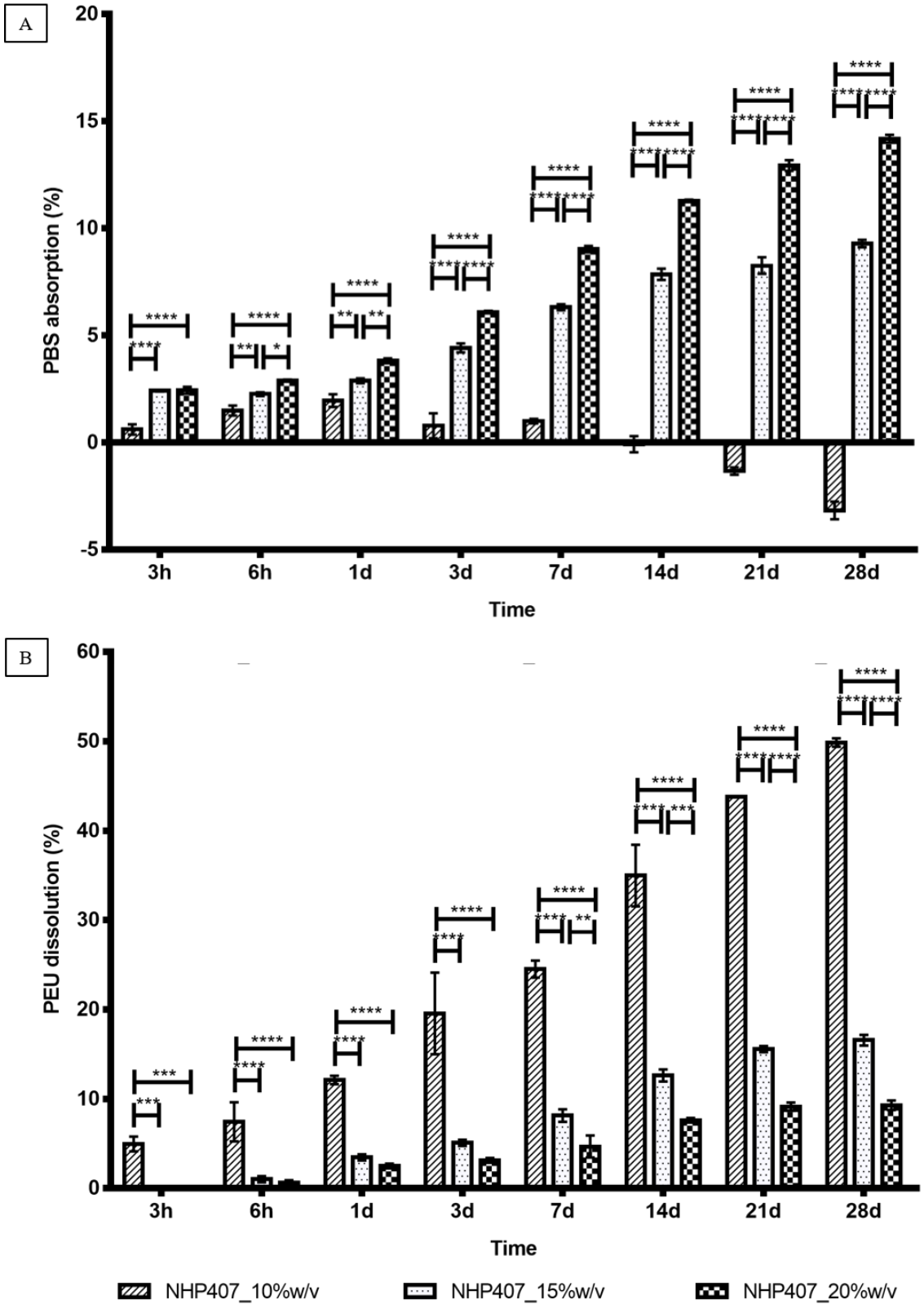

Figure 3.21 NHP407-based hydrogels at 10, 15 and 20 %w/v concentration: **(A)** PBS absorption and **(B)** weight loss (dissolution).

On the other hand, NHP407-based hydrogels with 10% w/v concentration showed a limited PBS absorption up to 7 days and, after 21 days, showed a negative change in weight (**Figure 3.21 A**), suggesting that dissolution phenomena had completely overcome gel swelling potential. The samples NHP407_15% w/v and NHP407-based hydrogels with 15 and 20% w/v reached a PBS uptake value of 9.3%±0.1% and 14.7%±0.1%, respectively, after 28 days' incubation in PBS.

3.2.6. Hydrogel Permeability

Permeability to FD4 was studied to model nutrient transport to the cells encapsulated within the hydrogels (**Figure 3.22 A**). **Figure 3.22 B** reports FD4 absorption as a function of time for all the analyzed systems (NHP407-based hydrogels at 10, 15 and 20 %w/v concentration).

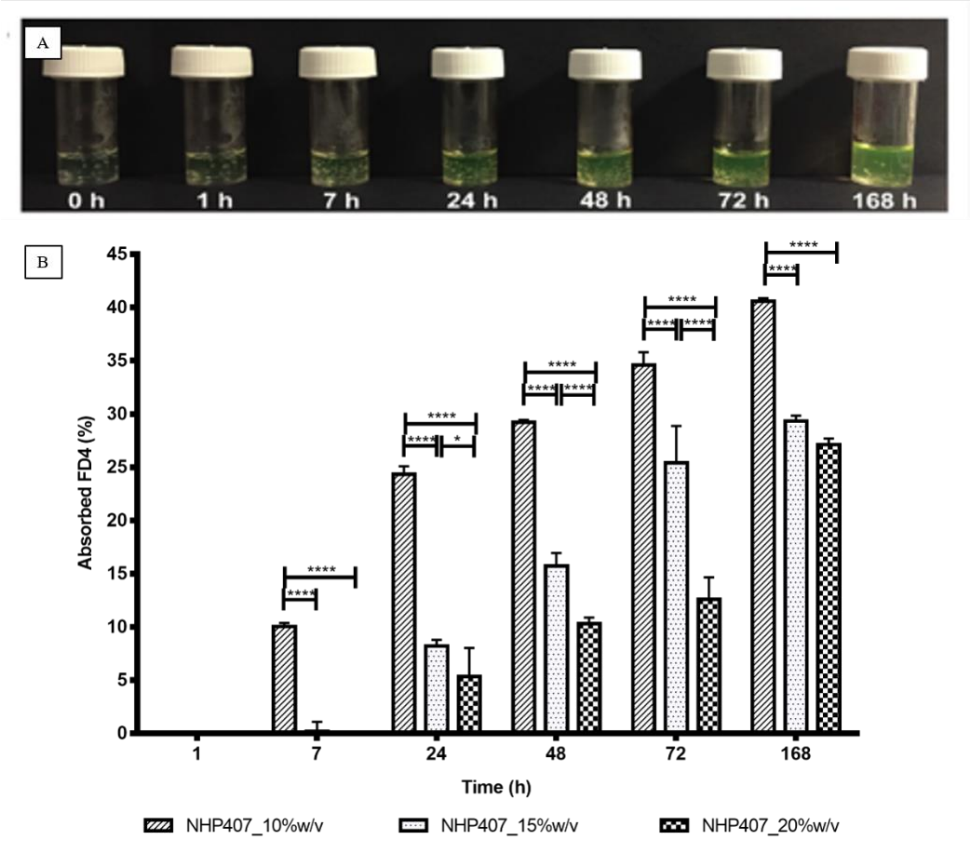

Figure 3.22 (**A**) **A**) Pictures of the samples incubated with an FD4 aqueous solution for different time intervals. (**B**) FD4 absorption by NHP407-based hydrogels at 10, 15 and 20 %w/v concentration.

The percentage of absorbed FD4 increased with increasing time and, at the same time, was significantly higher for less concentrated hydrogels.

3.2.7. Hydrogel Injectability and Printability

Injectability of NHP407-based hydrogels (10, 15 and 20 %w/v) through 0.20 and 0.25 mm internal diameter needles was demonstrated in different conditions. NHP407-based sol-gel systems at 10 and 15 %w/v concentration were injectable through both tested needles at 5, 25 and 37 °C. On the other hand, NHP407-based hydrogel at 20 %w/v concentration turned out to be injectable through both needles at 5 and 25°C, while injectability at 37 °C was observed only through 250 µm internal diameter needle (**Table 3.5**).

Table 3.5 NHP407-based sol-gel systems injectability

T	NHP407 10%w/v		NHP407 15%w/v		NHP407 20%w/v	
	0.20 mm	0.25 mm	0.20 mm	0.25 mm	0.20 mm	0.25 mm
5 °C	✓	✓	✓	✓	✓	✓
25 °C	✓	✓	✓	✓	✓	✓
37 °C	✓	✓	✓	✓	✗	✓

The capability of NHP407-based solution at 20 %w/v concentration to gel *in situ* keeping its shape was demonstrated by checking the gelation of its solution jet, equilibrated at 5°C, in contact with a water bath at 37°C (**Figure 3.23**). The same test was carried out on a P407-based hydrogel with the same polymer content.

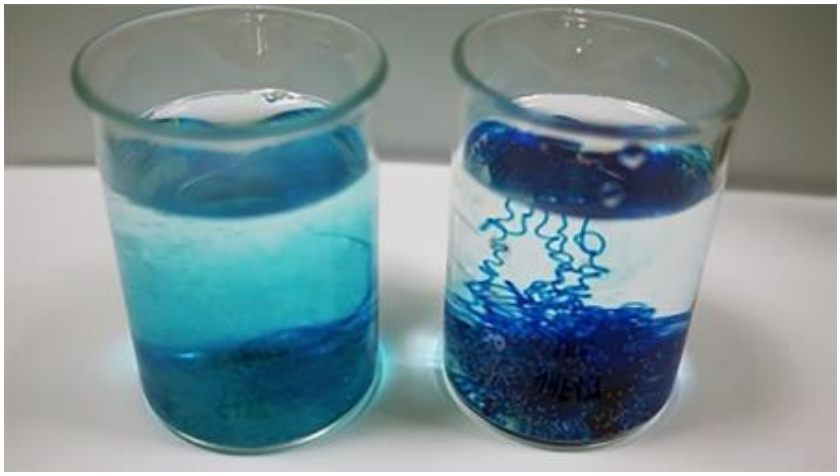

Figure 3.23 Injection of P407_20%w/v (left) and NHP407_20%w/v (right) solutions (conditioned at 5°C) in a water bath at 37°C.

NHP407-based solution at 10 and 15 %w/v showed a similar behavior to P407- and NHP407-based solution at 20 %w/v, respectively.

3.2.8. Hydrogel Biocompatibility

Preliminary cytotoxicity tests were carried out using HaCaT keratinocytes, C2C12 muscle cells and human fibroblasts (46 BR.1 N) to assess the biocompatibility of the newly developed NHP407 hydrogels (**Figure 3.24**).

In the case of keratinocytes, NHP407 hydrogel at 20% w/v concentration showed a significantly lower cytotoxicity than P407 hydrogel at the same concentration, while for C2C12 muscle cells and fibroblasts P407 hydrogels showed a higher level of biocompatibility compared with NHP1407 hydrogels at the same concentration (not significant difference).

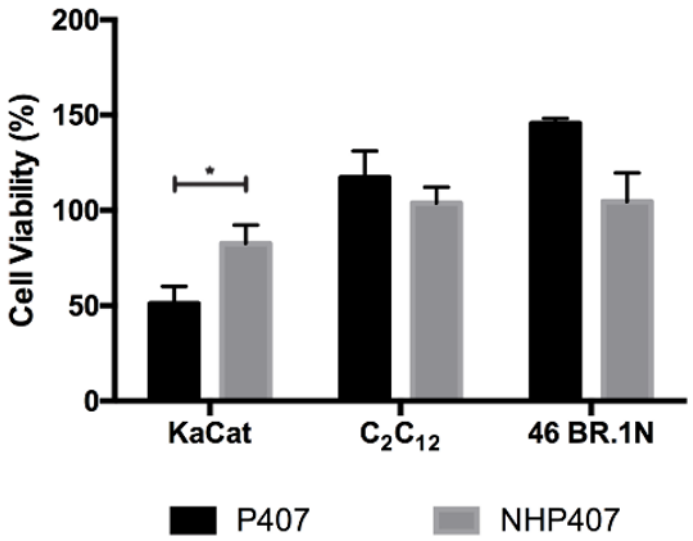

Figure 3.24 Cell viability measured through crystal violet assay on different cells in contact with eluates from P407 and NHP407 hydrogels (with 20% w/v concentration): HaCaT keratinocyte cells, C2C12 muscle cells and fibroblasts (46 BR.1 N). NHP407 hydrogels showed cytocompatibility (cell viability >80%) with all the analyzed cell phenotypes.

3.2.9. Biomolecule-loaded Hydrogels

Based on the previously collected data in terms of gelation properties and stability in aqueous media, NHP407-based hydrogels at 15 and 20 %w/v concentration were chosen to be tested as drug/biomolecule carriers.

Prior to study the *in vitro* release of the different tested antioxidant hydrophobic drugs and hydrophilic proteins, the gelation properties of drug/biomolecule-loaded hydrogels were studied to assess the effects of biomolecule addition on the gelation potential of the developed systems.

3.2.9.1. Thermo-sensitive behavior

The thermo-sensitive behavior of the drug/biomolecule loaded formulations was characterized as previously reported by means of tube inverting test and rheological characterization. No

significant differences in terms of gelation time at 37 °C and sol-gel transition temperature were observed among NHP407-based virgin hydrogels and those loaded with drugs/proteins (15 and 20 %w/v concentration, 1 mg/ml drug/molecule loading) by tube inverting tests. With regard to rheological characterization, instead, NHP407-based solutions loaded with drugs/proteins exhibited some differences compared to the virgin hydrogels, depending on the drug/biomolecule used and PUR concentration.

Results of LAOS tests carried out on NHP407-based sol-gel systems (15 and 20 %w/v concentration) encapsulating the drugs and the proteins are reported in **Figure 3.25Figure** .

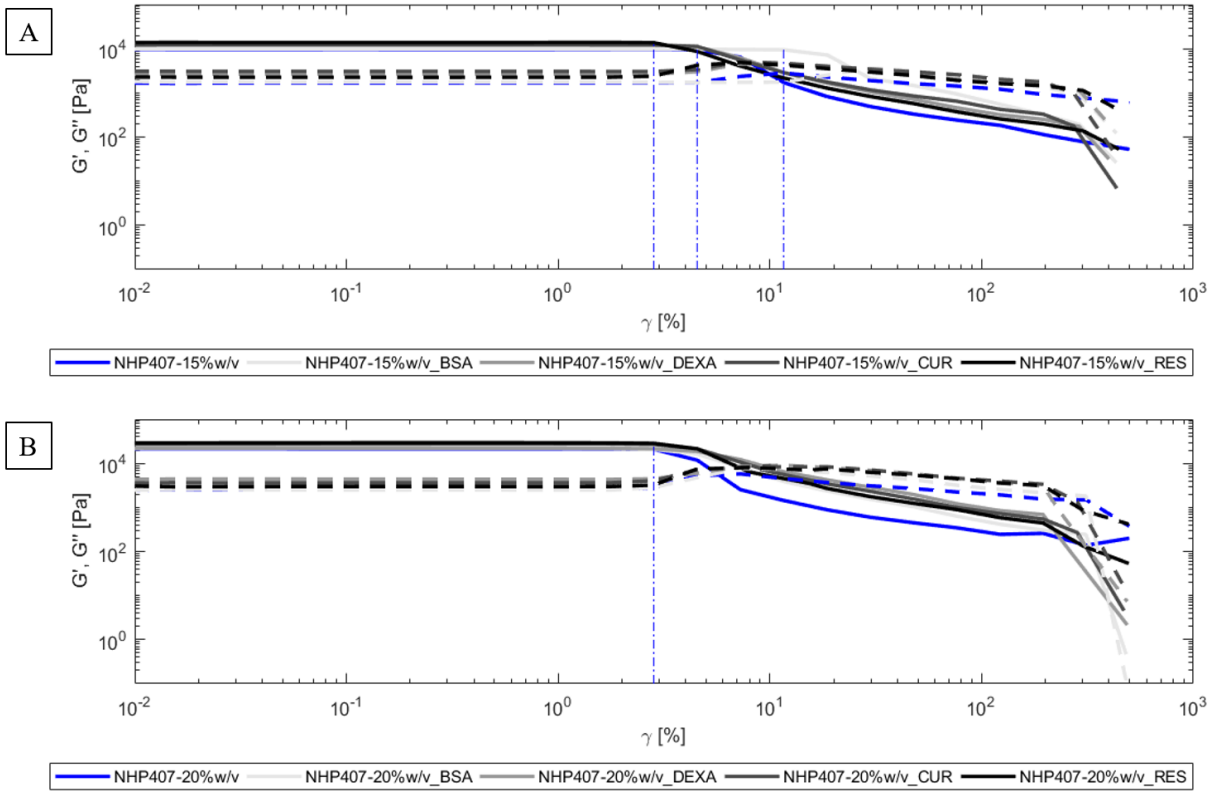

Figure 3.25 LAOS test: G' and G'' *versus* strain at 37 °C. Comparison between NHP407-based samples at **(A)** 15 and **(B)** 20 %w/v, encapsulating different biomolecules (BSA: bovine serum albumin, DEXA: dexamethasone, CUR: curcumin, RES: resveratrol) (solid line: G', dashed lines: G''). The blue dash-dotted lines identify the linear viscoelastic region.

Figure 3.26 summarizes the main parameters extracted from LAOS test results (i.e., maximum strain and shear within the linear viscoelastic (LVE) region, initial G' and G'' values and their offset, maximum G'' value, its offset with respect to the initial value and yield stress).

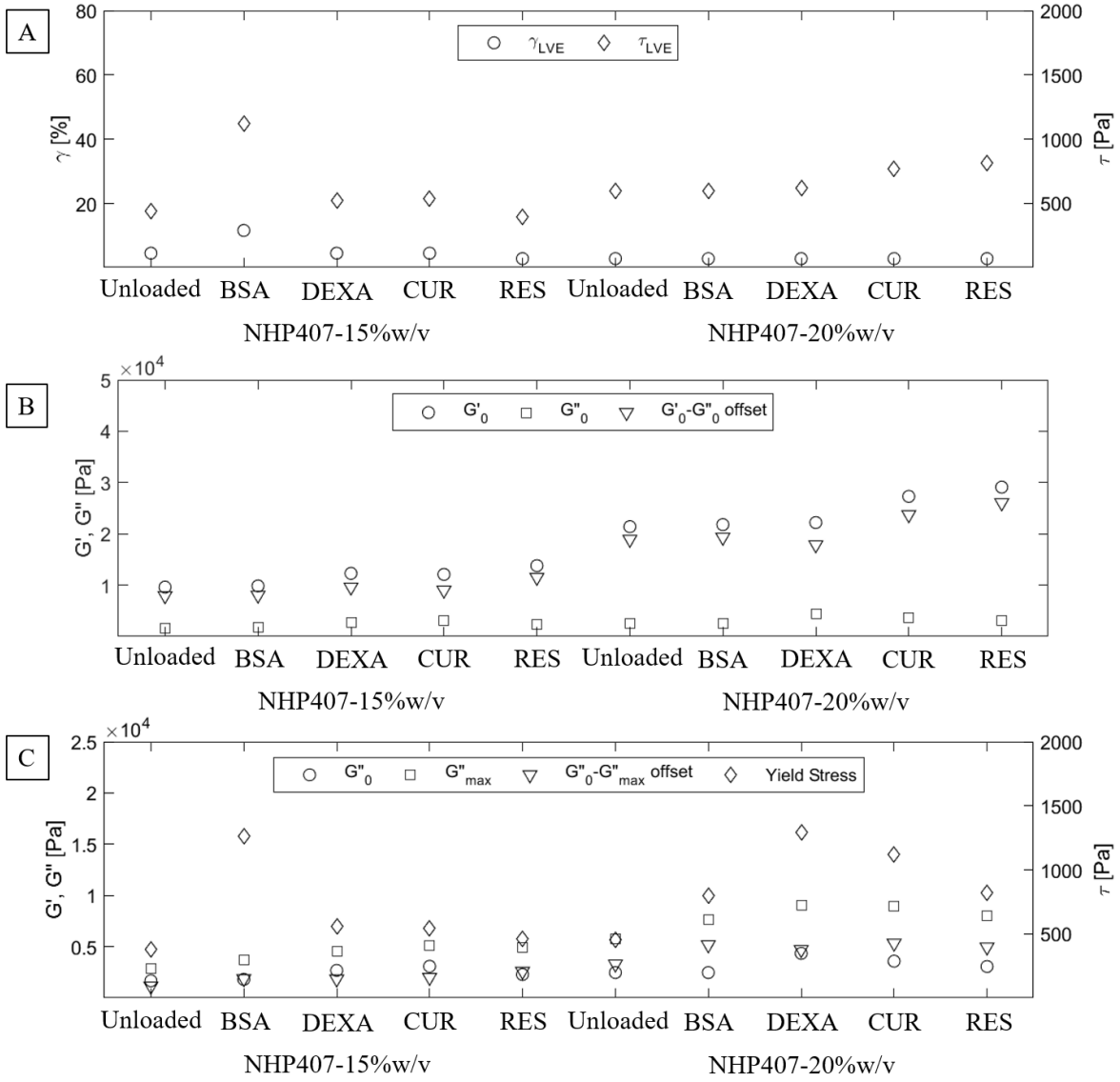

Figure 3.26 LAOS main parameters for NHP407-based sol-gel systems at 15 and 20 %w/v concentration. **(A)** Maximum strain and shear within the LVE region. **(B)** Initial G' and G'' values and their offset. **(C)** Initial and maximum G'' values, their offset and yield stress.

The addition of drug/biomolecule to NHP407-based samples with 15 %w/v concentration induced slight changes in the overall gel properties in a molecule-dependent way (i.e., depending on the drug molecular weight). For instance, upon addition of resveratrol (RES) LVE region of the resulting gels slightly decrease (4.53% and 2.83% for virgin and RES-loaded gel, respectively). On the other hand, loading of bovine serum albumin (BSA) induced an increase in LVE region extension (4.53% and 11.6% for virgin and BSA-loaded gel, respectively). The addition of dexamethasone (DEXA) and curcumin (CUR) seemed not to affect gel properties in terms of resistance to applied deformation (**Figure 3.25 AFigure** and **Figure 3.26 A)**. This behavior suggested that the addition of the hydrophobic drug with the lower molecular weight (RES: 228 Da) enhanced the gelation properties of the hydrogel, increasing its stiffness. The reason of this phenomenon probably lies in the formation of more stable micelles embedding the drug molecules, with RES working as nucleus of micellization. On the other, hydrophilic proteins probably position themselves between the micelles interacting with them, thus reducing the physical crosslinking of the hydrogel and forming a more elastic hydrogel.

Moreover, NHP407-based samples encapsulating RES also showed higher G'-G'' offset as well as higher offset between the initial G'' value and its maximum (**Figure 3.26 B**) as well as higher offset between the initial G'' value and its maximum (**Figure 3.26 C**). The same behavior, but less evident, was also visible in hydrogels encapsulating DEXA and CUR. The hydrogels containing BSA showed almost no differences with respect to the control (not-loaded NHP407 gel) in terms of G'-G'' offset and G''_0-G''_{max} offset.

NHP407 concentration increase to 20 %w/v seemed to almost completely undo the effects of biomolecule encapsulation on gel resistance to applied strain (**Figure 3.25 BFigure** and **Figure 3.26 B**). However, the formulations containing DEXA, CUR and RES showed slightly higher shear stress at the maximum of the linearity region, meaning that the shear within the hydrogels

increased despite the strain remaining constant, suggesting that by increasing PUR concentration the effects of drug/biomolecule loading could be mitigated.

However, the latter formulations also showed different G'-G'' offset and G''_0-G''_{max} offset compared to the unloaded hydrogel (**Figure 3.26 B** and **Figure 3.26 C**). In particular, the formulations containing CUR and RES showed higher offsets values; meanwhile the formulation encapsulating DEXA showed lower offset values. This behavior further confirmed that the addition of CUR and RES enhanced the gelation process of the hydrogels. The encapsulation of DEXA, instead, seemed to disturb this process. This phenomenon pointed out the relationship existing between the hydrophobic drug molecular weight and the resulting hydrogel behavior. In fact, LAOS results suggested that drugs with high molecular weight could obstacle micelle formation and, as a consequence, slow down the gelation process (DEXA: 392 Da). On the other hand, the addition of small drug molecules seemed to enhance micelle formation and packing, resulting in a stiffer hydrogel (CUR: 368 Da, RES: 228 Da). Concerning SAOS tests, the trends of G' and G'' as a function of the angular frequency of NHP407-based solutions at 15 and 20 %w/v encapsulating the considered drug/biomolecule are reported in **Figure 3.27**.

Figure 3.28 reports the main parameters extracted from SAOS test results (i.e., angular frequencies at G'-G'' crossover at different temperature and PUR concentration, G'-G'' offset at different angular frequencies).

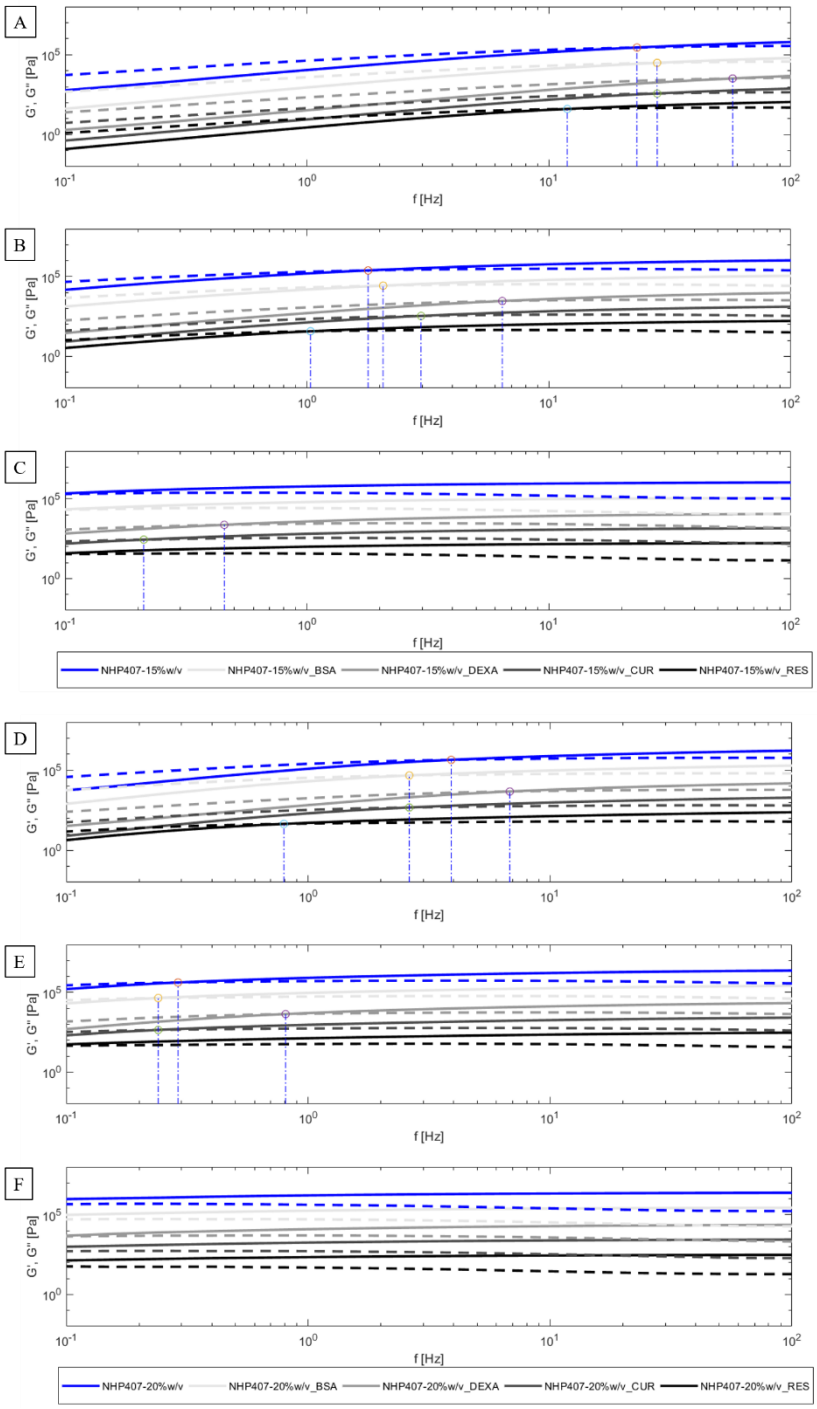

Figure 3.27 SAOS test: G' and G'' *versus* angular frequency. Comparison between NHP407-based sol-gel systems containing the investigated drug/biomolecule (1 mg/ml) with a PUR concentration of 15 %w/v at **(A)** 25, **(B)** 30 °C and **(C)** 37 °C; and with a PUR concentration of 20 %w/v at **(D)** 25, **(E)** 30 °C and **(F)** 37 °C**.** (solid line: G', dashed lines: G''; NHP407: blue -shifted $x10^{2}$-, NHP407_BSA: light grey -shifted $x10^{1}$, NHP407_DEXA: grey, NHP407_CUR: dark grey -shifted $x10^{-2}$-, NHP407_RES: black -shifted $x10^{-1}$-). The blue dash-dotted lines identify G'-G'' crossover.

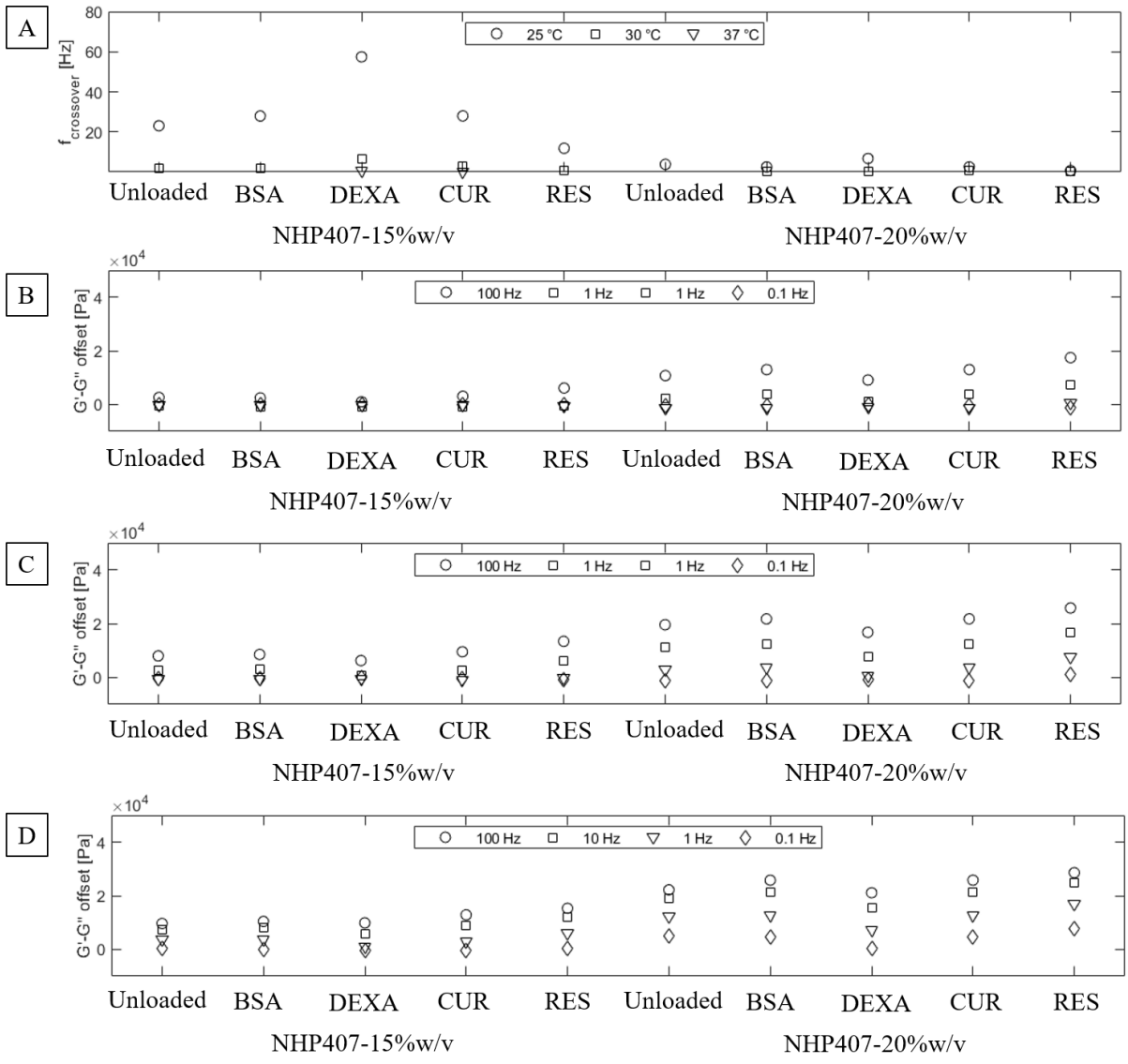

Figure 3.28 SAOS main parameters for NHP407-based sol-gel systems at 15 %w/v and 20 %w/v PUR concentration, containing the investigated drug/biomolecules. **(A)** ω at G'-G'' crossover. G'-G'' offset of the different concentrated solutions at **(B)** 25 °C, **(B)** 30 °C and **(C)** 37 °C.

The linear response of the hydrogels loaded with the drugs/biomolecule, at both the considered PUR-concentrations, showed some differences in terms of the frequency at the crossover between G' and G'' ($f_{crossover}$). The more significative differences are visible in the hydrogels loaded with RES, CUR and DEXA, in accordance with LAOS tests. Moreover, the SAOS results suggested once again that the concentration of the PUR affects the behavior of the loaded

hydrogels. In fact, at 25 °C the crossover frequency of NHP407-based formulations at 15 %w/v (**Figure 3.27 A** and **Figure 3.28 A**) and 20 %w/v (**Figure 3.27 D** and **Figure 3.28 A**) concentration decreased and increased upon RES and DEXA encapsulation, respectively. This phenomenon suggested that the higher amount of PUR chains dispersed in the medium reverses the effects of the addition of the hydrophobic drugs, probably because the reorganization of the amphiphilic PUR around the drugs is facilitated.

A similar behavior was observed also at 30 and 37 °C (**Figure 3.27 B, C**, **Figure 3.27 E, F** and **Figure 3.28 A**). However, a more evident reduction of $f_{crossover}$ was observed in NHP407-based hydrogels at 15 %w/v concentration loading CUR at 30 °C (**Figure 3.27 B** and **Figure 3.28 A**). This behavior is still well visible at 37 °C. On the other hand, the increase of the temperature canceled out the effect of the addition of the BSA, probably due to the increase of the hydrophobic interaction within the hydrogels. Concerning the 20 %w/v concentrated hydrogels, their behavior at 30 °C matched the trend at 25 °C. However, in this case, the crossover of the hydrogels loading RES went out of the range and thus not visible anymore (**Figure 3.27 E** and **Figure 3.28 A**). The 20 %w/v concentrated hydrogels at 37 °C showed a similar behavior, further confirming the hypothesis that the increase of PUR concentration mitigate the effect of the drugs/biomolecule encapsulation.

By adding DEXA both the PUR concentrated formulations at 25, 30 and 37 °C showed lower G'-G'' offset compared to the control (**Figure 3.28 B-D**), proving again that the addition of drugs with high molecular weight slows down the overall gelation process (the elastic components of the hydrogels turned less predominant over the viscous ones with respect to the control). The addition of CUR and RES, instead, increased the G'-G'' offset of the formulations (**Figure 3.28 B-D**), with a trend that follow again the drugs molecular weight: the lower is the

molecular weight, the higher is the G'-G'' offset. On the other hand, BSA addition seemed not to affect the G'-G'' offset too.

The trend of viscosity (η) as a function of temperature during the sol-to-gel transition of NHP407-based solutions at 15 and 20 %w/v concentration containing the considered drugs/biomolecules are reported in **Figure 3.29.**

Figure 3.30 shows the main parameters extracted from temperature ramp tests results (i.e., T_{onset}, viscosities at different temperatures -5, 10, 15, 20, 25, 30, 35 °C-).

NHP407-based hydrogels at 15 and 20 %w/v PUR content and loaded with CUR and RES exhibited lower T_{onset} compared to the native sol-gel systems (**Figure 3.29 A, B** and **Figure 3.30 A**). However, the addition of such drugs influenced also the slope of the curves, which became lower. This result pointed out that the addition of CUR and RES increased the gelation process in terms of micelle formation; however, the increase of the viscosity seemed to be slightly slower, balancing the overall process. This phenomenon was more evident on the hydrogels encapsulating CUR, further confirming the key role exerted by drug molecular weight in influencing the gelation process.

The addition of DEXA, instead, seemed not to have significative effects on the hydrogels in terms of T_{onset}. However, it influenced the slope of the curve too. In accordance with previously discussed data, BSA loading in the designed sol-gel systems did not affect the temperature driven sol-to-gel transition of NHP407-based hydrogels.

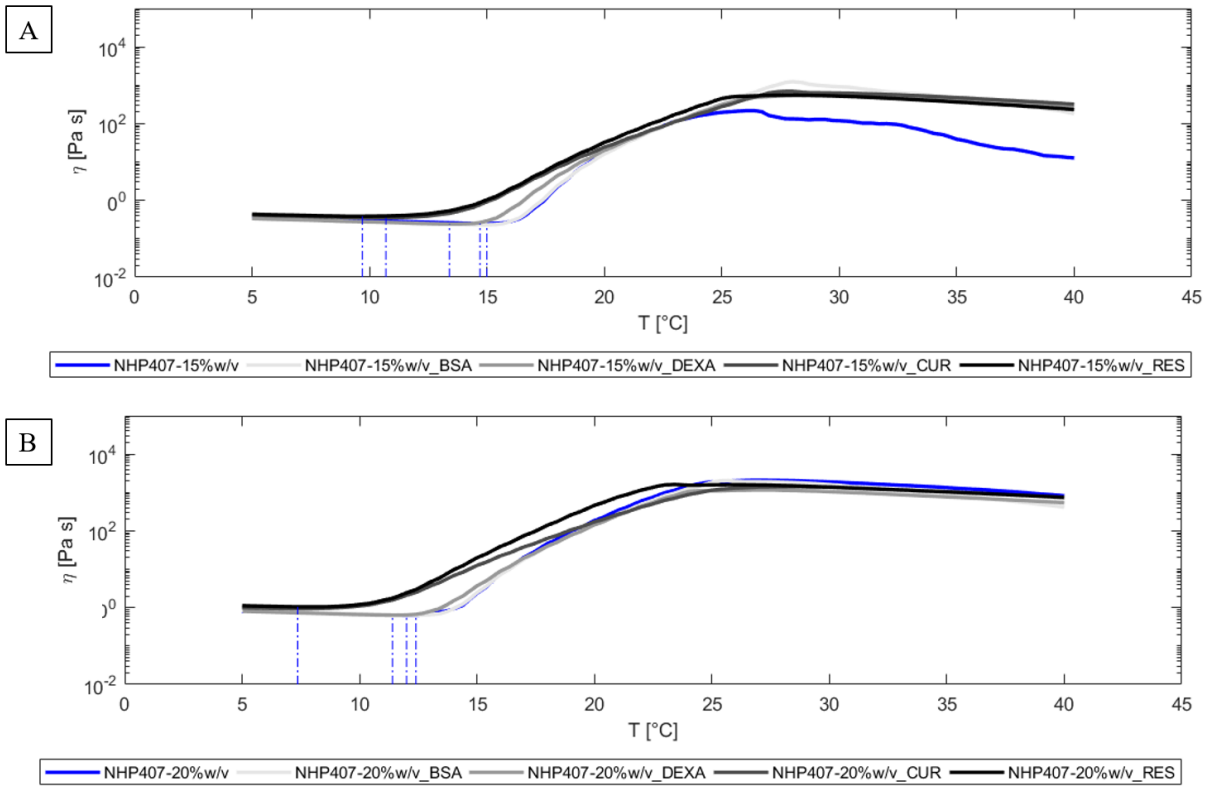

Figure 3.29 Temperature ramp test: viscosity *versus* temperature during the temperature-driven sol-to-gel transition. Comparison between NHP407-based samples at **(A)** 15 and **(B)** 20 %w/v concentration, loaded with drugs/biomolecules at a final concentration of 1 mg/ml. The blue dash-dotted lines identify T_{onset}.

As a consequence of the earlier beginning of the sol-to-gel transition, CUR- and RES-loaded sol-gel systems showed slightly higher viscosity with respect to the control samples and the other formulations (**Figure 3.30 C** and **Figure 3.30 D**).

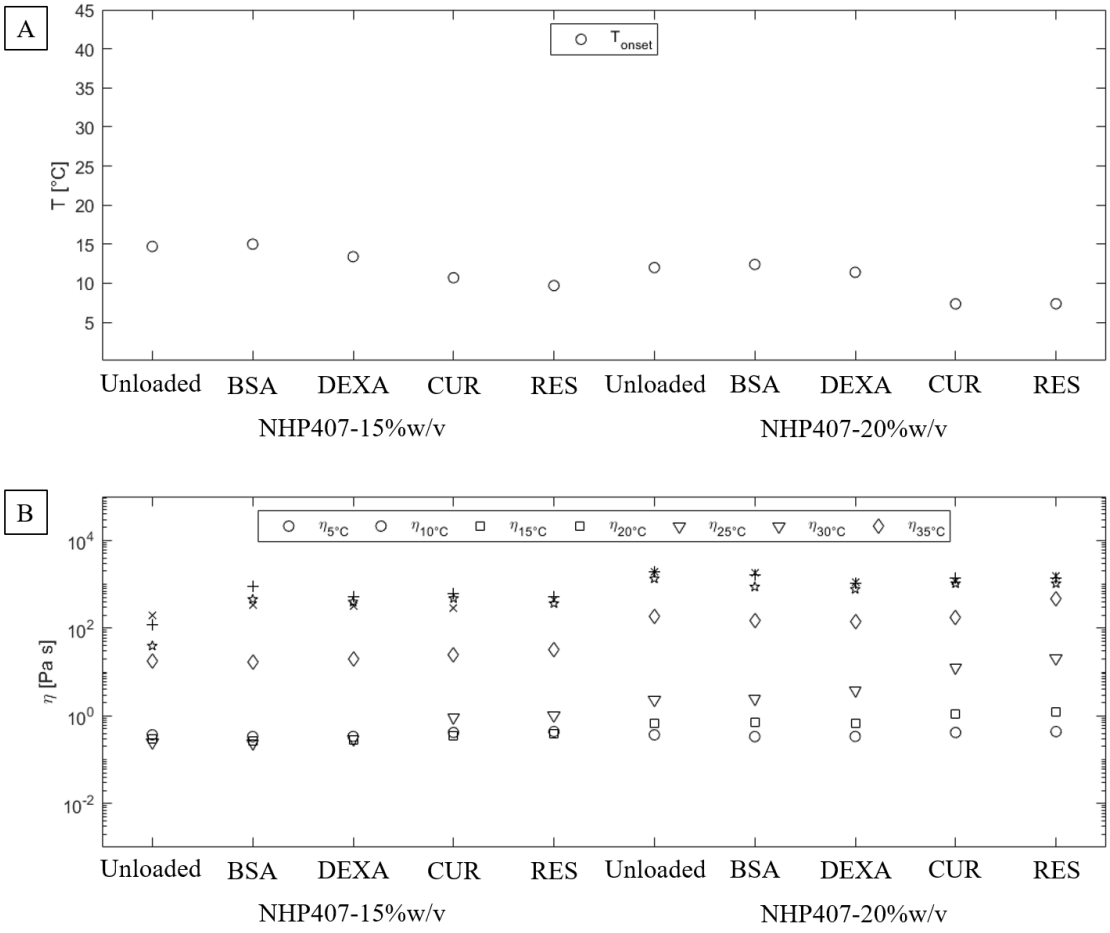

Figure 3.30 Main parameters of temperature-ramp tests carried out on NHP407-based sol-gel systems at .**(A-C)** 15 %w/v and **(B-D)** 20 %w/v PUR concentration and loaded with the investigated drugs/biomolecules. **(A-B)** T_{onset}, **(C-D)** viscosities at different temperatures (5, 10, 15, 20, 25, 30, 35 °C).

3.2.9.2. *In vitro* Drug Release Tests

Administration of anti-inflammatory drugs has been employed as a strategy to mitigate host response to implanted medical devices or transplanted cell-based therapeutics inhibiting the activities of inflammatory proteases and reactive oxygen species (ROS). The release kinetics of the hydrophobic antioxidant drugs dexamethasone -DEXA-, curcumin -CUR- and resveratrol –RES- has been studied to preliminary evaluate the potential of the selected hydrogels for drug

release applications. *In vitro* release profiles of DEXA, CUR and RES from NHP407- based hydrogels at 15 and 20 %w/v concentration in PBS (1 mg/mL of drug) are reported in **Figure 3.31**, **Figure 3.32** and **Figure 3.33**, respectively.

All the analyzed hydrophobic drugs showed a similar release profile from the selected hydrogels. A faster drug release was observed from NHP407-based formulations at 15 %w/v compared to the 20 %w/v concentrated ones. This result is ascribable to the lower concentration and biphasic nature at 37 °C of the 15 %w/v concentrated hydrogels compared to 20 %w/v concentrated formulations.

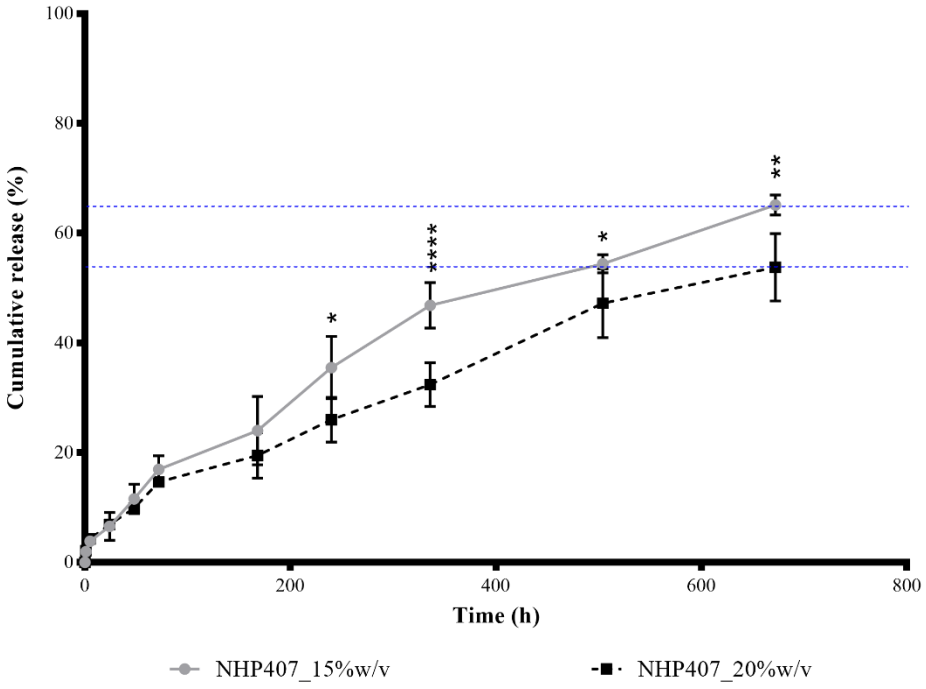

Figure 3.31 Dexamethasone (DEXA) release profile from NHP407-based hydrogels with 15 and 20 %w/v PUR concentration.

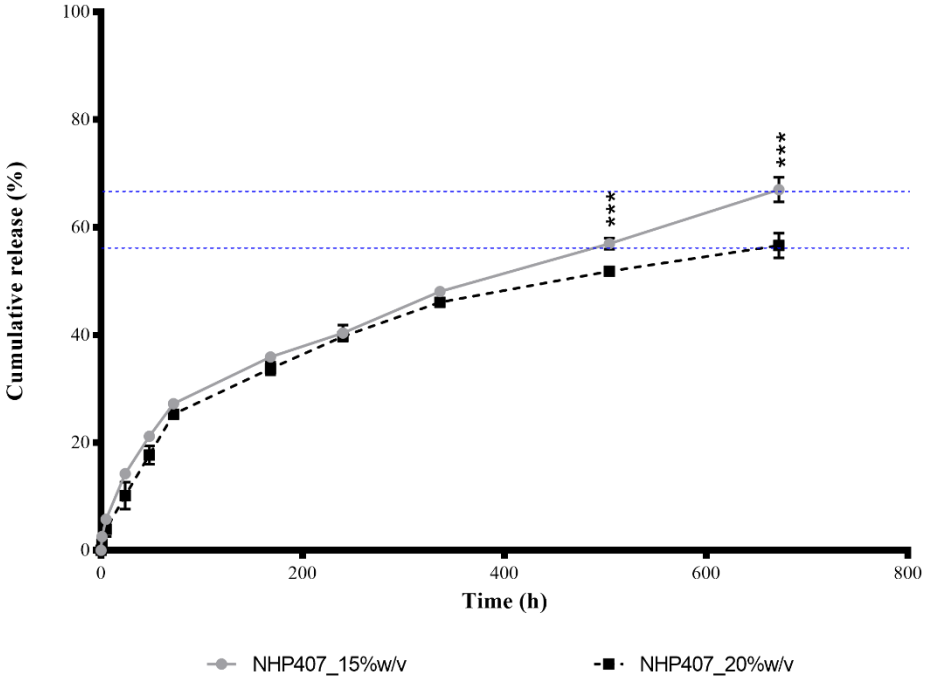

Figure 3.32 Curcumin (CUR) release profile from NHP407-based hydrogels with 15 and 20 %w/v PUR concentration.

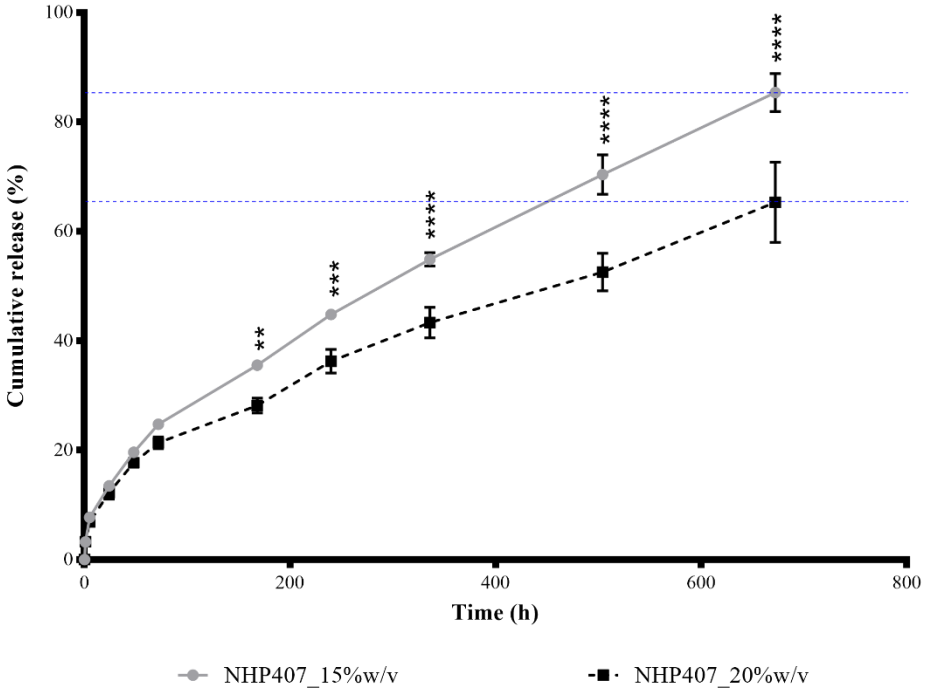

Figure 3.33 Resveratrol (RES) release profile from NHP407-based hydrogels with 15 and 20 %w/v PUR concentration.

In particular, as shown in **Figure 3.31** and **Figure 3.32**, on day 28, there were no significant differences in terms of percentage of drug released between DEXA- and CUR-loaded hydrogels (the hydrogels at 15 and 20%w/v concentration released about the 65 and the 55 % of the loaded DEXA and CUR, respectively). The similar behavior of DEXA and CUR can be correlated to their similarity in terms of molecular weight (DEXA: M_n = 392 Da, CUR: M_n = 368 Da).

On the other hand, on day 28, RES showed a significantly higher release with respect to DEXA- and CUR-loaded systems (the hydrogels at 15 and 20%w/v concentration released about the 85 and the 65% of the loaded RES, respectively) (**Figure 3.33**) probably because of its lower molecular weight (RES: M_n = 228 Da).

Finally, Peppas equations (**Equation 3** and **Equation 4**) were exploited to further characterize the nature of drug release kinetics from the studied hydrogels.[45] In detail, the release exponent *n*, indicative of the mechanism of drug release (diffusion-controlled and/or swelling-controlled), was estimated starting from release data. As shown in **Table 3.6**, the release factor *n* evaluated for all the analyzed drugs and hydrogels resulted to be comprised between 0.45 (diffusion-controlled drug release) and 0.89 (swelling-controlled drug release).

Table 3.6 Release exponent n (Peppas equation) of drugs encapsulated in NHP407-based hydrogels at 15 and 20 %w/v concentration

NHP407-based hydrogels	**n factor**		
	DEXA	**CUR**	**RES**
15 %w/v	0.61	0.56	0.49
20 %w/v	0.50	0.49	0.44

This result indicates that drug release was predominantly diffusion-controlled in both the analyzed hydrogel compositions, with almost no differences among the selected drugs.

However, the factor *n* of drug-loaded NHP407_15%w/v hydrogels was slightly higher than that of drug-loaded NHP407_20%w/v gels, in accordance with their higher susceptibility to dissolution phenomena.

3.2.9.3. *In vitro* Protein Release Tests

To build upon the results of material injections alone and to further encourage tissue regeneration and functional improvements material injections can be combined with the controlled release of growth factors or other bioactive molecules. To preliminary investigate the potential of the designed hydrogels as carrier of proteins, bovine serum albumin (BSA) and horseradish peroxidase (HRP) have been used as protein models. Beside protein release profile, the integrity and activity of the released BSA and HRP were also evaluated through SDS-PAGE and TMB assay, respectively.

With regard to protein release, the analyzed hydrophilic proteins showed a similar release kinetics: both proteins were completely released from NHP407-based hydrogels with 15 and 20 %w/v PUR concentration within 21 days. Moreover, release profile of encapsulated model proteins turned out to be PUR concentration-dependent, with a faster release from 15 %w/v concentrated hydrogels, in accordance with their lower PUR content with respect to formulations at 20 %w/v PUR concentration and their biphasic nature at 37 °C (**Figure 3.34** and **Figure 3.35**). In particular, as shown in **Figure 3.34**, BSA was completely released within 14 and 21 days from NHP407-based hydrogels with 15 and 20 %w/v PUR concentration, respectively. On the other hand, HRP was completely released within 10 and 14 days from NHP407-based hydrogels with 15 and 20 %w/v PUR concentration, respectively (**Figure 3.35**).

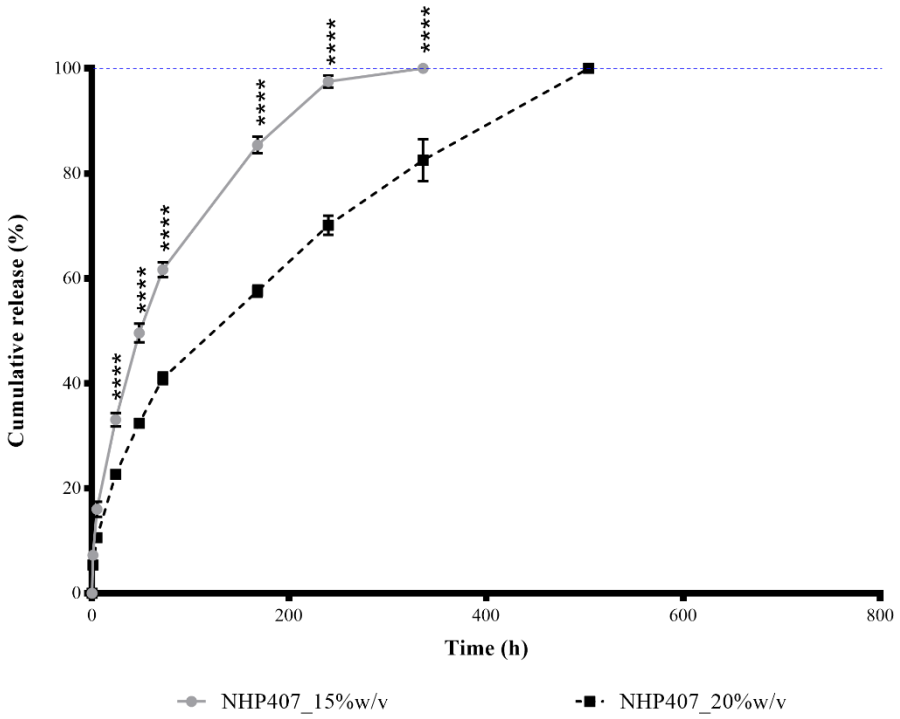

Figure 3.34 Bovine serum albumin (BSA) release profile from NHP407-based hydrogels with 15 and 20 %w/v PUR concentration.

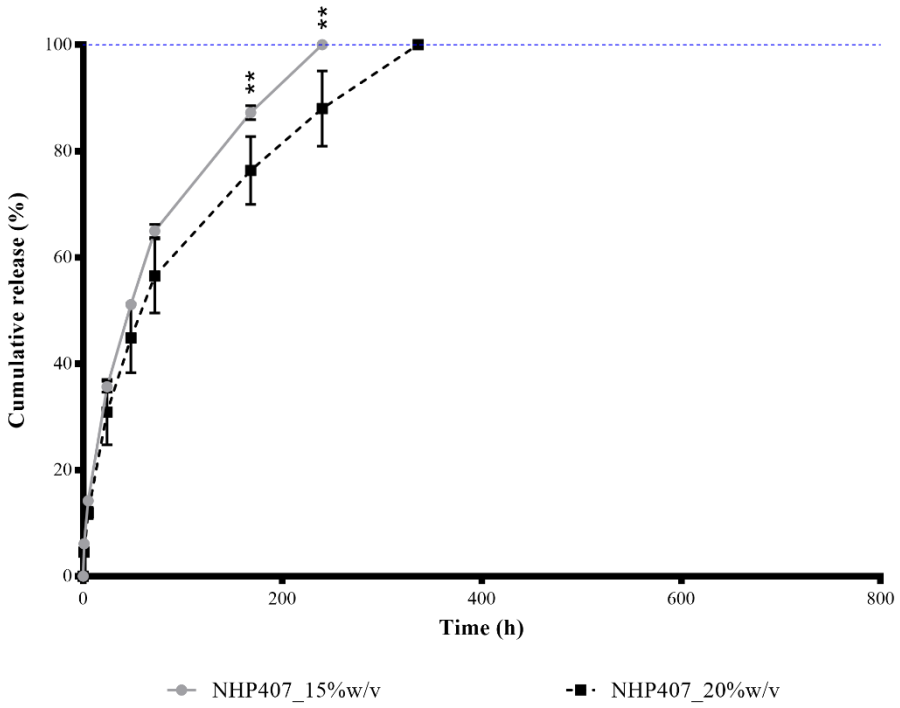

Figure 3.35 Horseradish peroxidase (HRP) release profile from NHP407-based hydrogels with 15 and 20 %w/v PUR concentration.

The faster release of HRP with respect to BSA (HRP release was completed one week before that of BSA for both the analyzed hydrogels) can be ascribed to its lower molecular weight (BSA: M_n = 66000 Da, HRP: M_n = 40000 Da), being both HRP and BSA globular proteins, water soluble and characterized by almost the same hydrodynamic diameter (approx. 8.0 and 7.5 nm for HRP and BSA, respectively).[51,52]

As done for drugs in the previous paragraph, also proteins release mechanism (diffusion-controlled and/or swelling-controlled) was characterized by Peppas equations. As shown in **Table 3.7**, the release exponent *n* resulted to be comprised between 0.45 (diffusion-controlled drug release) and 0.89 (swelling-controlled drug release) for both proteins and hydrogels.

Table 3.7 Release exponent n (Peppas equation) of proteins encapsulated in NHP407-based hydrogels at 15 and 20 %w/v concentration

NHP407-based hydrogels	**n factor**	
	BSA	**HRP**
15 %w/v	0.47	0.52
20 %w/v	0.47	0.53

The estimated *n* values resulted to be very close to 0.45, suggesting that protein release was predominantly diffusion-controlled. In this case, however, no differences in terms of *n* values were observed between the hydrogels with 15 and 20 %w/v PUR concentration, probably because the proteins are released from the hydrogels before dissolution/degradation effects could become evident.

Denaturing protein electrophoresis demonstrated that BSA did not undergo any degradation phenomena in response to its loading and release from both the hydrogels formulations.

As an example, **Figure 3.36** reports SDS-PAGE gel of BSA release solutions from the hydrogel with 15 %w/v PUR concentration at different time intervals. The single band for BSA in the release solutions appeared at the same position as in the native BSA solution (CTRL).

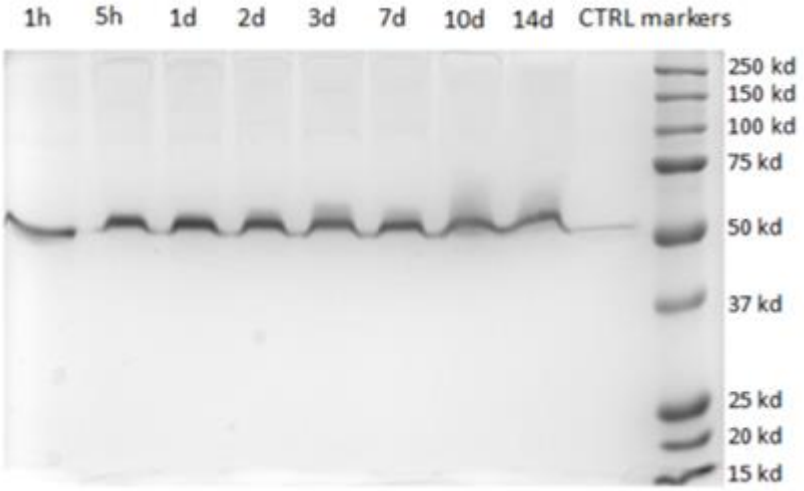

Figure 3.36 SDS-PAGE gel of BSA release solutions from hydrogels with 15 %w/v PUR concentration at different time intervals: lane 1 - 1h; lane 2 - 5h; lane 3 - 1d; lane 4 - 2d; lane 5 - 3d; lane 6 - 7d; lane 7 - 10d; lane 8 - 14d; lane 9 - native BSA solution (1mg/ml); lane 10 - protein molecular weight markers.

A suitable controlled delivery system should be also able to release a protein in its biologically active form. The biological activity of the released HRP from the two characterized formulations (15 and 20 %w/v) were studied by means of an enzymatic colorimetric assay (TMB assay). The release profile of active HRP from both 15 and 20 %w/v concentrated hydrogels is reported in **Figure 3.37**.

A significant loss of activity was detected on HRP release media (up to the 80-90% of the released HRP lose its activity within 1 day hydrogel incubation in aqueous media). Only the 20 and 25% of the loaded HRP was released in its active form from the hydrogels on day 10 and 14, respectively (**Figure 3.38**).

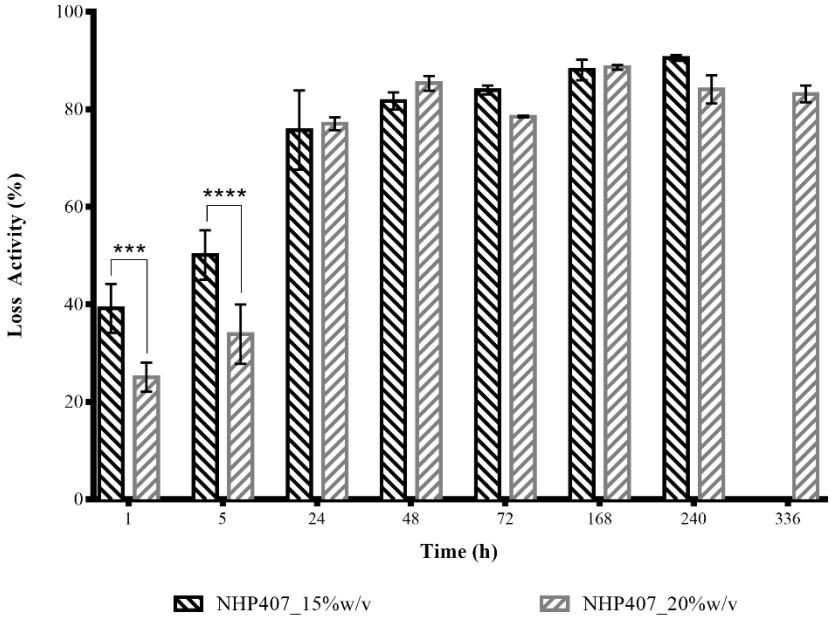

Figure 3.37 Evaluation of the loss in activity of the released HRP (TMB assay).

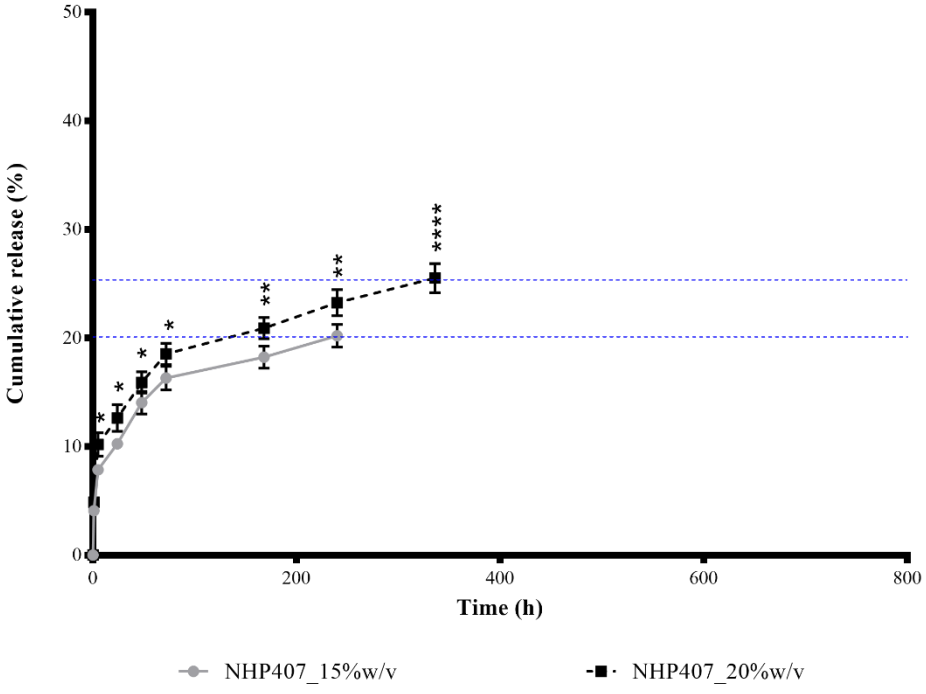

Figure 3.38 Active horseradish peroxidase (HRP) release profile from NHP407-based hydrogels with 15 and 20 %w/v PUR concentration.

By comparing the results of the two conducted colorimetric tests, the actual amount of released HRP, estimated through BCA assay, was higher (**Figure 3.35**) compared to the amount of active HRP detected by TMB assay (**Figure 3.38**). Hence, the relatively small quantity detected by TMB assay implies a partial inactivation of the released enzyme, instead of an incapability of the gels to release their payload. Nevertheless, up to 5 days of incubation, the active HRP released from the PUR-based systems was significatively higher compared to longer incubation time (**Figure 3.37**). Furthermore, the active HRP released by the 20 %w/v concentrated hydrogels is higher compared to the one released from the hydrogels at 15 %w/v concentration (75% and 60% of the released HRP was active, for the hydrogels with 20 and 15 %v/v PUR concentration, respectively). These results suggest that HRP inactivation cannot be correlated to the encapsulation process itself, which in fact was carried out in mild conditions, but rather to the interaction between the enzyme and the free polyurethane chains dispersed in the eluates after the gels started to dissolve. Amphiphilic polymers have indeed been found to cause conformational changes in protein structures that could be responsible for the progressive inactivation of the enzyme; additionally, small polymer chains could form hydrogen bonds with the enzyme active site, thus preventing its reaction with the substrate given by the activity test.[53] As a matter of fact, to support this hypothesis, the inactivation effect was more prominent for NHP407.based hydrogels with 15 %w/v PUR concentration, that according to the previously discussed stability tests lost about 5% of their initial weight after 1 day incubation in aqueous medium and, therefore, contained more free chains in their eluates which could interact with the released HRP (**Figure 3.21 B**). The release of biomolecules in their active form is a key issue when a new drug delivery system is designed. In this regard, the literature has already reported many approaches aiming at increasing HRP half-life. For instance, Al-Azzam and colleagues covalently grafted poly(ethylene glycol) moieties to HRP,[54] while other groups successfully

encapsulated the enzyme into micro- or nano-particles (e.g., acetylated dextran, silica) with no detrimental effects on its functionality.[55-57] Differently from micro- and nanocarriers, hydrogels do not show dimensional restrictions on the maximum payload they can encapsulate. Hence, in principle, the amount of payload encapsulated could be increased to a certain extent (based on the effects of loading procedure on the overall properties of the systems and biomolecule solubility) so that the released molecule in its active form exerts the desired therapeutic effect.

3.2.10. Polyurethane Functionalization Study

BOC de-protected NHP407 (with acronyms SHP407) ATR-FTIR spectrum confirmed the integrity of polymer chain bonds. **Figure 3.39** shows the ATR-FTIR spectra of SHP407 obtained using different chloroform/TFA ratios.

By varying the amount of TFA, the typical peaks of the polyurethane remained unvaried, demonstrating that any significant degradation occurred during the BOC de-protection process. The spectrum of the polymer obtained by deprotecting NHP407 with a Chloroform/TFA volume ratio of 50/50 v/v showed two additional picks at 516 and 1190 cm^{-1} ascribed to CF stretching vibration of TFA. For this material an additional cleaning step in diethyl ether would be required to completely remove TFA traces.

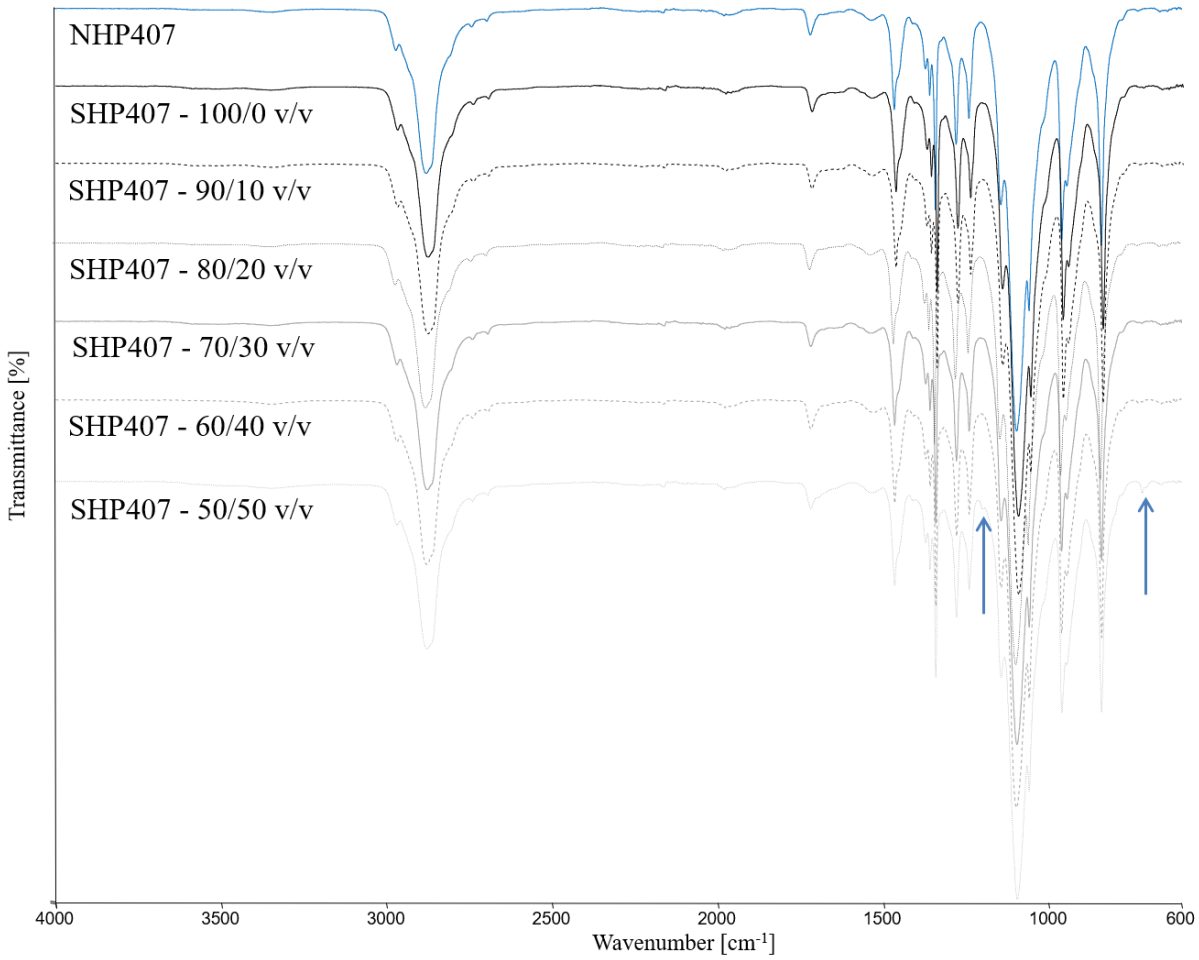

Figure 3.39 ATR-FTIR spectra of NHP407 and its deprotected form SHP407 obtained by varying the chloroform/TFA ratio during BOC cleavage reaction. Typical peaks of the polyurethane: 3347, 1722, 1675 and 1530 cm^{-1}.

After the cleavage of the BOC groups, polyurethane numeral molecular weight obtained by SEC was in the range of 43000-53000 Da, with a degradation percentage of 2-8.5 %. No significant increase in polydispersity index was observed for SHP407 samples, showing that the molecular weight distribution was mildly shifted to low molecular weights without further dispersion. The slight decrease in molecular weight after de-protection was overall negligible (**Figure 3.40**), as it fell within the typical error range of this kind of analysis.[58]

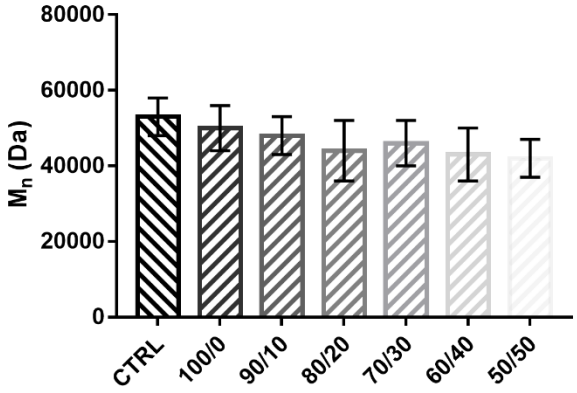

Figure 3.40 Number average molecular weight (M_n) of NHP407 (CTRL) and SHP407 as a function of chloroform/TFA volume ratio.

^{1}H-NMR spectroscopy was performed to demonstrate BOC cleavage. **Figure 3.41** shows ^{1}H NMR spectra of SHP407 obtained by reacting NHP407 with different TFA amounts (chloroform/TFA ratio 50/50, 80/20, 90/10, 95/5 and 100/0 v/v). A reduction in the area of the peak associated to the methyl protons of the BOC protecting group at 1.42 ppm was observed for all the samples analyzed, indicating a nearly complete de-protection. By reducing TFA amount, BOC de-protection efficiency was maintained. In addition, a partial de-protection (~ 70%) was achieved also with a 100% chloroform solution, as a consequence of the acidic environment it creates. Furthermore, all the other polymer signals in the 1H-NMR spectra remained unchanged indicating that the BOC cleavage treatment did not significantly affect polymer structure.

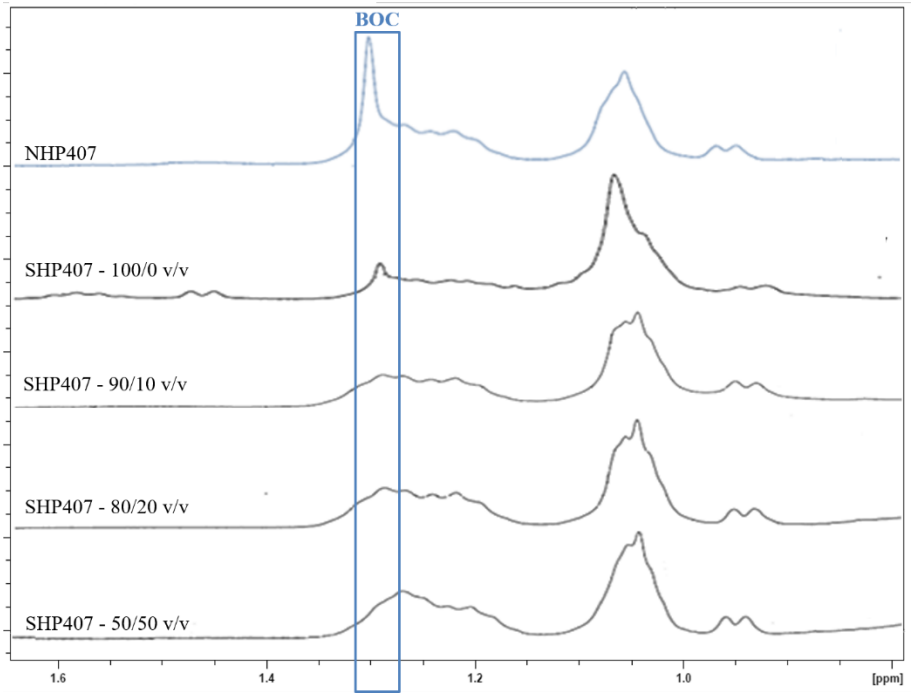

Figure 3.41 ^{1}H-NMR spectra of NHP407 and SHP407 obtained by varying the chloroform/TFA ratio.

The effectiveness of BOC group cleavage from the polyurethane chains was further assessed by quantifying the amount of free exposed amino groups through ninhydrin assay. NHP407 and BOC de-protected NHP407 (SHP407) were treated with Kaiser test reagents according to supplier instructions and changes in color solutions were observed. The control (NHP407) solution remained yellowish, while the solutions of de-protected polymer became bluish/purplish. The quantification of the free amino groups was performed applying Lambert-Beer's law to the peak found at 570 nm from UV-Vis Spectroscopy. No free amino groups were detected for NHP407, while the concentration of exposed amines (nmol NH_2/mg PUR) in SHP407 are reported in **Figure 3.42**. It is noteworthy that the reduction of the amount of TFA used for the de-protection reaction did not significantly influence the number of free amino groups exposed.

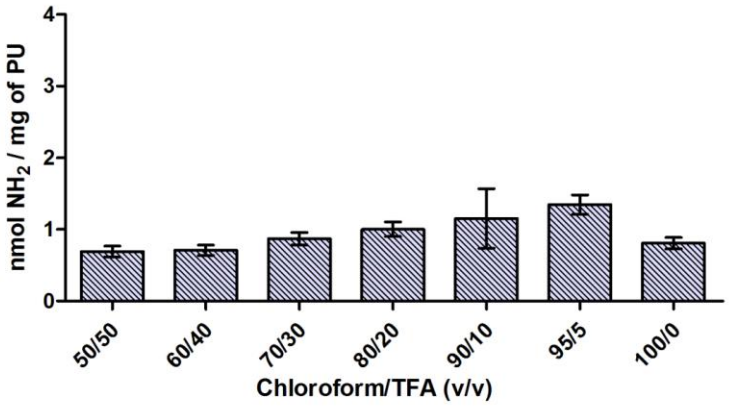

Figure 3.42 Quantification of free amino groups of SHP407 samples obtained by treating NHP407 with different chloroform/TFA ratios (Ninhydrin assay).

Based on the collected results, the chloroform/TFA volume ratio of 90/10 v/v could be selected as the best compromise to reduce both solvent costs and PUR degradation, while maintaining BOC de-protection efficiency.

3.3. Conclusions

In this chapter, an amphiphilic PUR with acronym NHP407 was synthesized by chain extending the commercially available triblock copolymer Poloxamer 407 with an aliphatic diisocyanate and an amino-acid derived diol. The success of its synthesis was assessed by infrared spectroscopy and size exclusion chromatography. Aqueous solutions based on NHP407 showed thermo-responsive behavior with micelle formation and packing with increasing temperature. NHP407-based micelles were characterized by dynamic light scattering and their critical micellar temperature was estimated. PUR-based micelles showed to be more organized compared to the P407-based ones, with a hydrodynamic diameter increasing with increasing temperature.

The gelation process of such systems was fully characterized through tube inverting test and rheological characterization. PUR-based hydrogels showed increased gelation properties compared to P407-based ones, in term of gelation speed and achievable mechanical properties. Moreover, such hydrogels were also characterized in terms of swelling and stability in water environment as well as nutrient permeation ability. Eventually, in order to assess the possibility to apply such systems as injectable cell/biomolecule carrier, injectability potential and cytotoxicity were also assessed.

From the reported data, two formulations with 15 and 20 %w/v PUR concentration were selected and further characterized to assess their potential for the encapsulation and release of biomolecules (i.e., antioxidant drugs and proteins). Interestingly, the addition of some hydrophobic antioxidant drugs turned out to make gelation process faster. In fact, drugs with lower molecular weight (i.e., curcumin and resveratrol) enhanced the gelation process working as a micellar nucleus. On the other hand, dexamethasone tended to slow down the gelation process, interfering with the formation of the micelles, as a consequence of its higher molecular

weight compared to curcumin and resveratrol. Drug molecular weight has been shown to affect also the release profile of the encapsulated drugs. In particular, drugs with lower molecular weight were released faster. Hydrophilicity has been shown to be another parameter affecting molecule release profile. In fact, proteins were released in higher amount and faster compared to the hydrophobic drugs, although their molecular weight was significantly higher (thousands Da *vs* hundreds Da). Moreover, the possibility to functionalize PUR backbone with bioactive moieties or functional groups by exploiting the primary amines exposed upon BOC de-protection, further increase the versatility of the designed sol-gel systems. For instance, functionalization via carbodiimide chemistry could be exploited to graft proteins or peptide sequences to enhance biocompatibility and guide cell behavior. In a different application, they could be exploited for chemical crosslinking to enhance hydrogel mechanical properties and stability in water environment.

The designed systems have thus shown promising properties for tissue engineering approaches. However, they still presented some drawbacks. For instance, the designed PUR-based hydrogels showed quite high viscosity, which could damage the encapsulated cells during the extrusion in bioprinting application. This aspect will be thoroughly discussed in chapter 4 of this thesis, dealing with the bioprinting process of PUR-based bioinks. Moreover, although NHP407-based hydrogels have demonstrated enhanced residence time in aqueous environment compared to P407-based ones, they still showed some stability issues in the form of thin extruded filaments. The following chapter will deal with the strategies applied to overcome this drawback.

References

[1] H. Kaji, G. Camci-Unal, R. Langer and A. Khademhosseini, *Biochim. Biophys. Acta.* **2011**: 1810.

[2] C.A. DeForest and K.S. Anseth, *Annu. Rev. Chem. Biomol. Eng.* **2012***: 3*.

[3] G. Camci-Unal, D. Cuttica, N. Annabi, D. Demarchi and A. Khademhosseini, *Biomacromolecules* **2013***: 14*.

[4] A.S. Hoffman, *Recent. Dev. Hydrogels* **2002***: 54*.

[5] N.A. Peppas, P. Bures, W. Leobandung and H. Ichikawa, *Eur. J. Pharm. Biopharm.* **2000***: 50*.

[6] B.V. Slaughter, S.S. Khurshid, O.Z. Fisher, A. Khademhosseini and N.A. Peppas, *Adv.Mater*. **2009**: *21*.

[7] A. Vashist, A. Vashist, Y.K. Gupta and S. Ahmad, *J. Mater. Chem*. **2014**: *B2.*

[8] T.R. Hoare and D.S. Kohane, *Polymer* **2008**: *49*.

[9] C. Tonda-Turo, S. Gnavi, F. Ruini, G. Gambarotta, E. Gioffredi, V. Chiono, I. Perroteau and G. Ciardelli, *J. Tissue Eng. Regen. Med.*, **2017**: *11*.

[10] S. Gnavi, L. Di Blasio, C. Tonda-Turo, A. Mancardi, L. Primo, G. Ciardelli, G. Gambarotta, S. Geuna and I. Perroteau, J Tissue Eng Regen Med, **2017**: *11*.

[11] J. Radhakrishnan, U.M. Krishnan, S. Sethuraman, *Biotechnol. Adv*. **2014**: *32*, 2.

[12] A.S. Hoffman. *Advanced Drug Delivery Reviews* **2012**: *64*.

[13] L. Yu and J. Ding, *Chem. Soc. Rev.* **2008**: *37*.

[14] E. Ruel-Gariepy and J.C. Leroux, *Eur. J. Pharm. Biopharm*. **2004**: *58*.

[15] B.G. Choi, H.P. Park, S.H. Cho, M.K. Oh, E.H. Kim, K. Park et al., *Biomaterials* **2010**: *31*.

[16] A.V. Kabanov, E.V. Batrakova and V.Y. Alakhov, *J. Control Release* **2002**: *82*.

[17] A.V. Kabanov and V.Y. Alakhov, *Crit. Rev. Ther. Drug Carrier Syst.* **2002**: *19*.

[18] S.F. Khattak, S.R. Bhatia and S.C. Roberts, *Tissue Eng*. **2005**: *11*.

[19] G. Dumortier, J.L. Grossiord, F. Agnely and J.C. Chaumeil. *Pharm. Res.* **2006**: *23*, 12.

[20] D. Chiappetta and A. Sosnik. *Eur. J. Pharm. Biopharm.* **2007**: *66*, 3.

[21] B.K. Nanjawade, F.V. Manvi, A.S. Manjappa, *J. Control Release* **2007**: *122*, 2.

[22] L. Bromberg, *J. Control Release* **2008**: *128*, 2.

[23] K.H. Sun, Y.S. Sohn and B. Jeong, *Biomacromolecules* **2006**: *7*.

[24] G. Niu, F. Du, L. Song, H. Zhang, J. Yang, H. Cao et al., *J. Control Release* **2009**: *138*.

[25] E. Volkmer, U. Leicht, M. Moritz, H. Wiese, S. Milz, P. Matthias et al., *J. Mater. Sci. Mater. Med.* **2013**: *24*.

[26] D. Cohn, A. Sosnik and A. Levy, *Biomaterials* **2003**: *24*.

[27] A. Sosnik, D. Cohn, J. San Román and G.A. Abraham, *J. Biomater. Sci. Polym.* **2003**: *14*, 3.

[28] X.J. Loh, H. Gan, H. Wang, S. Tan, K. Neoh, S. Jean Tan et al., *J. Appl. Polym. Sci.* **2014**: *131*.

[29] Lien Ai Pham-Huy, Hua He and Chuong Pham-Huy. *Int. J. Biomed. Sci.* **2008**: *4*, 2.

[30] M. Valko, M. Izakovic, M. Mazur, C.J. Rhodes and J. Telser, *Molecular and Cellular Biochemistry* **2004**: *266*, 1-2.

[31] H. Sies and D. Jones, in *Encyclopedia of Stress* (Ed. G. Fink), Elsevier, Amsterdam, NL **2007**, pp. 45-48.

[32] G. Filomeni, D. De Zio and F. Cecconi, *Cell Death and Differentiation* **2015**: *22.*

[33] B. Halliwell, *Drugs* **1991**: *42*, 4.

[34] E. Blanco, H. Shen and M. Ferrari, *Nature Biotechnology* **2015**: *33*.

[35] D. Park, W. Wu and Y.A. Wang, *Biomaterials* **2011**: *32*.

[36] M. Boffito, E. Gioffredi, V. Chiono, S. Calzone, E. Ranzato, S. Martinotti and G. Ciardelli, *Polym.Int*. **2016**: *65*.

[37] C. Pradal, K.S. Jack, L. Grøndahl and J.J. Cooper-White, *Biomacromolecules* **2013**: *14*.

[38] P. Alexandridis, J.F. Holzwarth and T.A. Hatton, *Macromolecules* **1994**: *27*.

[39] Xiaolei Li and Kyu Hyun, *Korea-Australia Rheology Journal* **2018**: *30*, 2.

[40] M. Bhattacharya, M.M. Malinen, P. Lauren, Y.R. Lou, S.W. Kuisma, L. Kanninen et al., *J. Control Release* **2012**: *164*.

[41] G. Ma, B. Miao and C. Song, *J. Appl. Polym. Sci*. **2010**: *116*.

[42] X V. Kumar, S. Mostafa, M.W. Kayo, E.P. Goldberg and H. Derendor, *Pharmazie* **2006**: *61*.

[43] M. Ghosh, A.T. Singh, W. Xu, T. Sulchek, L.I. Gordon, R.O. Ryan, *Nanomedicine* **2010**: *7*, 2.

[44] L. Camont, C.H. Cottart, Y. Rhayem, V. Nivet-Antoine, R. Djelidi, F. Collin, J.L. Beaudeux, D. Bonnefont-Rousselot, *Analytica Chimica Acta* **2009**: *634*, 1.

[45] F. Brandl, F. Kastner, R.M. Gschwind, T. Blunk, J. Tessmar, A. Göpferich, *J. Control Release* **2010**: *142*, 2.

[46] D. Park, W. Wu, and Y. Wang. *Biomaterials* **2011**: *32*.

[47] H. Altinok, G.A. Yu, S.K. Nixon, P.A. Gorry, D. Attwood and C. Booth, *Langmuir* **1997**: *13*.

[48] W. Brown, K. Schillen and S. Hvidt, *J. Phys. Chem*. **1992**: *96*.

[49] J. Dey, S. Kumar, S. Nath, R. Ganguly, V.K. Aswal and K. Ismail, *J. Colloid. Interface Sci.* **2014***: 415*.

[50] A.M. Pragatheeswaran and S.B. Chen, *Langmuir* **2013***: 29*.

[51] S. Tan, D. Gu, H. Liu, Q. Liu, *Nanotechnology* **2016**: *27*.

[52] B. Lorber, F. Fischer, M. Bailly et al., *Biochem. Mol. Biol. Educ*. **2012**: *40*.

[53] J. Guo, R. Zhong, W. Li et al., *Appl. Surf. Sci*. **2015**: *359*.

[54] W. Al-Azzam, E.A. Pastrana, B. King, J. Méndez, K. Griebenow, *J. Pharm. Sci*. **2005**: *94*.

[55] N. Kanthamneni, S. Sharma, S.A. Meenach et al., *Int. J. Pharm*. **2012**: *431*.

[56] F.P. Chang, Y. Hung, J.H. Chang et al., *ACS Appl. Mater. Interfaces* **2014**: *6*.

[57] Y.R. Chiu, W.J. Ho, J.S. Chao, C.J. Yuan, *J. Nanoparticle Res*. **2012**: *14*.

[58] Wolfgang Radke, *Journal of Chromatography A* **2004**: *1028*.

Chapter 4
Thermo- and Photo-sensitive Polyurethane-based Hydrogels

Abstract:

This chapter deals with the strategies adopted to further increase the stability of the polyurethane-based hydrogels designed in the previous chapter with attention to the design of thermo- and photo-sensitive sol-gel systems.

To this aim, three different families of thermo- and photo-sensitive hydrogels were designed and characterized. The first strategy involves the use of the previously designed PUR (NHP407) blended with an acrylate polymer (e.g., poly(ethylene glycol) acrylate) that upon UV/Vis irradiation forms a mesh entrapping the PUR-based micelles. The second approach, instead, deals with the design of a new family of PUR that expose acrylate moieties, in order to add photo-sensitivity to the resultant PUR-based hydrogel. Eventually, the last strategy involves the use of the latter PURs blended with an acrylate polymer (e.g., poly(ethylene glycol) acrylate) in order to obtain a double degree of crosslinking upon UV/Vis irradiation.

By adding the possibility to chemically crosslink the hydrogel structure, it was possible to design hydrogels with increased stability in water environment as well as mechanical properties.

The designed hydrogels were fully characterized in terms of physico-chemical properties and eventually two formulation were chosen to be applied in bioprinting technology.

Keywords: Polyurethane, Thermo- and Photo-sensitive Hydrogel, Photo-crosslinking

4.1. Introduction

NHP407-based bioinks showed significantly enhanced stability in aqueous environment in the shape of bulk scaffolds.[1] However, upon extrusion in the shape of thin filaments or casting as thin layers, their stability decreased drastically (from weeks/months to few hours).

Hence, different approaches can be exploited to further increase bioinks' stability in water environment as well as their mechanical properties (**Figure 4.1**).

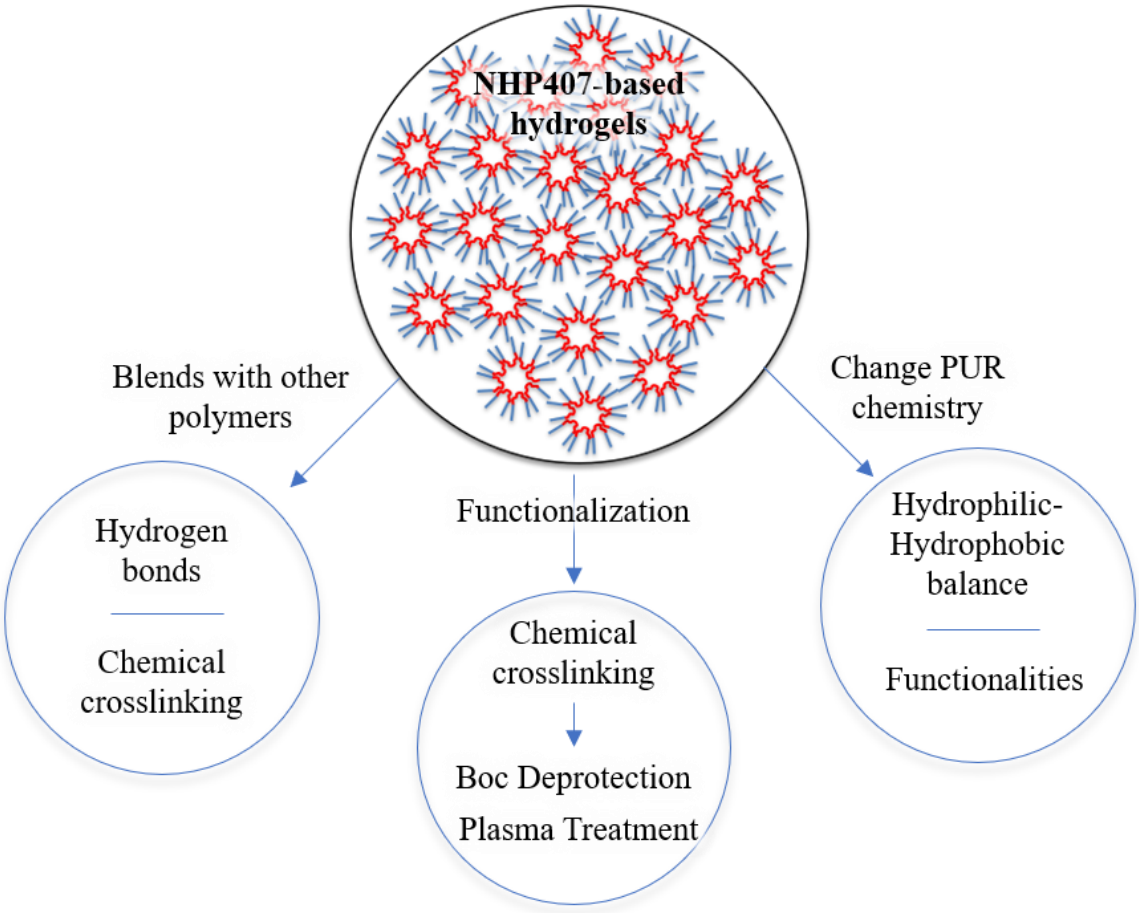

Figure 4.1 Different strategies to increase PU-based hydrogels stability in aqueous environment.

4.1.1. Overcoming Thermo-sensitive Hydrogels Drawbacks

In this work, two strategies have been tested to increase the stability of the thermo-sensitive hydrogels developed in the previous chapter: (i) the addition of a second component (blend) and (ii) the chemical modification of the PUR. Both the investigated approaches aimed at forming chemical crosslinks or enhancing the physical ones already present within and among the micelles.

According to the first approach, NHP407 has been blended with different polymers, such as water-soluble polymers rich of exposed hydrogen atoms (i.e., Poly(Vinyl Alcohol) -PVA- and Poly(Vinyl Pyrrolidone) -PVP-). The obtained hydrogels were expected to form more hydrogen bonds thus increasing physical interactions within the hydrogels.[2,3] However, the selected water-soluble polymers (1, 5, 10, 15, 20 and 25 %w/w with respect the NHP407) turned out not to be miscible with PUR aqueous solutions.

Hence, NHP407 was blended with reactive species able to crosslink/form crosslinks among PUR chains in particular conditions (i.e., L-3,4-dihydroxyphenylalanine -L-DOPA-[4,5] and Genipin[6,7]). The obtained hydrogels were expected to form a cross-linked mesh entrapping NHP407 micelles by DOPA polymerization (1, 0.75, 0.5, 0.25, 0.1 %w/w with respect the NHP407) and a chemical hydrogel by genipin (2:1 molar ratio with respect the NHP407) reaction with free amines of SHP407, respectively. Although an increase in gel filaments stability in water environment was observed, gel residence time was still unsatisfactory for long term applications. The results have been collected through visual inspection taking photos of the extruded filaments incubated in aqueous media over time (data not reported). Finally, the last investigated blending protocol foresaw the mixing of NHP407 with water-soluble photo-sensitive polymers (i.e., Poly(ethylene glycol) Diacrylate -PEGDA-[8-10], Diacrylated Poloxamer

P407[11] and Gelatin Methacrylate -GelMA-[12,13]). The obtained bioinks were expected to form a crosslinked mesh upon photoinitiator addition and UV/Vis irradiation.

The second strategy, instead, was based on the chemical modifications of the PUR. To this aim different new PURs were synthesized. Initially, a new PUR was designed starting from a different Poloxamer with a shorter molecular weight and a similar PEO/PPO balance compared to P407 (i.e., Poloxamer 237). However, aqueous solutions of the newly synthesized PUR appeared turbid and underwent gelation only at high concentrations (> 25 %w/v). Thus, two new PURs were successively designed with different hydrophilic/hydrophobic balance starting from PEG with molecular weight of 600 and 1500 Da, respectively, 1,6-hexamethylene diisocyanate and PCL diol with molecular weight of 530 and 1250 Da, respectively, as chain extender (i.e., P600HC530 and P1500HC1250). However, their solutions could not gel at all. Eventually, a new family of PURs was designed by incorporating acrylate photo-sensitive groups able to crosslink after activation (need of addition of a photo-initiator and UV/Vis irradiation) within PUR backbone. The new PURs were synthesized starting from Poloxamer 407, 1,6-hexamethylene diisocyanate and Hydroxyethyl methyl acrylate -HEMA- or Pentaerythritol triacrylate -PETA-. HEMA and PETA were used to end-cap the isocyanate-terminated prepolymer (i.e., acronym of new PURs: HHP407 and PHP407 for HEMA and PETA end-capped polymers, respectively) obtained by reacting P407 and HDI at 1:2 molar ratio.

In this chapter the design of thermosensitive and photocurable PUR-based bioinks will be reported.

4.1.2. Thermo- and Photo-sensitive Hydrogels Design

Among all the tested strategies, those that involved the design of thermo- and photo-sensitive PUR-based hydrogels have been proved to work better for the final application of these systems in 3D bioprinting. In fact, they can be printed by exploiting their thermo-sensitivity in the form of a biphasic sol/gel system or a fully developed gel, and photo-irradiated layer-by-layer or at the end of the process in order to increase their stability in aqueous environment. Moreover, this approach could allow a fine control of both the viscosity of the ink during the printing process and the final scaffold stiffness and stability in aqueous environment.

In particular, different bioink formulations have been optimized following four strategies:

- By blending the thermo-sensitive PUR (NHP407) and a photo-sensitive polymer that, upon irradiation, forms a mesh entrapping PUR micelles (i.e., PEGDA and GelMA) (**Figure 4.2 A**).
- By blending the thermo-sensitive PUR (NHP407) and a photo-sensitive polymer that, upon irradiation, takes part to the formation of the PUR micelles creating crosslinking within and among them (i.e., Poloxamer 407 diacrylate -P407-DA-) (**Figure 4.2 B**).
- By changing PUR chemistry and synthetizing a new PUR with pendant acrylate moieties (HHP407 and PHP407) to form crosslinked micelles and bridges between them through UV light irradiation (**Figure 4.2 B**).
- By blending the latter PURs with PEG-DA or GelMA, thus obtaining two different levels of crosslinking (**Figure 4.2 C**).

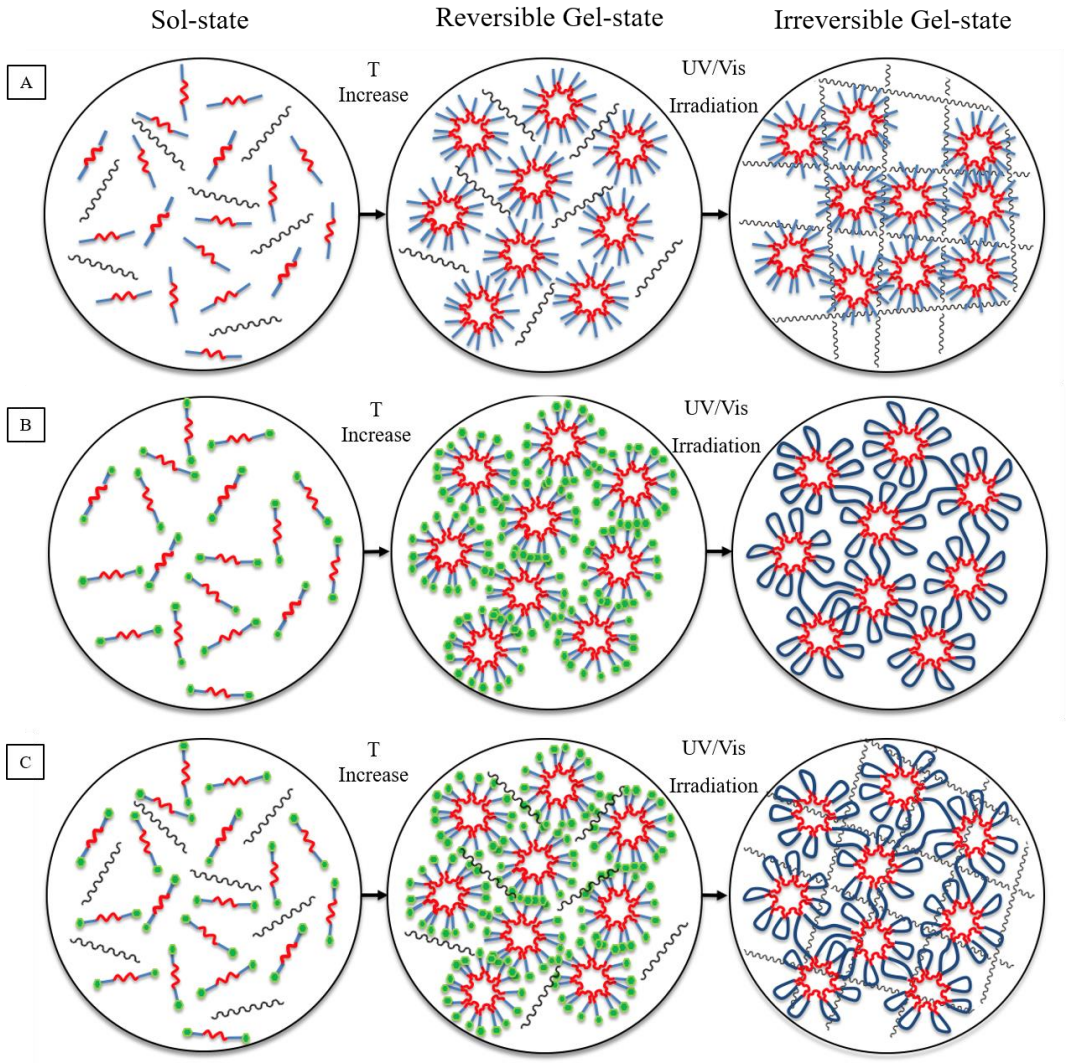

Figure 4.2 Representations of the different tested strategies and expected thermo- and photo-sensitive behavior: **(A)** upon irradiation, the acrylate water-soluble polymer forms a mesh entrapping PUR micelles; **(B)** upon irradiation, the acrylate PUR forms crosslinked micelles; **(C)** two different degrees of crosslinking are involved.

4.2. Materials and Methods

4.2.1. Synthesis of Acrylated Amphiphilic Poloxamer-Based Polyurethanes

In order to further enhance PUR-based hydrogel stability in aqueous media, the previously reported PUR chemistry has been adapted to synthesize amphiphilic PURs with pendant acrylic moieties. To this purpose, two different PURs were designed with one and three terminal acrylic moieties, respectively.

4.1.1.1. Reagents and Solvents

Poloxamer 407 (P407, M_n≈12600 Da, 70%w/w PEO), 1,6-diisocyanatohexane (HDI), dibutyltin dilaurate (DBTDL), hydroxyethyl methyl acrylate (HEMA) and pentaerythritol triacrylate (PETA) were purchased from Sigma Aldrich, Italy. P407, HEMA and PETA were dried overnight under reduced pressure at room temperature to remove residual water before use. HDI was distilled under reduced pressure before use. All solvents were purchased from Sigma Aldrich, Italy in the analytical grade. Anhydrous 1,2 dichloroethane (DCE) was prepared over activated molecular sieves for at least 8 hours before use. Molecular sieves were activated in an oven at 120 °C for at least 8 hours. Glassware required for the synthesis, magnets, spatulas and tweezers were dried overnight in an oven at 120 °C.

4.1.1.2. Synthesis Steps

Poloxamer-based acrylated PURs were synthesized through a two-step procedure in inert atmosphere using anhydrous 1,2 dichloroethane (DCE) as solvent and starting from P407 as macrodiol, HDI as diisocyanate and HEMA or PETA as end-capping molecules, respectively. During the first step, P407 (20%w/v in DCE) was reacted with HDI (1:2 molar ratio with respect to P407) for 2.5 h at 80°C, in the presence of the catalyst DBTDL (0.1%w/w with respect to P407 weight) to form the prepolymer. In the second step, the prepolymer end-capping molecule (HEMA and PETA 3% w/v in anhydrous DCE, 1:2 molar ratio with respect to the Poloxamer) was added and the reaction lasted 2.5 h at 25°C. The reaction was finally stopped with methanol and the polymer was collected by precipitation in petroleum ether (4:1 volume ratio with respect to DCE). The polymer was purified by dissolution in DCE (20%w/v) followed by precipitation in diethyl ether and methanol (98:2 v/v) (5:1 volume ratio with respect to DCE), dried overnight under the fume hood and finally washed in diethyl ether (5 g x 100 ml). After washing, the collected material was dried overnight under vacuum at room temperature, grinded and stored in nitrogen atmosphere at 5 °C protected from the light.

4.1.1.3. Polyurethane Nomenclature

The synthesized PURs had acronyms HHP407 and PHP407, where the first letter (H and P) indicates the prepolymer end-capping molecule (HEMA and PETA, respectively), H corresponds to HDI, while P407 refers to Poloxamer 407.

4.1.2. Physico-Chemical Characterization

Attenuated Total Reflectance Fourier Transform Infrared (ATR-FTIR) spectroscopy and Size Exclusion Chromatography (SEC) were exploited to assess the success of PURs synthesis, following the protocols previously reported (paragraph 3.1.2.1 and 3.1.2.2).

4.1.3. Hydrogel Preparation

In order to prepare thermo- and photo-sensitive hydrogels, the photoinitiator (2-hydroxy-1-[4-(2-hydroxyethoxy) phenyl]-2-methyl-1-propanone -Irgacure 2959 or I2959-[14], Sigma Aldrich, and 2,4,6-trimethylbenzoylphosphinate -LAP-[15], TCI) was first solubilized in aqueous medium at room temperature (0.05 %w/v). Eventually, the obtained solution is cooled down at 5 °C and used to solubilize the PURs powder at 5 °C to avoid micellization and/or gelation during solution preparation.

4.1.4. Hydrogel Thermo-sensitivity Characterization

Micellization properties and thermal behavior of PUR-based aqueous solutions were studied by means of DLS measurements, [1,16] CMT estimation, [1,17] tube inverting[1] test and rheological characterization[1], following the previously reported protocols (paragraph 3.1.4.1, 3.1.4.2, 3.1.4.3 and 3.1.4.4). PUR-based hydrogel injectability was also evaluated as previously mentioned (paragraph 3.1.7).

4.1.5. Hydrogel Photo-sensitivity Characterization

4.1.5.1. Micelle Dimensions

To see the effect of the UV irradiation on micelle dimension, Dynamic Light Scattering (DLS) measurements were performed following the protocol previously described (paragraph 3.1.4.1). Samples were first prepared at 0.5 and 1% w/v concentration in phosphate buffered saline (PBS, pH 7.4); then, the photoinitiator I2959 was added at 0.05% v/v. A first measurement was performed before the photo-crosslinking; then the samples were irradiated under stirring for 10 minutes at 10 mW/cm^2 and left to equilibrate overnight in order to perform the second measurement in stationary conditions.

4.1.5.2. Photo-Crosslinked Scaffolds Preparation

250 µl of PURs solutions at 15% w/v were deposited in an appropriate toroidal mold to obtain samples with an approximate 2 mm thickness and 10 mm diameter. The mold was placed on a 12 mm round glass dish, that was used as support for the sample after mold removal. Irgacure 2959 was added as photo-initiator, at a concentration of 0.05% w/v with respect to the PUR solution. The polymeric solutions were then put at 37 °C and irradiated with a LED emitting UV light at 365 nm at 10 mW/cm^2 for 6 minutes to induce photo-polymerization. Photo-initiator concentration, irradiation intensity, exposure time were chosen according to previous literature studies,[18] in order to avoid cellular damage in future applications.

4.1.5.3. Swelling, Stability and Permeability Test in Aqueous Medium

Swelling and stability test were performed on the PURs-based photo crosslinked hydrogels (15 %w/v), using circular shaped samples prepared as previously described (paragraph 4.1.5.2). The test was carried out following the previously reported protocol (paragraph 3.1.5).

To assess the efficacy of the photo-crosslinking, stability and degradation tests were also performed on un-crosslinked samples with the same shape and considering the same time points. All results are reported as mean ± standard deviation.

Permeability studies were also carried out on the circular shaped samples obtained in the same way, and following the previously reported protocol (paragraph 3.1.6).[19]

4.1.5.4. Photo-rheology

Photo-rheological tests were conducted to assess the kinetics of gel photo-polymerization. Photo-rheological measurements were carried out on a stress-controlled rheometer (MCR302, Anton Paar GmbH) equipped with a photo-rheological modulus and a Peltier system for temperature control. The rheometer was equipped with a portable laser emitting in the UVA (a filter on 365 nm wavelength was applied in order to cut the other wavelengths) region of the UV spectrum with an irradiation intensity of about 10 mW/cm^2 (LightningCure Spot light source LC8, Hamamatsu). Differently from rheological characterization, for photo-rheology a quartz lower plate was used to allow sample irradiation during the analysis. The analysis was conducted using a 25mm parallel plate geometry, in isothermal conditions at 37 °C and with a gap between the two plates set at 200 µm to mimic the real working condition of photo-crosslinking the hydrogels upon extrusion through a needle. Each tested sample was poured on the lower plate set at 10 °C (instead of 0 °C to avoid quartz fogging) in the sol state and equilibrated at 37 °C for 5 minutes before analysis onset to allow the sol-to-gel transition.

The measurements were performed at 37 °C with constant strain (1 %). The data were collected for 1 min without UV irradiation, followed by 1 or 3 min of photo-crosslinking and then another minute with no light irradiation. Changes in storage modulus before, during and after laser irradiation were measured as a function of exposure time.

4.1.6. Synthesis of Photo-sensitive Polymers

4.1.6.1. Reagents and Solvents

Poloxamer 407 (P407, M_n≈12600 Da, 70%w/w PEO), poly(ethylene glycol) (PEG, M_n≈3450 Da), triethylamine (TEA), acryloyl chloride (AC), gelatin, methacrylic anhydride (MA) and glycidyl methacrylate (GM) were purchased from Sigma Aldrich, Italy. P407 and PEG were dried overnight under reduced pressure at room temperature to remove residual water before use. All solvents were purchased from Sigma Aldrich, Italy in the analytical grade. Anhydrous dichloromethane (DCM) was prepared over activated molecular sieves for at least 8 hours before use. Molecular sieves were activated in an oven at 120 °C for at least 8 hours. Glassware required for the synthesis, magnets, spatulas and tweezers were dried overnight in an oven at 120 °C.

4.1.6.2. Poly(Ethylene Glycol) Diacrylate and Diacrylated Poloxamer P407 Synthesis

Polyethylene glycol diacrylate (PEG-DA) and Diacrylated Poloxamer 407 (P407-DA) were synthesized by reacting PEG and P407 with Acryloyl chloride (AC). Briefly, three vacuum/nitrogen cycles were performed (2min / 1min) to dry the glassware before the addition of PEG or Poloxamer 407. Other three vacuum/nitrogen cycles were performed (2min / 1min)

on dried PEG or P407 added in the reaction flask. Then, the polymers were solubilized in anhydrous DCM (30 %w/v) and three vacuum/nitrogen cycles (1min / 1min) were performed. A TEA solution in anhydrous DCM (15 %v/v, 2:1 molar ratio with respect to PEG or Poloxamer 407) was added slowly with a glass syringe and three vacuum/nitrogen cycles were performed (1min / 1min). Finally, AC was solubilized in anhydrous DCM (15 %v/v) at 4:1 molar ratio with respect to PEG or Poloxamer 407 and added very slowly with a glass syringe. After the last three vacuum/nitrogen cycles (1min / 1min), the regents were allowed to react for 24 hours at room temperature, protected from the light. The reacted mixture was then moved to a separatory funnel and 1.5 M K_2CO_3 water solution was added (approx. 1/4 of the total volume of DCM inside the separatory funnel). The funnel was tapped and shook vigorously for a few seconds, venting to release CO_2. The process was repeated until no more gas was released (the solution should have the consistency of a milky white emulsion). The solution was allowed to separate for 20 hours at room temperature, protected from the light, and eventually the lower organic phase was collected. Finally, anhydrous $MgSO_4$ was added until the mixture went from a lumpy consistency to a well-dispersed mixture of powder and organic solvent. The mixture was vacuum filtered through a Buchner funnel to remove $MgSO_4$, the solution was rotary evaporated to concentrate the polymer and precipitated in diethyl ether (DEE, 1:5 volume ratio with respect to the DCM). The polymer was finally collected through vacuum filtration using a Buchner funnel, dried overnight under the hood at room temperature and stored at 5 °C under vacuum protected from the light.

4.1.6.3. Gelatin Methacrylate Synthesis

Gelatin Methacrylate (GelMA) was synthesized by reacting gelatin with different amount of MA and GM leading to a different grade of methacrylation. Briefly, gelatin (5% w/v in

phosphate buffered saline, pH 7.4) was reacted with MA or GM adding them slowly at 1, 5, 10 %w/w concentration with respect to gelatin. After 3 hours, 500 mL of PBS was added to stop the reaction and the solution was transferred to a dialysis tube (cut off 12 kDa) and dialyzed against demineralized water at room temperature for one week (dialysis medium exchange twice a day). The solution was finally transferred to centrifugation tubes and freeze-dried for 5-7 days at -80 °C (Martin Christ ALPHA 2-4 LSC). GelMa was then stored under vacuum at 5 °C protected from the light.

4.1.6.4. Physico-Chemical Characterization

Attenuated Total Reflectance Fourier Transform Infrared (ATR-FTIR) spectroscopy and Proton Nuclear magnetic resonance (^{1}H-NMR) spectroscopy was exploited to assess the successful acrylation of PEG, P407 and gelatin.

The chemical characterization was carried out following the previously reported protocol (paragraph 3.1.2.1 and 3.1.2.3).

Concerning the ^{1}H-NMR analyses of GelMA, the natural polymers were solubilized in deuterated water instead of deuterated DMSO as for the other analyzed polymers.

4.1.7. Statistical analysis

Results are reported as mean ± standard deviation following the previously reported method (paragraph 3.1.11).

4.2. Results and Discussion

4.2.1. Polyurethane Chemical Characterization

ATR-FTIR spectroscopy was exploited to assess the success of PURs synthesis. **Figure 4.3** shows the ATR-FTIR spectra of Poloxamer P407 (the macrodiol used during the synthesis) and the polyurethanes HHP407 and PHP407.

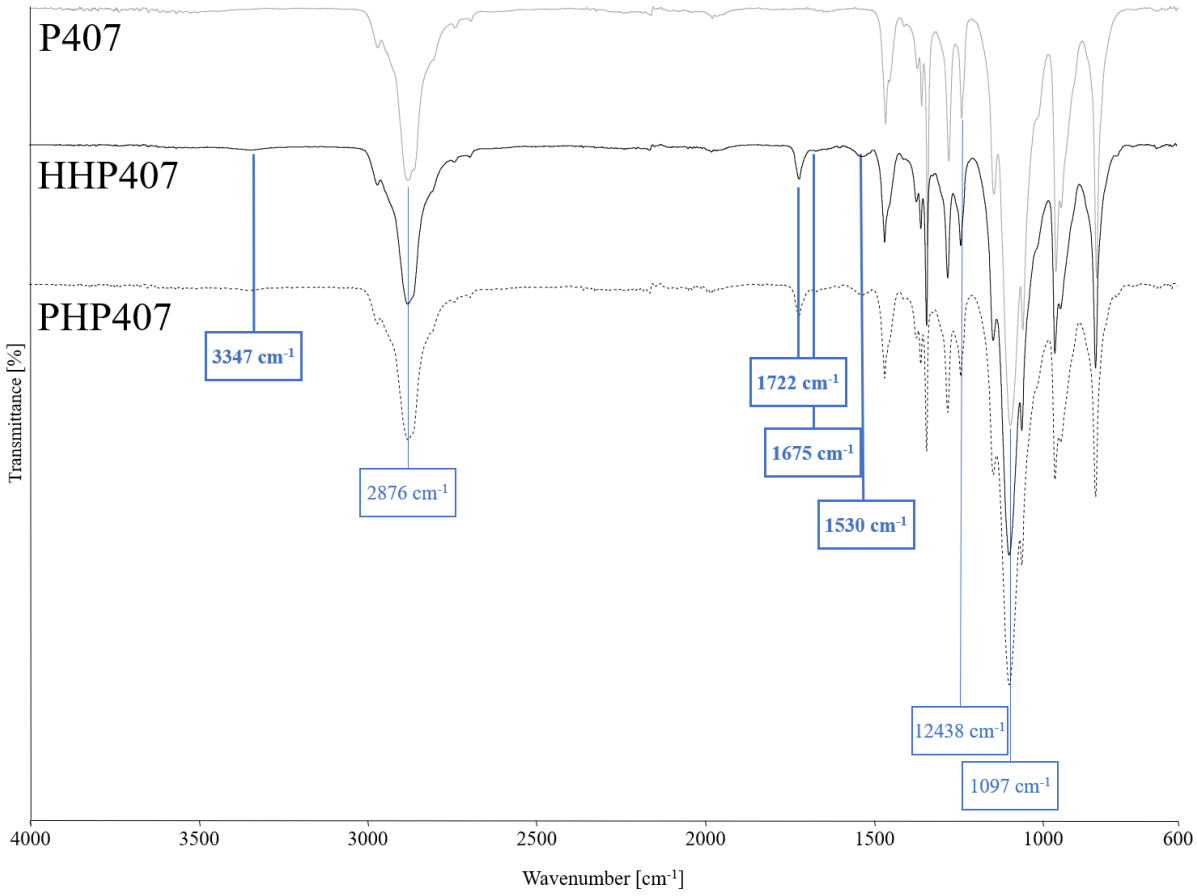

Figure 4.3 ATR FTIR spectra of P407 (solid grey), HHP407 (solid black) and PHP407 (dashed black). Differences between the two spectra, proving successful PURs synthesis, are highlighted at 3347, 1722, 1675 and 1530 cm^{-1}. The peaks at 2876, 1238 and 1097 cm^{-1} are typical of P407.

PURs spectra demonstrated synthesis success: two new bands appeared at 1722 cm^{-1} and 1675 cm^{-1} (the latter is less visible with respect the NHP407 spectrum (**Figure 3.3**)), which can be

ascribed to the stretching vibration of free and bounded carbonyl groups (C=O) (amide I), respectively, while the peak at 1530 cm^{-1} represents N-H bending vibrations (amide II), indicating the formation of urethane linkages. The urethane and amide groups also showed absorption at 3347 cm^{-1}, ascribed to N-H stretching. The complete conversion of the monomers was proved by the absence of unreacted diisocyanate absorption peak at 2200 cm^{-1}.

The characteristic peaks of the acrylate groups, the carbonyl group (C=O) stretching vibration and the alkene group (C=C) stretching vibration at 1720 cm^{-1} and 1640 cm^{-1}, respectively, were not clearly visible because they were overlapped with PUR typical bands.

Polyurethanes average numeral molecular weight (M_n) obtained by SEC was in the range of 40000-48000 Da, with a polydispersity index of 1.6. However, due to the end-capping reaction of the prepolymer, the molecular weight of the PUR was not expected to increase significantly with respect to native P407. Thus, although PUR synthesis protocol was highly repeatable, the stoichiometric ratio within the macrodiol and the diisocyanate was not completely respected, leading to a partial chain extension of the prepolymer chains during the first step of the synthesis. In other to overcome this drawback, an optimization of synthesis first step in terms of temperature and timing would be required to minimize the risk of chain extension during the pre-polymerization reaction.

4.1.1. Micelle hydrodynamic diameter

DLS measurements were performed to study the hydrodynamic diameter of the polymeric structures formed by HHP407 and PHP407 solubilized in PBS as a function of solution concentration and temperature. Moreover, micelle hydrodynamic diameter was also evaluated before and after the addition of a photoinitiator (I2959, 0.05 %w/v) and the exposure of the samples to UV light (365 nm, 10 mW/cm^2, 10 min).

As an example, **Figure 4.4 A** and **Figure 4.4 B** reports light scattering intensity patterns for a 1 %w/v concentrated solution of HHP407 and PHP407 at four different temperatures (25, 30, 37 and 45 °C), respectively.

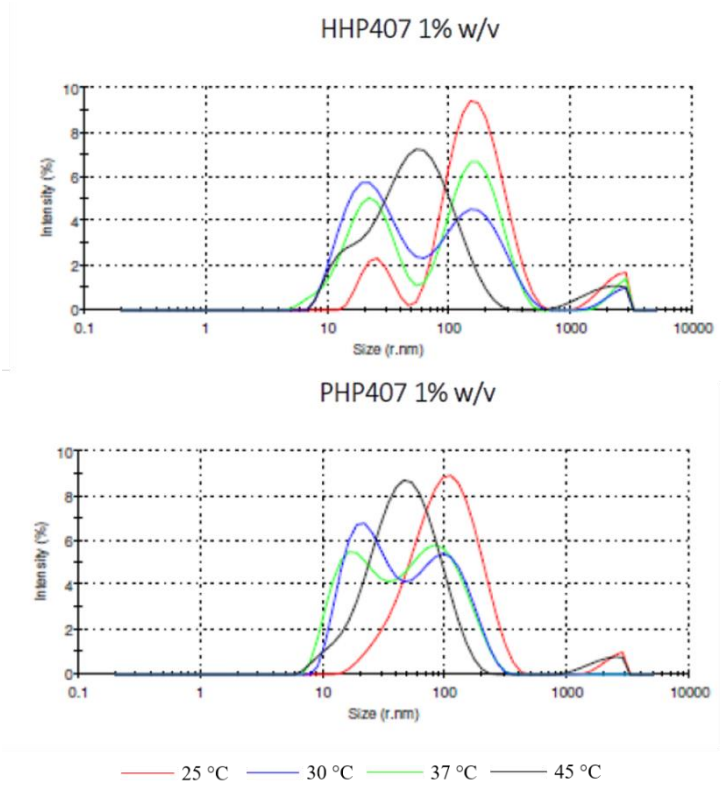

Figure .4.4 DLS patterns of **(A)** HHP407- and **(B)** PHP407-based solutions with 1 %w/v PUR concentration at 25, 30, 37 and 45 °C.

The size distribution among unimers, micelles and aggregates turned out to be temperature-sensitive. HHP407- and PHP407-based solutions showed a bimodal size distribution by intensity, with micellar structures becoming progressively prevalent with increasing temperature. Moreover, the structures formed at 25 °C seemed to be larger than the ones present at higher temperatures; this could be due to the presence of uncoiled and free chains in solution that have not formed ordered structures yet and appear as bigger aggregates.

Compared to NHP407-based solutions (**Figure 3.4 B**), HHP407- and PHP407- based ones formed more dynamically unstable micelles, as demonstrated by the great variability between

the distributions registered at different temperatures. Moreover, the comparison between the micelle size of the different PURs pointed out that the NHP407-based micelle are smaller with respect the other PUR-based micelle, and the HHP407-based micelle are smaller than the PHP407-based micelle (19.70, 29.72 and 32.45 nm diameter for NHP407-, HHP407, and PHP407-based micelles) (**Figure 4.5**). The reason of this phenomenon probably lies on the steric hindrance of the acrylic moieties. In fact, these results pointed out that the micelle hydrodynamic diameter increased with increasing the number of exposed acrylic groups.

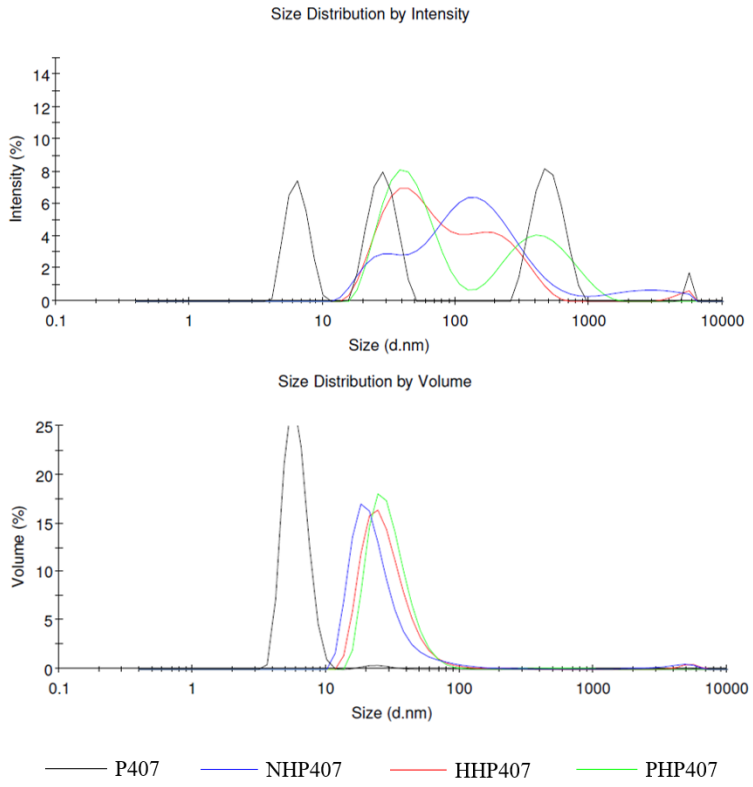

Figure 4.5 DLS patterns for P407-, NHP407-, HHP407- and PHP407-based solutions with 1 %w/v concentration at 37 °C.

Figure 4.6 reports DLS results for HHP407 and PHP407-based solutions at a 1% w/v concentration and 37 °C, before and after UV irradiation.

The effect of UV irradiation was not highly pronounced due to the presence of the previously mentioned big aggregates even before UV irradiation. However, HHP407-based solutions

showed an increase in the intensity on the peak centered at 100 nm and a slight decrease in intensity of the peak centered at about 20 nm, suggesting the formation of new larger aggregates resulting from photopolymerization. On the other hand, no relevant changes in micelle/aggregate size distribution were observed for PHP407-based solutions.

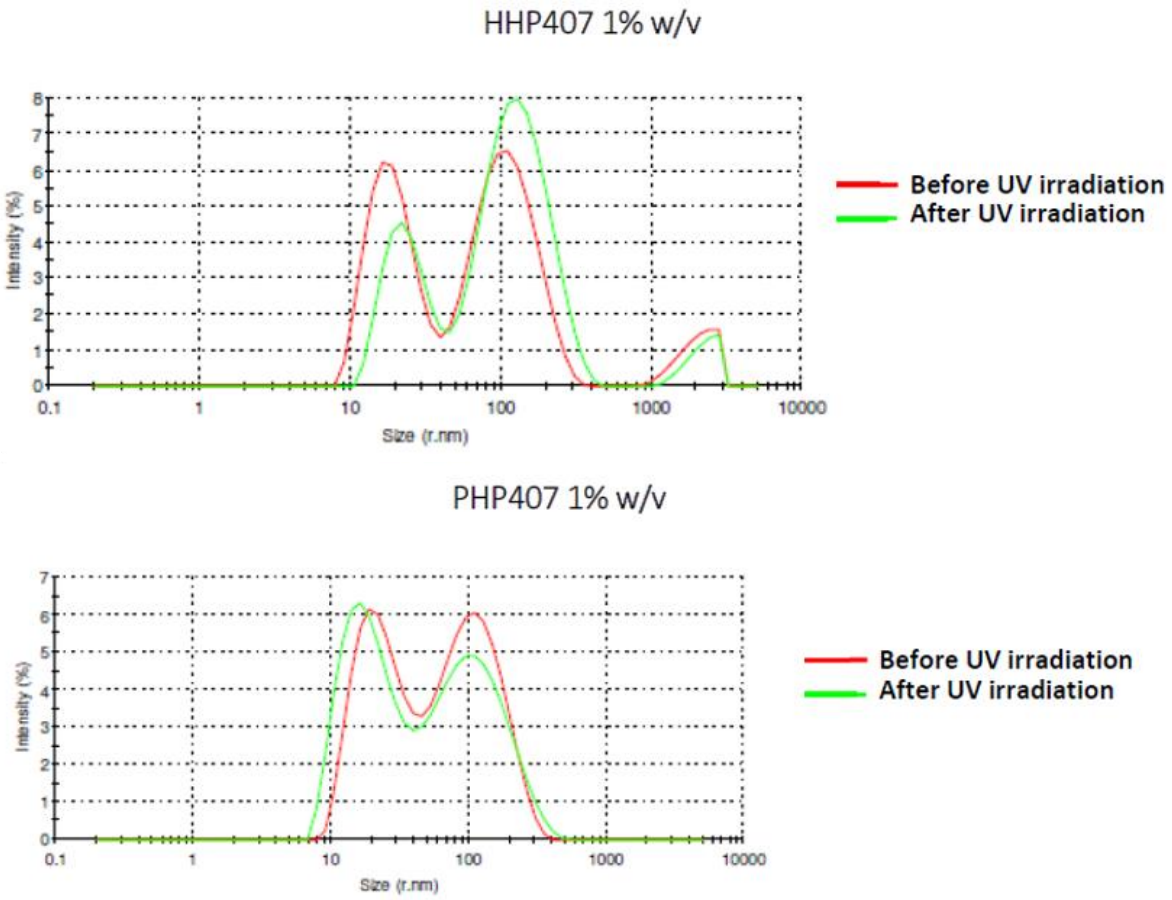

Figure 4.6 DLS patterns for HHP407- and PHP407-based solutions with 1 %w/v concentration at 37 °C, before and after the UV irradiation.

4.1.1.1. Critical Micellar Temperature Estimation

With increasing temperature, the UV-visible spectrum of both HHP407 and PHP407 solutions added with DPH showed a strong absorption peak at 356 nm, attributed to DPH dye solubilization into the hydrophobic micelle core, thus suggesting micelle formation. In addition,

the intensity of such absorbance band increased with increasing temperature, indicating the progressive formation of micelles and the achievement of a higher level of organization among the micelles (**Figure 4.7 A**). The CMT of the analyzed samples was estimated from the first inflection of the sigmoidal curve of the absorption intensity at 356 nm versus temperature, as it was caused by the formation of hydrophobic domains (**Figure 4.7 B**).

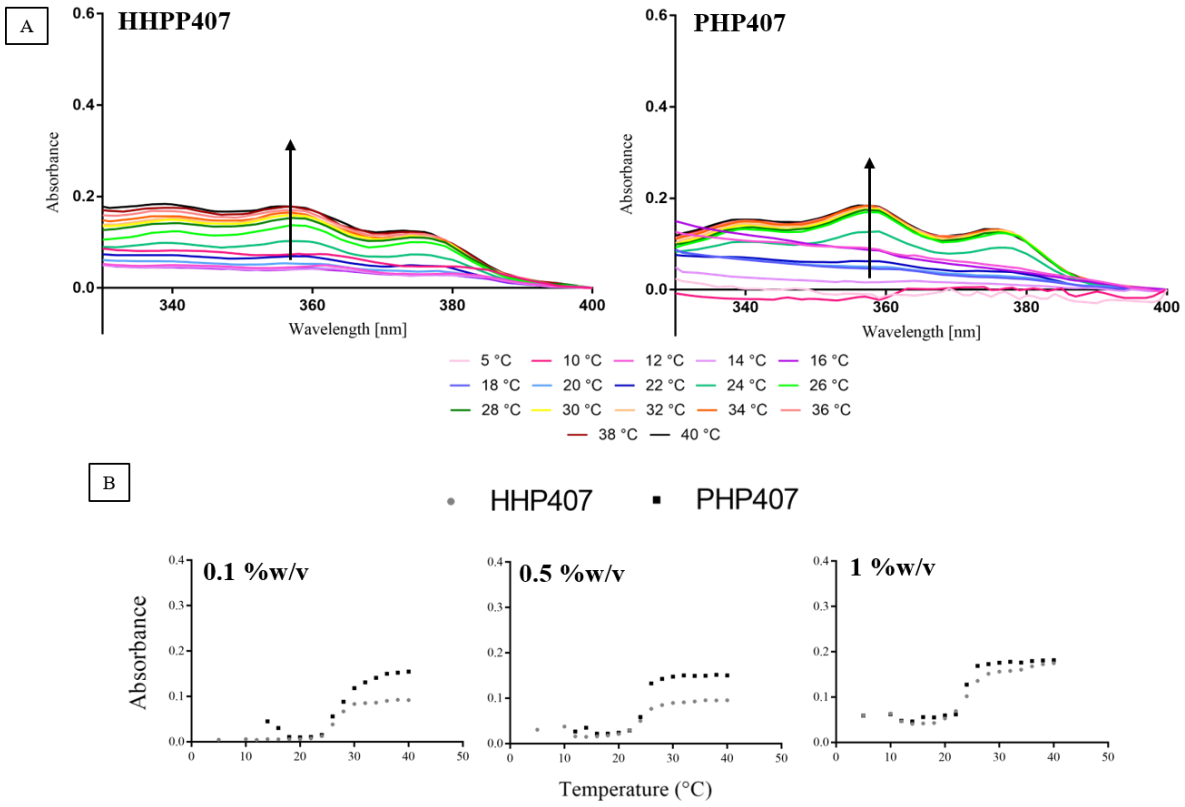

Figure 4.7 (A) UV−visible absorption spectra of DPH/HHP407 and DPH/PHP407 solutions (1 %w/v) at different temperatures (5-40 °C). The appearance of an absorption peak at 356nm (due to DPH solubilization into the hydrophobic micelle core) proved micelle formation. **(B)** Absorption intensity of DPH/HHP407 and DPH/PHP407 solutions (0.1, 0.5 and 1 %w/v concentration) at 356 nm as a function of temperature. CMT was defined as the temperature corresponding to the first inflection of the sigmoidal curve.

CMT values obtained for HHP407 and PHP407 solutions are listed in **Table 4.1** as a function of copolymer concentration. For both HHP407 and PHP407 solutions, the progressive increase

of polymer concentration caused a decrease of CMT. At the same polymer concentration, HHP407- and PHP407-based solutions showed the same CMT as NHP407-based solutions, in agreement with SEC results.

Table 4.1 CMT values obtained for HHP407- and PHP407-based solutions.

Concentration (%w/v)	Critical Micellar Temperature (°C)*	
	HHP407	PHP407
0.1	24	24
0.5	23	23
1	22	21

4.1.2. Thermo-sensitive Behavior Characterization

4.1.2.1. Tube Inverting Test

Figure 4.8 reports the sol-gel transition curves of HHP407- and PHP407-based sol-gel systems, compared to NHP407-based solutions. The sol-gel transition (gelation) temperatures and the critical gelation concentrations are reported in **Table 4.2** and **Table 4.3**, respectively.

HHP407- and PHP407-based solutions, as expected from their chemical and structural similarity, showed no significant differences in terms of LCGT values and CGC. Moreover, sol-gel systems based on the two newly synthesized PURs showed only slight differences with respect to the previously characterized compositions based on NHP407. In particular, they showed slightly lower LCGT values in agreement with their slightly lower molecular weight compared to NHP407. No differences were observed in terms of CGC value (6 ±1 % w/v).

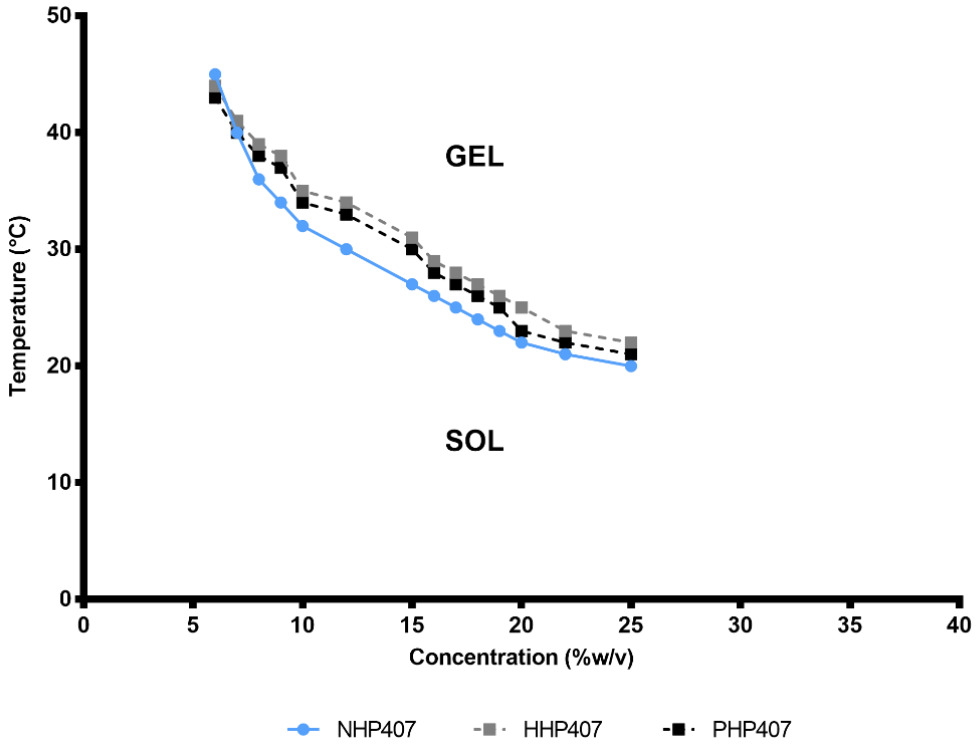

Figure 4.8 Sol-gel-sol transition curves for HHP407- and PHP407-based solutions in PBS compared to NHP407-based ones.

Table 4.2 Gelation Temperature for HHPP407- and PHP407-based solutions in PBS.

Concentration (%w/v)	**HHP407 Gelation Temperature (°C)**	**PHP407 Gelation Temperature (°C)**
7.5 %w/v	41±1 °C	40±1 °C
10 %w/v	35±1 °C	34±1 °C
12.5 %w/v	34±1 °C	33±1 °C
15 %w/v	31±1 °C	30±1 °C
17.5 %w/v	27±1 °C	26±1 °C
20 %w/v	25±1 °C	23±1 °C

Table 4.3 Critical Gelation Concentration for HHP407- and PHP407-based solutions in PBS.

Formulation	Critical Gelation Concentration (°C)
HHP407	6±1 °C
PHP407	6±1 °C

Gelation time at 37 °C of various HHP407- and PHP407-based aqueous solutions was also studied to evaluate hydrogel gelation potential in physiological conditions (**Figure 4.9**)

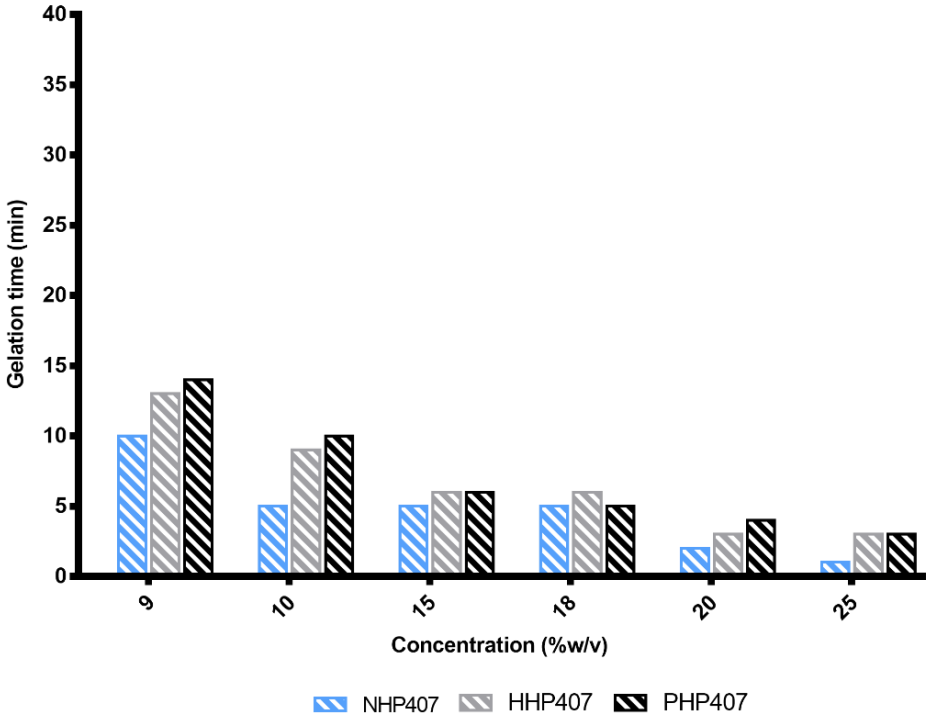

Figure 4.9 Gelation time at 37 °C of HHP407- and PHP407-based solutions, compared to NHP407-based ones.

HHP407- and PHP407-based solutions substantially showed the same gelation time in physiological conditions within the error range of ±1 minute. However, with respect to NHP407-based solutions, sol-gel systems based on the newly synthesized PURs showed a slightly slower gelation kinetics, in accordance with their lower molecular weight and tube inverting test results.

4.1.1.1. Rheology

Information about the gelation properties of HHP407- and PHP407-based solutions was obtained by means of LAOS, SAOS and temperature ramp tests, as previously reported.

The trends of storage modulus (G'), loss modulus (G'') and shear stress (τ) as a function of strain (γ) for HHP407-based and PHP407-based hydrogels at 10, 15 and 20 %w/v and 37 °C are reported in **Figure 4.10**. **Figure 4.11** reports the key parameters extracted from LAOS results (i.e., maximum strain and shear within the linear viscoelastic (LVE) region, initial G' and G'' values and their offset, maximum G'' value, its offset with respect to the initial value and yield stress).

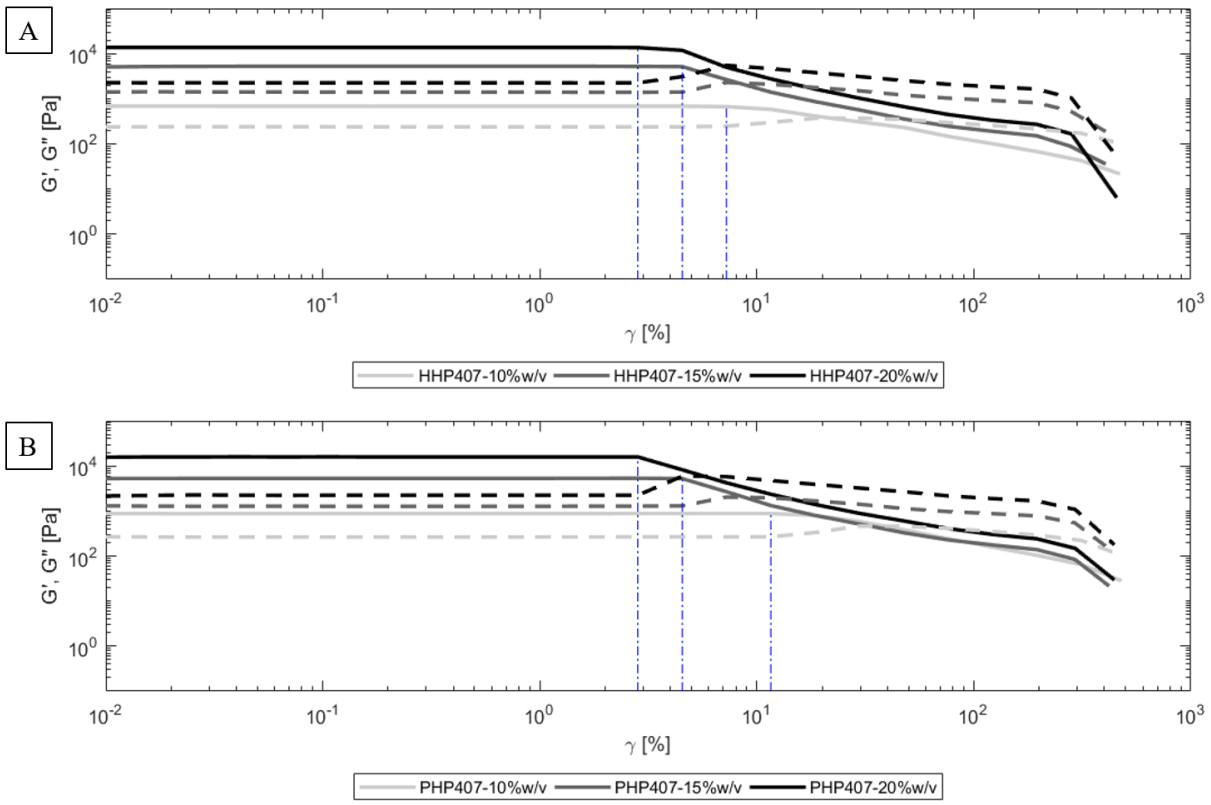

Figure 4.10 LAOS test: G', G'' and τ *versus* strain at 37 °C. Comparison between **(A)** HHP407- and **(B)** PHP407-based sol-gel systems at 10, 15 and 20 %w/v (solid line: G', dashed lines: G'', dotted lines: τ). The blue dash-dotted lines identify the linear viscoelastic region.

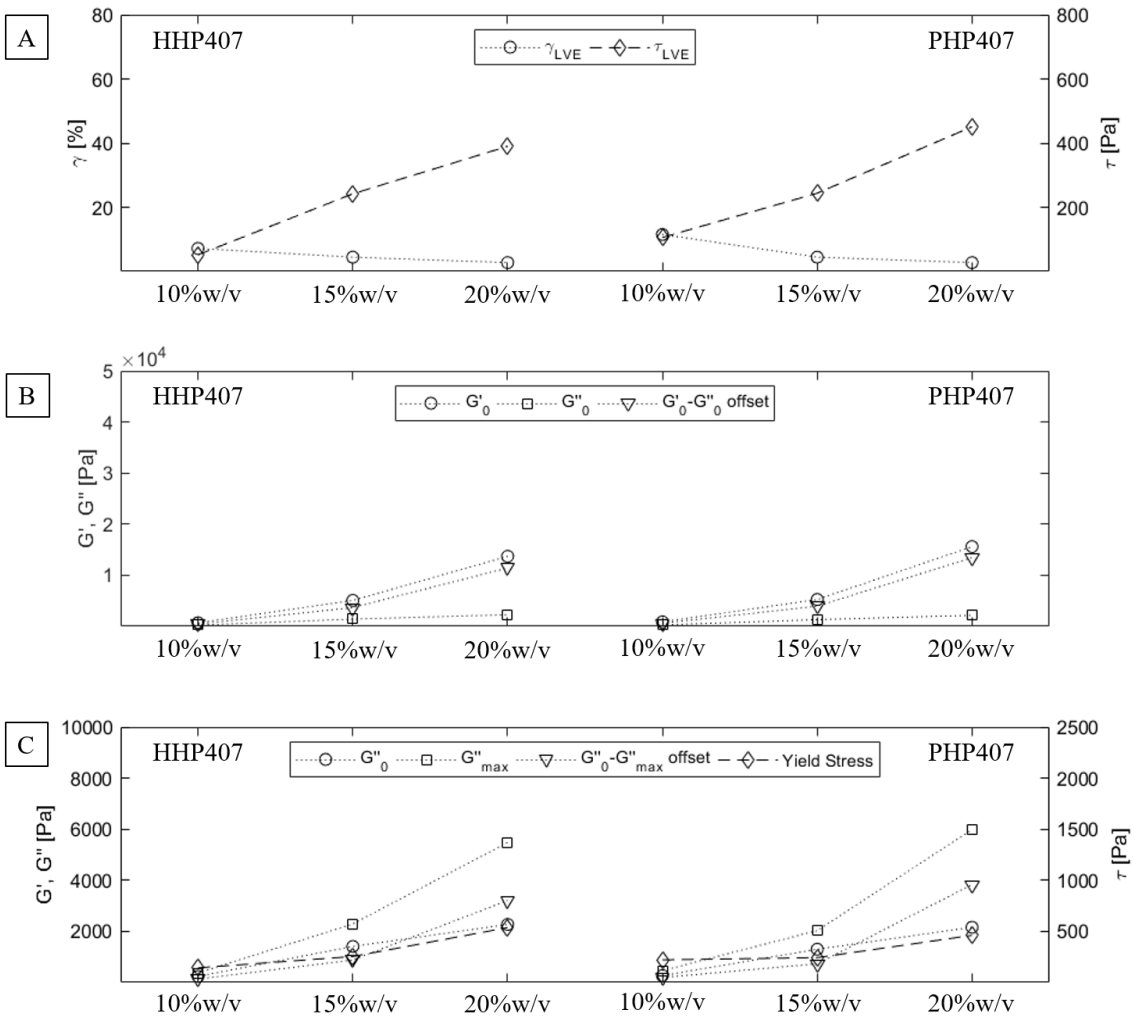

Figure 4.11 LAOS main parameters for HHP407- and PHP407-based sol-gel systems at 10, 15 and 20 %w/v concentration. **(A)** Maximum strain and shear stress within the LVE region. **(B)** Initial G' and G'' values and their offset. **(C)** Initial and maximum G'' values, their offset and yield stress.

Both PUR-solutions showed decreased resistance to deformation (LVE region) with increasing concentration and substantially the same LVE extension, with the exception of the formulation at 10 %w/v PUR concentration (**Figure 4.10** and **Figure 4.11 A**).

HHP407- and PHP407-based solutions also showed higher G' and G'' values as well as their offset with increasing polymer concentration (**Figure 4.11 B**). A similar trend was observed for G'' maximum value and its offset with respect to its initial value as well as for gel yield stress (**Figure 4.11 C**). By comparing the two PURs, the previously mentioned parameters exhibited

a slightly higher value in PHP407-based sol-gel systems with 20 %w/v concentration compared to HHP407-based ones with the same composition.

Figure 4.12 and **Figure 4.13** report results from LAOS tests carried out on NHP407-, HHP407- and PHP407-based hydrogels at 15 %w/v and 37 °C.

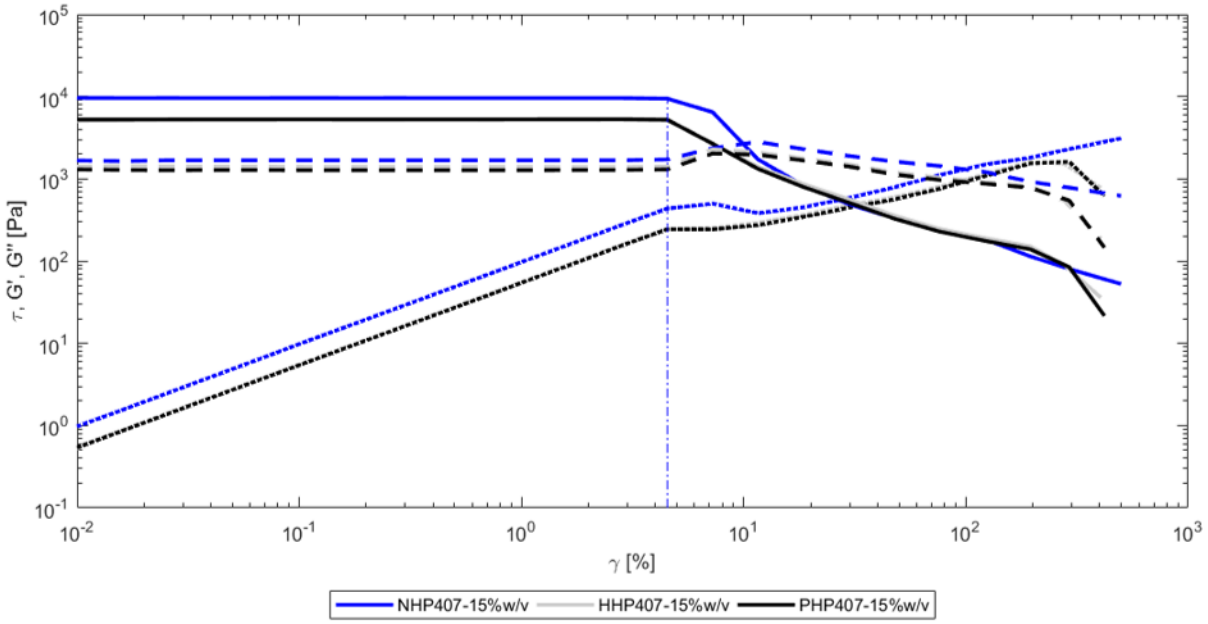

Figure 4.12 LAOS test: G', G'' and τ versus strain at 37 °C. Comparison between NHP407-, HHP407- and PHP407-based hydrogels 15 %w/v (solid line: G', dashed lines: G'', dotted lines: τ). The blue dash-dotted lines identify the linear viscoelastic region.

All the PUR-based sol-gel systems show similar properties in terms of LVE region extension (**Figure 4.12** and **Figure 4.13 A**). However, NHP407-based samples showed higher G' and G'' values, higher G'-G'' offset as well as higher G'' maximum value and higher offset between it and its initial value (**Figure 4.13 B** and **Figure 4.13 C**). These results further confirmed the slight superiority of NHP407-based hydrogels in terms of gelation properties, as a consequence of its slightly higher molecular weight compared to HHP407 and PHP407.

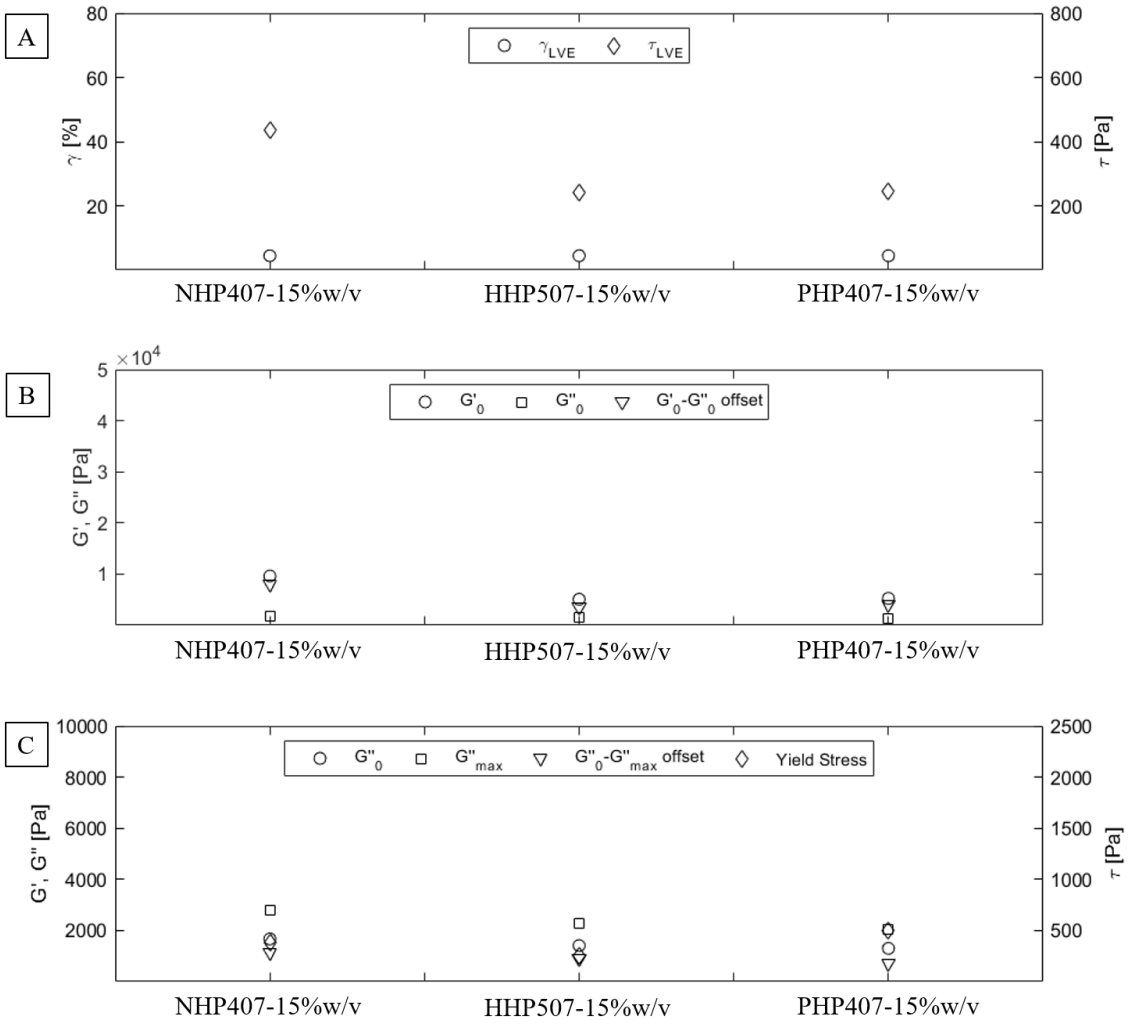

Figure 4.13 LAOS main parameters for NHP407-, HHP407- and PHP407-based hydrogels at 15 %w/v. **(A)** Maximum strain and shear within the LVE region. **(B)** Initial G' and G'' values and their offset. **(C)** Initial and maximum G'' values, their offset and yield stress.

Concerning SAOS tests, the trends of G', G'' and complex viscosity as a function of angular frequency of HHP407- and PHP407-based hydrogels at 10, 15 and 20 %w/v and 37 °C are reported in **Figure 4.14**.

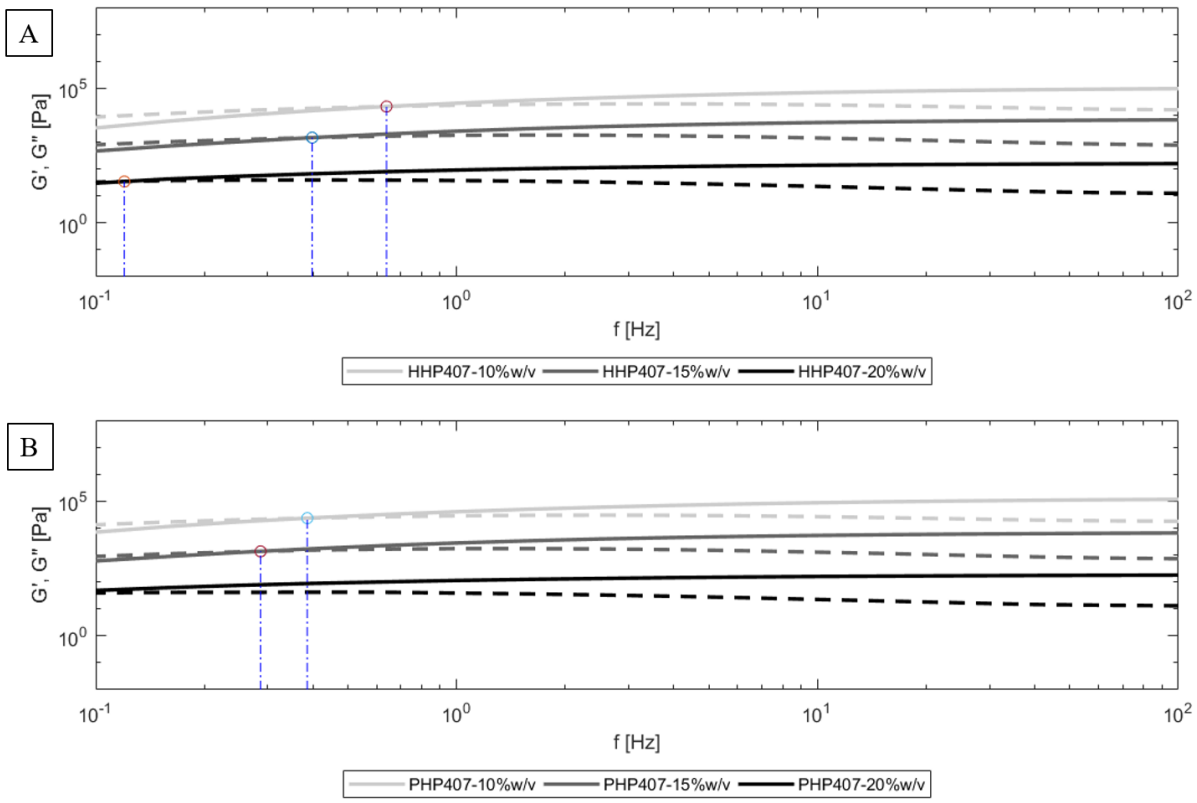

Figure 4.14 SAOS test: G', G'' and complex viscosity *versus* angular frequency at 37 °C. Comparison between **(A)** HHP407- and **(B)** PHP407-based gels at 10, 15 and 20 %w/v (solid line: G', dashed lines: G'', dotted lines: complex η; PUR-10%w/v: light grey -shifted $x10^2$-, PUR-15%w/v: grey, PUR-20%w/v: black -shifted $x10^{-2}$-). The dash-dotted blue lines identify G'-G'' crossover.

For both the PURs, with increasing PUR concentration the $f_{crossover}$ decreased. This phenomenon, already assessed on NHP407-based hydrogels, suggested that the gelation process turned more efficient with increasing PUR content in the formulation.

Figure 4.15 summarizes the key parameters extracted from SAOS results obtained at 37 °C (i.e., angular frequency at G'-G'' crossover at different PUR concentrations, G'-G'' offset at different angular frequencies).

HHP407- and PHP407-based sol-gel systems showed substantially the same thermo-responsive gelation properties in term of $f_{crossover}$ (**Figure 4.15 A**) and G'-G'' offset (**Figure 4.15 B**).

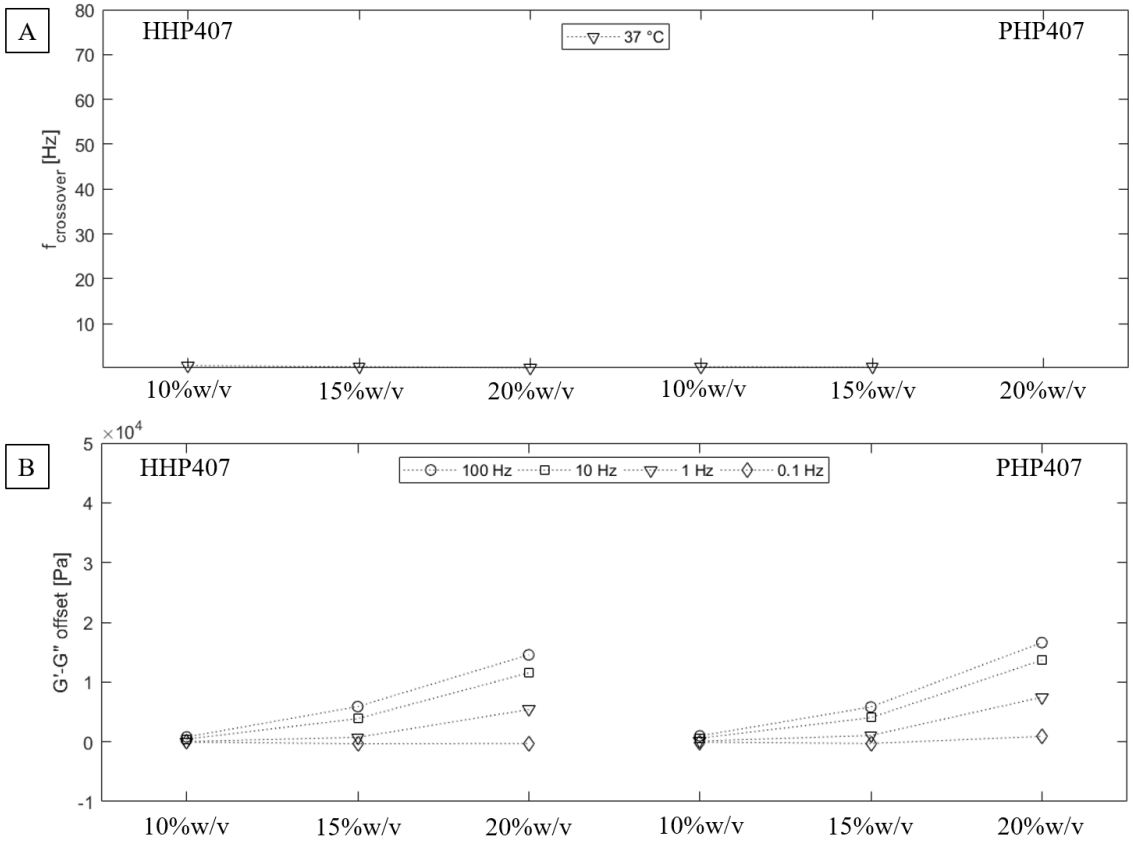

Figure 4.15 SAOS main parameters for HHP407- and PHP407-based sol-gel systems at 10, 15 and 20 %w/v, and 37 °C. **(A)** f at G'-G'' crossover. **(B)** G'-G'' offset of the different investigated formulations at 0.1, 1, 10 and 100 Hz.

Figure 4.16 and **Figure 4.17** show the SAOS results and the extracted characteristic parameters for NHP407-, HHP407- and PHP407-based sol-gel systems at 15 %w/v and 37 °C.

NHP407-based hydrogels showed lower $f_{crossover}$ compared to HHP407- and PHP407-based samples (**Figure 4.16** and **Figure 4.17 A**) as well as higher G'-G'' offset values (**Figure 4.17 B**). These results are in accordance with the previously reported data, showing NHP407-based formulations owning better gelation properties.

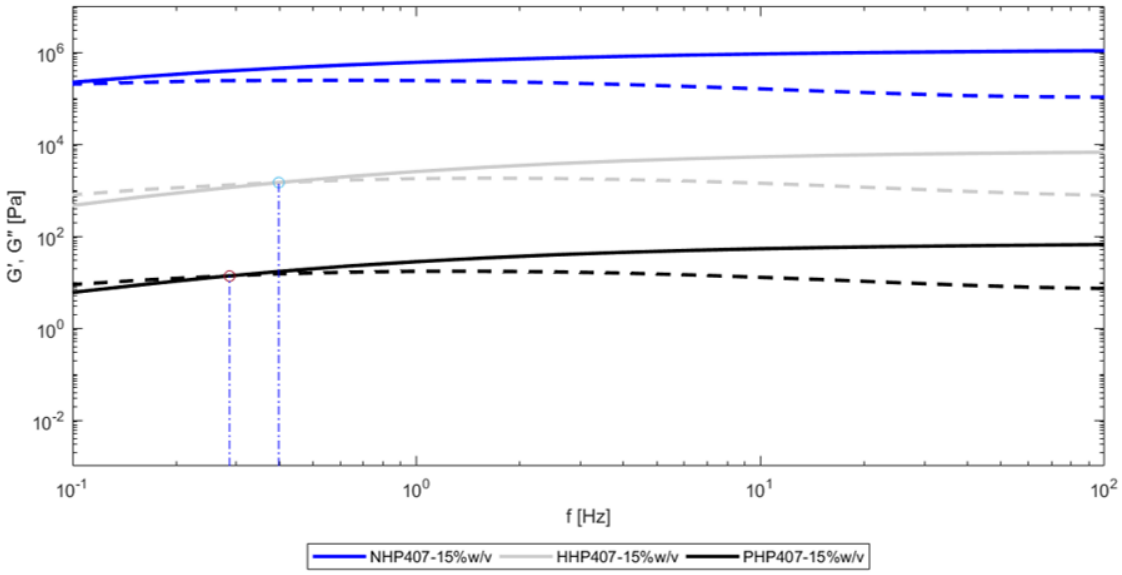

Figure 4.16 SAOS test: G', G'' and complex viscosity *versus* frequency at 37 °C. Comparison between NHP407-, HHP407- and PHP407-based hydrogels at 15 %w/v concentration and 37 °C (solid line: G', dashed lines: G'', dotted lines: complex η; NHP407-15%w/v: blue -shifted x10^{2}-, HHP407-15%w/v: light grey, PHP407-15%w/v: black -shifted x10^{-2}-). The blue dash-dotted lines identify the G'-G'' crossover.

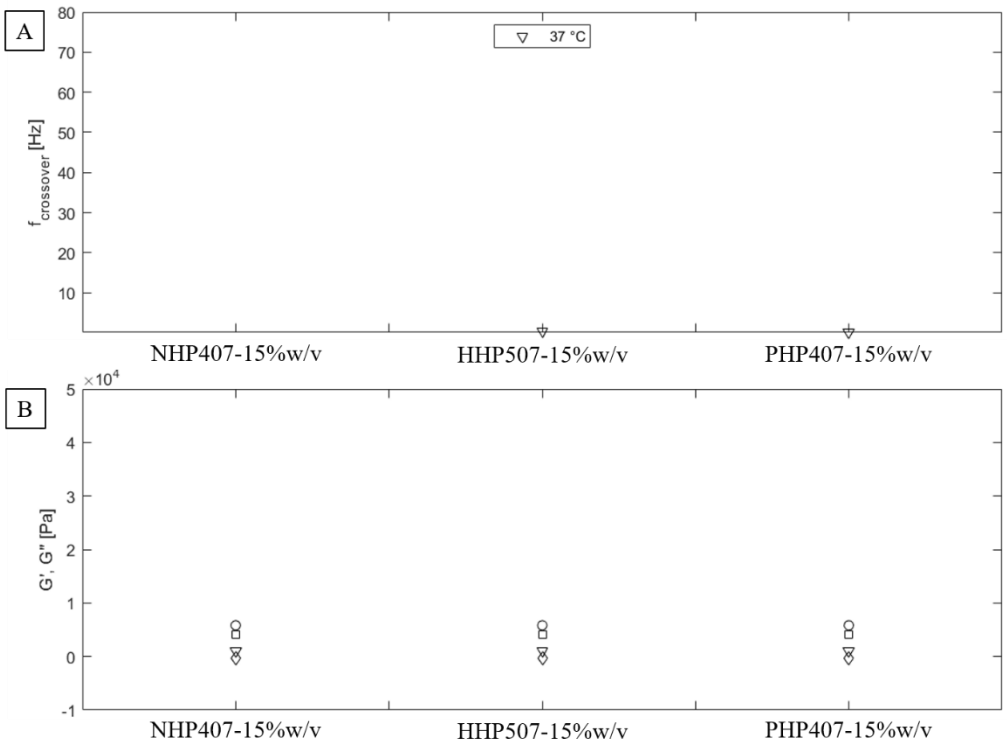

Figure 4.17 SAOS characteristic parameters for NHP407-, HHP407- and PHP407-based systems at 15 %w/v concentration and 37 °C. **(A)** f at G'-G'' crossover. **(B)** G'-G'' offset at 0.1, 1, 10 and 100 Hz.

The trend of viscosity (η) as a function of temperature during the sol-to-gel transition of HHP407- and PHP407-based solutions at 10, 15 and 20 %w/v is reported in **Figure 4.18**. All the analyzed concentrations showed a similar trend of the viscosity. In accordance with previously reported data, viscosity initially decreased as a function of temperature, as typical of fluid systems, and finally reached a minimum value (at T_{onset}); then, it started to increase until a maximum before decreasing again due to gel melt fracture.

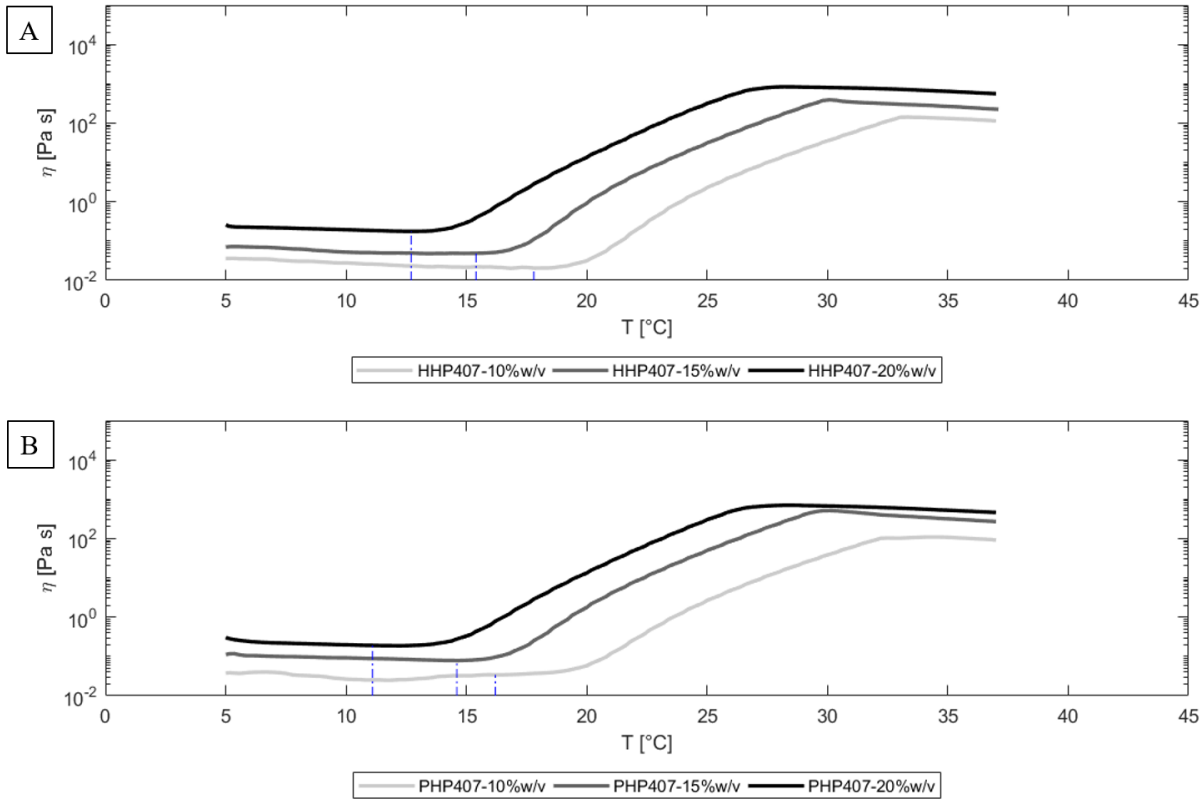

Figure 4.18 Temperature ramp test: viscosity *versus* temperature during the temperature-driven sol-to-gel transition. Comparison between **(A)** HHP407- and **(B)** PHP407-based sol-gel systems at 10, 15 and 20 %w/v concentration. The dash-dotted blue lines identify T_{onset}.

Figure 4.19 reports the values of the main parameters extracted from temperature ramp test results (i.e., T_{onset}, viscosities at different temperatures -5, 10, 15, 20, 25, 30, 35 °C-).

HHP407- and PHP407-based hydrogels exhibited lower T_{onset} with increasing PUR concentration (**Figure 4.18** and **Figure 4.19 A**). Moreover, as expected, viscosity increased with increasing PUR concentration (**Figure 4.18** and **Figure 4.19 B**). Being PUR concentration the same, no differences were observed between hydrogels prepared starting from the two investigated PURs, in accordance with results previously discussed.

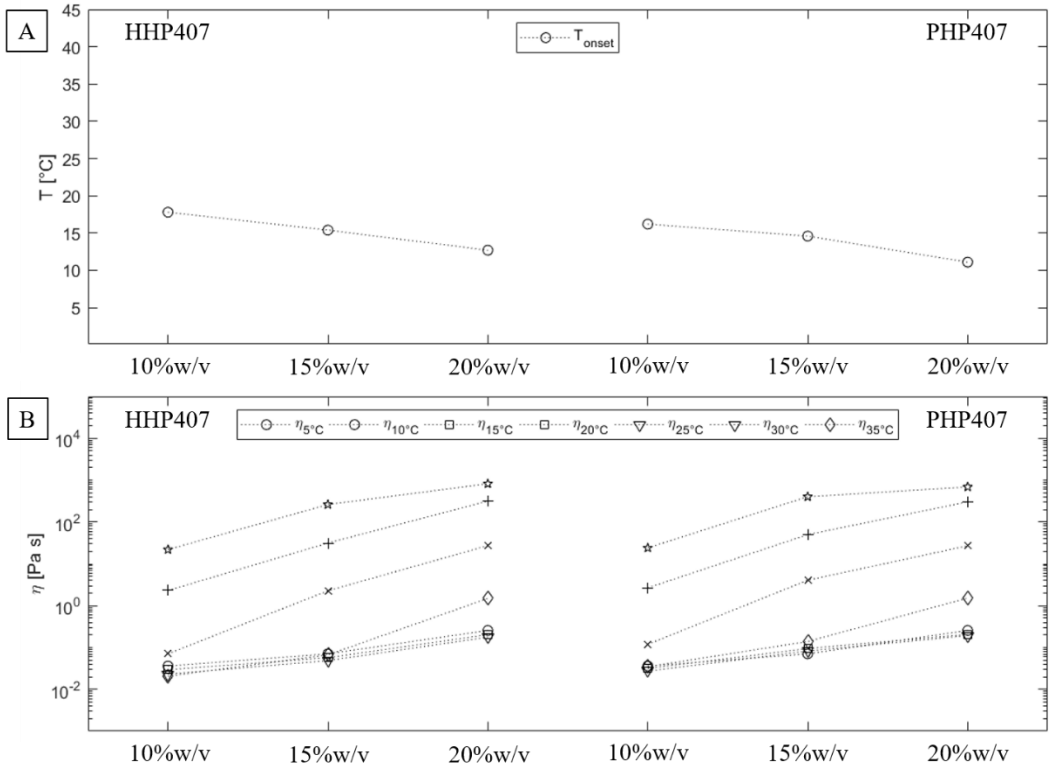

Figure 4.19 Characteristic parameters extracted from temperature-ramp test results for HHP407- and PHP407-based hydrogels at 10, 15 and 20 %w/v concentration. **(A)** T_{onset}, **(B)** viscosities at different temperatures (5, 10, 15, 20, 25, 30, 35 °C).

Figure 4.20 and **Figure 4.21** compare hydrogels prepared from HHP407 and PHP407 (15 %w/v concentration) with the previously designed sol-gel systems based on NHP407 at the same PUR concentration.

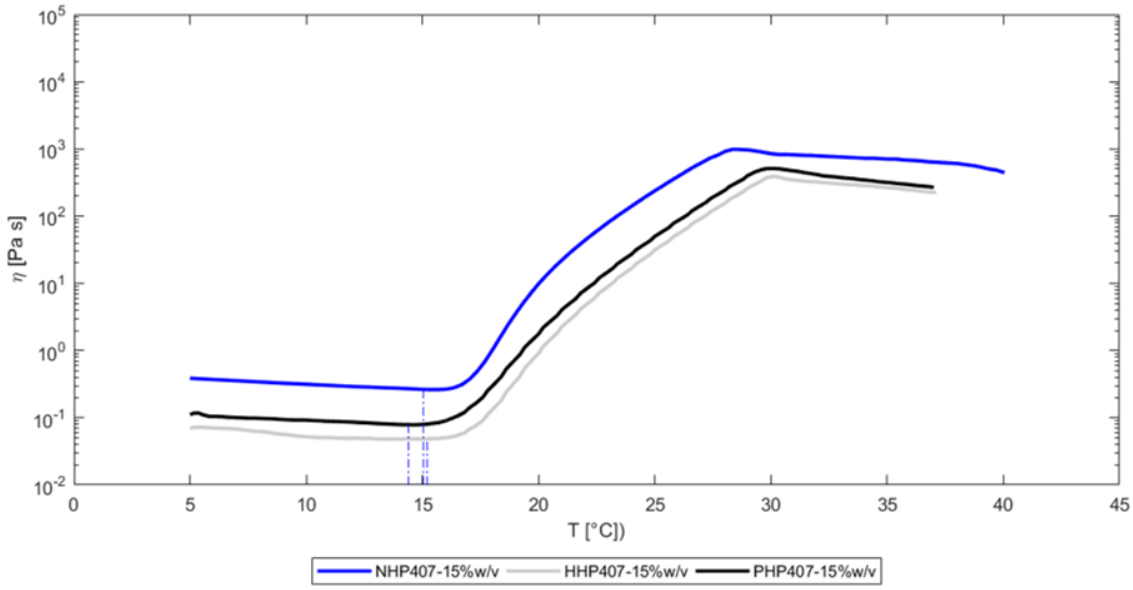

Figure 4.20 Temperature ramp test: viscosity *versus* temperature during the temperature-driven sol-to-gel transition. Comparison between NHP407-, HHP407- and PHP407-based solutions at 15 %w/v concentration. The dash-dotted blue lines identify the T_{onset}.

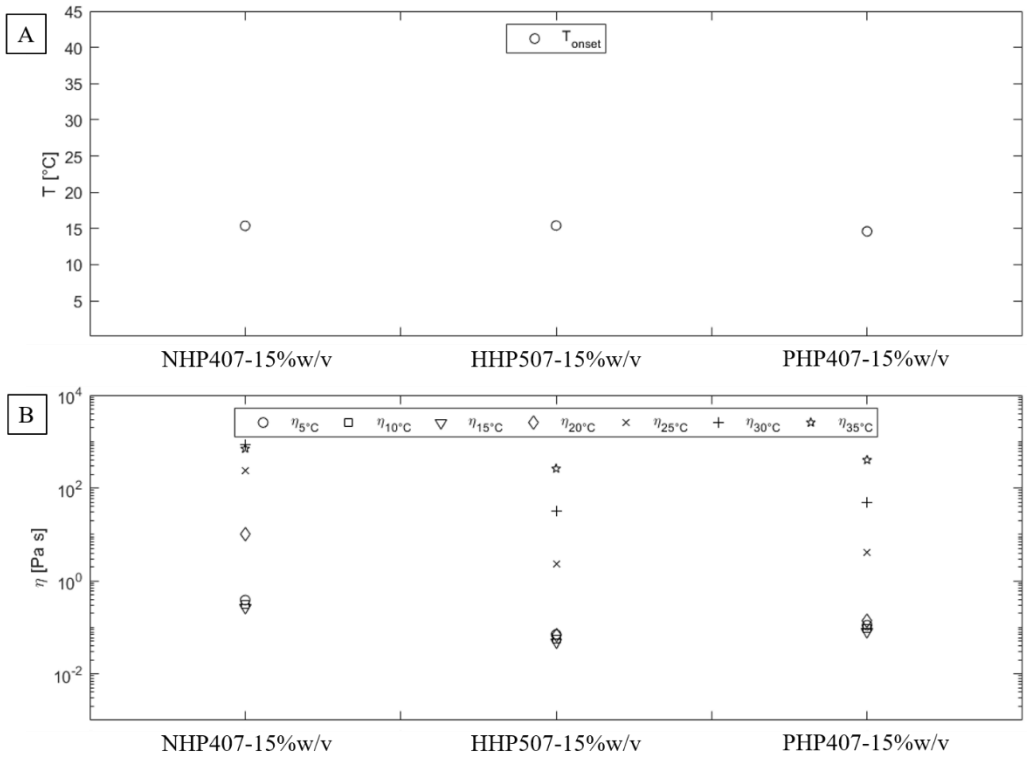

Figure 4.21 Main parameters extracted from temperature ramp tests resulted: **(A)** T_{onset}, **(B)** viscosities at different temperatures (5, 10, 15, 20, 25, 30, 35 °C) of NHP407-, HHP407- and PHP407-based samples at 15 %w/v concentration.

All the formulations based on the three different PURs showed a similar trend of viscosity *versus* temperature. T_{onset} values were approximately the same for all the formulations (**Figure 4.20** and **Figure 4.21 A**); however, viscosity of NHP407-based sol-gel system was higher compared to that of the other analyzed formulations, in accordance with SEC results (**Figure 4.20** and **Figure 4.21 B**). In fact, thanks to the higher molecular weight of NHP407, the resultant hydrogels are expecting to be more stable and elastic.

4.1.2. Hydrogel Injectability and Printability

Injectability of HHP407- and PHP407-based hydrogels (10, 15 and 20 %w/v concentration) through 0.20 and 0.25 mm internal diameter needles was demonstrated in the same conditions as for NHP407-based hydrogels except for the 20 %w/v concentrated hydrogels (**Table 4.4**).

Table 4.4 HHP407- and PHP407-based solutions injectability tests.

T	**HHP407 10%w/v**		**HHP407 15%w/v**		**HHP407 20%w/v**	
	0.20 mm	0.25 mm	0.20 mm	0.25 mm	0.20 mm	0.25 mm
5 °C	✓	✓	✓	✓	✓	✓
25 °C	✓	✓	✓	✓	✗	✓
37 °C	✓	✓	✓	✓	✗	✗
T	**PHP407 10%w/v**		**PHP407 15%w/v**		**PHP407 20%w/v**	
	0.20 mm	0.25 mm	0.20 mm	0.25 mm	0.20 mm	0.25 mm
5 °C	✓	✓	✓	✓	✓	✓
25 °C	✓	✓	✓	✓	✗	✓
37 °C	✓	✓	✓	✓	✗	✗

4.1.3. Photo-sensitive Behavior Characterization

4.1.3.1. Photo-rheology

Photo-rheological tests were performed to evaluate the kinetics of gel photopolymerization induced by exposure to UV light. The graph in **Figure 4.22** reports the trend of storage modulus (G') as a function of time of PHP407 and HHP407 formulations at 10, 15 and 20 %w/v PUR concentration. Initially the samples were equilibrated at 37 °C for 5 min, then G' value for registered for a total of 3 minutes divided in three steps: 1 minute before UV light irradiation + 1 minute of light irradiation + 1 minute after light switching off.

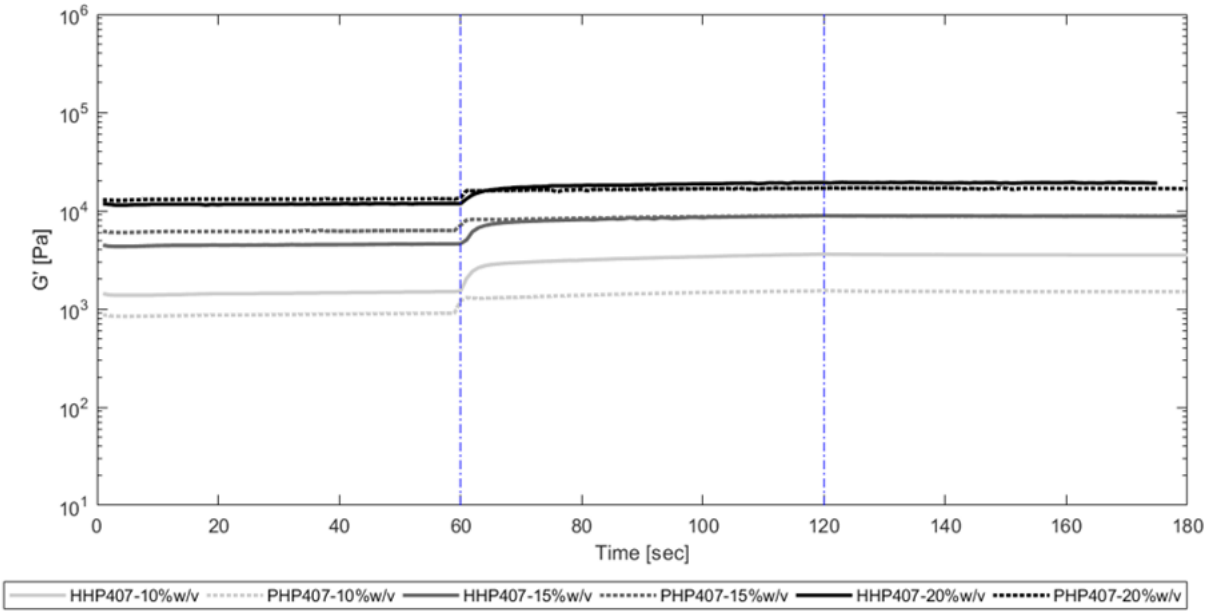

Figure 4.22 Photo-rheology tests of HHP407- and PHP407-based sol-gel systems at 10, 15 and 20 %w/v concentration. The dash-dotted blue lines identify the test steps: at 60 seconds the UV source is turned on, while at 120 seconds the UV source is turned off.

These three steps were clearly visible by analyzing the obtained curves. Initially (UV source off) G' values remained constant, meaning that the samples were in a quiescent state with no ongoing transitions. Immediately after irradiation beginning, G' values increased as a

consequence of hydrogel photopolymerization and the creation of inter-micelles cross-links; then, G' trend progressively reached a plateau when all the available crosslinking sites were reacted. When eventually UV lamp was turned off again the G' values remained constant, highlighting the irreversibility of the photo-crosslinking reaction.

Figure 4.23 summarizes the key parameters extracted from photo-rheological characterization (i.e., initial G' and maximum G' values upon crosslinking, and their offset). The higher the G'_0-$G'_{crosslinked}$ offset value is the higher is the crosslinking degree of the hydrogels. Based on PUR chemistry and on their similarity in molecular weight, the higher number of acrylate moieties within PHP407 was expected to create hydrogels with a more efficient photo-responsive behaviour. On the contrary, HHP407-based sol-gel systems showed higher G'_0-$G'_{crosslinked}$ offset compared to PHP407-based ones. In fact, although the acrylic moieties in HHP407 chains are less numerous, the photocrosslinking step turned out to be more efficient in HHP407-based hydrogels compared to PHP407-based ones. This phenomenon can be probably attributed to the steric hindrance of the triple acrylic moieties that end-cap PHP407 chains. Furthermore, acrylic groups are normally more reactive with respect the methacrylic ones.[20]

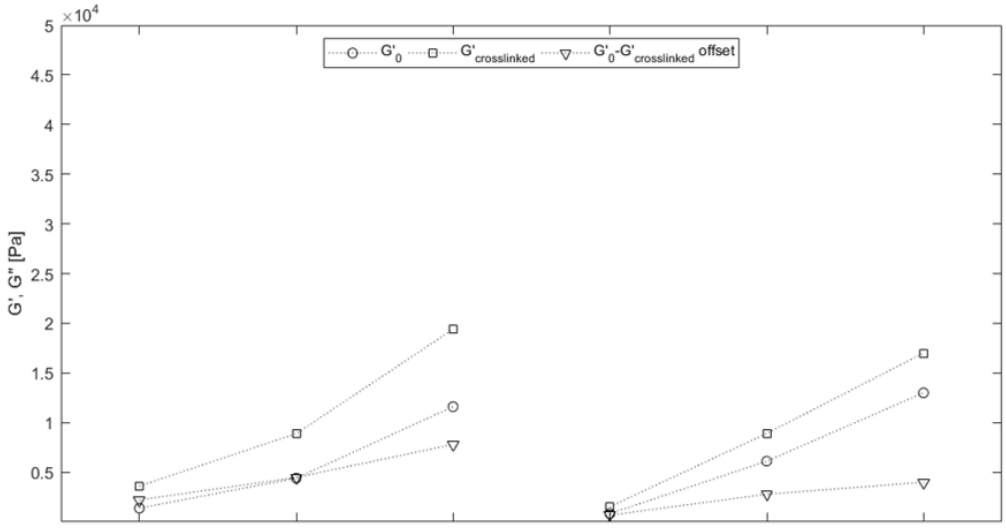

Figure 4.23 Trend of the offset between the initial value of G' at its value upon crosslinking for HHP407- and PHP407-based solutions at 10, 15 and 20 %w/v.

4.1.4. Hydrogel Swelling and Stability

Stability tests were performed on circular shaped gels obtained as previously described (**Figure 4.24**) to evaluate their behavior in aqueous environment and their ability to swell absorbing the surrounding medium (PBS). A comparison between the behavior of the gels obtained only through thermal gelation and the photo-crosslinked ones was also performed to assess the capability of photo-curing to effectively enhance hydrogel stability in aqueous environment.

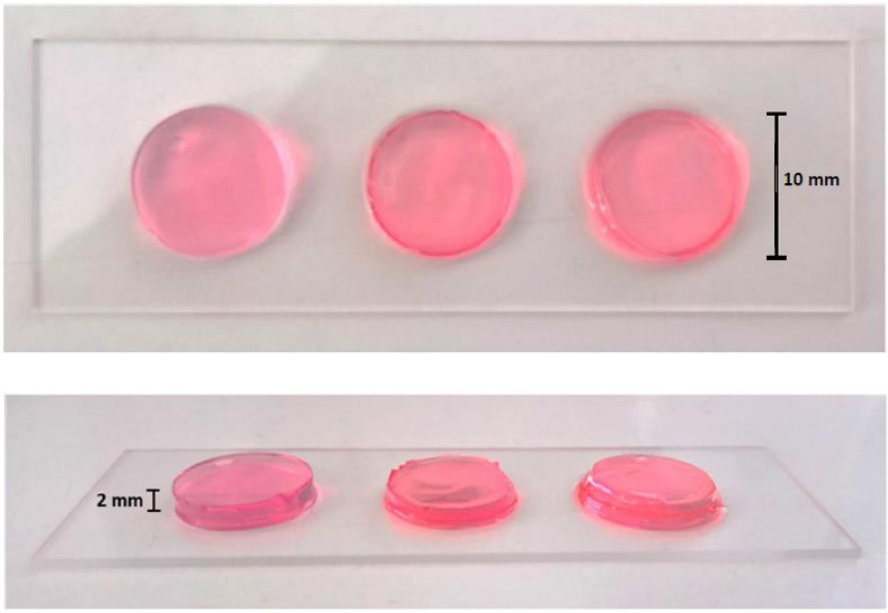

Figure 4.24 Examples of hydrogels obtained through photo-polymerization and colored with Direct Red 80. The diameter and height of the circular shaped samples were approximately 10 and 2 mm, respectively.

The ability of the two different types of photo-crosslinked hydrogels to absorb an aqueous medium as well as their stability in aqueous medium were evaluated using **Equation 1** and **Equation 2**. Results are reported in **Figure 4.25 A** and **Figure 4.25 B**.

For HHP407-based gels, an increase in the sample weight (i.e., absorption of PBS) was detectable from 15 minutes up to 1-3 days. Whereupon, HHP407-based hydrogels showed a stabilization in the sample weight, suggesting the achievement of an equilibrium, until 1 month.

However, after 56 incubation in aqueous media, HHP407-based hydrogels showed a decrease in sample weight with a great variability (**Figure 4.25 A**). On the other hand, PHP407-based hydrogels showed similar sample weight until day 1, followed by a decrease in weight, reaching the 100 % reduction in weight after 3 weeks.

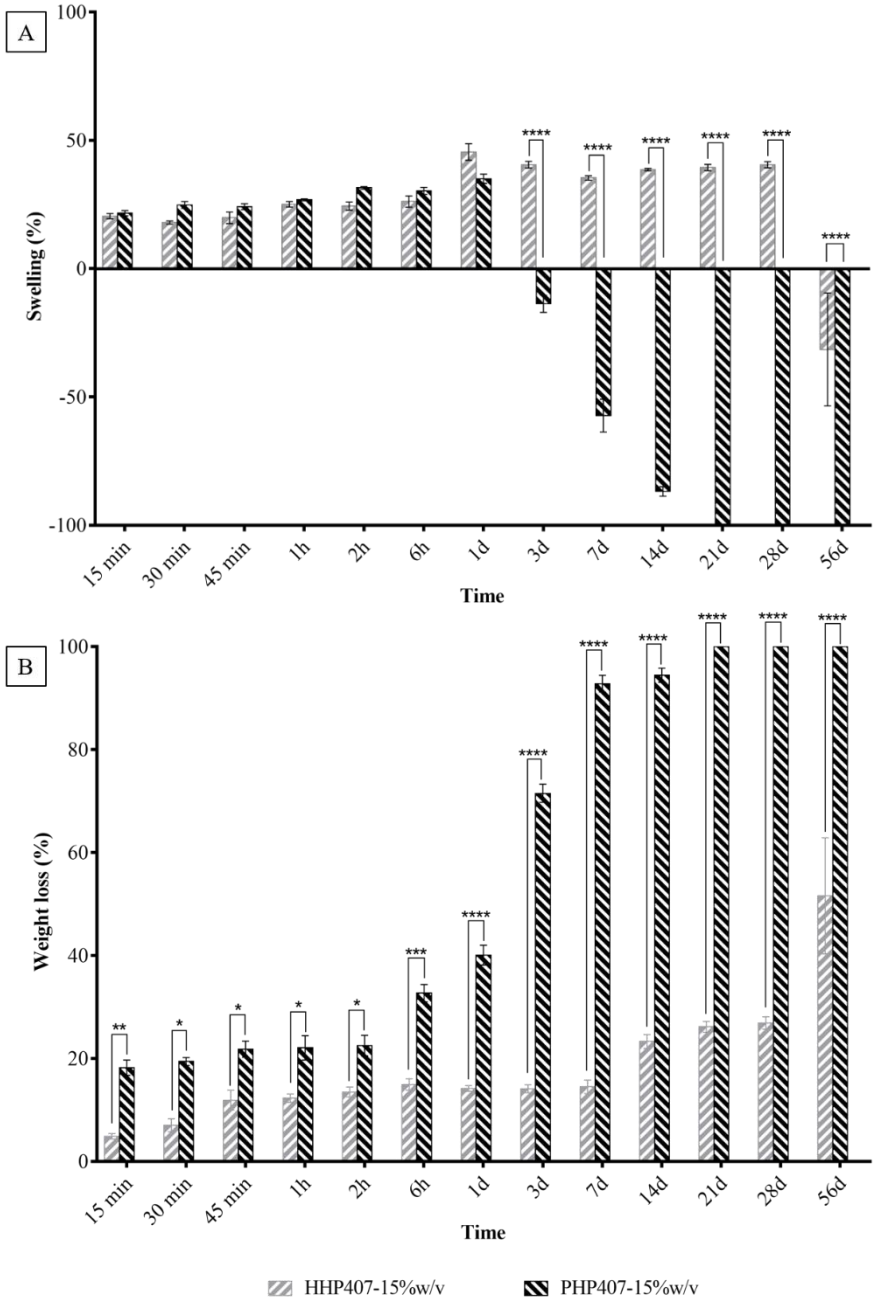

Figure 4.25 HHP407- and PHP407-based hydrogel at 15 %w/v concentration: **(A)** PBS absorption and **(B)** weight loss (dissolution/degradation).

Concerning PUR weight loss, HHP407-based hydrogel weight loss increased up to 56 days incubation time, when the instability, already detected from swelling data, became evident (**Figure 4.25 B**). On the other hand, PHP407-based hydrogels were completely dissolved after 14 days incubation in aqueous environment. This behavior probably results from the lower efficacy of the photo-crosslinking process of PHP407-based sol-gel systems with respect to HHP407-based ones, as already observed through photo-rheology. In fact, for PHP407-based hydrogels, the solubilization of the samples became prevalent over PBS absorption after 3 days incubation, thus resulting in negative percentages of swelling and in a significant increase in weight loss compared to HHP407-based hydrogels with the same composition.

Contrary to our first hypothesis, the presence of a larger number of acrylic groups did result in a higher degree of crosslinking, probably because the three terminal acrylate groups create a steric hindrance between themselves, thus reducing the effectiveness of the photo-curing step.

Figure 4.26 and **Figure 4.27** compare PBS absorption and stability in aqueous environment of photo-crosslinked (gel network resulting from the thermally driven sol-to-gel transition followed by stabilization through UV crosslinking) and not-photo-crosslinked (gel network resulting from the thermally driven sol-to-gel transition) HHP407- and PHP407-based hydrogels.

These results further proved the enhanced effect of the photo-crosslinking process on HHP407-based hydrogels (**Figure 4.26 A** and **Figure 4.27 A**) with respect to PHP407-based ones (**Figure 4.26 B** and **Figure 4.27 B**).

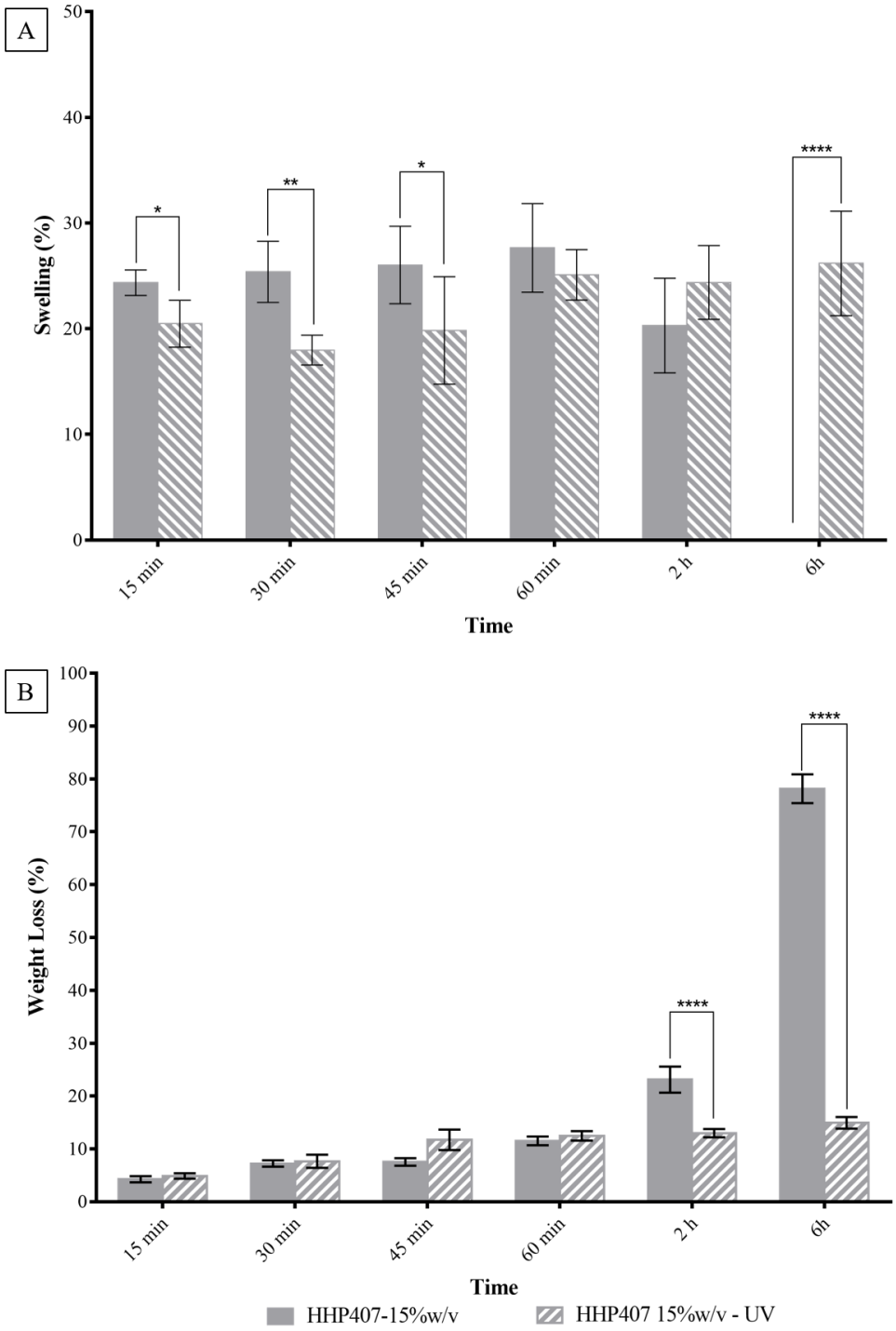

Figure 4.26 PBS absorption of photo-crosslinked (gel network resulting from the thermally driven sol-to-gel transition followed by stabilization through UV crosslinking) and not-photo-crosslinked (gel network resulting from the thermally driven sol-to-gel transition) **(A)** HHP407- and **(B)** PHP407-based hydrogels at 15 %w/v concentration.

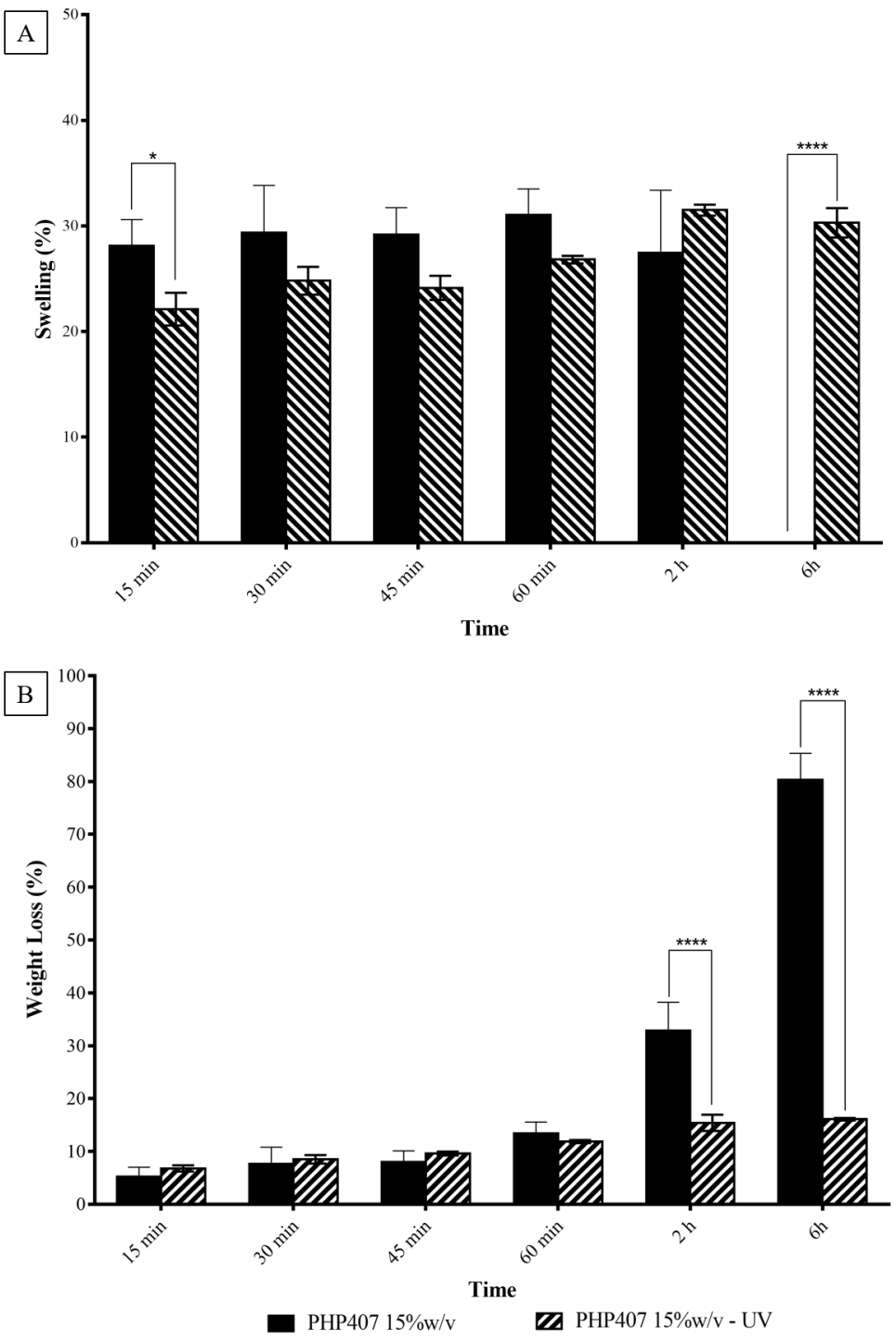

Figure 4.27 Weight loss (dissolution/degradation) of photo-crosslinked (gel network resulting from the thermally driven sol-to-gel transition followed by stabilization through UV crosslinking) and not-photo-crosslinked (gel network resulting from the thermally driven sol-to-gel transition) **(A)** HHP407- and **(B)** PHP407-based hydrogels at 15 %w/v concentration.

The photo-crosslinking process prolonged the life of the samples from a few hours to 1-3 days, when solubilization became prevalent leading to a complete dissolution of UV-treated PHP407 gels within 1 week incubation in PBS (**Figure 4.26 B** and **Figure 4.27 B**).

On the other hand, for HHP407-based gels, the photo-crosslinking process clearly affected the stability of the samples in aqueous environment: as for PHP407, thermosensitive hydrogels (not-UV cured samples) completely destabilized after a few hours of incubation in PBS, while, as already demonstrated, the photo-crosslinked samples were still present after 56 days incubation.

4.1.5. Hydrogel Permeability

Permeability tests to FD4, a model molecule of nutrients, were performed on the previously described circular-shaped UV-cured gels to demonstrate their ability to absorb nutrients from the surrounding environment.

Figure 4.28 shows the change in color of the samples prepared starting from HHP407 and PHP407, and incubated in a FD4 solution at 37 °C for different time intervals. The samples, initially transparent, turned out to be able to retain FD4 molecules becoming yellowish.

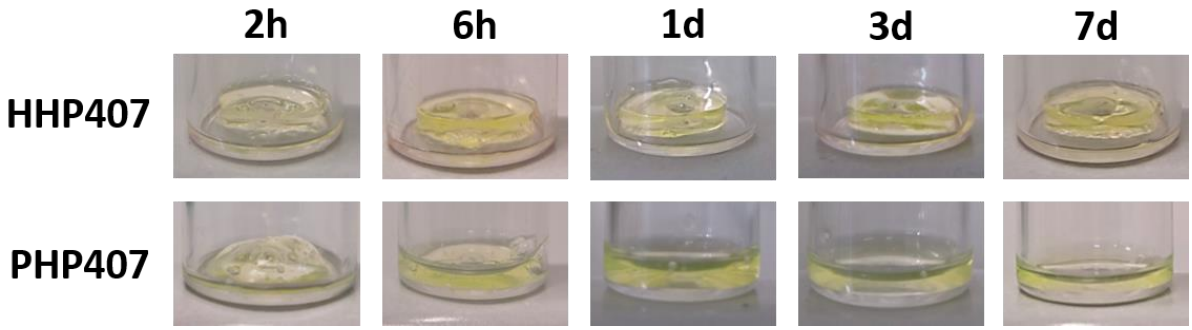

Figure 4.28 Samples of HHP407- and PHP407-based hydrogels with 15 %w/v PUR concentration in a FD4 solution for different time intervals. The yellow color indicates the absorption of the fluorescent molecule.

To quantify the molecule absorbed by the hydrogels, an UV measurement was performed at 490 nm (main absorption peak of FD4) after every time point considered. The quantification of the absorbed FD4 was not cumulative and indirectly obtained by measuring the amount of FD4 still present in the incubation solution at each analyzed time point. Results are reported in **Figure 4.29**.

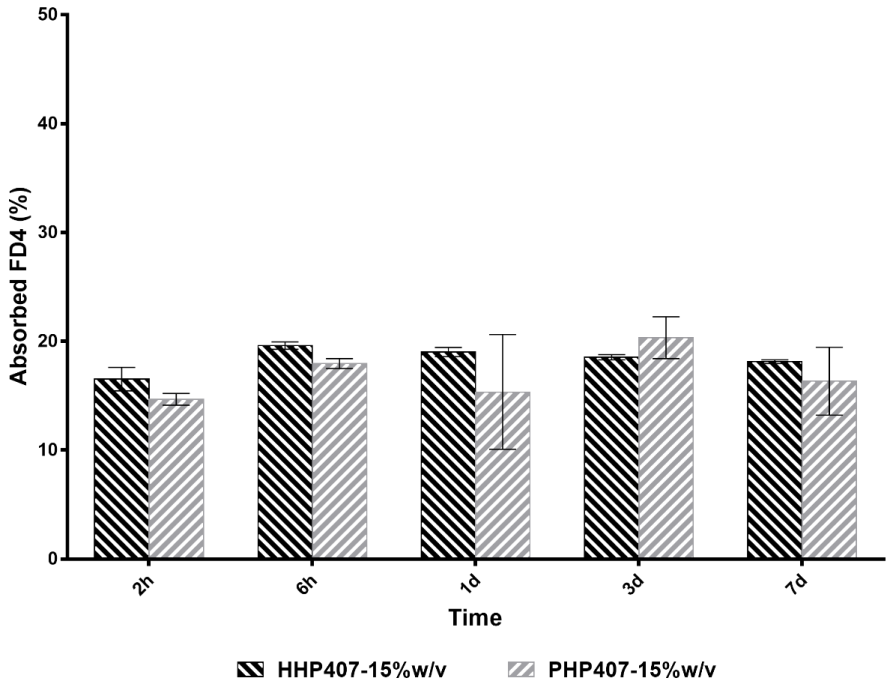

Figure 4.29 Percentage of FD4 absorbed by the HHP407- and PHP407-based hydrogels over time.

For all the tested hydrogels, the percentage of absorbed FD4 reached a value around 20% after 6h incubation and remained approximately stable until 7 days. For HHP407-based hydrogels, a continuous exchange of FD4 between the hydrogel and the medium can be hypothesized, in accordance with previously reported results on the stability of the gels in aqueous medium. On the other hand, as previously demonstrated, for PHP407-based hydrogels solubilization overcame swelling phenomena after 1d incubation. For this reason, it was not possible to correctly define the kinetics of molecule exchange for these gels for the longest time points

analyzed. To evaluate the ability of the hydrogels to release biomolecules, cell waste products and drugs, a qualitative test was also performed. In this case, it was not possible to measure the amount of FD4 released because during UV-curing the aromatic rings of fluorescein interacted with the applied UV irradiation, resulting in changes in its absorption spectrum, as confirmed also by the observed changes in the color of the samples. However, the capability of the gels to release the encapsulated colored molecule was evident from the yellowish color assumed by the incubation medium (PBS) (**Figure 4.30**).

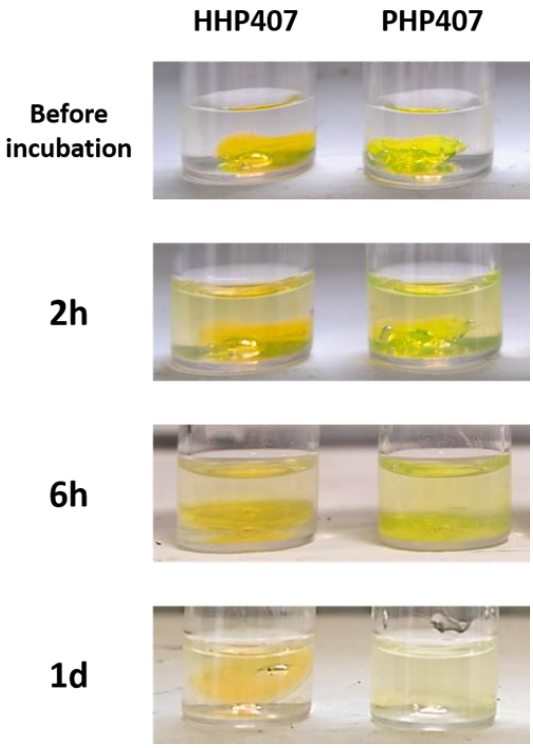

Figure 4.30 Release of FD4 from HHP407, PHP407 and CLP407 gels with the previously optimized composition. The yellow color of the medium is indicative of the release of the molecule from the gels

To better visualize the change in the yellow color intensity, a higher concentration of FD4 (5 mg/ml) was used. The most significant change in color was detectable after 2h incubation (burst release).

4.1.6. Photo-sensitive Polymer Chemical Characterization

Figure 4.31 shows the ATR-FTIR spectra of PEG, PEG-DA, P407 and P407-DA. The acrylate polymers showed the characteristic peaks of carbonyl group (C=O) stretching vibration and alkene group (C=C) stretching vibration at 1725 cm^{-1} and 1630 cm^{-1}, respectively.

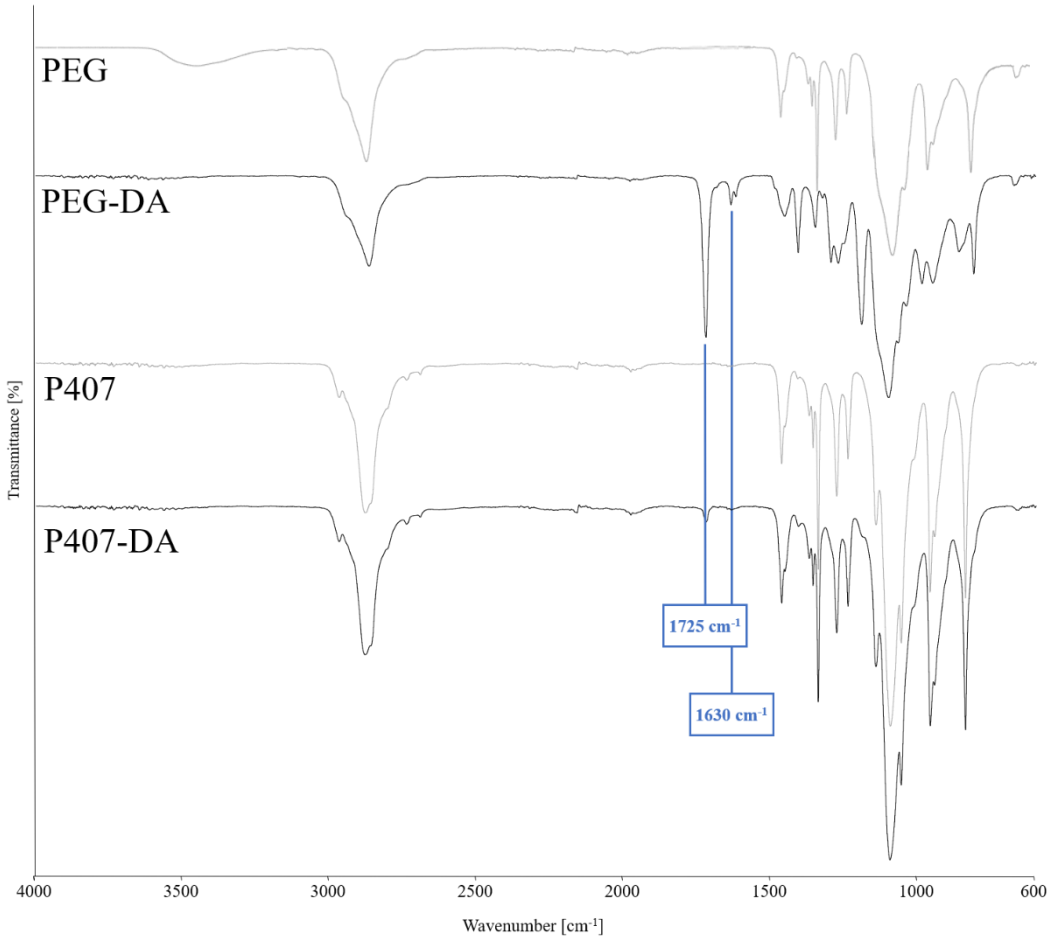

Figure 4.31 ATR FTIR spectra of PEG, PEG-DA, P407 and P407-DA. Differences between the spectra, proving successful polymer functionalization with acrylate moieties, are highlighted at 1725 and 1630 cm^{-1}.

^{1}H-NMR was exploited to assess the success of the acrylation process. **Figure 4.32** reports the ^{1}H-NMR spectra of PEG, PEG-DA, P407, P407-DA. The appearance of the new peaks at 6.0, 6.2 and 6.3 ppm demonstrated the success of the acrylation reaction.

Figure 4.33, instead, shows the ^{1}H-NMR spectra of gelatin and GelMA synthesized with MA and GM.

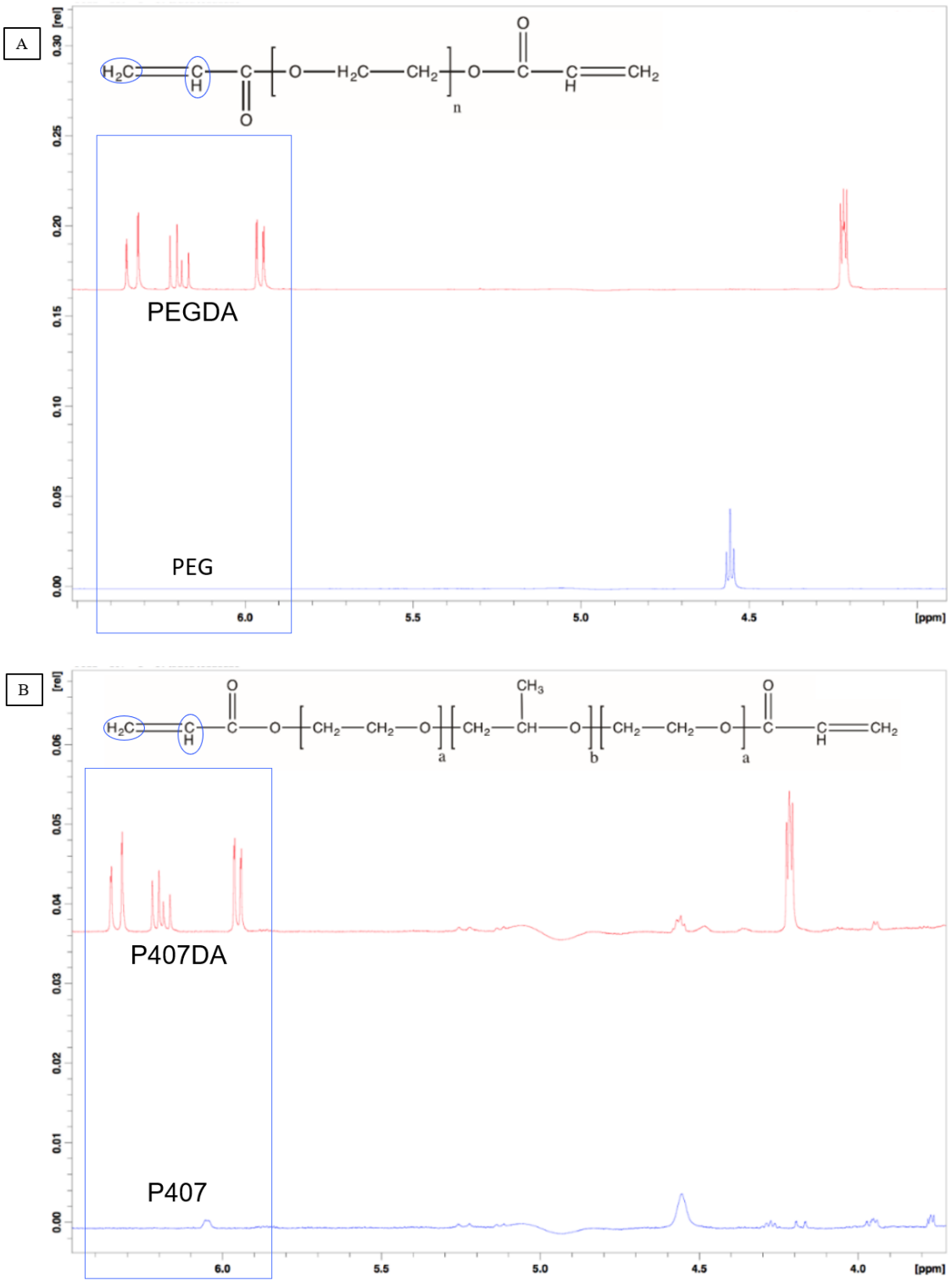

Figure 4.32 ^{1}H NMR spectra of **(A)** PEG-DA and **(B)** P407-DA, compared to their precursors.

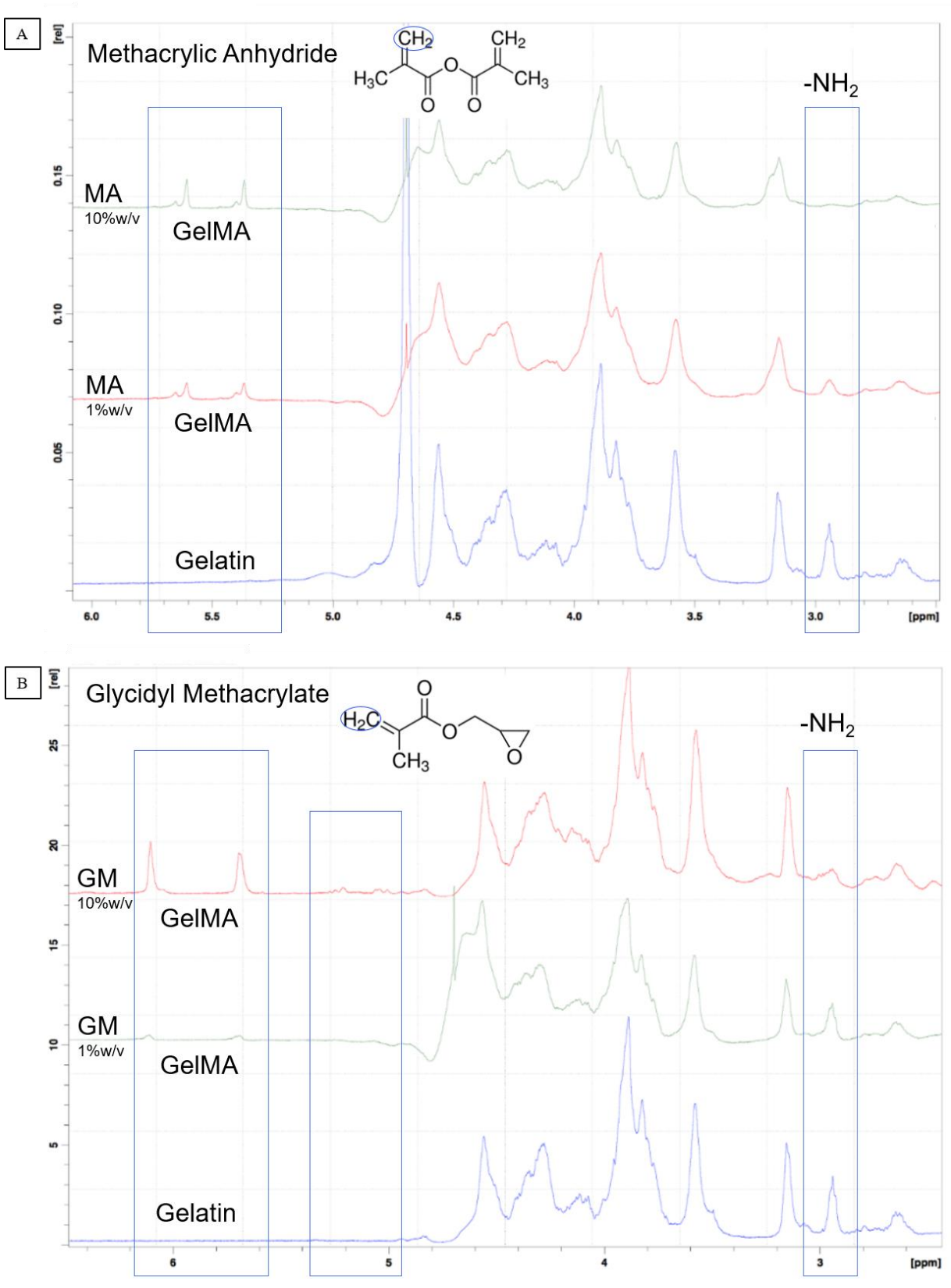

Figure 4.33 ^{1}H NMR spectra of GelMA synthesized starting from **(A)** MA and **(B)** GM.

The appearance of the peaks at 5.4 and 5.7 ppm demonstrated the success of the methacrylation reaction by using AM as reagent. By using GM, instead the two peaks were a bit shifted but still present (at 5.9 and 6.1 pmm). The degree of methacrylation increased with increasing concentration of AM and GM, as assessed by the decrease in intensity of the peak relative to amino groups, reaching approx. a 100 % degree of methacrylation by using a 10 %w/v of AM and GM during the grafting reaction.

4.1.7. Thermo- and Photo-sensitive Bioink Design

In order to further increase the bioink stability and finely tune its mechanical properties, the PURs were blended with the synthetized photo-sensitive polymers.

However, GelMA (for concentration higher than 1 %w/v) precipitated within the bioink forming turbid solutions and its addition to PUR hydrogels at a final concentration of 1 %w/v turned out to be not enough to significantly increase bioink stability in aqueous media. Hence, this kind of formulations was excluded. Concerning P407-DA-based formulations, they showed poor G' increase (in the order of 4-5 kPa) upon irradiation similarly to what detected with pure HHP407- and PHP407-based sol-gel systems. Thus, among all the tested formulations, the ones containing PEGDA showed the better results, and they were chosen for the next experiments.

Moreover, HHP407 was selected to be further characterized in blend with PEGDA, due to its higher and more efficient photo-sensitivity compared to PHP407. By blending HHP407 and PEGDA two degree of cross-linking are expected (coming from the PEGDA mesh and the crosslinked micelles). On the other hand, by blending NHP407 with PEGDA only one degree of crosslinking is expected (coming from the PEGDA mesh).

Both the two formulations (i.e., NHP407/PEGDA- and HHP407/PEGDA-based) were rheologically characterized.

4.1.7.1. Photo-sensitive Behavior Characterization

Figure 4.34 and **Figure 4.35** report the results of photo-rheological characterization carried out on NHP407/PEGDA- and HHP407/PEGDA- based sol-gel systems.

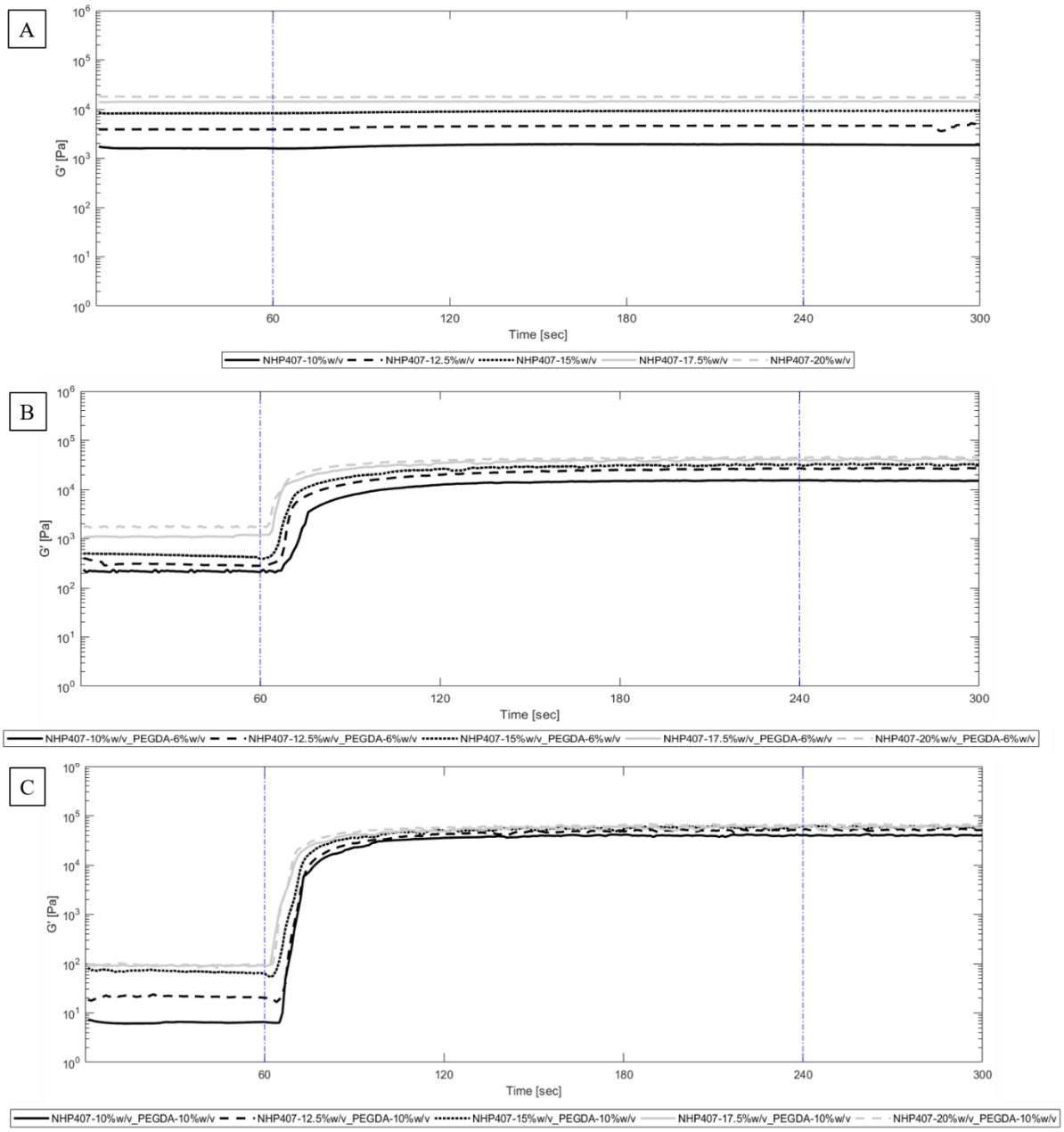

Figure 4.34 Trend of G' *vs* time as assessed by photo-rheological test for NHP407/PEGDA-based solutions at different PUR and PEGDA concentration: **(A)** stand-alone; blended with PEGDA **(B)** at 6 and **(C)** 10 %w/v concentration. The dash-dotted blue lines identify the test steps: at 60 seconds the UV source is turned on, while at 120 seconds the UV source is turned off.

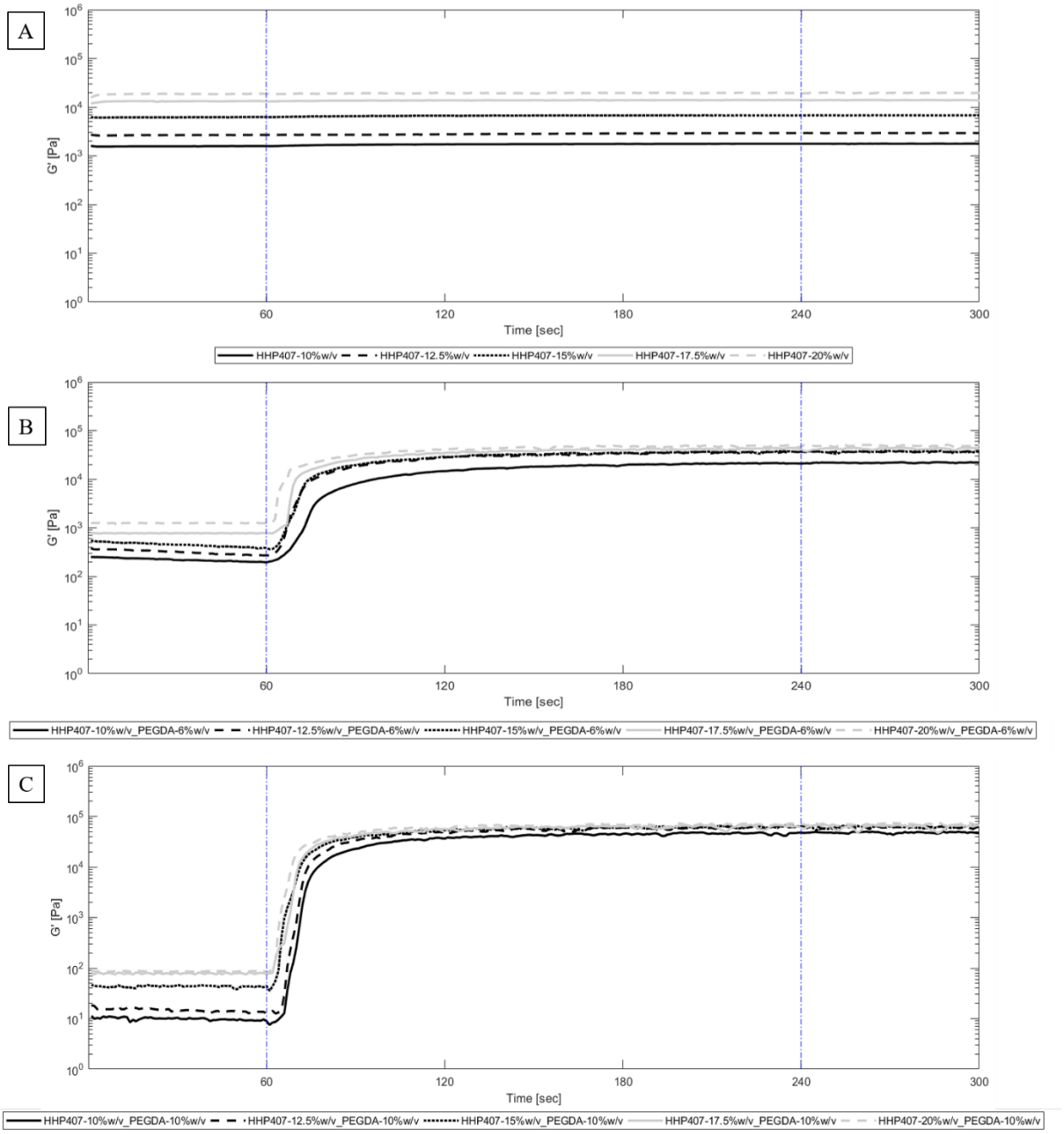

Figure 4.35 Trend of G' *vs* time as assessed by photo-rheological test for HHP407/PEGDA-based solutions at different PUR and PEGDA concentration: **(A)** stand-alone; blended with PEGDA **(B)** at 6 and **(C)** 10 %w/v concentration. The dash-dotted blue lines identify the test steps: at 60 seconds the UV source is turned on, while at 120 seconds the UV source is turned off.

All the characterized formulations showed a similar trend of the storage modulus (G') as a function of time, before and upon UV irradiation. Pure HHP407-based sol-gel systems (with no

addition of PEGDA) (**Figure 4.35 A**) exhibited G' values remaining almost constant even after the crosslinking step. In fact, as previously reported in paragraph 4.1.3.1, HHP407-based hydrogels did not show a significant increase in terms of G' (approx. 50 % increase in G' for 15 %w/v concentrated samples) upon UV light irradiation. On the other hand, NHP407-based formulations did not exhibit any photo-sensitivity, as further confirmed by the absence of changes in G' values upon UV irradiation (**Figure 4.35 B**).

The addition of PEGDA significantly affected the trend of G' upon photo-curing (**Figure 4.34 B** and **Figure 4.35 B**). In fact, G' value started to increase monotonically few seconds after UV source was switched on. A complete photo-crosslinking was achieved in approximately 30 sec, with G' increasing until a plateau value was reached. Upon achievement of the plateau, the photo-crosslinking process has been assumed to be completed with the PEGDA mesh completely built up. With increasing PUR concentration, G' initial and final (upon photocuring) values increased for both the formulations.

By increasing PEGDA concentration from 6 to 10 %w/v, G' initial value decreased and the G' value upon crosslinking increased (**Figure 4.34 C** and **Figure 4.35 C**) as a consequence of the plasticizing effect of poly(ethylene glycol) and the formation of a strong PEGDA mesh, respectively.

Figure 4.36 summarizes the main parameters extracted from the results of photo-rheological tests (i.e., G' initial value, G' value upon crosslinking and the offset between them).

Compared to the NHP407-based formulations, HHP407-based ones showed higher G' value after crosslinking and a higher offset between its initial and final value, as a consequence of the double degree of crosslinking that can be achieved within HHP407/PEGDA-based hydrogels compared to those based on NHP407/PEGDA blends.

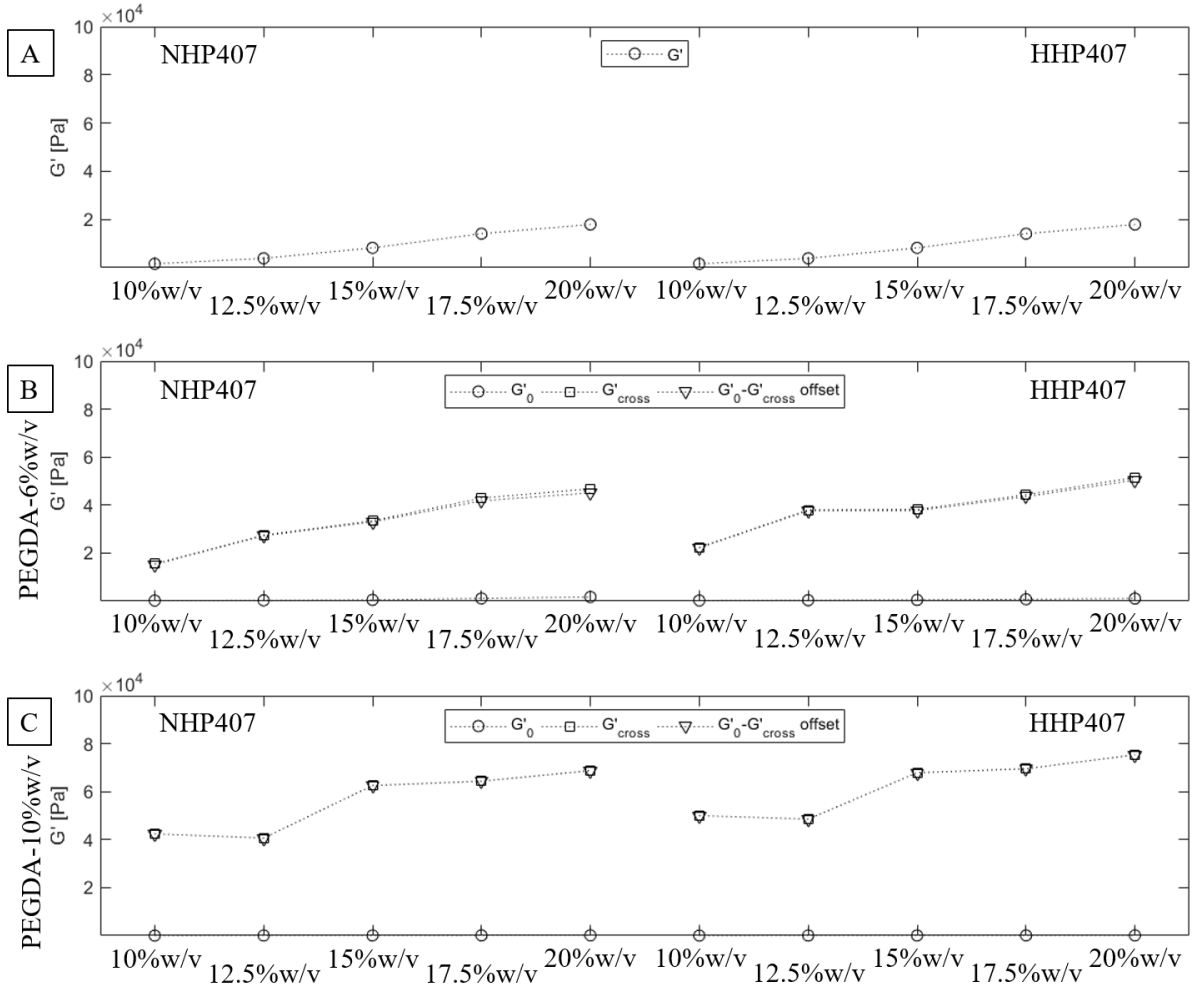

Figure 4.36 Main parameters extracted from photo-rheological test results: NHP407/PEGDA- and HHP407/PEGDA-based sol-gel systems at different PUR and PEGDA concentrations, stand-alone and blended with PEGDA (6 and 10 %w/v). **(A)** G' initial values virgin NHP407- and HHP407-based hydrogels (not-blended with PEGDA). G' initial and final (upon crosslinking) value and their offset of NHP407/PEGDA- and HHP407/PEGDA-based hydrogels: **(B)** 6 %w/v, **(C)** 10 %w/v PEGDA concentration.

Figure 4.37 shows the trend the G' *versus* time of HHP407- and PHP407-based formulations with the same PUR concentration (kept at 12.5 %w/v) and different PEGDA contents (0, 6, 8 and 10 %w/v concentration).

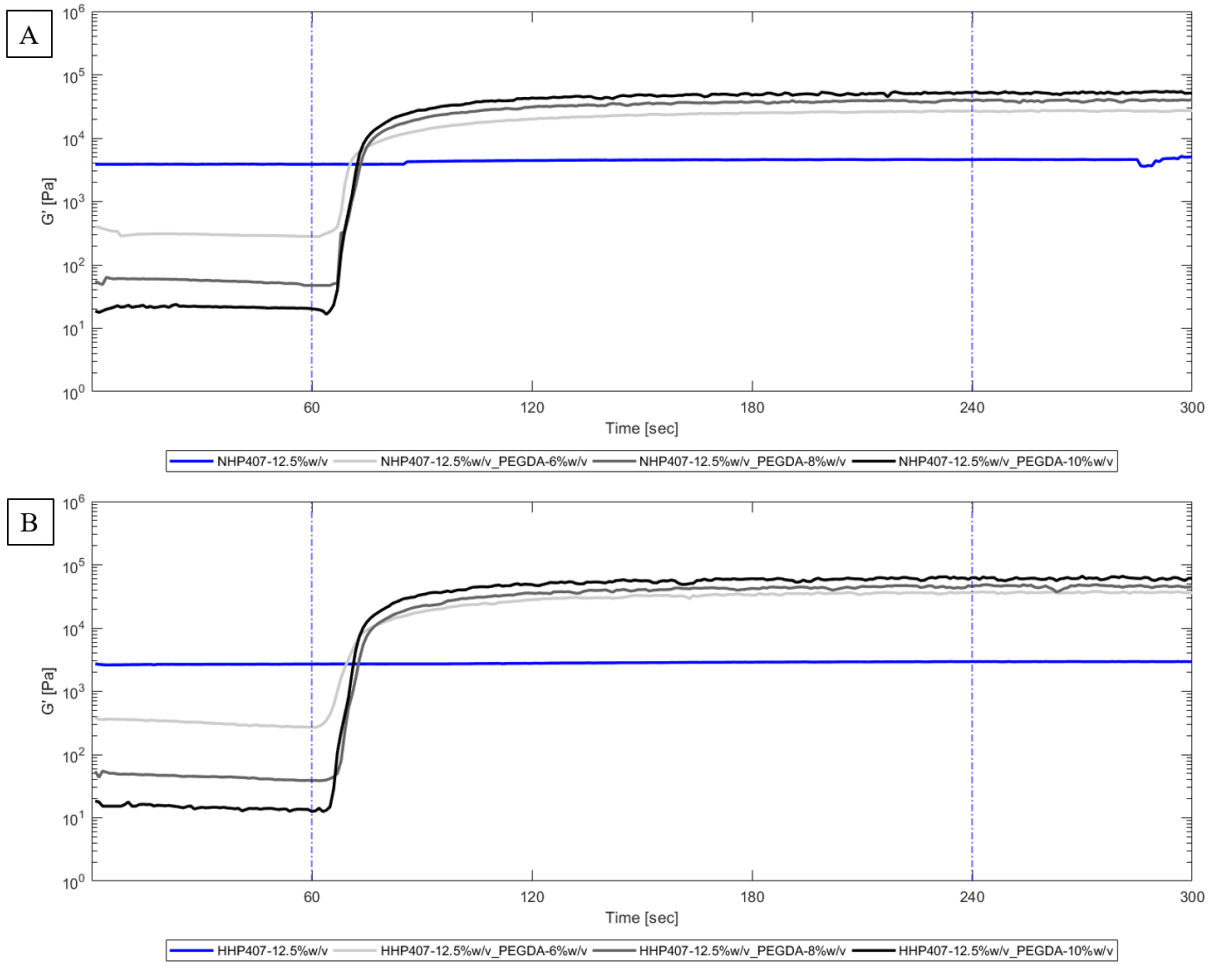

Figure 4.37 Trend of G' *vs* time as assessed by photo-rheological test for **(A)** NHP407- and **(B)** HHP407 -based sol-gel systems at 12.5 %w/v PUR concentration, blended with different amounts of PEGDA. The dash-dotted blue lines identify the test steps: at 60 seconds the UV source is turned on, while at 120 seconds the UV source is turned off.

As already observed, hydrogel formulations containing PEGDA showed lower G' initial value with respect to those based on the PURs alone, and this decrease became more evident with increasing PEGDA concentration. This phenomenon probably lies on the plasticizing effect of PEGDA that alters the gelation process of the hydrogels and their shear-thinning behavior. On the other hand, as previously observed, the G' values upon crosslinking increase by increasing the PEGDA concentration.

Figure 4.38 reports the previously mentioned main parameters extracted from the photo-rheology tests for the HHP407- and PHP407-based formulation with 12.5 %w/v of PURs.

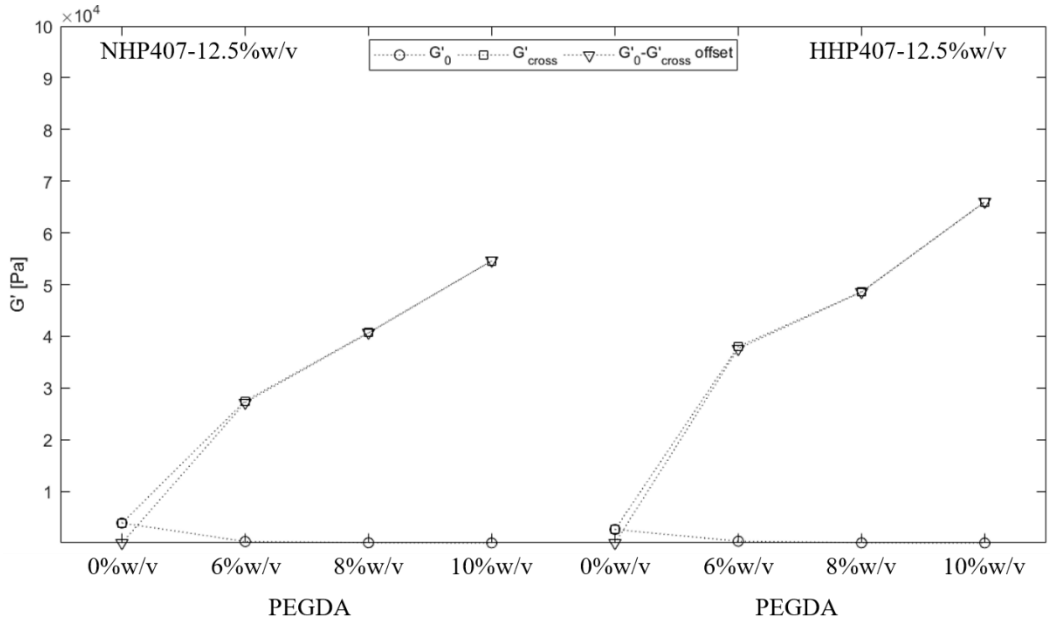

Figure 4.38 Values of the offset between the initial value of G' at its value upon crosslinking of HHP407- and PHP407-based hydrogels at 12.5 %w/v and blended with different concentrations of PEGDA.

The offset between the G' initial value and its value after crosslinking increase by increasing the PEGDA concentration as a consequence of a higher degree of crosslinking. One more time is possible to assess that the HHP407-based formulations give rise to hydrogel with higher mechanical properties compared to the NHP407-based ones.

The overall G' values upon crosslinking of the tested formulations are reported in **Table 4.5**.

Table 4.5 Bioink G' values after the photo-crosslinking process.

NHP407	PEGDA	$G'_{crosslinked}$ value (kPa)	HHP407	PEGDA	$G'_{crosslinked}$ value (kPa)
10%w/v	0%w/v	1.77±0.01	10%w/v	0%w/v	1.91±0.02
	6%w/v	15.16±0.17		6%w/v	21.23±0.68
	10%w/v	39.95±0.88		10%w/v	46.77±1.90
12.5%w/v	0%w/v	4.58±17,92	12.5%w/v	0%w/v	6.77±0.19
	6%w/v	26.31±0.67		6%w/v	35.92±1.02
	8%w/v	38.59±1.19		8%w/v	44.94±2.02
	10%w/v	51.17±1.78		10%w/v	60.23±2.45
15%w/v	0%w/v	9.21±0.04	15%w/v	0%w/v	10.92±0.18
	6%w/v	31.83±0.86		6%w/v	36.09±1.13
	10%w/v	58.72±1.36		10%w/v	62.52±1.56
17.5%w/v	0%w/v	14.40±0.10	17.5%w/v	0%w/v	15.93±0.35
	6%w/v	40.46±1.34		6%w/v	43.05±1.46
	10%w/v	58.84±3.05		10%w/v	63.32±2.97
20%w/v	0%w/v	17.50±0.21	20%w/v	0%w/v	19.56±0.68
	6%w/v	44.47±1.09		6%w/v	48.95±1.62
	10%w/v	64.88±1.83		10%w/v	69.46±2.30

Furthermore, the different photo-sensitive behavior of the formulations obtained using different photo-initiators was assessed (**Figure 4.39**).

I2959-loaded hydrogels showed lower photo-crosslinking speed and G' values upon crosslinking, as a consequence of its lower efficiency at 365 nm. In fact, I2959-based formulations showed a higher delay of the crosslink after the UVA source was turned on, compared to LAP-based one. Moreover, the final G' value upon the irradiation was slightly

lower for I2959-based formulations. For these reasons, LAP was selected as photo-initiator to add to the PUR-based bioink formulations.

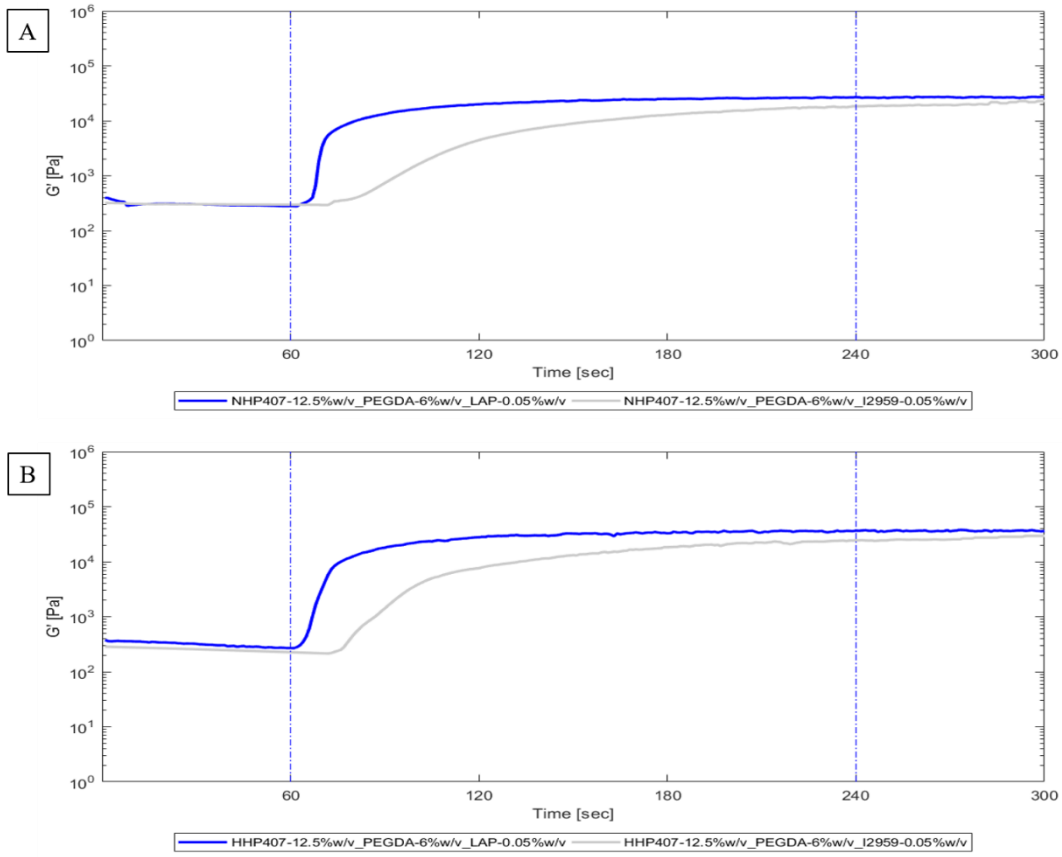

Figure 4.39 Trend of G' *vs* time as assessed by photo-rheological test for **(A)** NHP407- and **(B)** HHP407 -based sol-gel systems at 12.5 %w/v PUR concentration, blended with 6 %w/v of PEGDA and two different photo-initiators (i.e. LAP and I2959). The dash-dotted blue lines identify the test steps: at 60 seconds the UV source is turned on, while at 120 seconds the UV source is turned off.

4.1.7.2. Thermo-sensitive Behavior Characterization

PUR/PEGDA-based formulations were characterized by mean of rheology to study the effects of the addition of PEGDA on the thermo-sensitive behavior of the hydrogels. Information about the different gelation properties of PUR/PEGDA hydrogels were obtained through LAOS, SAOS and temperature ramp tests.

The trends of storage (G') and loss (G'') moduli, and shear stress (τ) as a function of applied strain (γ) for NHP407/PEGDA- and HHP407/PEGDA based sol-gel systems ([PUR] = 12.5 %w/v, [PEGDA] = 0, 6, 8 and 10 %w/v) are reported in **Figure 4.40**

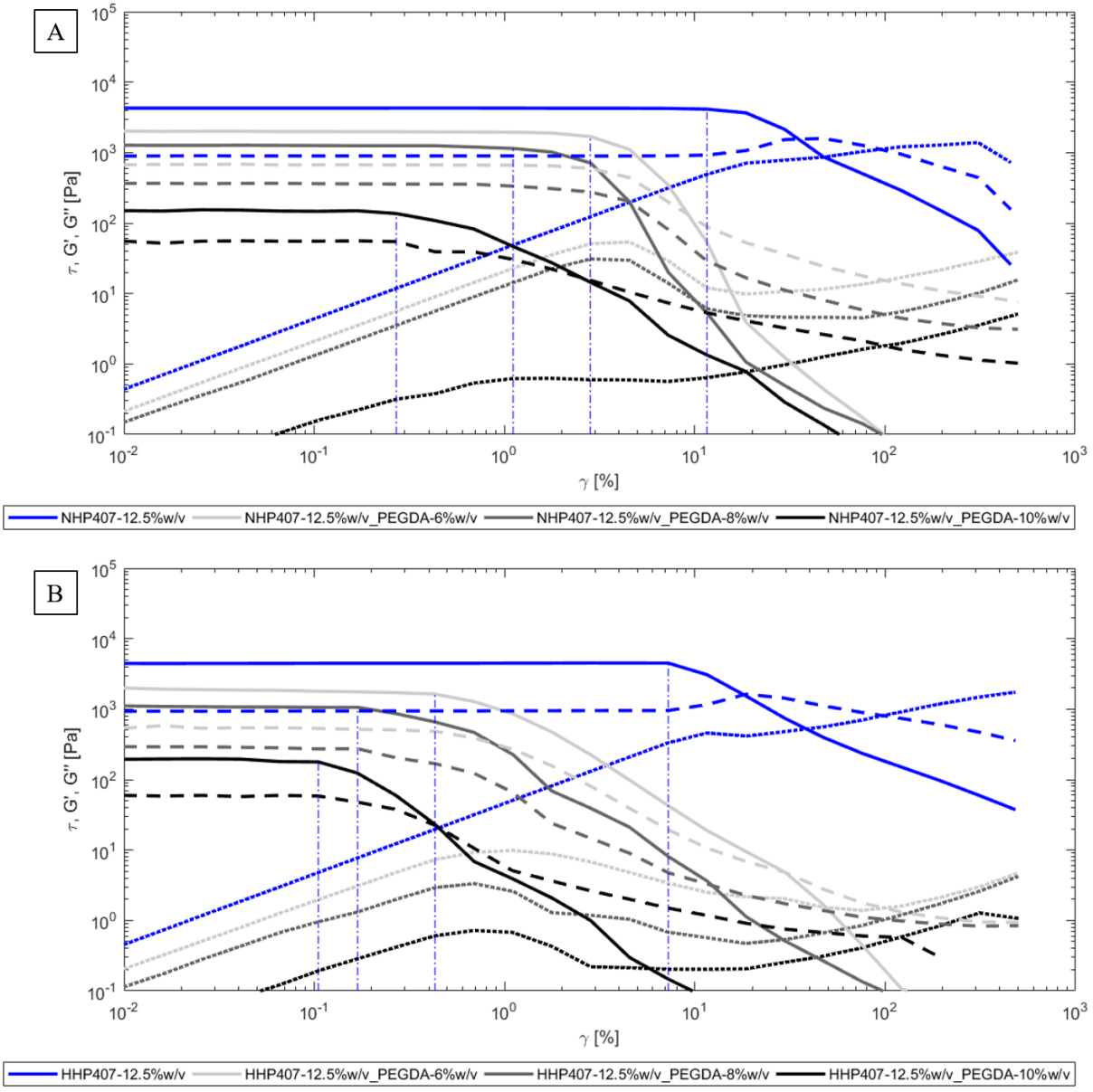

Figure 4.40 LAOS test: G', G'' and shear stress (τ) trend *versus* strain (γ) at 37 °C. Comparison between **(A)** NHP407/PEGDA- and **(B)** HHP407/PEGDA-based hydrogels (solid line: G', dashed lines: G'', dotted lines: τ). The blue dash-dotted lines identify the linear viscoelastic region.

Figure 4.41 reports the characteristic parameters extracted from LAOS tests.

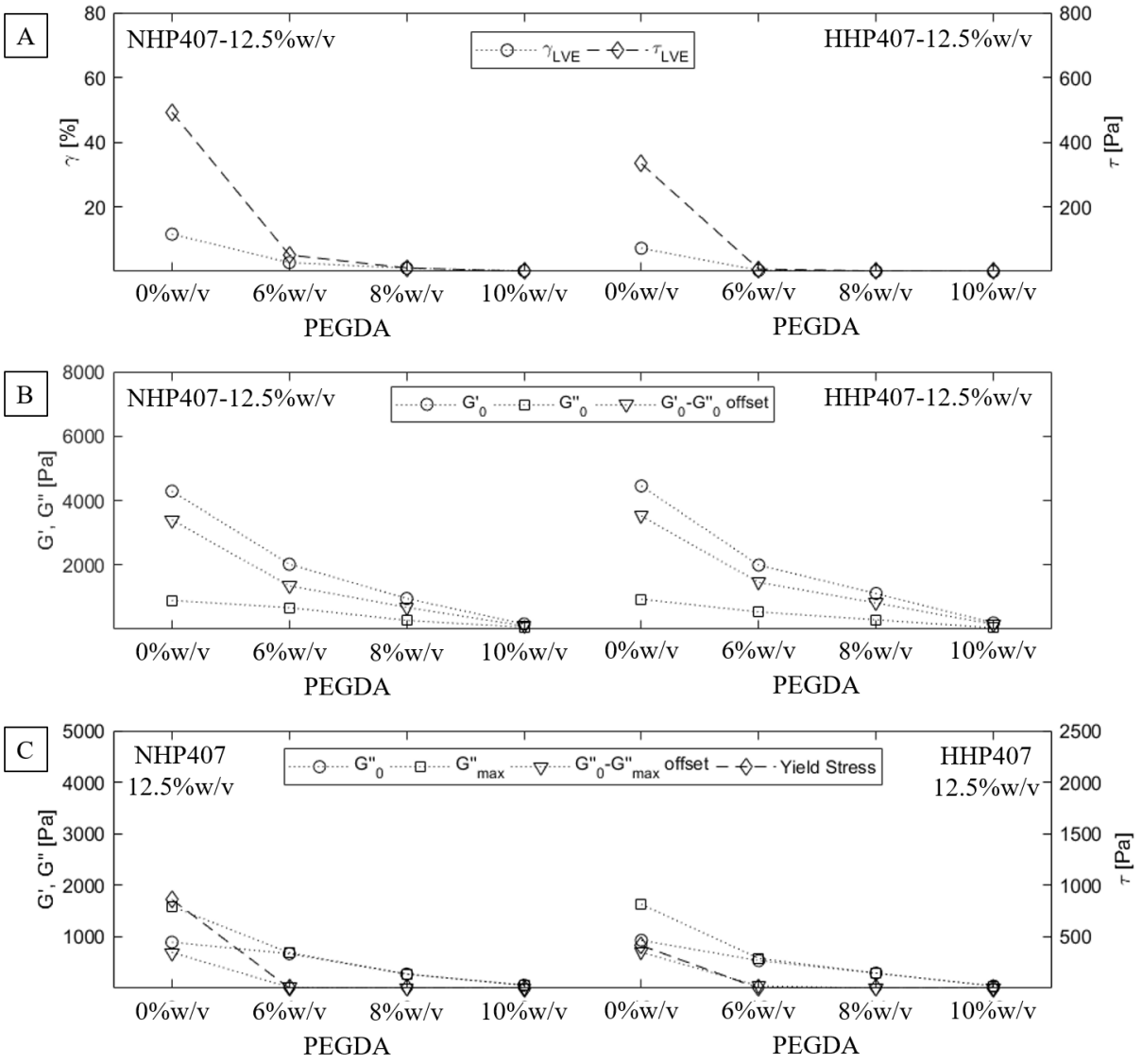

Figure 4.41 LAOS main parameters for NHP407/PEGDA- and HHP407/PEGDA-based hydrogels. **(A)** Maximum strain and shear within the LVE region. **(B)** Initial G' and G'' values and their offset. **(C)** Initial and maximum G'' values, their offset and yield stress.

The extension of the LVE region decreased with increasing PEGDA concentration in both NHP407- and HHP407-based formulations. However, the linearity region turned out to be less extended in HHP407-based formulations compared to NHP407-based ones (**Figure 4.40** and **Figure 4.41 A)**. This behavior, probably, due to the plasticizing effect of PEGDA that reduces the resistance to deformation of the hydrogels. The reason of this difference between the

NHP407- and HHP407-based formulations probably lies on the bigger dimension of the HHP407-based micelles (as assessed from DLS results). In fact, the PEGDA chains probably disturb more the smaller and organized NHP407-based micelles when a shear is applied to the hydrogels with respect the bigger and less organized HHP407-based micelles.

On the other hand, both NHP407- and HHP407-based formulations showed similar G'-G'' offset, suggesting that the resultant thermo-sensitive hydrogels showed the same balance between the viscous and the elastic components (**Figure 4.41 B**). Furthermore, the addition of PEGDA changed the non-linear response of the resultant hydrogels: the behavior of the hydrogels changed from Type III (G'' weak strain overshoot phenomenon) to Type I (strain thinning: G' and G'' decrease), probably because PEGDA molecules tend to interfere with micelle formation and work as lubricant among them.

Similar results were also obtained from SAOS tests for the linear response of such hydrogels (**Figure 4.42**). The frequency at the G'-G'' crossover decreased with increasing the concentration of PEGDA, meaning that the gels containing a higher amount of PEGDA were more developed. Moreover, the thermo-sensitive behavior reported and thoroughly discussed in the previous chapter was still present in PEGDA containing sol-gel systems, with the frequency at the G'-G'' crossover decreasing with increasing temperature.

Figure 4.43 shows the main parameters extracted from SAOS tests results. SAOS results further confirmed the differences existing between NHP407- and HHP407-based hydrogels, with the latter showing slightly lower frequency values at the G'-G'' crossover compared to NHP407-based ones (**Figure 4.42**, **Figure 4.43 A**). HHP407-based solutions also showed slightly higher G'-G'' offset compared to the NHP407-based ones (**Figure 4.43 B** and **Figure 4.43 C**).

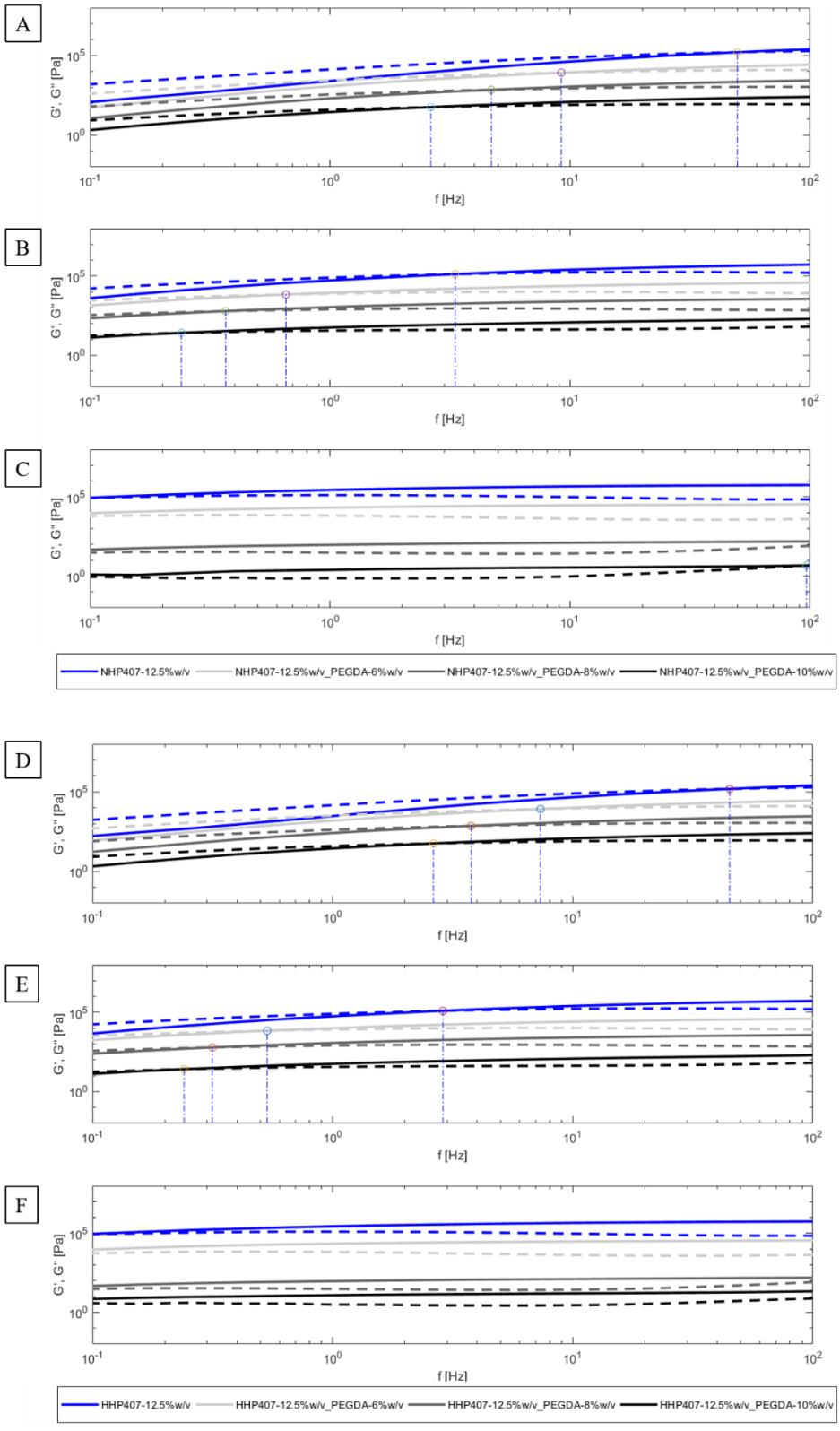

Figure 4.42 SAOS test: G' and G'' *versus* angular frequency at **(A, D)** 25, **(B, E)** 30, **(C, F)** 37 °C. Comparison between **(A-C)** NHP407/PEGDA- and **(D-F)** HHP407/PEGDA- based sol-gel systems (solid line: G', dashed lines: G'', dotted lines: complex η). The blue dash-dotted lines identify G'-G'' crossover.

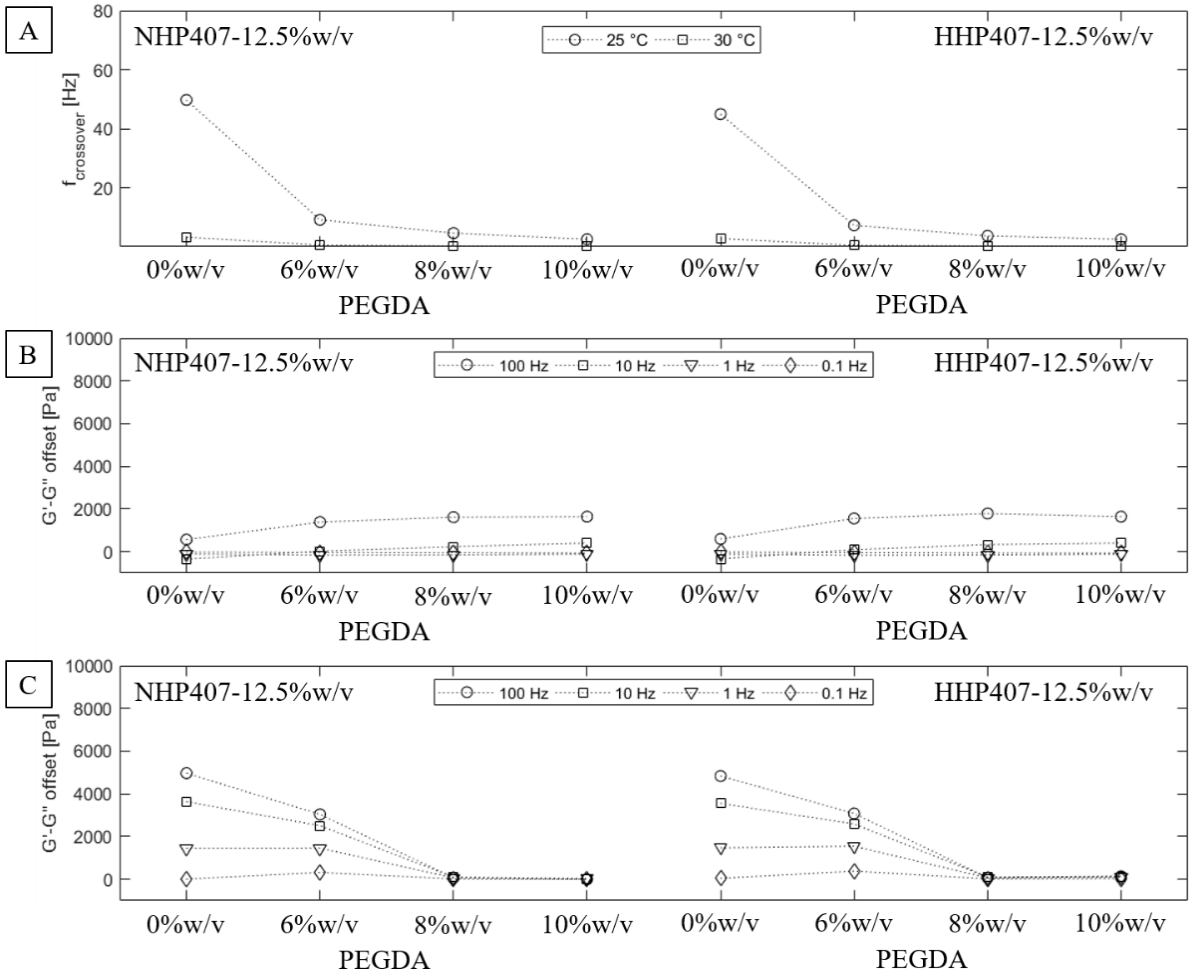

Figure 4.43 SAOS main parameters for NHP407/PEGDA- and HHP407/PEGDA-based sol-gel systems at 12.5 %w/v PUR concentration. **(A,)** f at G'-G'' crossover. G'-G'' offset of the analyzed formulations at 0.1, 1, 10 and 100 Hz, at **(B)** 25 °C and **(C,)** 37 °C.

SAOS tests also evidenced the shear thinning behavior of the designed hydrogels (**Figure 4.44**), with complex viscosity decreasing with increasing shear rate.

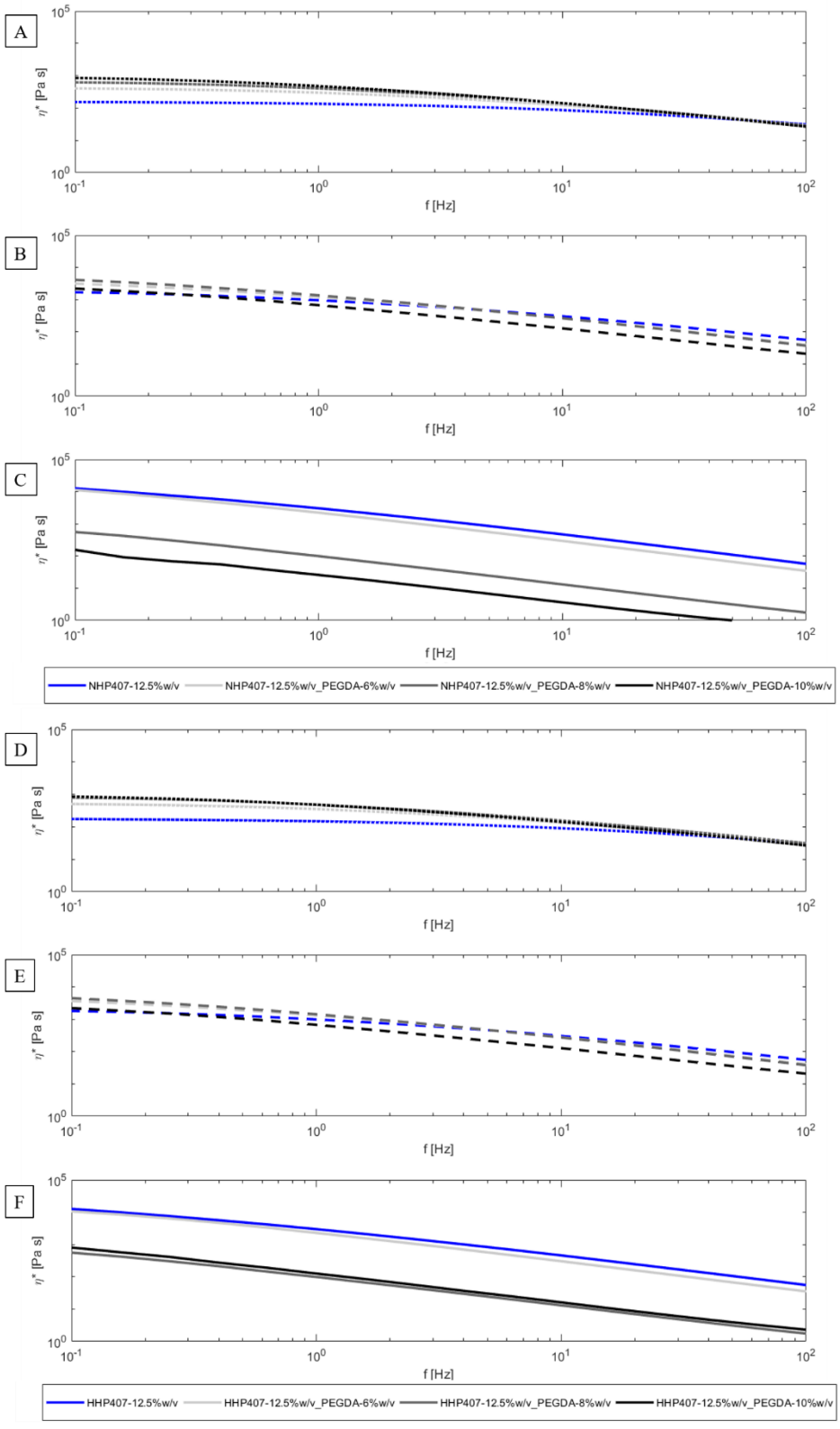

Figure 4.44 Viscosity *versus* angular frequency. Shear thinning behavior of **(A-C)** NHP407/PEGDA- and **(D-E)** HHP407/PEGDA-based hydrogels at different concentration and temperatures: **(A, D)** 25 °C, **(B, E)** 30 °C and **(C, F)** 37 °C.

The shear thinning behavior became more evident with increasing PEGDA content in the formulations and temperature, as a consequence of PEGDA chains acting as lubricant among PUR-based micelles. This phenomenon turned out to be more and more evident by increasing temperature.

At 25 °C (**Figure 4.44 A** and **Figure 4.44 D**) viscosity values were higher for the formulations containing higher PEGDA content; however, with increasing frequency, this trend reversed showing a lower viscosity with increasing PEGDA concentration (**Figure 4.45 A**). At 30 °C (**Figure 4.44 B** and **Figure 4.44 E**) the behavior was similar but the change in the trend of viscosity happened at lower frequencies (**Figure 4.45 A**).

At 37 °C (**Figure 4.44 C** and **Figure 4.44 F**), instead, the viscosities of the formulations containing higher concentration of PEGDA were lower over all the analyzed range of frequencies.

Moreover, even in this case, slight differences between NHP407- and HHP407-based formulations could be observed, with HHP407/PEGDA-based formulations showing a less marked shear-thinning behavior. This result confirmed the hypothesis that PEGDA influenced the behavior of the hydrogels with more organized micelles at higher extent.

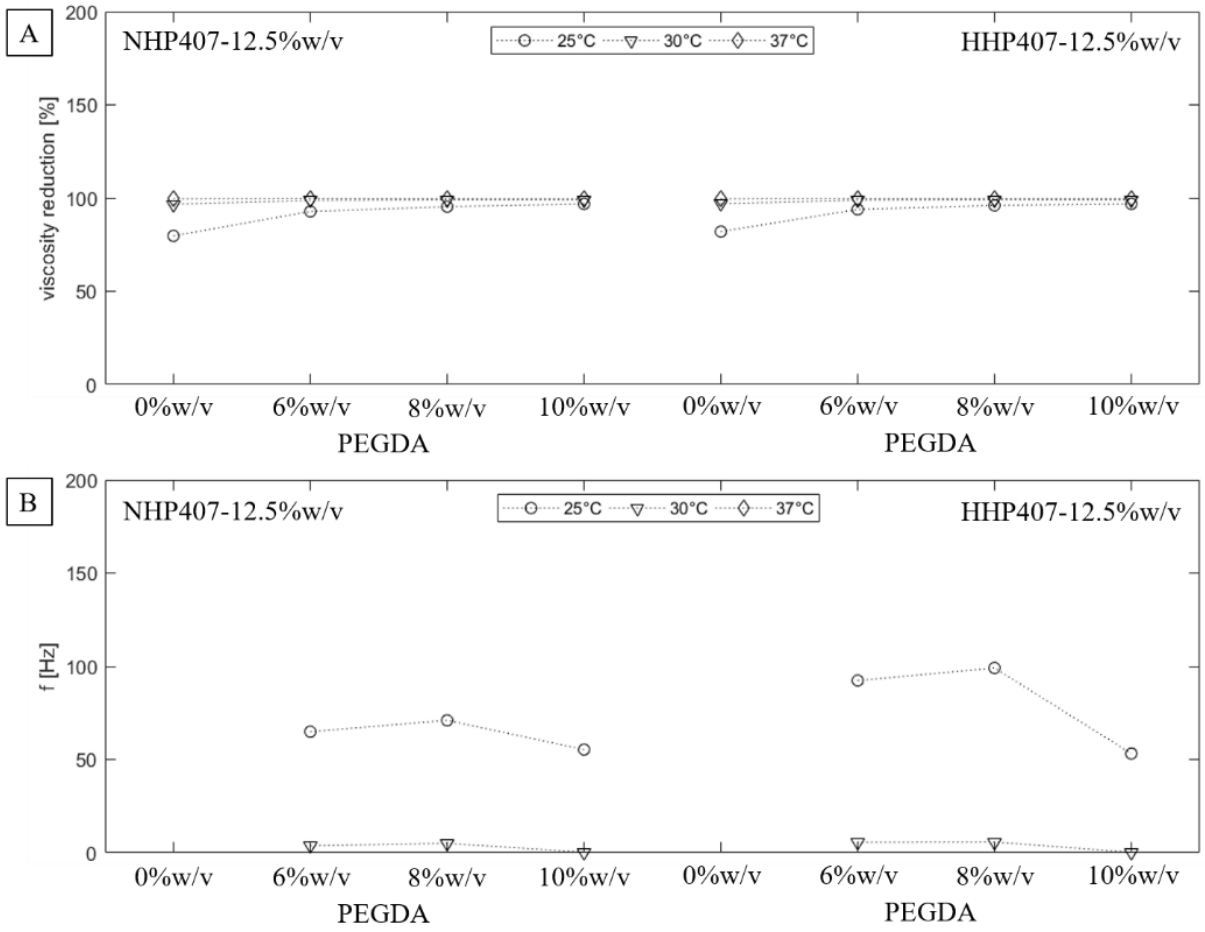

Figure 4.45 SAOS parameters for NHP407/PEGDA- and HHP407/PEGDA-based sol-gel systems at 12.5 %w/v PUR concentration. **(A,)** viscosity reduction (%) obtained as difference between the viscosity at 0.1 and 10 Hz. **(B)** f at the crossover between the viscosity trend of the PUR/PEGDA- and PUR standalone formulations

The trend of viscosity (η) as a function of temperature during the sol-to-gel transition of PUR/PEGDA formulations is reported in **Figure 4.46.** All the analyzed formulations showed a similar trend of viscosity. As previously discussed, viscosity initially decreased as a function of temperature (sol state), until a minimum value (at T_{onset}) was reached; then, viscosity sharply increased until a maximum before decreasing again (due to the melt fracture).

Figure 4.47 summarizes the key parameters extracted from temperature ramp test results.

Both the PUR/PEGDA-based hydrogels exhibited similar T_{onset} with increasing PEGDA (**Figure 4.46** and **Figure 4.47 A, C**); however, NHP407-based ones exhibited slightly lower

viscosity with increasing PEGDA concentration compared to HHP407-based ones (**Figure 4.46** and **Figure 4.47 B, D**).

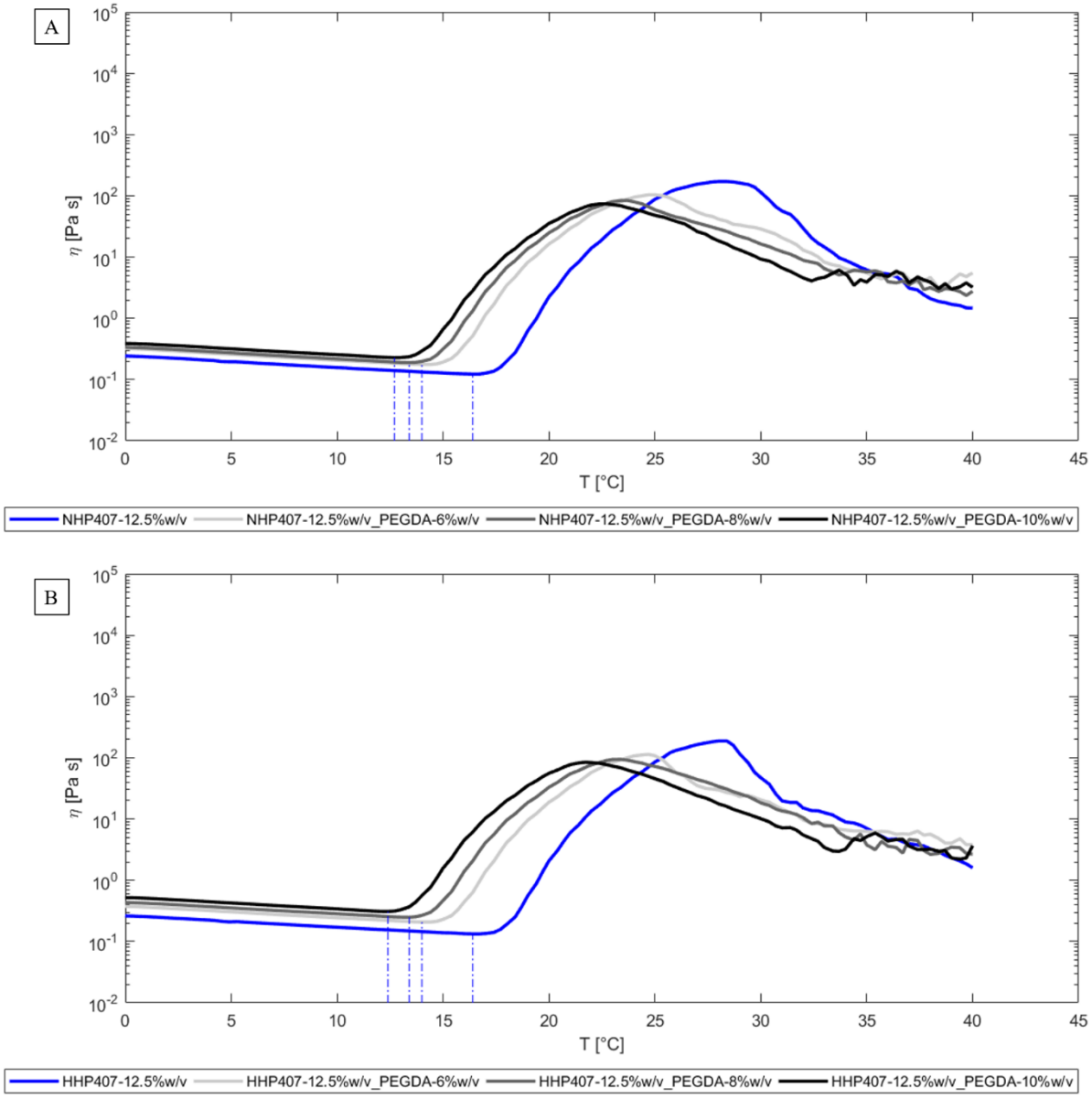

Figure 4.46 Temperature ramp test: viscosity *versus* temperature during sol-to-gel transition. Comparison between **(A)** NHP407/PEGDA- and **(B)** HHP407/PEGDA-based sol-gel systems. The blue dash-dotted lines identify T_{onset}.

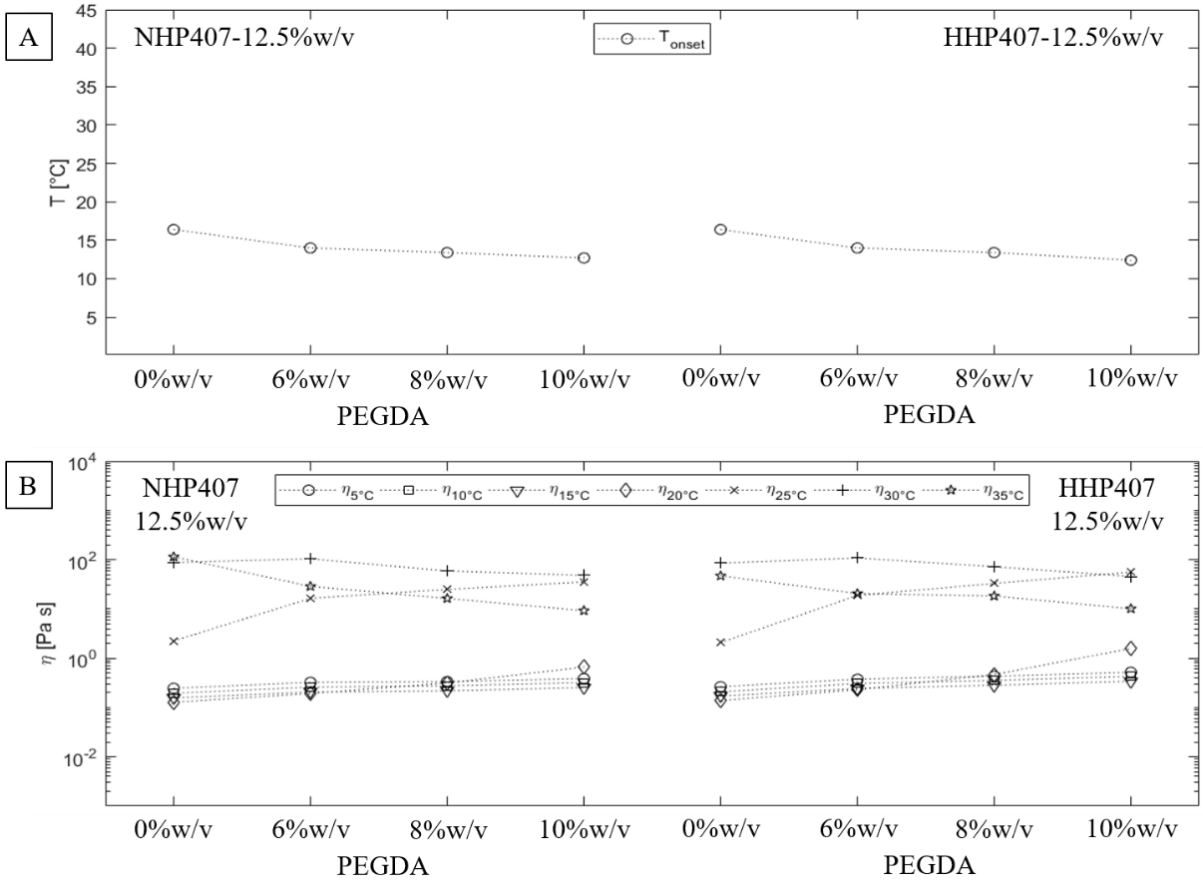

Figure 4.47 Main parameters extracted from temperature ramp test results: NHP407/PEGDA- and HHP407/PEGDA-based hydrogels. **(A)** T_{onset} , **(B)** viscosities at different temperatures (5, 10, 15, 20, 25, 30, 35 °C).

The overall rheological characterization of such hydrogels pointed out that the addition of PEGDA increased the overall gelation properties of the hydrogels. Moreover, slight differences between HHP407/PEGDA- and the NHP407/PEGDA-based formulations have been highlighted, with HHP407/PEGDA-based hydrogels showing a higher degree of development at 37 °C, higher G' and G'' values, higher viscosities, but less marked shear-thinning behavior.

4.2. Conclusions

In the form of thin filaments, NHP407-based formulations showed limited residence time in aqueous environment (in the order of hours), which makes them unsuitable as bioinks for bioprinting applications. In other to overcome this drawback, in this chapter novel thermo-sensitive and photo-curable injectable formulations have been designed. Thermo-sensitivity can be first exploited to print the designed bioinks according to a CAD model; then the printed structures can be photo-cured in "cell-friendly" conditions to provide the scaffolds with an additional stabilization through covalent bonds. A wide plethora of formulations has been designed, according to two different approaches: (i) synthesizing new amphiphilic PURs with acrylic moieties (PHP407 and HHP407), which solutions show both thermo- and photo-sensitivity; (ii) adding a water-soluble acrylate polymer (e.g., PEGDA) to the thermo-sensitive formulations designed in the previous chapter (based on NHP407).

According to the first approach, two PURs have been designed with one (HHP407) and three (PHP407) acrylate moieties, respectively; in order to make their solution photo-sensitive. HHP407- and PHP407-based solutions showed similar thermo-sensitive behavior with respect to NHP407-based ones developed and characterized in Chapter 3, with the formation of slightly bigger and less organized micelles, as well as lower gelation properties (i.e., higher gelation temperatures and gelation time at 37 °C). Nevertheless, their photo-sensitivity allowed the formation of chemical crosslinks among the micelles upon the addition of a photo-initiator and the UV irradiation, that resulted in enhanced stability in aqueous environment (up to 80% at 1 day incubation).

Despite the lower acrylate moieties, the HHP407-based hydrogels showed a more efficient photo-sensitive behavior (i.e., a higher increase of G' and micelles dimension upon crosslink). On the other hand, the thermo-sensitive behavior of the two PUR-based hydrogels resulted

almost the same. For this reason, HHP407 was selected as the best candidate for the design of thermo- and photo-sensitive bioinks for bioprinting.

However, despite the significant increase in terms of water stability provided by the photo-curing step, HHP407-based formulations still suffered of relatively low stability in water environment, as resulted from the stability tests performed on 210 μm thick casted scaffolds. Therefore, as a contingency plan, HHP407 was blended with PEGDA in other to further improve the stability of the gels in aqueous media. Hence, two different kinds of thermo- and photo-sensitive bioinks were designed based on blending amphiphilic PURs with diacrylate poly(ethylene glycol): (i) blends of NHP407 and PEGDA which hydrogels are expected to form a crosslinked mesh entrapping the PUR-based micelles upon UV irradiation, and (ii) blends of HHP407 and PEGDA which hydrogels are expected to own two different degrees of crosslinking coming from the PEGDA-based mesh and the crosslinked PUR-based micelles.

NHP407/PEGDA- and HHP407/PEGDA-based formulations were characterized in terms of thermo- and photo-sensitivity. Their properties were studied by changing both PUR and PEGDA content in the formulations (PUR concentration within the range 10-20 %w/v, PEGDA concentration within the range 6-10 %w/v), showing the possibility to modulate the bioink mechanical properties by changing the hydrogel formulation and constituent concentration. Furthermore, the difference UV response using two different photo-initiator was studied as well as the influence of the irradiation time on the hydrogel mechanical properties. Such tests show the better efficiency of LAP at 365 nm wavelength compared to the I2959, and the possibility to tune the bioink mechanical properties by changing the irradiation time.

The designed systems have shown promising properties for bioprinting approaches. In particular, their bicomponent nature could be exploited to finely tune both the thermo- and the photo-responsive behavior. For instance, it has been demonstrated that the modulation of PUR

and PEGDA content in the blends could allow a fine control of both gelation properties and shear thinning behavior. Furthermore, water stability and bioink mechanical properties have been proven to be strongly influenced by changing PEGDA concentration (and also HHP407 concentration in the case of HHP407/PEGDA-based formulations) and UV irradiation time. The designed formulations will be used a bioinks for bioprinting in the next chapter.

References

[1] M. Boffito, E. Gioffredi, V. Chiono, S. Calzone, E. Ranzato, S. Martinotti and G. Ciardelli, *Polym Int*. **2016**: *65*.

[2] N. Chen and J. Zhang, *Chin. J. Polym. Sci.* **2010**: *28*, 903.

[3] E. Karavas, G. Ktistis, A. Xenakis and E. Georgarakis*, Eur. J. Pharm. Biopharm*. **2006**: *63*, 2.

[4] B.P. Lee, J.L. Dalsin and P.B. Messersmith, *Biomacromolecules* **2002**: *3,* 5.

[5] L.A. Burzio and J.H. Waite, *Protein Science* **2001**: *10*.

[6] Fwu-Long Mi, Yu-Chiun Tan, Huang-Chien Liang, Rong-Nan Huang and Hsing-Wen Sung, *Journal of Biomaterials Science* **2001**: *12*, 8.

[7] Sung-Ching Chen, Yung-Chih Wu, Fwu-Long Mi, Yu-Hsin Lin, Lin-Chien Yu and Hsing-Wen Sung, *Journal of Controlled Release* **2004**: *96*, 2.

[8] A. Cavallo, M. Madaghiele, U. Masullo, M.G. Lionetto and A. Sannino, *J. Appl. Polym. Sci*. **2016**: *134*.

[9] Kuk Hui Son and Jin Woo Lee, *Materials* **2016**: *9*, 854.

[10] F. Markus, F. Dreher, S. Laschat, S. Baudis, G.E.M. Tovar, A. Southan, *Polymer* **2017**: *108*.

[11] C.R. López-Barrón, R. Chen, N.J. Wagner and P.J. Beltramo, *Macromolecules* **2016**: *49*, 14.

[12] J.W. Nichol, S.T. Koshy, H. Bae, C.M. Hwang, S. Yamanlar and A. Khademhosseini, Biomaterials **2010**: *31*, 21.

[13] Z. Wang, Z. Tian, F. Menard and K. Kim, *Biofabrication* **2017**: *9*, 4

[14] C.G. Williams, A.N. Malik, T.K. Kim, P.N. Manson and J.H. Elisseeff, *Biomaterials* **2005**: 26, 11.

[15] B.D. Fairbanksa, M.P. Schwartza, C.N. Bowmana and K.S. Anseth, *Biomaterials* **2009***: 30*, 35.

[16] Pradal C, Jack KS, Grøndahl L and Cooper-White JJ, Biomacromolecules 14:3780–3792 (2013).

[17] Alexandridis P, Holzwarth JF and Hatton TA, Macromolecules 27:2414–2425 (1994).

[18] M.A. Shaker and H.M. Younes, *J. Control Release* **2015**: *217*.

[19] Bhattacharya M, Malinen MM, Lauren P, Lou YR, Kuisma SW, Kanninen L et al., J Control Release 164:291–298 (2012).

[20] F.D. Kuchta, A.M. Van Herk and A.L. German, *Macromolecules* **2000**: *33*, 10.

Chapter 5

Bioprinting

Abstract:

This chapter deals with the application of the thermo- and photo-sensitive bioinks developed in Chapter 4 in bioprinting application. The printing setup and parameters were optimized in order to maximize the printing resolution and fidelity as well as the cell viability during the printing and photo-crosslinking processes.

In particular, a commercially available bioprinter (Inkredible +, CELLINK) was modified in order to print the designed thermo- and photo-sensitive bioinks. The main modifications involved the addition of a surface heater to control the temperature over the printing platform, and the design of a photo-crosslinking system based on a 365 nm LED and an intensity controller to be assembled on the second cartridge of the instrument. Eventually, the printing and photo-crosslinking procedures were studied separately in order to select the best parameters and conditions that allow printing resolution and cell viability maximization. The best conditions of each procedure were finally combined to 3D print cellularized scaffolds in the shape of circular multi-layered constructs with a grid pattern.

Furthermore, 3D printed scaffolds stability and water uptake as well as their mechanical properties were assessed.

Keywords: Polyurethane, Thermo- and Photo-sensitive Hydrogel, Bioprinting, Printing Setup, Mesenchymal Stem Cells.

5.1. Introduction

5.1.1. Bioprinting Process

The use of hydrogels/bioinks as printing materials offers the possibility to fabricate cellularized scaffolds by printing the cells embedded inside the material, avoiding cell seeding issues after fabrication (e.g., poor cell colonization) and allowing an efficient cell distribution within the constructs.[1-3] In this context, bioink design and printing process need to be carefully optimized to guarantee cell viability and homogenous distribution within the bioink, minimize shear stress applied to the cells during the printing steps, and maximize printing resolution and fidelity.[2,4-6] Bioink design is particularly crucial for extrusion-based bioprinting, which requires bioinks with tunable viscosity through a fast gelation mechanism and shear thinning properties in order to make cell encapsulation easy, reduce the stress applied to the cells and maintain the shape after being extruded in the form of a thin filament.[6]

The bioprinting process can be divided in three main steps: (i) bioink preparation and cell encapsulation (**Figure 5.1**), (ii) printing/extrusion of the bioink (**Figure 5.2**) and (iii) crosslinking of the printed structures in order to fix the shape (**Figure 5.3**).

In this thesis work, the thermo-sensitive nature of the developed PUR-based hydrogels helped cell dispersion, since cells have been added and homogeneously distributed within the hydrogels at a temperature lower than LCST, i.e., in a sol or semi-gel phase (5-15 °C). After being loaded within the syringe, the cellularized hydrogels have been subjected to a fast sol-gel transition (few minutes) prior to printing by increasing the temperature, avoiding cell sedimentation on the bottom of the syringe (**Figure 5.1**).

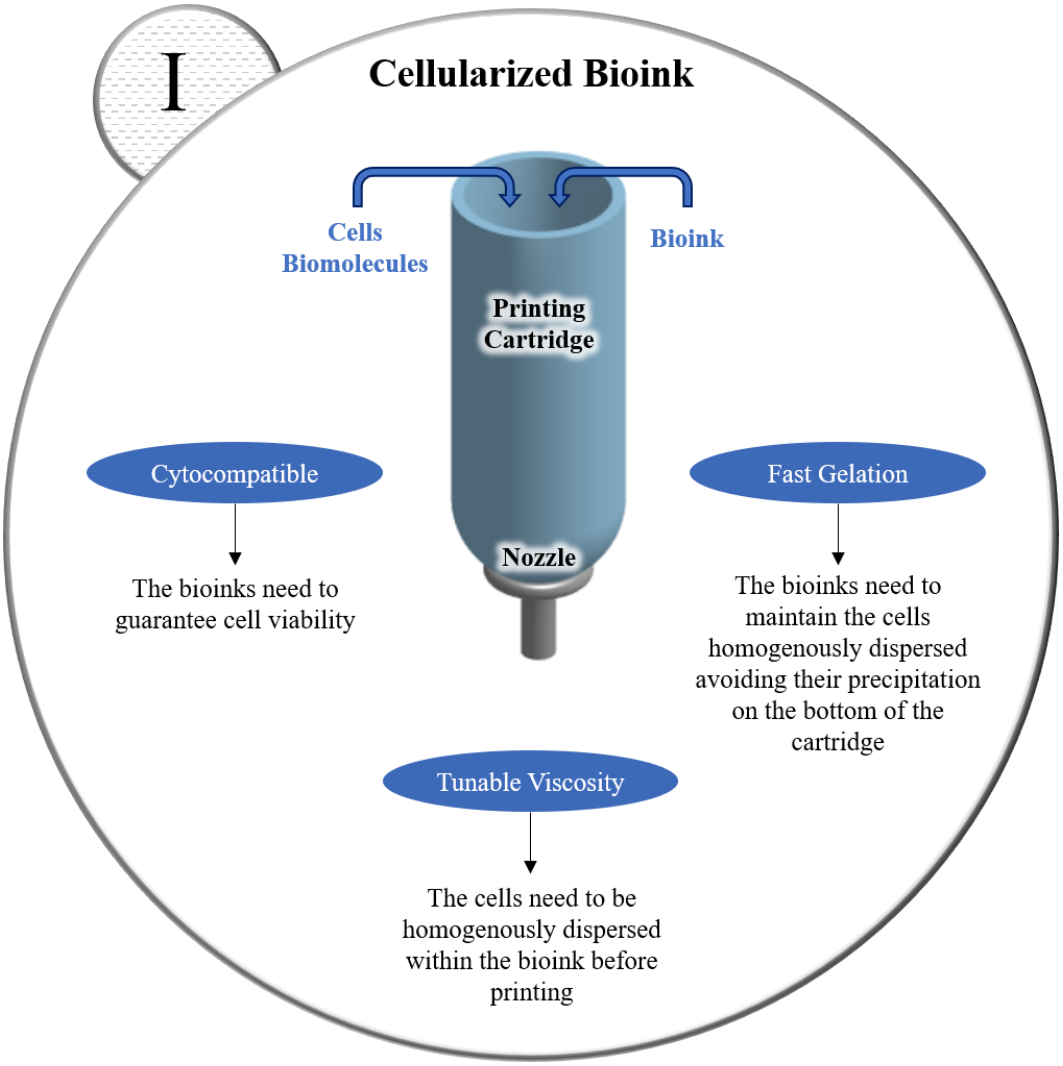

Figure 5.1 First bioprinting step (cellularized bioink preparation) and bioink properties.

Due to the need of bioinks with relatively high viscosity, shear thinning properties are essential for bioinks applied in extrusion-based bioprinting.[5,6] In fact, it helps in reducing cell suffering due to the shear stress applied during the extrusion through the nozzle. The shear thinning behavior of the designed bioinks, in particular those based on blends with PEGDA, turned out to be very useful in making the printing process easier (e.g., by reducing the printing pressure and increasing the speed) and improving both printing resolution and cell viability (**Figure 5.2**). Moreover, the thermo-sensitive nature of the proposed PUR-based hydrogels allowed a fine modulation of viscosity by changing the printing temperature. Viscosity modulation was thus

exploited to print the bioinks in the biphasic or gel state, thus maximizing printing resolution and cell viability using different nozzles and printing parameters.

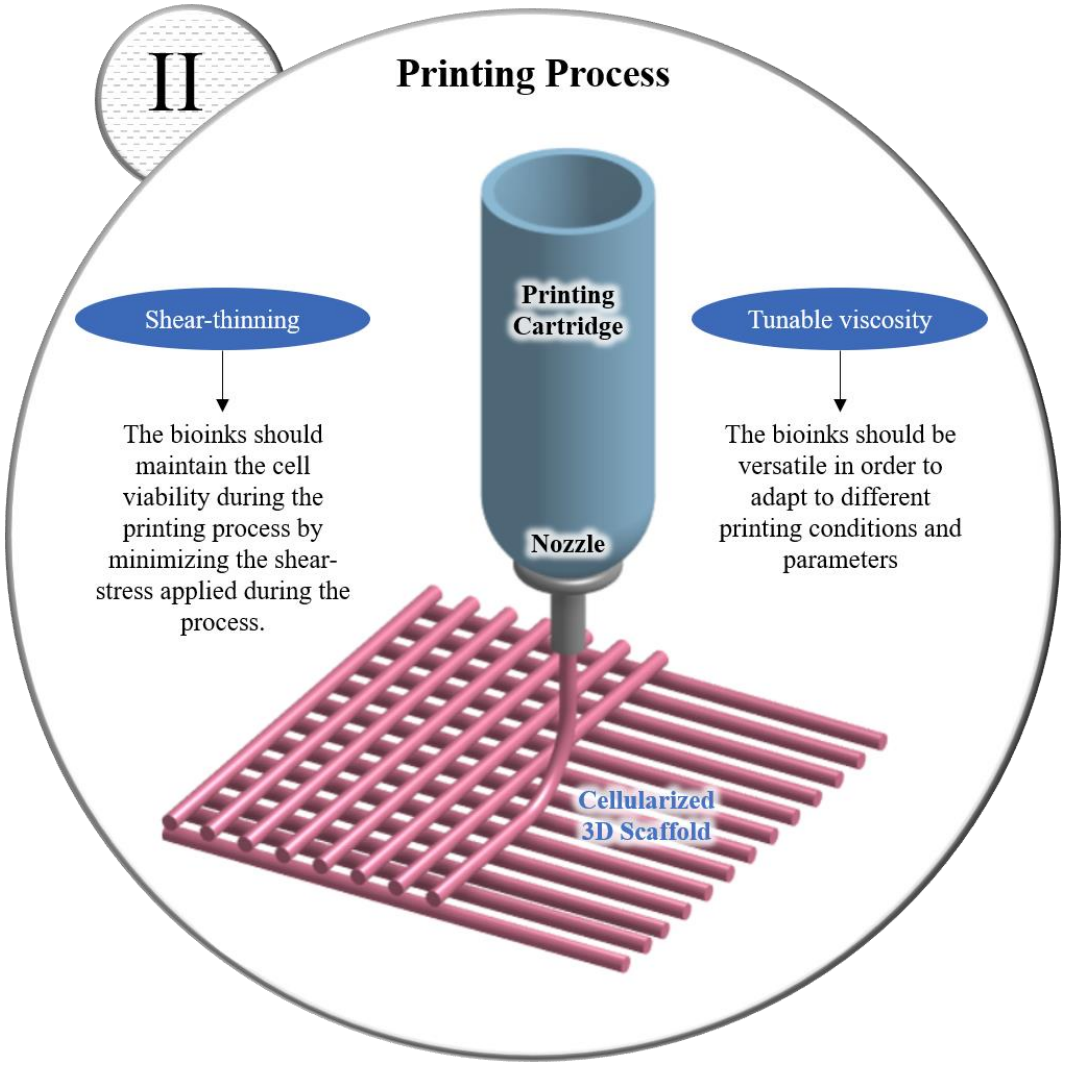

Figure 5.2 Second bioprinting step (printing process) and bioink properties.

When the bioink is extruded in the shape of thin filaments (210-450 µm) it needs to undergo a fast sol-gel transition in order to fix the shape and support the successive printed layers (**Figure 5.3**). The fast sol-to-gel transition of the designed systems helped in rapidly fixing the shape at 37 °C.

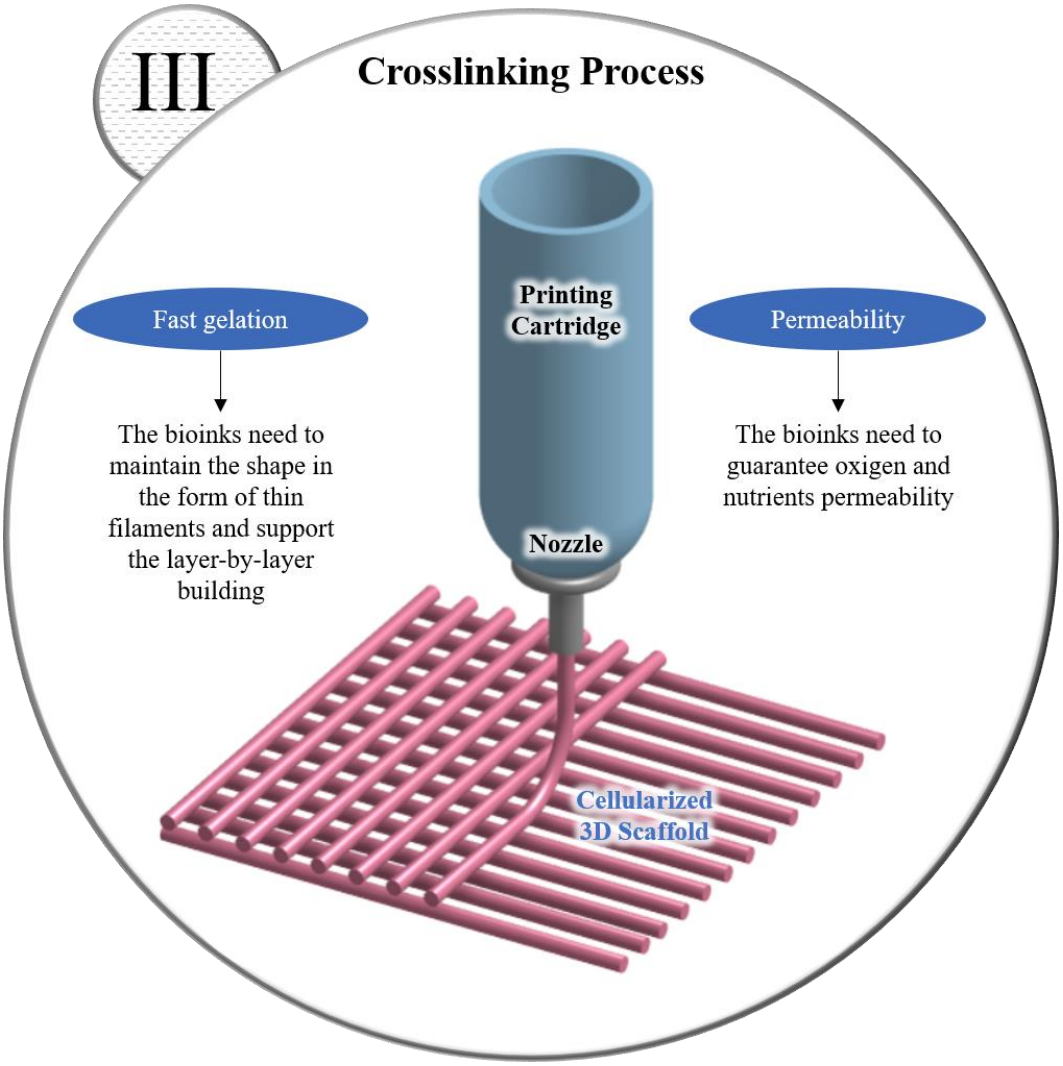

Figure 5.3 Third bioprinting step (crosslinking process) and bioink properties.

However, the physical crosslinking originated by the hydrophobic interactions and hydrogen bonds of thermo-sensitive sol-gel systems alone would not guarantee enough stability of the printed structures in water environment, as thoroughly discussed in the previous chapter. Thus, a second crosslinking step, involving the photo-sensitive components of the bioink, was added to the process (**Figure 5.4**). This last step, performed every layer or on the final scaffold, created a chemical crosslinked mesh that drastically increased scaffold water stability as well as its mechanical properties.

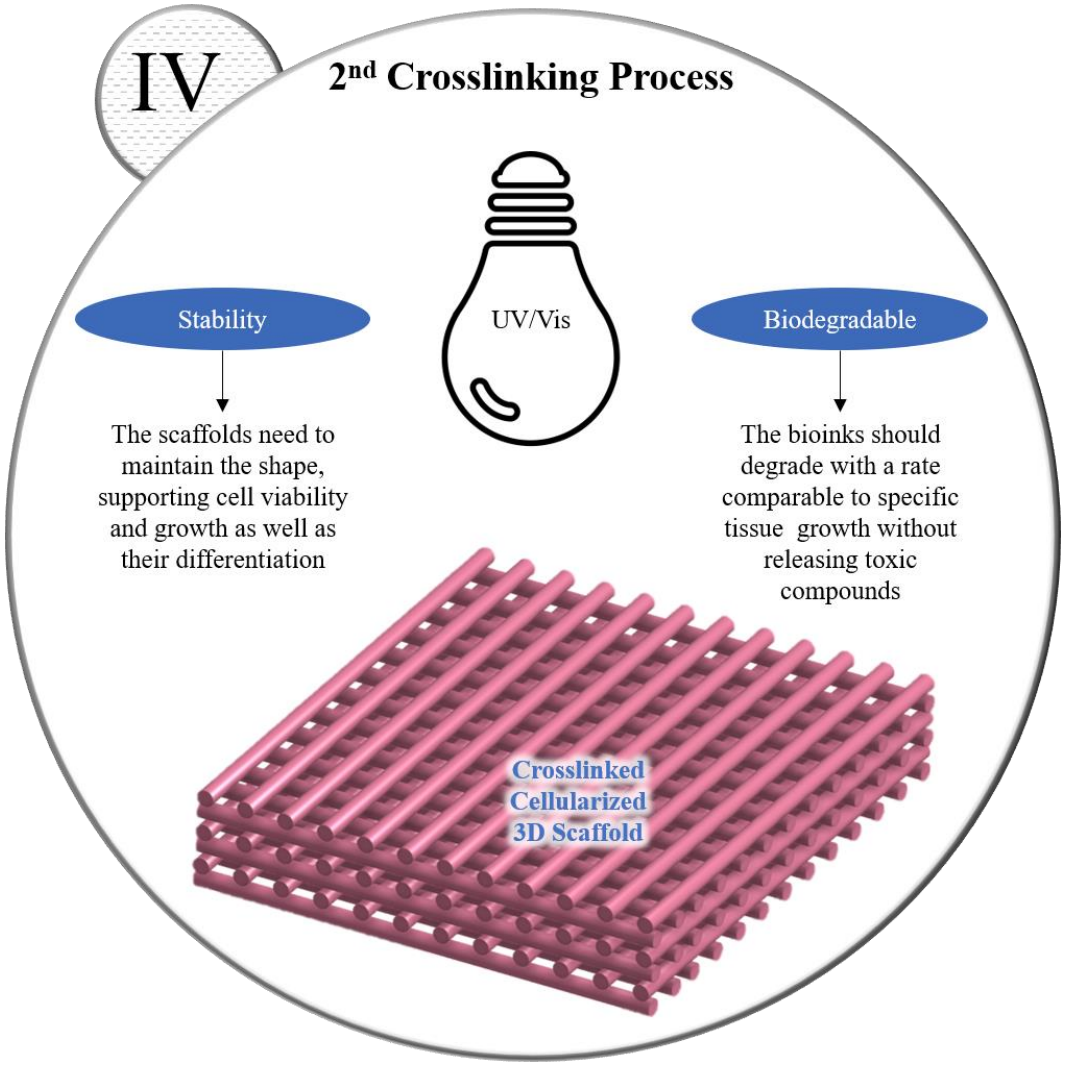

Figure 5.4 Extra bioprinting step (second crosslinking process) and bioink properties.

The next paragraphs report a detailed description of the bioprinting process and its biological validation using the previously designed thermo- and photo-sensitive bioinks and human mesenchymal stem cells, as well as the 3D printed scaffolds physico-chemical and biological characterization.

5.2. Materials and Methods

5.1.1. Bioprinter Modifications

A commercial bioprinter (Inkredible +, CELLINK) was modified in order to be able to print thermo- and photo-sensitive bioinks. The Inkredible + bioprinter is a pneumatic extrusion-based system with two extrusion heads with temperature control (**Figure 5.5**).

The temperature over the extrusion cartridges of the Inkredible + bioprinter can be increased from room temperature to 130 °C, thus allowing a fine control of the viscosity of the thermo-sensitive component of the bioink during the printing process. This allowed to easily encapsulate the cells below room temperature and successively tune the viscosity in order to print the bioinks in the gel or biphasic sol-gel state. However, in the original set-up of the printer no temperature control is possible on the printing platform. This results in the impossibility to maintain the temperature of the extruded structures that is a key point to fix the shape and avoid the flattering of the extruded filaments and the collapse of the layers on each other.

Hence, in order to be able to print thermo-sensitive inks with a sufficient resolution and printing fidelity, a surface heater on the printing platform of the Inkredible + was added. In this way the printed structures can be maintained around 37 °C, thus fixing their shape by exploiting the thermo-sensitivity of the designed bioinks. A surface heater with a temperature controller was designed and fabricated (SOLID HEAT, Singapore). The heater was designed as a (128 x 86 x 2.5 mm) silicon layer embedding a heater coil in order to fit the printing platform, guarantee waterproofness and maintain the surface flat. Two thermocouples were added to detect the temperature of the heater and the printing platform, respectively (heater control and monitor). An aluminum surface (0.9 mm) was glued on the silicon surface heater to enhance heat transfer.

Figure 5.5 Inkredible + bioprinter (CELLINK).

In order to mount the surface heater on the Inkredible +, a hole was necessary to pass the wires through the printing platform (**Figure 5.6**). Instead of piercing the original platform a new platform was 3D printed with ULTIMEKER 2 fused deposition modeling 3D printer using PLA as building material. The 3D model was prepared with SolidWorks software and sliced with Cura software. The surface heater was eventually glued on the new platform and a mechanical end-stop switch was added on the side of the platform to allow the homing and the calibration of the z axis.

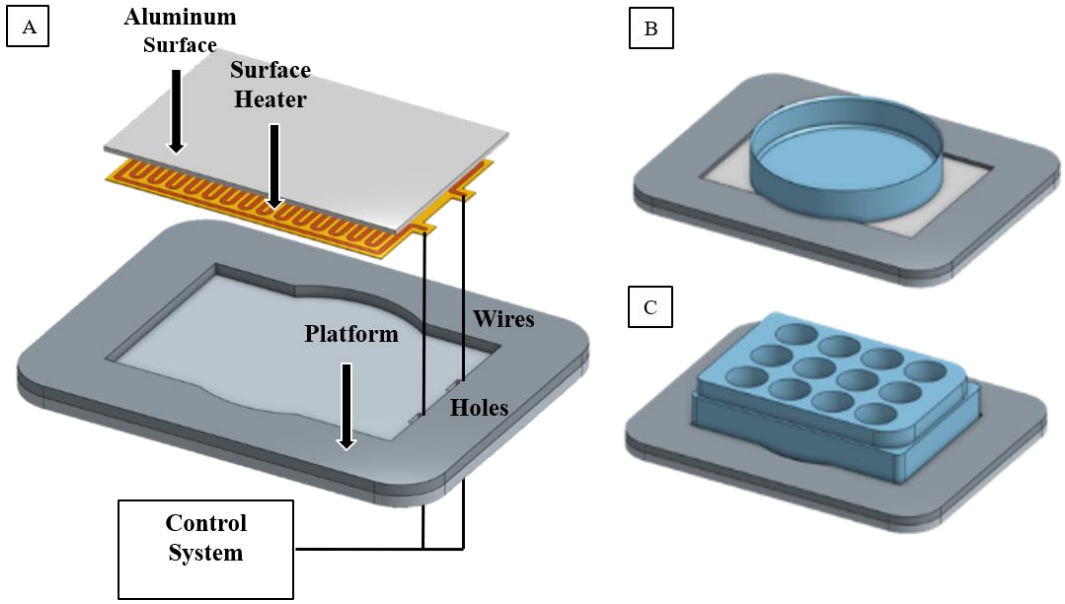

Figure 5.6 (A) Model of the 3D printed printing platform with the holes and the surface heater. **(B, C)** Model of the platform with a petri dish and a multiwell plate, respectively

The Inkredible + was initially equipped with a 405 nm led source mounted behind the two extrusion heads and in a position more elevated with respect of the nozzles. The 405 nm wavelength was initially chosen in order to use 2,4,6-trimethylbenzoylphosphinate -LAP- as photoinitiator. However, the first crosslinking tests pointed out the process is not really efficient and quite slow (**Figure 5.7**).

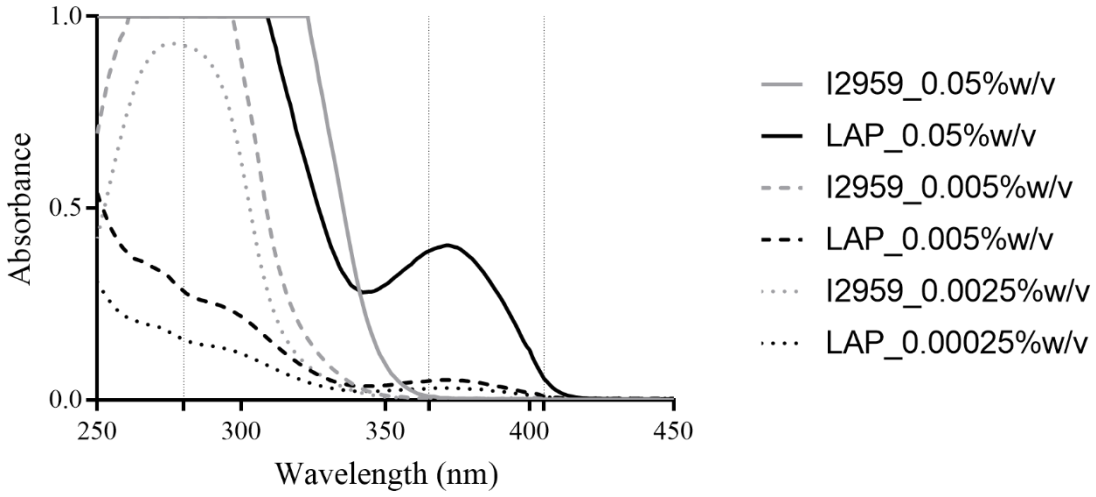

Figure 5.7 UV-Vis spectra of I2959 and LAP aqueous solutions

For this reason, as well as for the possibility to use also 2-hydroxy-1-[4-(2-hydroxyethoxy) phenyl]-2-methyl-1-propanone) - Irgacure 2959 or I2959- as photoinitiator, a 365 nm led was mounted inside the bioprinter exploiting one of the extrusion heads as support thus allowing to control its position directly from the software of the bioprinter. 365 nm wavelength was chosen because it is at the threshold between UV and visible spectra and literature works have reported its cytocompatibility and safety in terms of DNA denaturation and mutation at low energy densities (in the range tens mJ/cm^2).[7-10]

The Inkredible + is currently also available with a 365 nm led mounted behind the two extrusion heads and in a position more elevated with respect of the nozzles. However, this set-up does not allow to properly control the irradiation step: (i) no possibility to modulate light intensity, (ii) difficulty in centering the light beam on a specific spot, (iii) partial light shading by the extrusion head, and (iv) impossibility to reduce the distance between the led and the printing platform due to the extrusion heads' intrusion. UV-shielded cartridges have been purchased (SAN-EI TECH) to avoid the crosslinking of the ink within the cartridge and the consequent clogging of the nozzle. In order to mount the third-part cartridges inside the extrusion heads, the valve/cartridge adaptors were also changed. In order to make the instrument safe for the user, a UV light shield film was put on the transparent surfaces of the printer case.

The 365 nm led was chosen in order to have an irradiation system with a power density of 5-50 mW/cm^2 on a surface of 1-2 cm^2 (**Figure 5.8**). A led controller was built in order to forward a constant current to the led and a power meter was added to control its intensity.

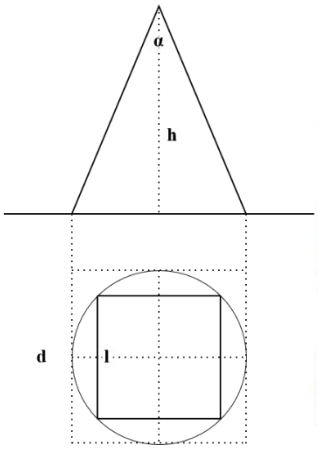

$$l = \frac{d}{2}\sqrt{2}$$

$$d = \frac{2*l}{\sqrt{2}}$$

$$B = \frac{P}{4*\pi*h^2}$$

$$h = \frac{d}{2}\cot\alpha$$

$$\alpha = \operatorname{arccot}\frac{2*h}{d}$$

Figure 5.8 Intensity *versus* distance calculations for led design.

Initially the LED was mounted directly on a PCB board connected to the controller (**Figure 5.9 A**). However, after many hours of use, the led started to become unstable probably because of the temperature increase due to the high electric current needed to power the led. Hence, the led has been mounted on a heat dissipater to avoid temperature increase (**Figure 5.9 B** and **Figure 5.9 C**).

Both the wavelength and the stability of the forward power density of the led were checked to ensure the stability of the crosslinking system.

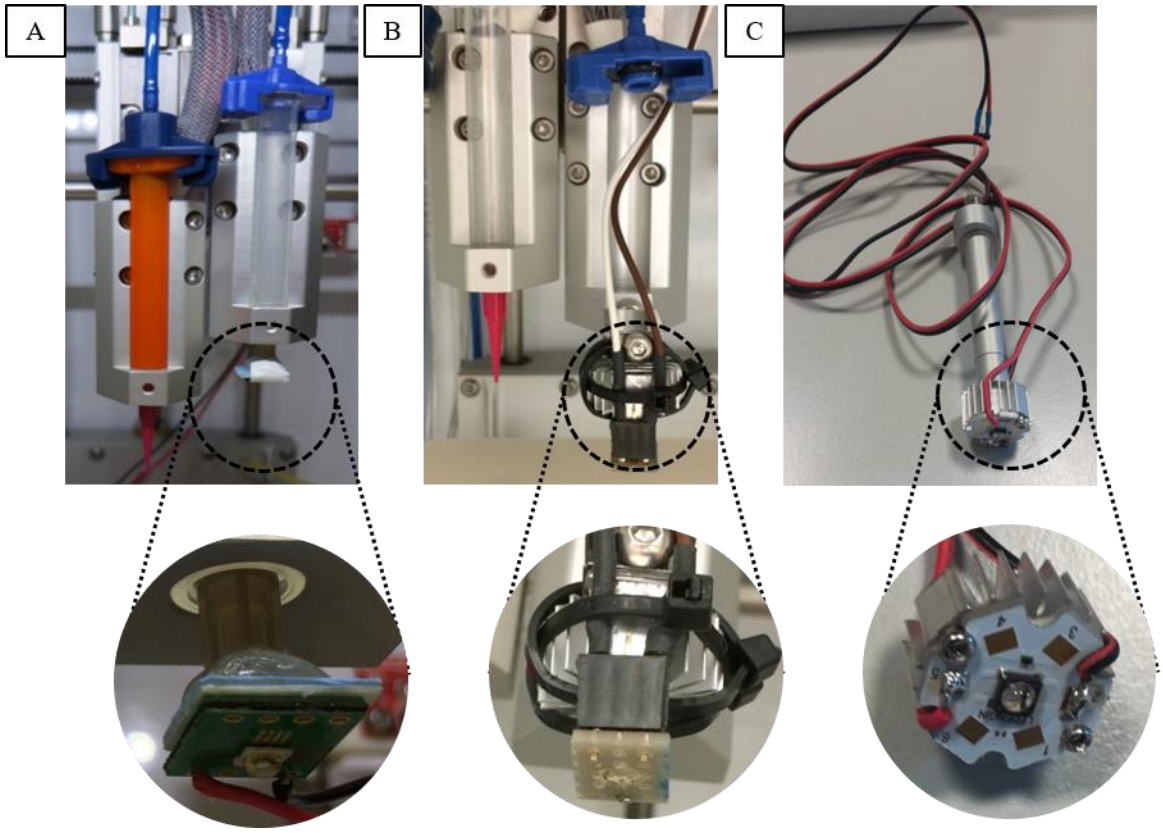

Figure 5.9 Pictures of the crosslinking system: **(A)** led mounted directly on the PCB board **(B)** led attached to a heat dissipater **(C)** final crosslinking system.

5.1.2. Custom Made G-CODE

Typically, the 3D printing process involves three steps: (i) preparation of a 3D model in the form of STL file, (ii) slicing of the model through a slicing program in order to obtain the G-CODE (code used to communicate to the 3D printer the actions and the movements to be performed), (iii) printing of the 3D structures layer-by-layer (**Figure 5.10**).

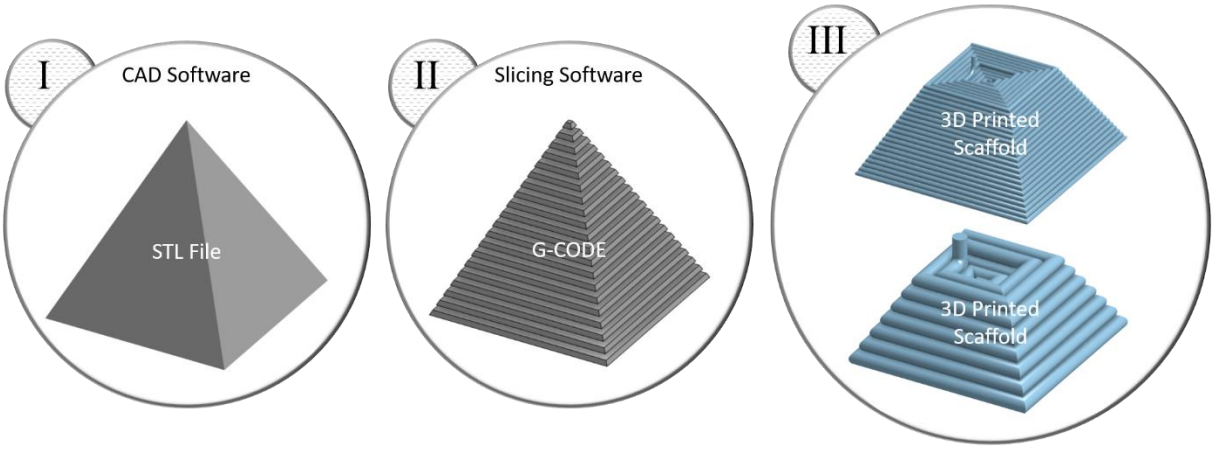

Figure 5.10 3D printing process steps: **(I)** design of STL file from biomedical images or CAD software; **(II)** slicing of the 3D model in 2D slices and G-CODE formulation; **(III)** printing of the model layer-by layer (the resolution depend on the slicing process and the nozzle diameter).

This approach works well with complex objects, when the focus is more on the final shape than the internal structure. However, in TERM application a precise control on all parameters and nozzle movements is mandatory.

Initially, NHP407-based inks were printed from a continuous filament in the shape of 1.5x1.5 cm squares with 4 layers and a 90/90° grid pattern. The scaffold was designed by creating a STL file with the desired dimensions with SolidWorks. The STL file was then sliced through the Slicer software in order to obtain the grid pattern of the different layers and the relative G-CODE (**Figure 5.11 A**). Eventually the obtained G-CODE was uploaded on Repetier-Host Software to control the bioprinter's movements/actions. By printing the structures using a continuous filament, during the changes of direction of the nozzle, the filament was pulled because of ink high viscosity (**Figure 5.11 B**). The pulling of the extruded filament did not allow to properly deposit it and caused a loss in resolution and sometimes the fusion of two consecutive filaments.

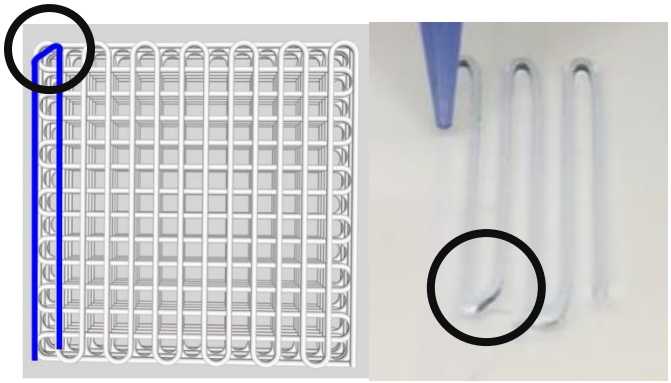

Figure 5.11 Preview and printed filaments artifact.

As the Inkredible + does not allow to control the pressure during the printing process, the only available way to overcome this issue consisted in reducing the speed of the nozzle. Although the resolution problem was partially solved, the printing process became very slow because the speed of the nozzle had to be reduced, particularly during the direction changes.

Hence, a custom-made printing process was finally designed to print highly resolved circular scaffolds based on thermo- and photo-sensitive bioinks. The overall process consisted of two steps. (i) A constant pressure extrusion, in which the pressure valve is closed during all direction changes to avoid pulling of the filament by the printing nozzle, that has detrimental effects on both resolution and geometry fidelity. (ii) The photo-crosslink of each layer, in which the UV led (mounted on the second extrusion head of the Inkredible +) is centered on the scaffold and lowered at the proper distance.

With the aim of printing even more complicated 3D structure, an optimization of the printing process is crucial. Particularly, by using the Slicer software, it was not possible to automatically add to the G-CODE the commands to open/close the pressure valves and adjust the led positions (second extruder). For this reason, a first C script was coded in order to read the G-CODE that is obtained from the slicing process and write a new G-CODE with the on/off commands for the valves and the commands of the photo-crosslinking process (**Figure 5.12**).

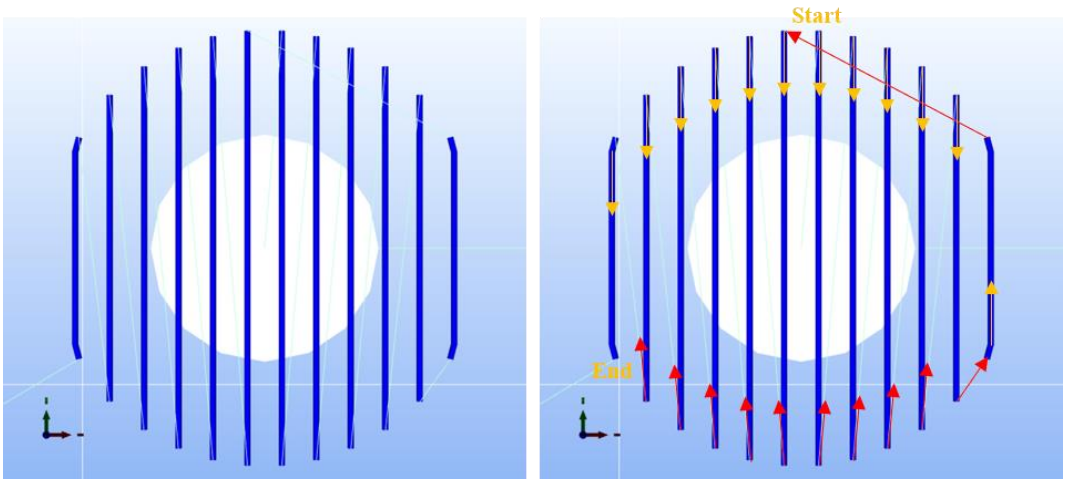

Figure 5.12 Preview of the movements performed by the printer according to the G-CODE obtained from the classic approach and adding the on/off commands for the pressure valve. The thick dark blue lines (yellow arrows direction) identify the printed filaments (pressure valve on), while the thin light blue lines (red arrows direction) represent the movement of the nozzle without printing (pressure valve off).

By exploiting the new G-CODE the printing process was still affected by artefacts: the fast change in the direction of the extrusion head at the end of each filament caused its pulling. In order to avoid this phenomenon, the C script was changed in order to further increase the printing resolution and fidelity (**Figure 5.13**).

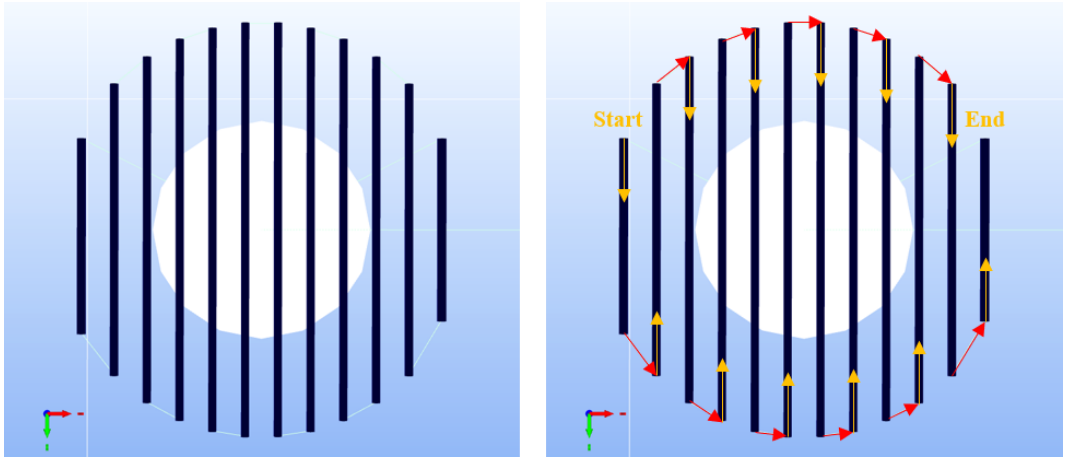

Figure 5.13 Preview of the movements (x and y axes) performed by the printer following the custom-made G-CODE. The thick black lines (yellow arrows direction) identify the printed filaments (pressure valve on), while the

thin light blue lines (yellow arrows direction) represent the movement of the nozzle without printing (pressure valve off).

The same C script was also coded in order to add to the G-CODE the commands that provides the actions for the photo-crosslinking process at the end of each layer. Moreover, a second C script was coded to allow the printing on different multiwall. To this aim, the script reads the previously modified G-CODE and writes a new G-CODE changing the X and Y coordinates to center the nozzle and the led on a specific well, and the Z coordinate to avoid any crash of the nozzle on the well walls every time the printer switches from extruder 1 to extruder 2 with the led (**Figure 5.14).**

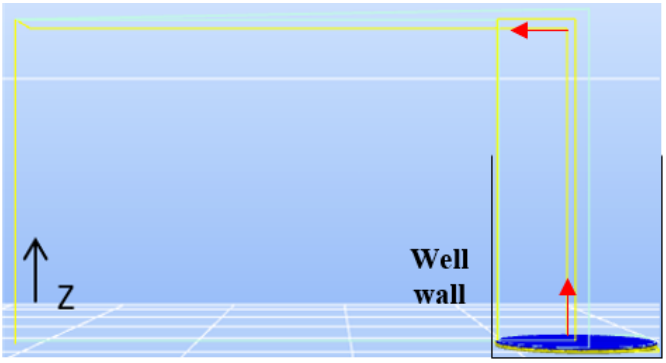

Figure 5.14 Preview of the movements (z axis) performed by the printer following the custom-made G-CODE. The process allows to center the LED and to control both distance and irradiation time.

The whole process had to be repeated every time the scaffold design (i.e., dimension, number of layers, filament diameter, gap, infill angle) or printing parameters (i.e., printing speed, movements without printing speed) were changed. In order to make changes easier, a new C script was coded to directly write the custom-made G-CODE, without starting from a G-CODE generated by the slicing software. In the second version of the custom-made G-CODE, diagonal movements were avoided and the nozzle continued in the same direction of the previously printed filament before changing its direction horizontally to print the next filament. In this way,

the smooth change of position allowed the filament to be deposited, avoiding any pulling phenomenon (**Figure 5.15**).

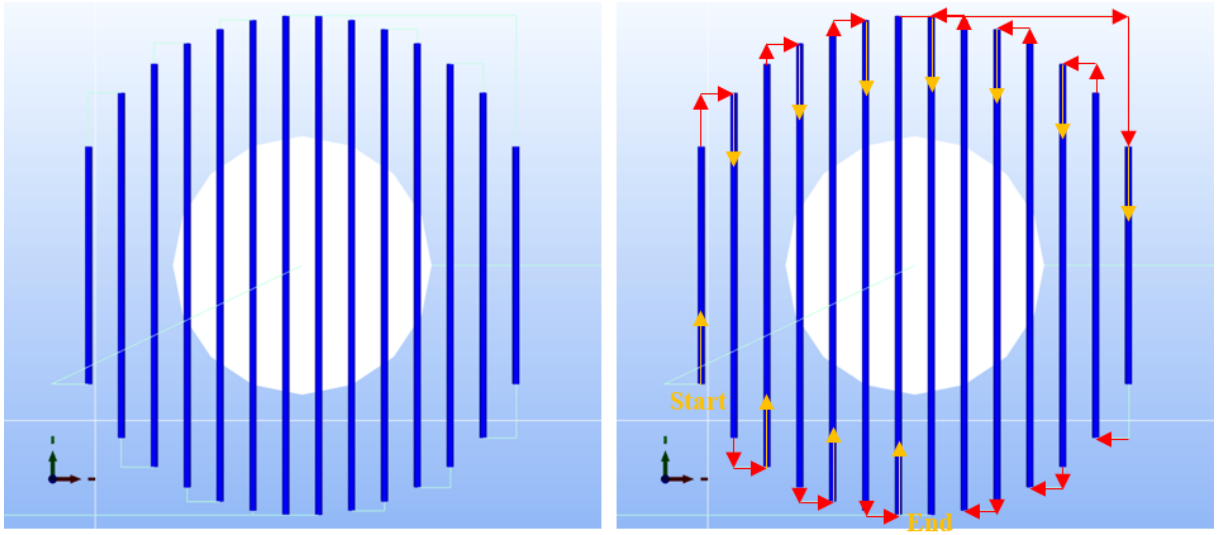

Figure 5.15 Preview of the movements (x and y axes) performed by the printer following the custom-made G-CODE. The thick dark blue lines (yellow arrows direction) identify the printed filaments (pressure valve on), while the thin light blue lines (red arrows direction) represent the movement of the nozzle without printing (pressure valve off).

Figure 5.16 shows the overall printing/photo-crosslinking process of a two layer circular scaffold with grid geometry following the custom-made G-CODE. The control over all the process as well as the possibility to turn on/off the pressure valve is expecting to allow the printing of more complex structures in the future.

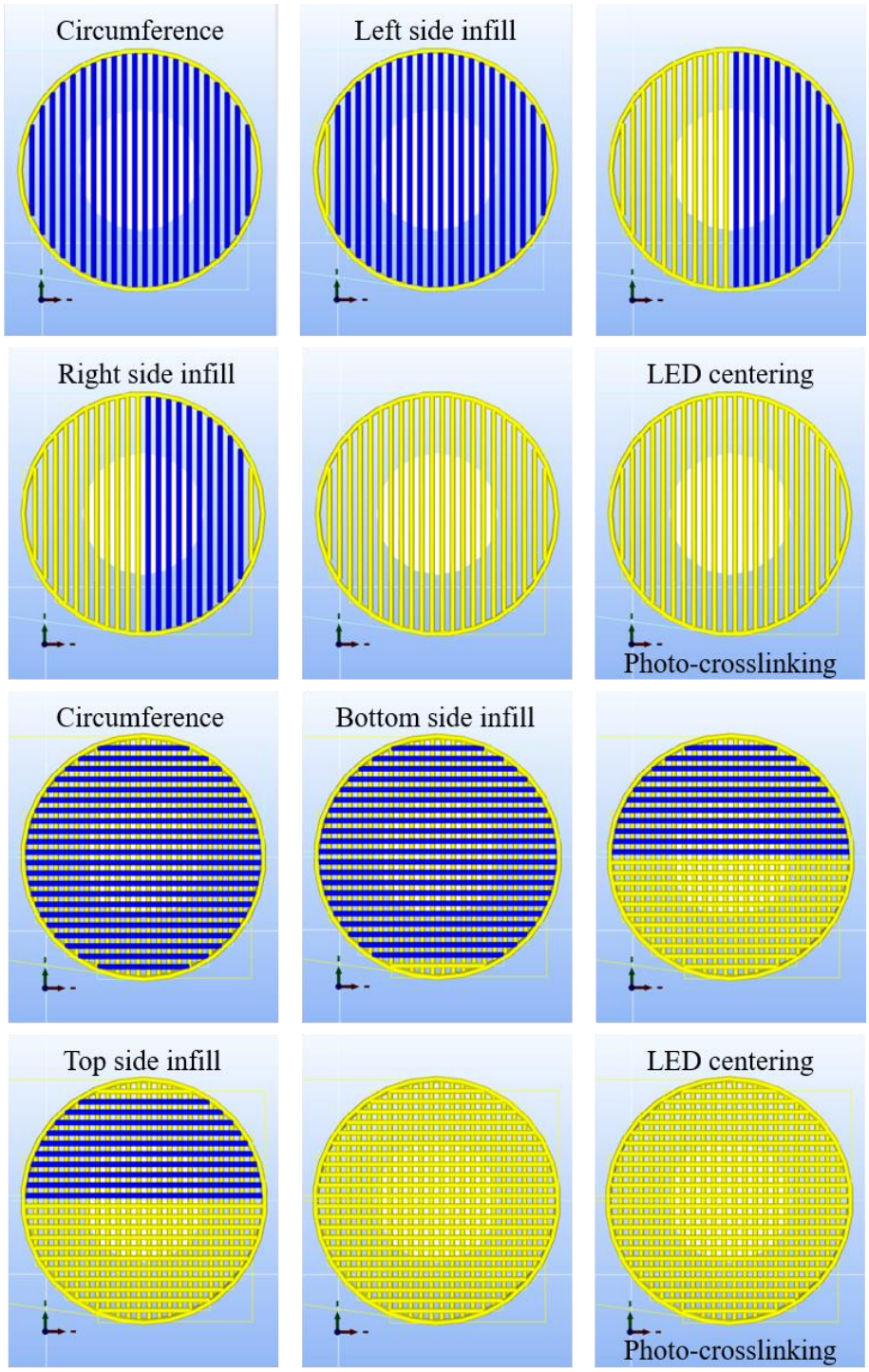

Figure 5.16 Preview of the customized printing process.

The entire C script and the obtained G-CODE are reported in **Appendix 1**.

5.1.3. Cellularized Bioink Preparation

Human mesenchymal stem cells, such as bone marrow-derived mesenchymal stem cells, have been proved to be valuable candidates in TERM applications, due to their ability to self-renew indefinitely, their autologous origin and the possibility to direct their differentiation into different cell phenotypes.[11-19]

Thermo/photo-sensitive bioinks were prepared as previously reported (Chapter 4) in glass vials and kept at 5 °C. MSCs were collected, counted and resuspended in order to have 1 million cells in few µL (10-20 µL). A water bath at 5 °C was then prepared and put inside the biosafety cabinet (BSC). Eventually the glass vials with the bioinks were transferred inside the BSC in the water bath at 5°C. The cells were added to the bioinks formulations and dispersed by pipetting up and down while maintaining the glass vial within the water bath at 5°C.

5.1.3.1. Media and Reagents

Human bone marrow-derived mesenchymal stem cells (MSCs) were purchased from ATCC (PCS-500-012). MSCs were cultured in T175 cell culture plate (Corning) previously coated with a gelatin solution (0.1 %w/v) in deionized (DI) water and incubated at 37 °C for 1 hour. The MSCs were passaged until passage 6 before using them.

MSC culture medium was prepared by adding to Dulbecco's Modified Eagle Medium -DMEM- (Gibco 11965) 10 %v/v of Fetal Bovine Serum -FBS- heat inactivated (Gibco 10270), 1 %v/v of Penicillin-Streptomycin -PEN-STREP- (Gibco 10378) and 0.001% of 1x Basic Fibroblast Growth Factor -bFGF-. MSC culture medium was store at 5 °C for not more than 4 weeks.

MSC freezing medium was prepared by adding to DMEM 50 %v/v of FBS heat inactivated and 10% Dimethyl Sulfoxide -DMSO- (Sigma Aldrich D2650). MSC freezing medium was prepared just before its use.

5.1.3.2. Mesenchymal Stem Cell Culture

MSCs were first thaw by immerging the cryovial (10^6 cells/mL) in a 37 °C water bath for 2-3 min. Once thawing, the cells were dispersed in 13 mL of MSC culture medium within a 50 mL centrifuge tube. The cells were then collected by centrifugation (5 minutes at 300 G and 25-37 °C) in order to remove the freezing media containing DMSO. After removing the freezing medium, the cells were dispersed in 5 mL of fresh MSC culture medium and counted upon staining with Trypan blue 50/50 (EVE Automatic cell Counter -EVS-050-). The cells were then plated inside a gelatin-coated T175 flask after addition of 20 mL of MSC culture medium. The MSC culture media was changed every other day. The cells were passaged at 80-90% confluency (usually 7-10 days).

In order to collect the MSCs from the flask, the culture medium was first aspirated and the flask was washed with Dulbecco's Phosphate Buffer Saline -DPBS- (13 mL) to remove FBS traces. Trypsin-EDTA (EthyleneDiamine Tetraacetic Acid) solution in DMEM (0.05 %w/v) was added (2-3 mL) and the cells were incubated at 37 °C for 2-3 minutes to detach them from the flask. MSC culture medium was then added to neutralize trypsin (13 mL) and the cells within the medium were transferred in a 50 mL centrifuge tube and centrifuged for 5 minutes at 300 G and 25-37 °C. MSC culture medium was added (1 mL) and the cells were counted. Successively the MSC were passaged or freeze.

In order to freeze them, after cells collection into a pellet through centrifugation, the supernatant was aspirated off and freezing medium was added (10^6 cells/mL). The cells were then transferred inside a cryovial and put in freezing container (Mr. Frosty) at -80 °C for 4/6 hours. Eventually the cryovials were placed in liquid nitrogen tank for long term storage.

5.1.3.3. Cell Label

Before encapsulation in the designed bioinks, MSCs were labeled with PKH26 cell membrane linker (Sigma Aldrich) following vendor protocol.[20, 21]

Briefly, MSCs were cultured and collected according to the previous cell culture protocol. The cells were then washed with fresh medium w/o FBS and collected again (centrifugation at 350 G for 5 min). The cells were eventually resuspended in 1 mL of Diluent C and added to 1 mL of Dye Solution in Diluent C. The cells were then mixed and incubated for 5 min with periodic mixing. The staining process was stopped by adding 2 mL of FBS and incubating for 1 min. The labeled cells were collected (centrifugation at 350 G for 5 min) and washed twice with compete MSC culture medium.

5.1.4. Biological Validation of the Bioprinting Process

One of the most critical aspect in the designed bioinks concerns their formulations and polymer contents:

By increasing the concentration of the thermo-sensitive component (NHP407 or HHP407), the viscosity of the hydrogel increases. Thus, the cells could be subjected to a greater shear stress during the extrusion of the bioink, with the risk to break their membrane. On the other hand, by decreasing the concentration of the thermo-sensitive component (NHP407 or HHP407), the printing resolution is affected due to reduction of the hydrogel strength and the resultant collapse of the lower layers.

By increasing the concentration of the photo-sensitive component (PEG-DA or HHP407), instead, the flow of oxygen and nutrient through the scaffold is expected to decrease, with the risk of cell hypoxia. However, as previously demonstrated (Chapter 4) the addition of PEGDA increase the shear-thinning behavior of the bioinks reducing the share stress applied to the cells.

On the other hand, by decreasing the concentration of the photo-sensitive component (PEG-DA or HHP407), the scaffolds stability in water environment and their mechanical properties could be affected.

Another key aspect for the bioprinting process is the sterility of the system (both bioinks and instruments).

Concerning the cartridges and the nozzles, two different methods have been tested: (i) autoclave and (ii) 70%v/v EtOH/H_2O washings (x2) followed by autoclaved DI H_2O washings (x2). In order to assess sterility DMEM without antibiotics was pushed through the cartridges and nozzles, and incubated at 37 °C. The medium was then visually checked under the inverted microscope in order to detect contamination up to 7 days.

Concerning the bioinks sterilization, instead, because of the low viscosity of photoinitiators and PEGDA solutions, it was possible to sterilize them by filtration through a 0.2 µm syringe filter. On the other hand, due to their thermo-sensitive behavior, PUR-based solutions were not suitable for sterilization via filtration. Hence, PUR powders were sterilized before solubilization through UV light exposure under the biosafety cabinet (254 nm for 1 hour). The bioinks sterility was assed by incubating them with DMEM without antibiotics and visually checking the latter up to 7 days, to detect contamination.

Other critical aspects for the bioprinting are the printing (e.g. applied pressure -30÷200 kPa-, nozzle diameter -200÷450 µm-, nozzle speed -150÷300 mm/min- and temperature -25-37 °C-) and crosslinking parameters (e.g. UV light intensity -2.5÷10 mW/cm^2-, irradiation time -1÷6 min-, photoinitiator type and concentration - Irgacure 2959 and LAP, 0.05÷1 %w/v).

In fact, by increasing printing pressure, the process can be accelerated, as a consequence of the increased feed rate and printing speed. On the other hand, higher pressure induces higher shear stress applied on the encapsulated cells, and thus decreased cell viability.

The nozzle diameter affects both the resolution (the smaller the nozzle diameter is the higher the resolution is) and the shear stress applied to the cells (it increases with decreasing the nozzle diameter, and as a consequent cell viability decreases).

By increasing printing temperature, the thermo-sensitive bioink formulations become more stable and can better maintain the shape. However, the pressure needed to print the bioink increases with a consequent decrease in cell viability.

By increasing UV light intensity, the photocrosslinking process is expected to become faster and more efficient. However, too high UV intensity might damage the encapsulated cells.

The mentioned parameters are usually connected to each other and to the bioink formulation (e. g., by increasing PUR concentration or printing temperature, or by decreasing nozzle diameter, the pressure needed to print the scaffold increases). For this reason, the effects of each previously described aspect on the resulting constructs were studied separately in order to minimize cell death and maximize printing resolution. In order to assess the biocompatibility of the materials and the effects of the printing/photo-crosslinking process, cell viability and proliferation assays have been performed (Presto blue and Live/Dead assay, respectively).

5.1.4.1. Printing Parameters

Cell viability during the extrusion process, as previously discussed, is mainly affected by the shear stress applied to the encapsulated cells as well as the biocompatibility of the bioink itself. For thermo-sensitive bioinks such as the NHP407- and HHP407-based ones, the shear stress within the hydrogels and the printing resolution are affected by many factors (**Figure 5.17**): (i) bioink composition and viscosity, (ii) nozzle diameter and (iii) printing parameters (i.e. temperature, pressure and printing speed).

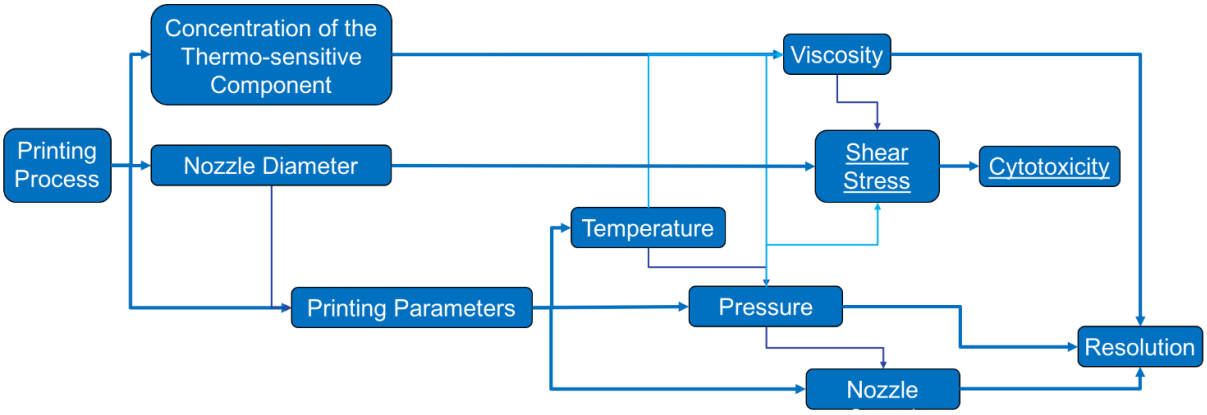

Figure 5.17 Printing parameters interconnection.

Because many factors are involved in the process, in order to perform the printing test, the feed rate and the temperature were kept constant (i.e. 50 µL/min and 25 °C, respectively). The feed rate was previously calculated by weighing different ink samples (inks of different PUR concentration have been tested) extruded with different pressures and estimating the hydrogels density by weighing a specific volume of the hydrogels. The temperature was chosen from the rheological data (Chapter 4), because all the formulation turned out to be biphasic sol-gel systems. The 210 µm nozzle was selected among the tested nozzles (i.e. 450, 250, 210 µm) because it represented the worst and more critical condition for cell viability.

Due to the rheological similarity between the two PURs (NHP407 and HHP407) only NHP407-based formulations were tested. In fact, the latter PUR owned higher viscosity and higher G' modulus, thus representing the worst case in terms of shear stress applied to the cells (Chapter 4).

In order to verify the cytocompatibility of the printing process, solutions with different concentrations of NHP407 (10, 12.5, 15 and 17.5 %w/v) were printed upon MSCs encapsulation. MSCs (passage 6) were expanded until they reached approximately 85% confluence and then mixed with the hydrogels (obtained by solubilizing the thermosensitive

component in DMEM at the desired concentration) at 5 °C (1 M cells/mL). The hydrogels were transferred into the bioprinter cartridges and stored at 5°C for 5 min in order to remove the air bubbles. Successively, the cartridge was mounted inside the bioprinter with the nozzle and warmed at 25 °C for 5 minutes before the beginning of the printing process to allow a complete gelation of the systems. Finally, the hydrogels were printed inside a 24 well plate in the shape of circular scaffold (scaffold dimeter: 1 cm, filament diameter: 210 µm, gap between the filaments: 210 µm) obtained through the custom-made G-Code and using the previously determined pressures and a nozzle of 210 µm. In this way, approximately 18.5 µL were extruded (20 k cells / well) in each well. Eight different samples for each concentration were printed in order to simulate the printing of 8 consecutive layers. The cell viability of the cells embedded within the extruded bioinks was assessed by Live-Dead assay, according to manufacturer's protocol, immediately after the printing. Briefly, the reagents were first solubilized in PBS and added to each sample. After samples incubation at 37 °C for 1 hour, a fluorescence microscope (Olympus IX73) was used to detect the signals of live and dead cells.

5.1.4.2. Photo-crosslinking Parameters

Cell viability during the photocuring process can be affected by different factors such as (i) wavelength and power density of the light, (ii) photoinitiator type and concentration and (iii) bioink composition and components concentration (**Figure 5.18**).

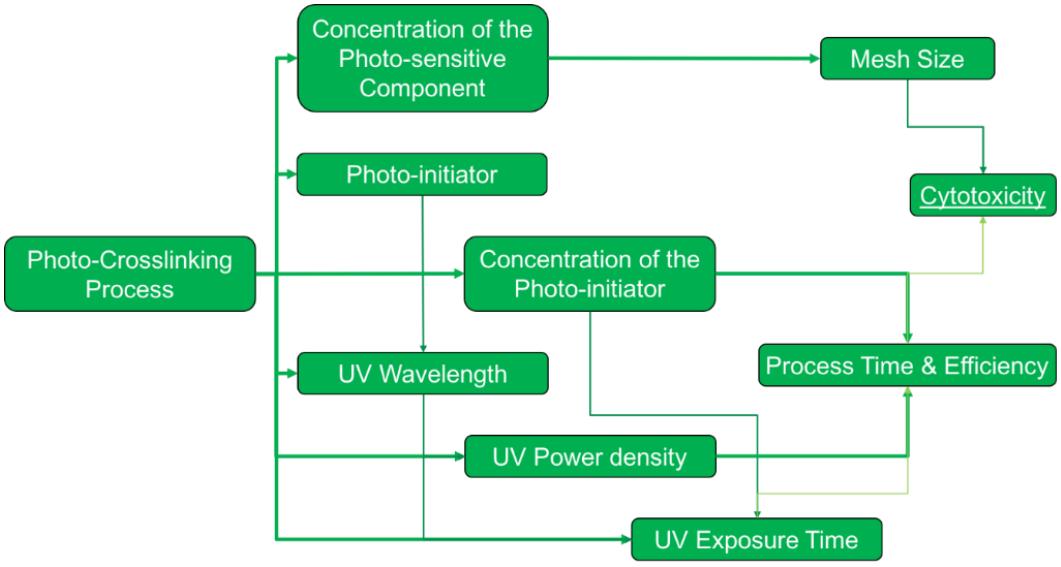

Figure 5.18 Photo-crosslinking parameters interconnection

UV-light induced cytotoxicity was assessed by testing the effects of different power densities and exposure times to a 365 nm light source. MSCs (passage 6) were seeded in 24 well plate and expanded until they reached approximately 85% confluency (1 mL of medium containing 500K/mL cells for each well). Eventually they were exposed to 365 nm UV light at different power densities (5, 7.5 and 10 mW/cm^2) for different exposure times (1, 3 and 6 minutes). Cell viability was assessed by Live-Dead assay after 24 hours from the irradiation, according to manufacturer's protocol. Briefly, the reagents were first solubilized in Phosphate Buffered Saline (PBS) and added to each sample. After samples incubation at 37 °C for 30 minutes, a fluorescence microscope (Olympus IX73) was used to detect the signals of live and dead cells. Three samples for each condition were prepared and tested.

Photoinitiator induced cytotoxicity was assessed by testing the effects of Irgacure2959 (I2959) and lithium acylphosphinate salt (LAP) on MSC viability. MSCs (passage 6) were seeded in 24 well plate and expanded until they reached approximately 85% confluency (1 mL of medium containing 500K/mL cells for each well). After 24 hours, MSCs were exposed to I2959 and LAP solutions at 0.05, 0.10, 0.25, 0.50, 0.75 and 1 %w/v concentrations. To this aim, LAP was

solubilized at 1 %w/v in DMEM and then diluted at each analyzed concentration, while I2959 was first solubilized at 10 %w/v in EtOH:H_2O (70:30 v:v) and then diluted at each tested concentration by adding DMEM. MSCs were incubated with the photoinitiators for different periods of time (30 minutes, 3 hours and 3 days). At the end of the exposure time, the medium containing the photoinitiators was removed, the samples were washed twice with Dulbecco's Phosphate-Buffered Saline (DPBS) and fresh Dulbecco's Modified Eagle Medium (DMEM) was added. Cell viability was assessed by performing PrestoBlue assay at different time points (day 0 -i.e. at the end of the exposure time-, 1, 3, 5, 7, 10), according to manufacturer's protocol. Briefly, 1mL of DMEM containing PrestoBlue reagent was added to each sample and fluorescence was measured through a plate reader after incubation at 37 °C for 1h. Three samples for each condition were prepared and tested. The different exposure times have been selected so as to simulate the printing process: (I) 30 minutes is the approximate time that the cells spend inside the cartridge in contact with the photoinitiator before the scaffold is printed and crosslinked. (II) 3 hours is the approximate time required for the complete swelling of the scaffold in the cell culture medium (if residual photoinitiator inactivated by the photo-crosslinking process is still present, its concentration will be reduced by the progressive medium absorption). (III) 3 days has been selected to simulate the pessimistic scenario that the photoinitiator is not completely inactivated during the photocrosslinking reaction and remains inside the printed structures in its native state.

In order to assess the cytocompatibility of the photo-sensitive polymers, PEGDA solutions at different concentrations were tested with MSCs. In detail, cell viability inside the photo-crosslinked structures was assessed by crosslinking the cellularized scaffolds obtained by casting PEGDA solutions with different concentrations (2.5, 5, 7.5 and 10 %w/v) and loaded with MSCs inside a 24 well plate in the form of a thin layer with 210 μm thickness (thus

simulating the thickness of the extruded filament from the bioprinter). MSCs (passage 6) were expanded until they reached approximately 85% confluence and then mixed with the hydrogels (obtained by solubilizing PEGDA in DEMEM at the desired concentration and adding 0.1 %w/v of LAP) at room temperature (500 K cells/mL). The hydrogels were poured in a 24 well plate in order to have a final thickness of approx..210 µm (around 40 µL). Successively, each scaffold was photo-crosslinked for 60 seconds (365 nm at 10 mW/cm^2) and 2 mL of DMEM were added. Cell survival and viability were assessed by Live-Dead assay and PrestoBlue assay, respectively, according to manufacturer's protocols.

5.1.5. Scaffolds Resolution

The 3D printed scaffold based on the different bioink formulation were analyzed under an inverted microscope (Zeiss Primovert) in order to assess their resolution and fidelity. In particular, both the scaffolds printed at 37 and 25 °C were studied in order to detect also the influence of the temperature on the printing resolution. The scaffold designed was the same as previously reported. The printing resolution was estimated by measuring the thickness of the extruded filaments and the gap between them, applying ImageJ to the collected images.

5.1.6. Scaffolds Swelling and Stability

Swelling and stability test were performed on the previously reported 3D printed scaffolds made of four layers and grid pattern, using different NHP407/PEGDA- and HHP407/PEGDA-based formulation and different UV irradiation time (i.e., 30 and 60 sec). Such tests were performed in order to assess the possibility to tune scaffold residence time in aqueous media by changing the bioink components as well as the printing parameters. The adopted protocol was the same

as previously reported (based on **Equation 1** and **Equation 2 -** Chapter 3 and 4), with the exception of the time steps. In fact, incubation time of the samples was here increased up to 2 months in order to assess long term stability.

The stability in water environment was also assessed by means of scanning electron microscopy (SEM) imaging (LEO 1420 microscope, Zeiss).

5.1.7. Scaffolds Mechanical Properties

Scaffold mechanical properties were estimated by means of Atomic force microscopy (AFM) nanoindentation and compression test.

Nanoindentation was preliminary performed in order to estimate the local stiffness sensed by the encapsulated cells as well as to assess the possibility to modulate scaffold mechanical properties working on the printing protocol and the ink formulation. The tests were performed on a Bioscope RESOLVE AFM system (Bruker) using PFQNM-LC probes (17 um high, 70 nm radius, and k=0.1N/m). The instrument was set on Force Spectroscopy in Liquid mode, and Sneddon model was applied to the data. The samples were prepared by gluing the previously reported 3D printed scaffolds (circular, 4 layers and grid pattern) on a glass bottom petri and by eventually adding PBS in order to perform the test in wet conditions.

Compression tests were performed in order to assess the overall scaffold mechanical properties. The instrument (Instron 5548 MicroTester) was equipped with a 10 kN cell load, and the tests were performed in wet conditions keeping the samples immerged in PBS. The compression speed and shear threshold were set a 10 mm/min and 70%, respectively.

5.1.8. Cellularized Scaffolds

Eventually, the best printing conditions and bioink formulations to maximize cell viability, printing resolution and fidelity were combined in order to print cellularized scaffolds.

Printing resolution was evaluated under inverted microscope using ImageJ to measure the thickness of the extruded filaments. Cell viability within the scaffolds was assessed by labeling the MSCs with a cell membrane tracker (PKH26, Sigma Aldrich) according to the previously reported protocol (paragraph 5.1.3.3) and checking them under the fluorescent microscope at different incubation times. According to manufacturer's instructions, alive cells are expected to be colored in red/orange, while, in case of cell death, colored emission is expected to disappear as a consequence of cell membrane desegregation. The cell distribution within the 3D structure was assessed by confocal microscope imaging (at Nikon Imaging Center, Singapore).

The cell growth was estimated by means of Presto Blue assay and MTT assay following the vendor protocols.

5.2. Results and Discussion

5.3. Mesenchymal Stem Cell Culture

Figure 5.19 reports the inverted microscope images of MSCs cultured on petri dishes at different time points. Normally, after 7-10 days the cells reached confluency.

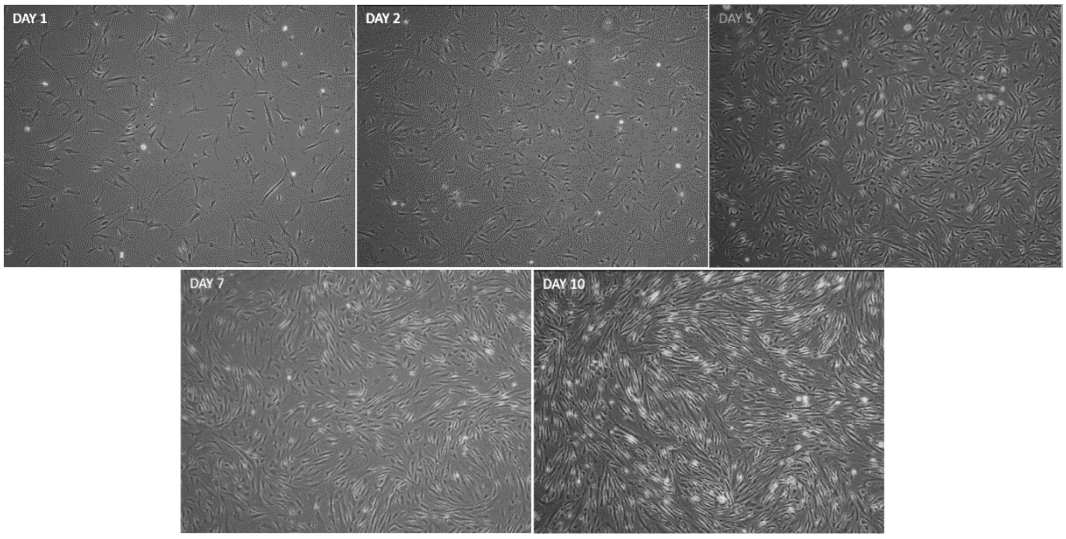

Figure 5.19 Inverted microscope images of MSCs culture over time (1-10 days).

Figure 5.20 shows the fluorescence microscope image of MSCs labeled with PKH26 cell membrane linker.

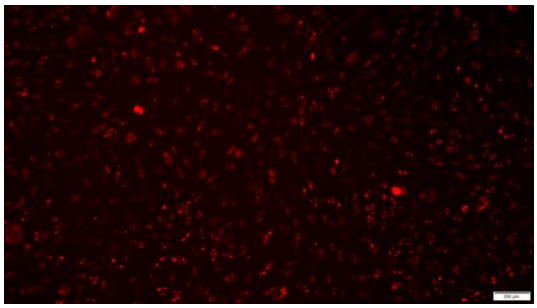

Figure 5.20 Fluorescence microscope image of MSCs labeled with the cell membrane linker.

Alive cells appeared red, while dead cells completely lose their fluorescence as a consequence of cell membrane breakage.

5.1.1. Bioprinter Modifications

The addition of the surface heater showed to be mandatory for the printing of the designed thermo- and photo-sensitive bioinks. **Figure 5.21** shows the pictures of the 3D printed scaffold before and after the addition of the surface heater.

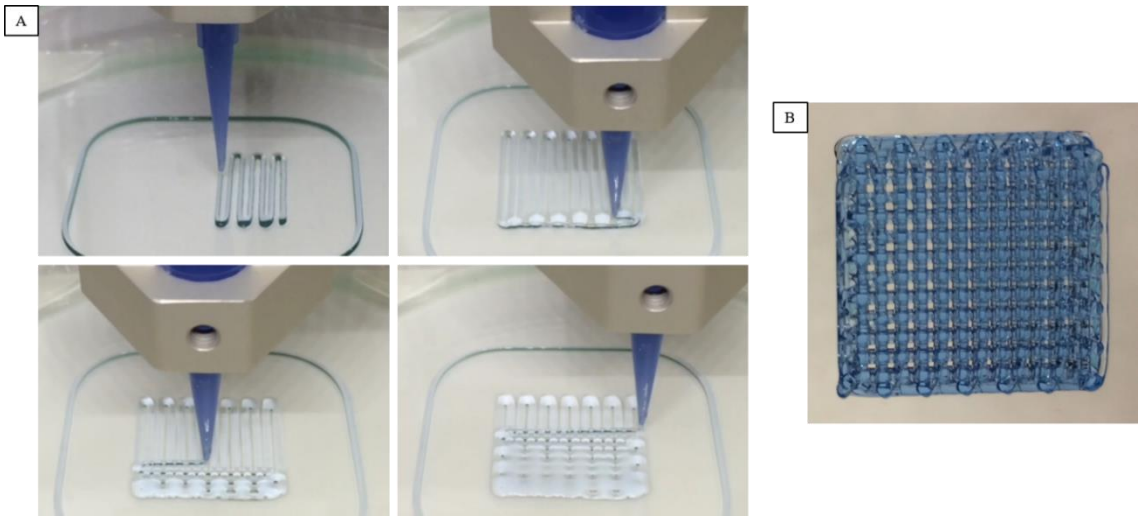

Figure 5.21 NHP407_15%w/v printed **(A)** before and **(B)** after the addition of the surface heater on the printing platform

Before the addition of the surface heater the bioinks could not maintain the shape of the extruded filaments and the layers tended to collapse on each other (**Figure 5.21 A**). The control over the temperature on the printing platform allowed the bioink to maintain the shape just exploiting its thermo-sensitivity (**Figure 5.21 B**).

However, as previously mentioned, in order to increase the stability in water environment of the 3D printed scaffolds, a photo-crosslinking step was added to the process. To this aim a 365 nm LED was added inside the bioprinter. The final photo-crosslinking layout allowed to irradiate the 3D printed structure with an UV light at approximately 365 nm (**Figure 5.22Figure**) with a constant power density (**Figure 5.23**).

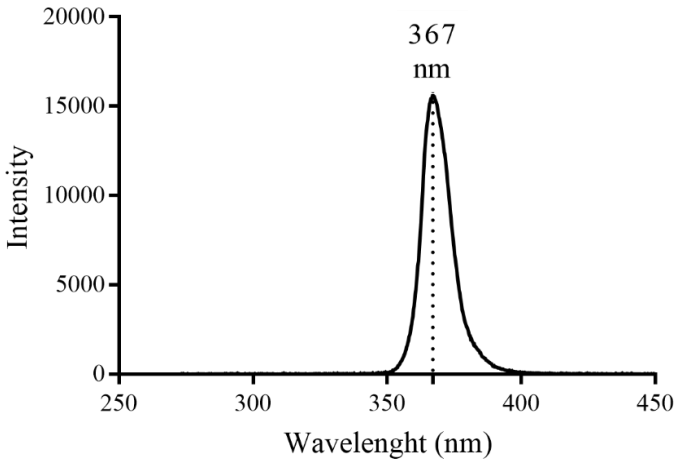

Figure 5.22 LED wavelength spectrum (the pick is centered on 367 nm).

The LED power density, measured at approximately 2 cm and using the highest electric current forwarded to the LED, has been shown to be constant over time and with a value of approximately 40 mW/cm^2 (**Figure**). For the photo-crosslinking step, the LED distance was set at 1 cm in order to irradiate approximately a 15x15 mm area with at least the 80% of the intensity and avoiding the irradiation of the neighboring scaffolds. The forwarded electric current was then adjusted in order to obtain the desired power density.

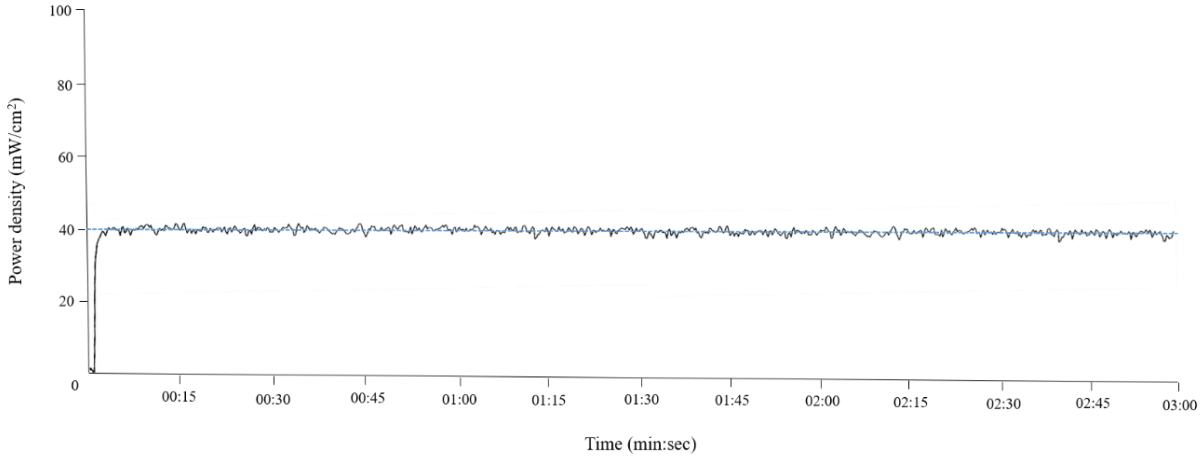

Figure 5.23 LED power density of 40 mW/cm^2 measured over 3 minutes.

5.1.2. Custom-made G-CODE

By exploiting the custom-made G-CODE both the printing and the photo-crosslinking processes were finely tuned. **Figure 5.24** shows the 3D printed scaffold obtained by using the designed G-CODE.

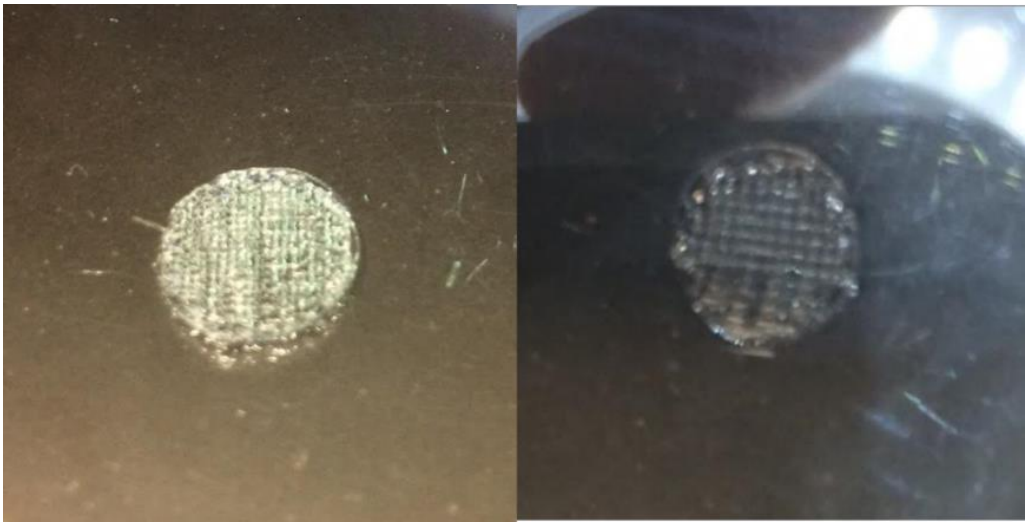

Figure 5.24 Pictures of the 3D printed circular scaffold (4 layers, grid pattern) obtained using the custom-made G-CODE and 210 and 450 µm nozzle diameter, respectively.

5.1.3. Bioprinting Process Validation

In order to biologically validate the entire process, sterilization of the bioprinting system and the bioinks was first tested. Both the sterilization methods tested for the syringes and the nozzles have been showed to keep the process sterile. No contamination was detected within the media put in contact with the syringes and the nozzles up to 2 weeks. The second process, based on the EtOH/H_20 washings, was finally selected being less time consuming. The tests carried out on the bioinks also showed the maintenance of sterility.

Bioinks with different content of their constituents were tested (10, 12.5, 15 and 17.5 %w/v for the PURs and 2.5, 5, 7.5 and 10 %w/v for PEG-DA) in order to improve printing resolution and

cell viability, as well as gel residence time in aqueous environment and the mechanical properties of the final printed structures. Furthermore, different printing (e.g., pressure, printing speed) and photo-crosslinking parameters (e.g., UV light intensity, photoinitiators concentration) have been tested with the same goal of maximizing cell viability and scaffold structural and mechanical properties as well as stability in aqueous environment.

The printing and photocrosslinking processes were studied separately and eventually the best formulations and parameters were combined in order to print thermo- and photo-sensitive bioinks.

5.1.3.1. Printing Process

Since many factors are involved during the printing process, feed rate, temperature and nozzle diameter were kept constant (i.e. 50 µL/min, 25 °C, 210 µm respectively) during the printing test.

Figure 5.25 shows the results of the feed rate test. By increasing PUR content in the formulation, both viscosity and the pressure needed to extrude the bioinks through a nozzle increase.

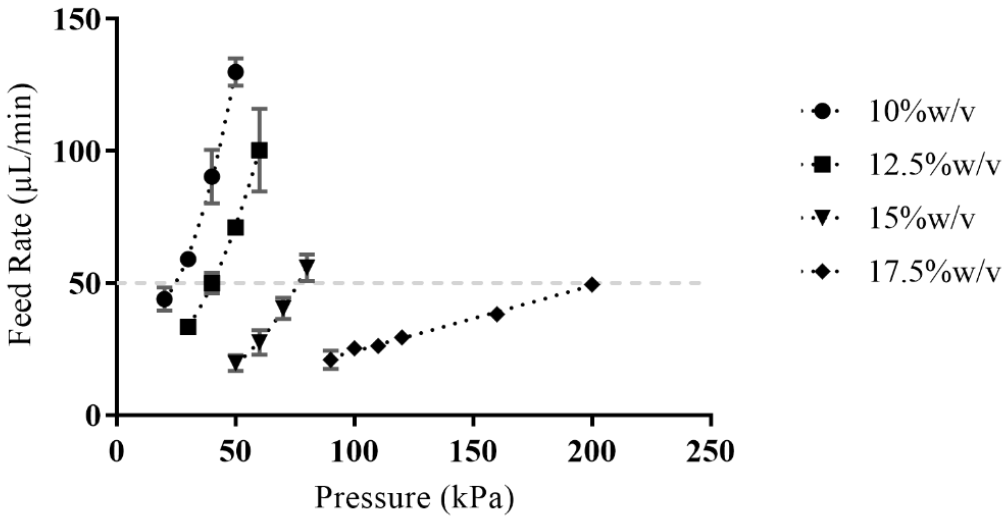

Figure 5.25 Feed rate *vs* pressure for different PUR formulations.

The further addition of PEGDA to the formulation is expected to increase the shear thinning behavior of the bioinks (as demonstrated in Chapter 4), reducing the pressure needed for the extrusion

Figure 5.26 shows the fluorescence microscope images of PUR-based cellularized inks (10, 12.5, 15 and 17.5 %w/v) immediately after the printing process. Each investigated composition was printed forming 8 different layers in a 24 well-plate (30 kPa, 60, 80 kPa and 200 kPa for PUR hydrogels at 10, 12.5, 15 and 17.5 %w/v concentration, as resulted from the previous test).

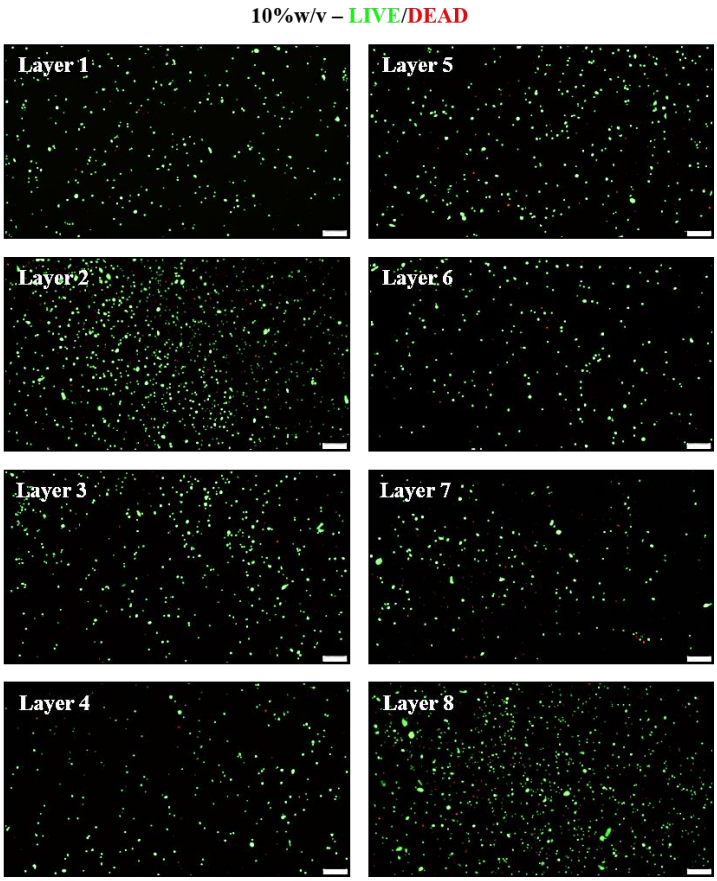

12.5%w/v – LIVE/DEAD

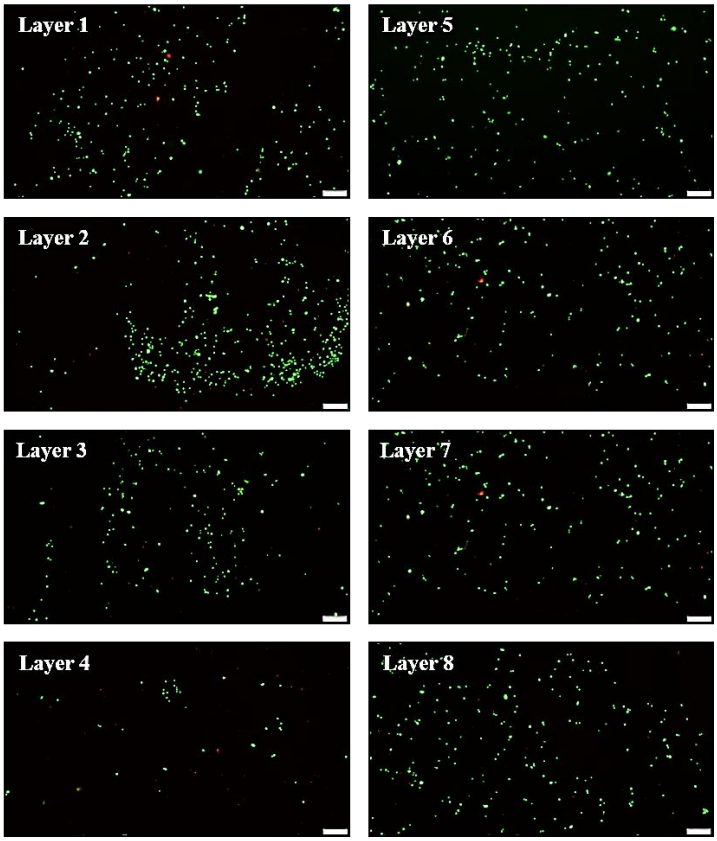

15%w/v – LIVE/DEAD

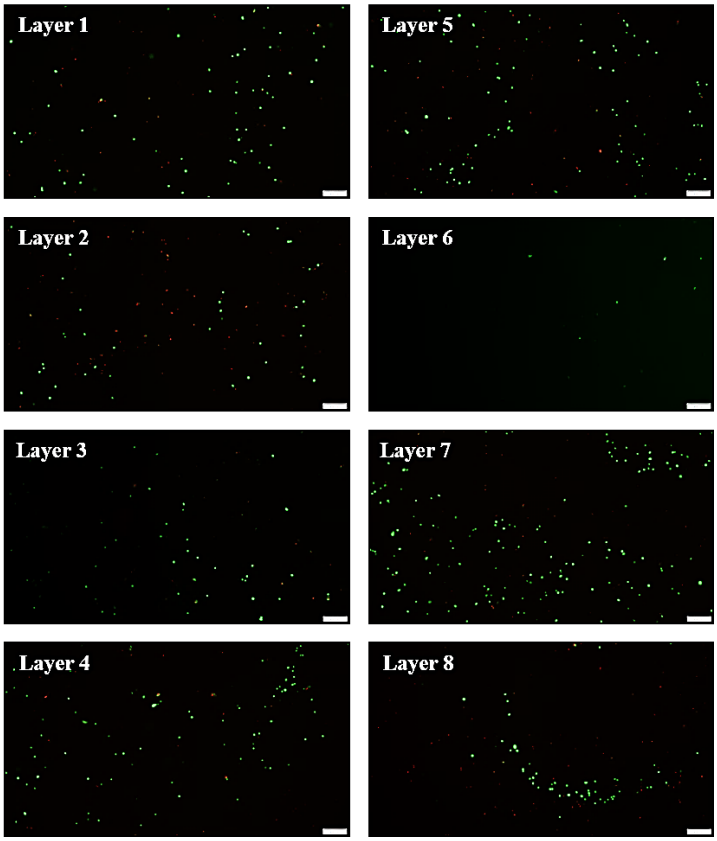

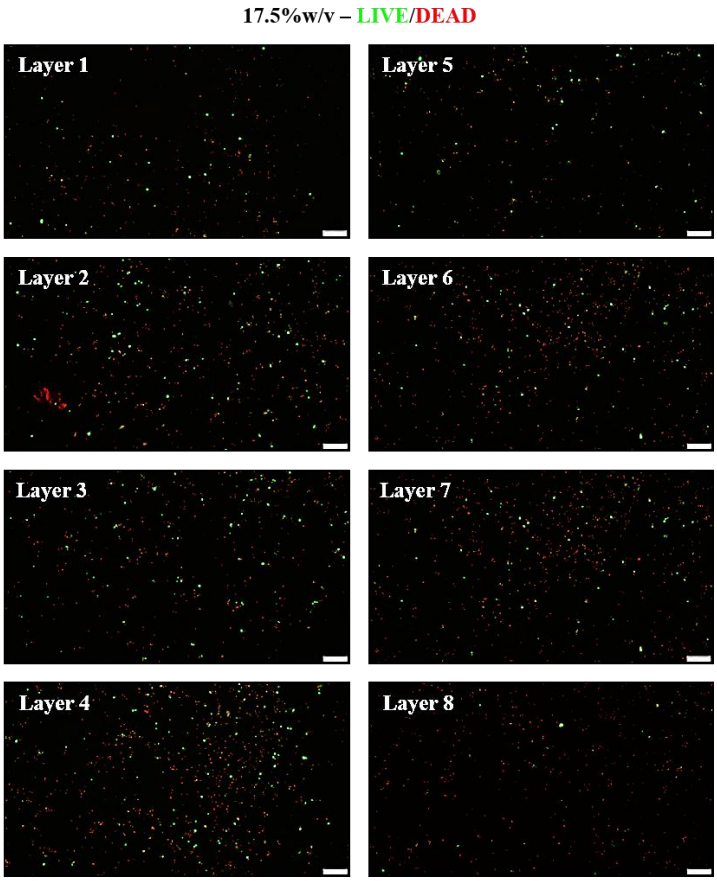

Figure 5.26 Live/Dead assay performed on the cellularized PUR-based bioinks after the printing process (green: calcein AM - live, red: ethidium homodimer-1 - dead).

Due to absence of the photo-sensitive component and thus the photocrosslinking process, the scaffolds were not able to maintain the shape. The cells appeared to be round shaped probably because of the absence of adhesion ligands on the hydrogels and the soft nature of the hydrogels. As a consequence of the shear stress applied to the encapsulated cells, cell viability decreased with increasing PUR content within the hydrogels (**Figure 5.27**).

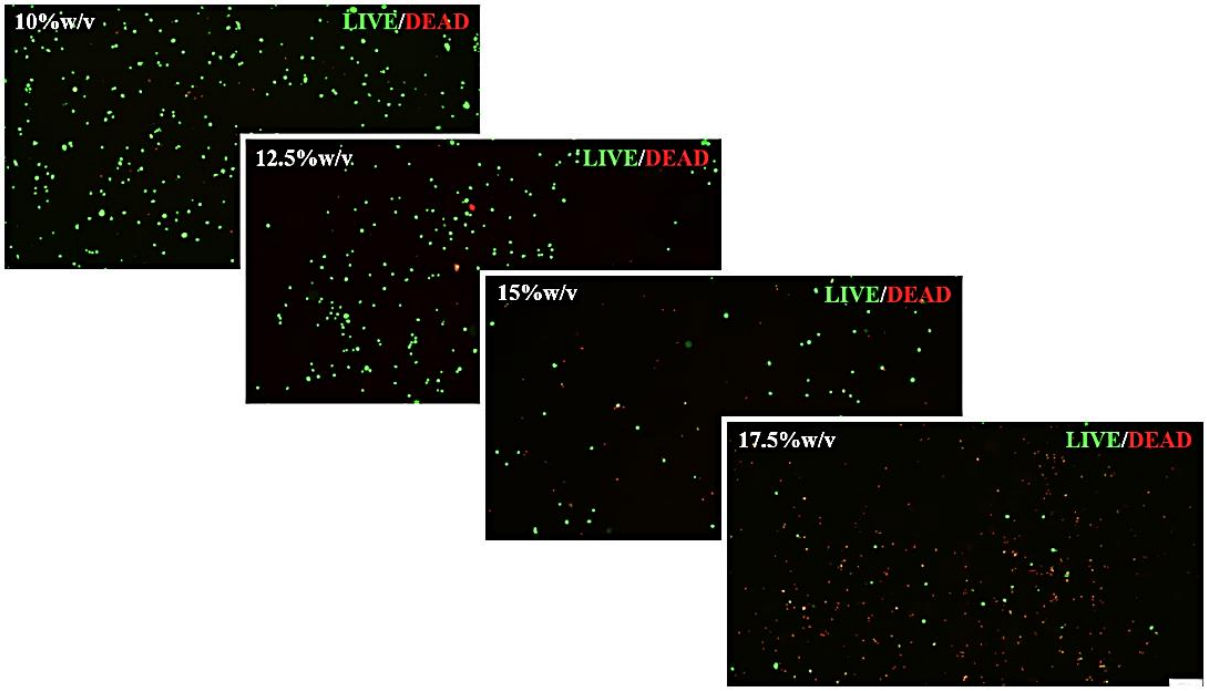

Figure 5.27 Live/Dead assay performed on the cellularized PUR-based bioinks after the printing process (first layer of each formulation).

Formulations at 15 and 17.5 %w/v PUR concentration drastically decreased cell viability (**Figure 5.28**). In order to overcome this issue, the bioinks could be printed at lower temperature in order to decrease the viscosity and thus the shear stress applied to the embedded cells. However, the Inkredible + did not allow to reduce the temperature over the syringe holders below the room temperature.

Hydrogels at 10 and 12.5 %w/v PUR concentration, instead, minimally affected cell viability during the printing process (**Figure 5.28**).

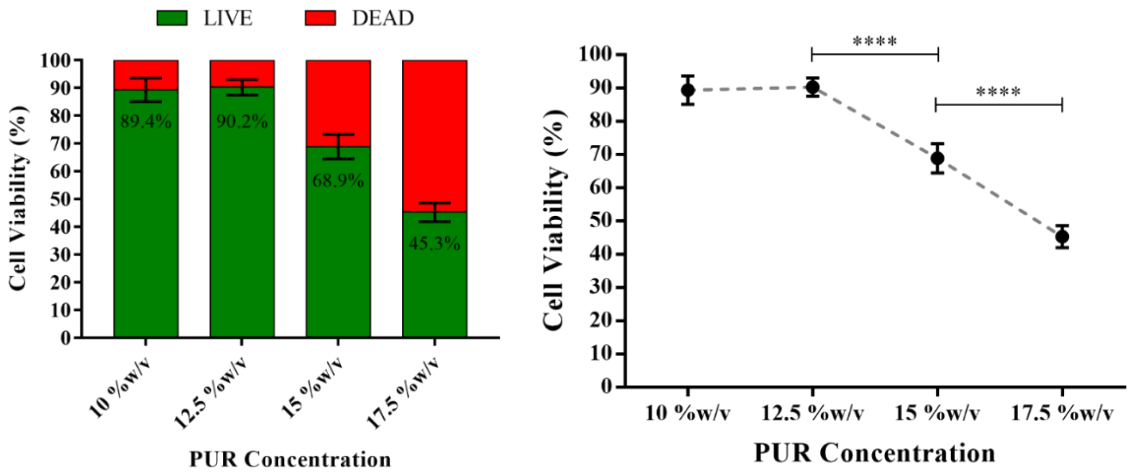

Figure 5.28 (A) Live/Dead assay results. **(B)** Cell viability of MSCs encapsulated within the bioinks after the printing process.

Whereas formulations with a 10 %w/v PUR concentration turned out to require a printing temperature of 37 °C in order to guarantee a good resolution, 12.5 %w/v concentrated bioinks could be successfully printed at room temperature reaching a good printing resolution, while maintaining the cells homogenously distributed and viable over different layers (**Figure 5.29**).

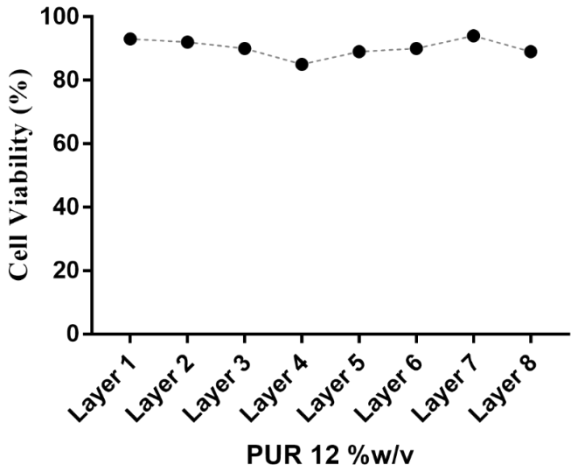

Figure 5.29 Cell viability of MSCs encapsulated within the 12.5 %w/v concentrated bioink after the printing process, over 8 different layers.

For these reasons, bioinks with a 12.5 %w/v PUR concentration were selected as the most promising formulations to maximize both printing fidelity and cell viability.

5.1.3.2. Photo-crosslinking Process

Figure 5.30 reports Presto-Blue assay results performed on MSCs exposed to the photoinitiators (I2959 and LAP).

The carried out tests evidenced that the cytotoxicity effect of the photoinitiators is higher with increasing their concentration and the exposure time to the cells. Even though the cells exposed to the photo-initiators show a similar trend over the time with respect the control (cells incubated without photo-initiators), by increasing the photoinitiator concentration the cells grew slower and slower compared to the control.

Additionally, both the tested photo-initiators have been proved to be reduce the cell viability in a concentration-dependent way. However, LAP showed a less toxic effect compared to the I2959. Based on this consideration and on its higher solubility in water and higher efficiency at 365 nm wavelength (as demonstrated in Chapter 4), LAP was selected as photoinitiator in the present work.

Exposure time turned out to affect cell behavior too, with cell viability decreasing with increasing exposure time. Among the tested samples, the 0.05 %w/v concentrated one was selected as the best condition for the next experiments, showing a lower toxicity on the cells.

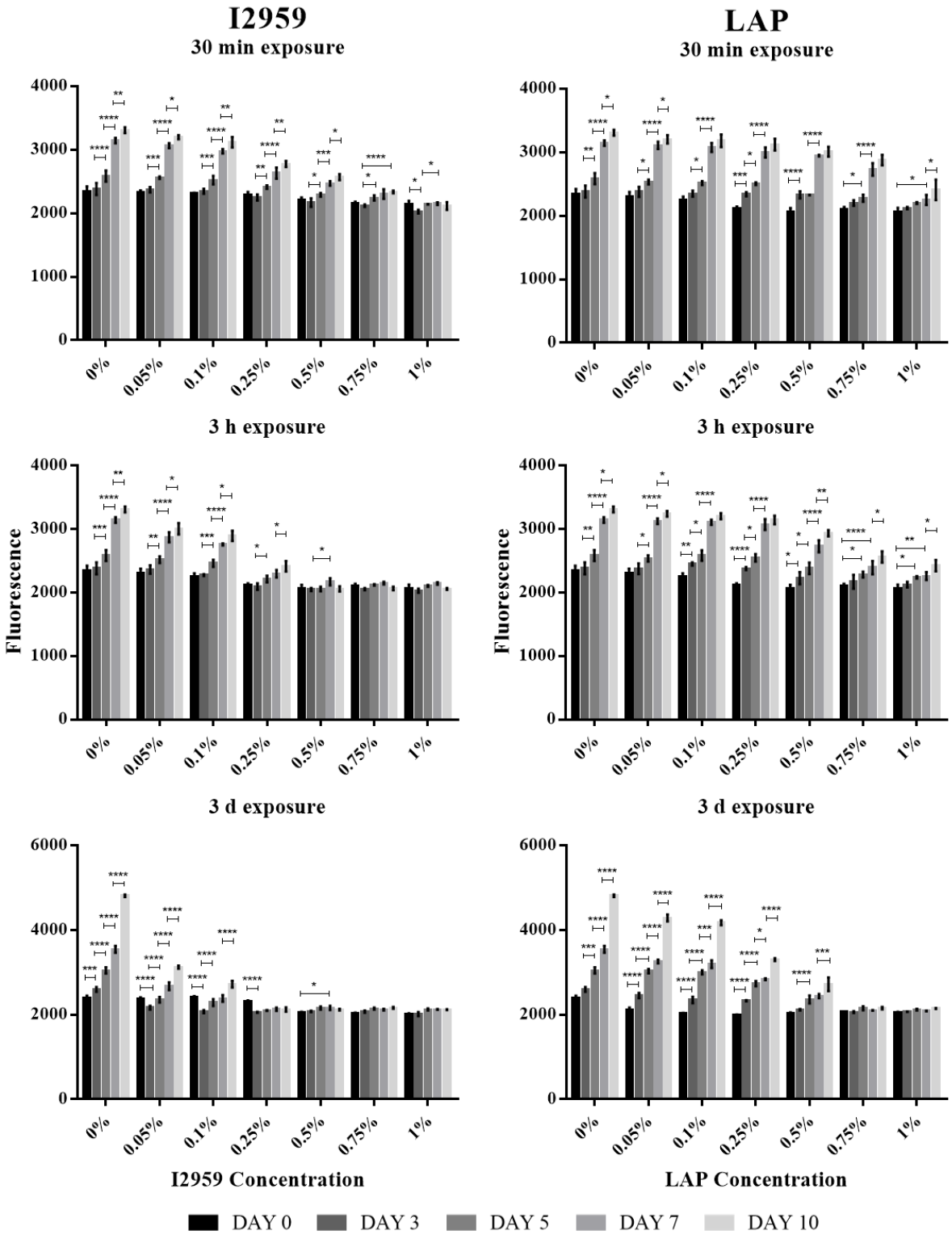

Figure 5.30 Presto Blue assay performed on MSCs exposed to I2959 and LAP at different concentrations.

Figure 5.31 shows the fluorescence microscope images of the cellularized inks 24 h after UV light exposure (different exposure time and power densities were tested).

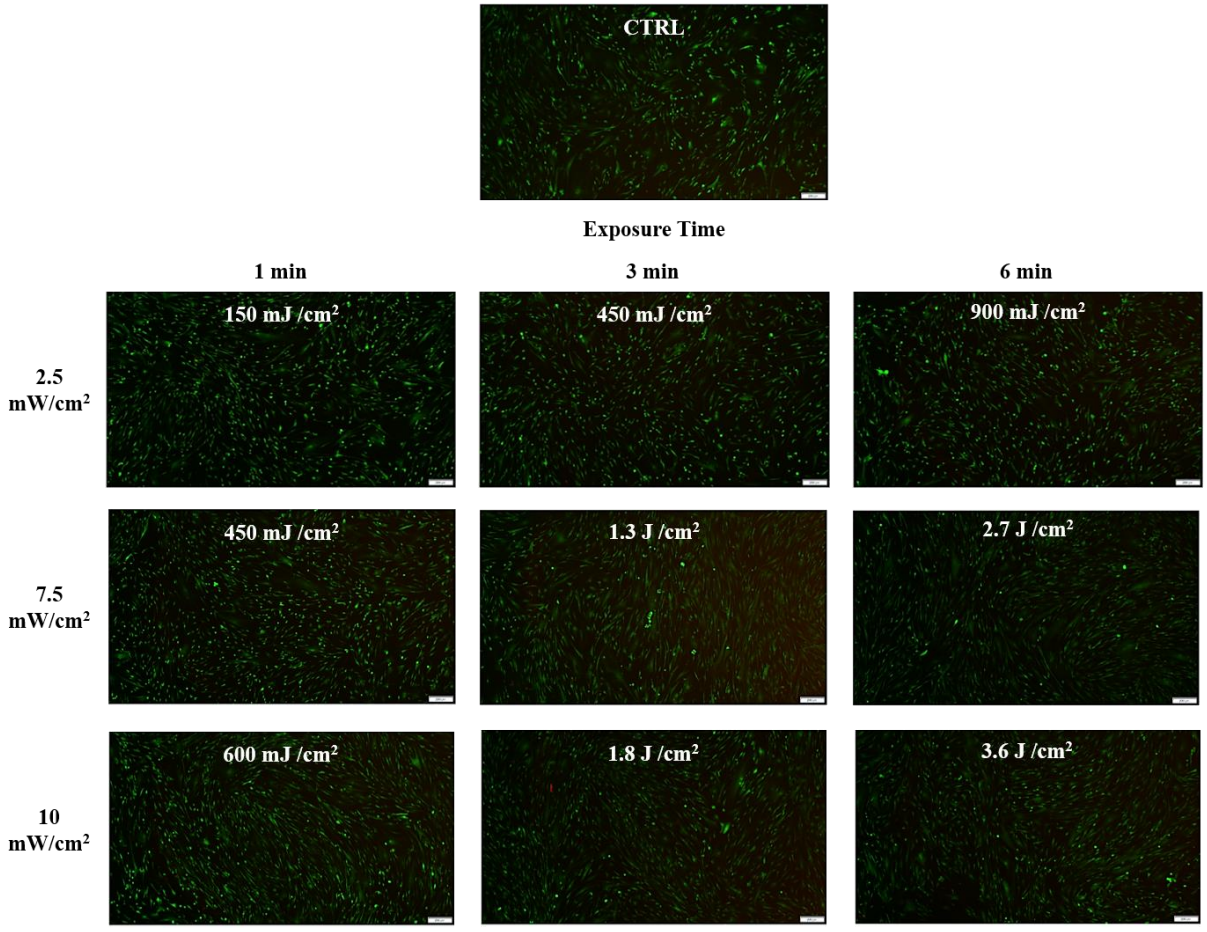

Figure 5.31 Live/Dead assay performed on MSCs exposed to 365 nm UV light with different power densities and exposure times

All the tested power densities and exposure times did not significantly affect cell survival (**Figure 5.32**). Long term experiments should have been performed to better evaluate the potential DNA damage. However, based tests on carried out and on literature data, a power density of 10 mW/cm^2 has been selected for the future tests, allowing an efficient and fast photo-crosslinking with no risk to mutate the cell's DNA.[7-10]

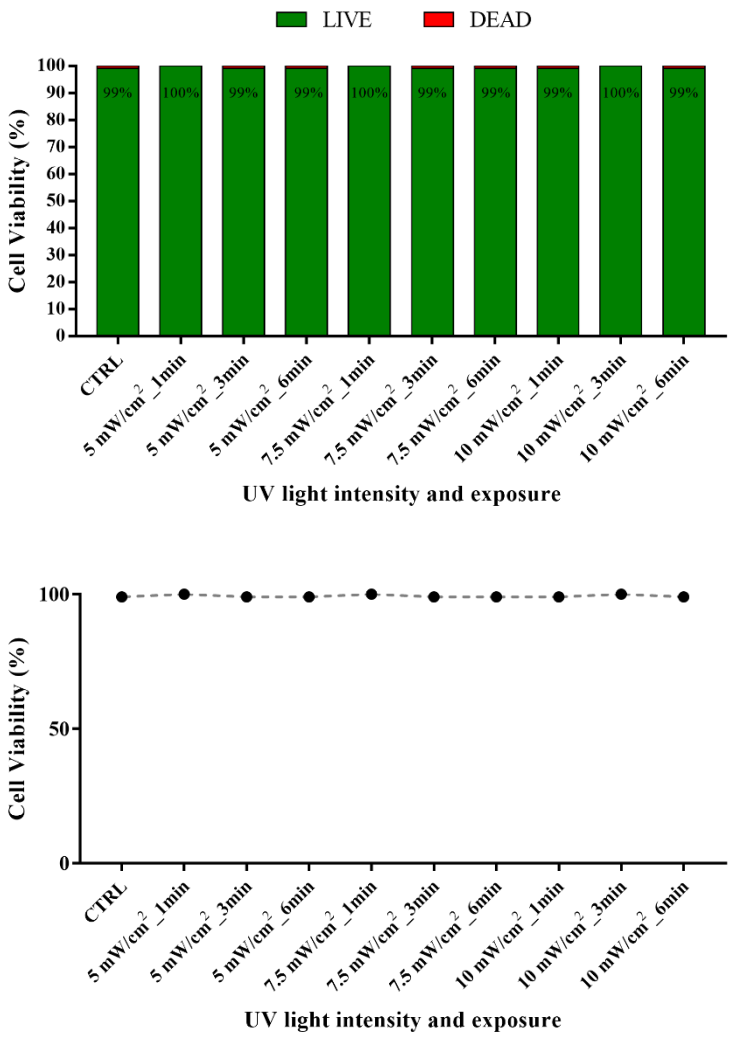

Figure 5.32 (A) Live/Dead assay results. **(B)** Cell viability of MSCs encapsulated within the bioinks after UV irradiation.

Figure 5.33 shows the fluorescence microscope images of the cellularized bioink based on PEGDA, upon photo-crosslinking, at different incubation time. All the tested PEGDA compositions (i.e., 2.5, 5, 7-5 and 10%w/v) did not significantly affect cell survival. However, the cells were sometimes difficult to visualize due to the poor fluorescent signal and the meniscus effect causing all the cells within the hydrogel to move close to the well's walls.

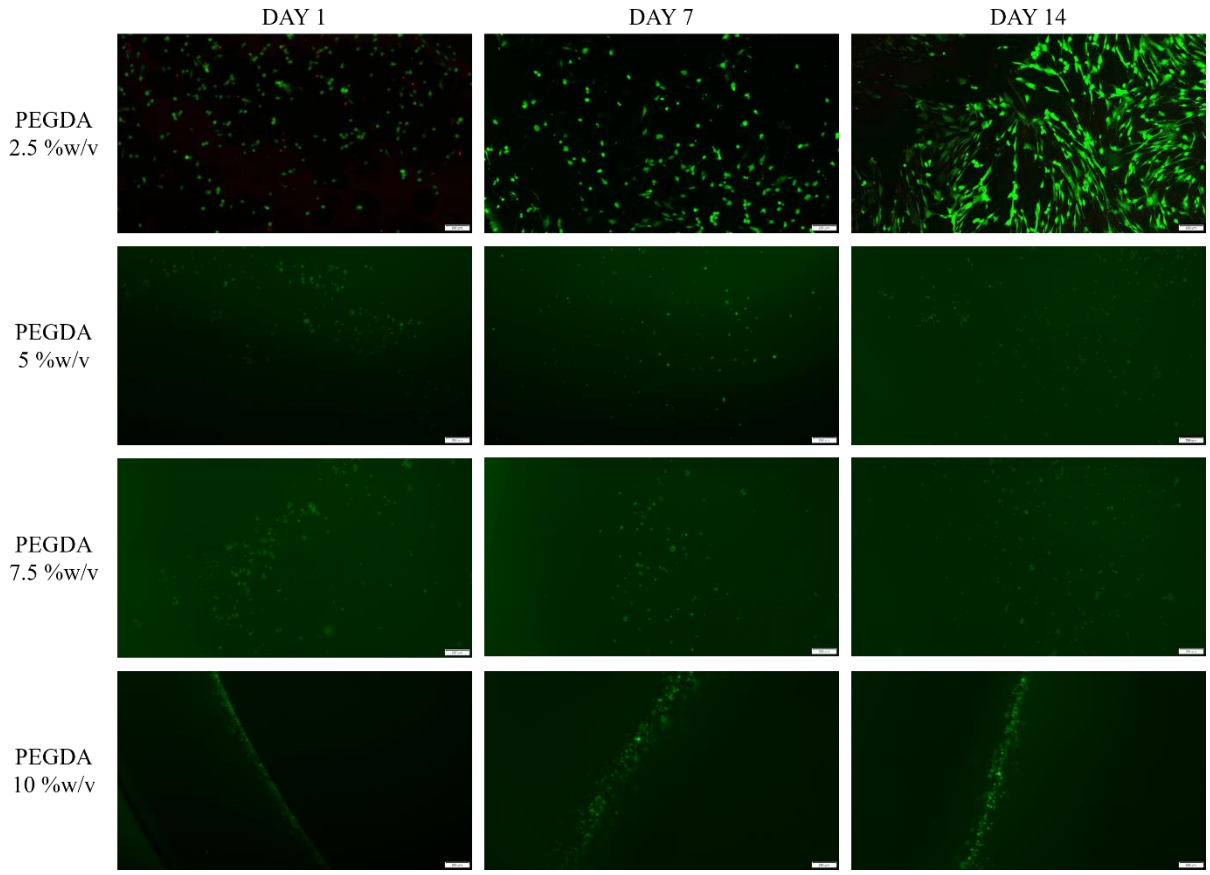

Figure 5.33 Live/Dead assay performed on MSCs embedded within PEGDA-based hydrogels, over different incubation time.

Only the cells encapsulated in the 2.5 %w/v concentrated PEGDA-based hydrogels spread after 14 days incubation time, as a consequence of the progressive PEDGA degradation, which resulted in the release of cells from the hydrogels and their adhesion on the well. Due to its poor stability in aqueous media, this composition was excluded from the final investigated formulations. On the other hand, cells embedded in the other investigated compositions turned out to be more difficult to stain and the meniscus effect further worsen the proper visualization of the cells. For these reasons, a proper and rationalized selection of the amount of PEGDA to be blended with the PURs was not possible. Hence, as a contingency plan, PEGDA formulations with the highest and the lowest investigated concentration (i.e., 5 and 10 %w/v) were selected to simulate extreme conditions.

5.1.4. Printing Resolution

Printing resolution was tested by printing different bioink formulations at 37 °C and 25 °C, using the optimized printing parameters.

Figure 5.34 shows the inverted microscope images of a NHP407/PEGDA formulation with PUR and PEGDA concentrations of 12.5 and 10 %w/v, respectively, printed at 37 °C with the 210 µm nozzle using different gaps between the extruded filaments.

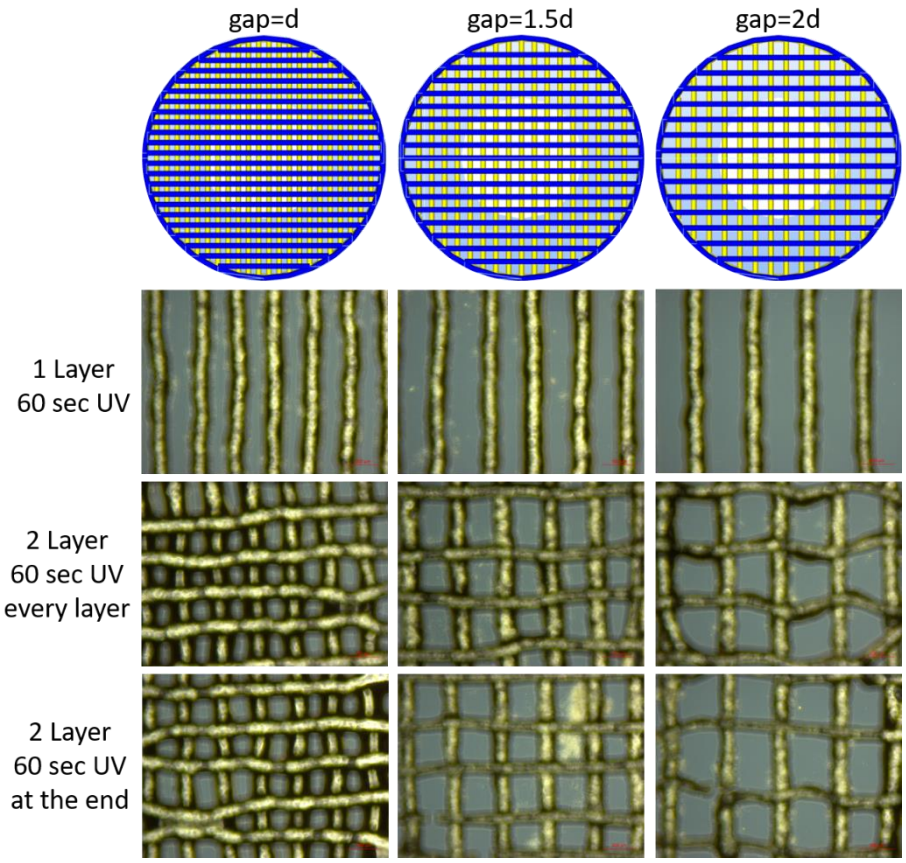

Figure 5.34 Inverted microscope images of the printed scaffolds with NHP407/PEGDA (12.5 %w/v and 10 %w/v, respectively) formulation at 37 °C.

Although the printing resolution of the filament diameter and the gaps between the filaments were satisfactory, the printing fidelity of the scaffolds was quite low. The filaments appeared bended and rough, and some consecutive filaments were fused together.

On the other hand, by printing at 25 °C, scaffolds with higher resolution and printing fidelity were printed (210±30 µm). **Figure 5.35** shows the inverted microscope images of different 3D printed scaffolds obtained from different bioinks. Both NHP407/PEGDA and HHP407/PEGDA bioink formulations showed high printing resolution. However, HHP407/PEGDA formulations needed higher pressures to be printed compared to NHP407/PEGDA formulations with the same PUR and PEGDA content (10-20 kPa more than the corresponding NHP407 formulation). The reason of this phenomenon probably lies on the different effect of the addition of PEGDA to the PUR-based formulations, discussed in the previous chapter (Chapter 4).

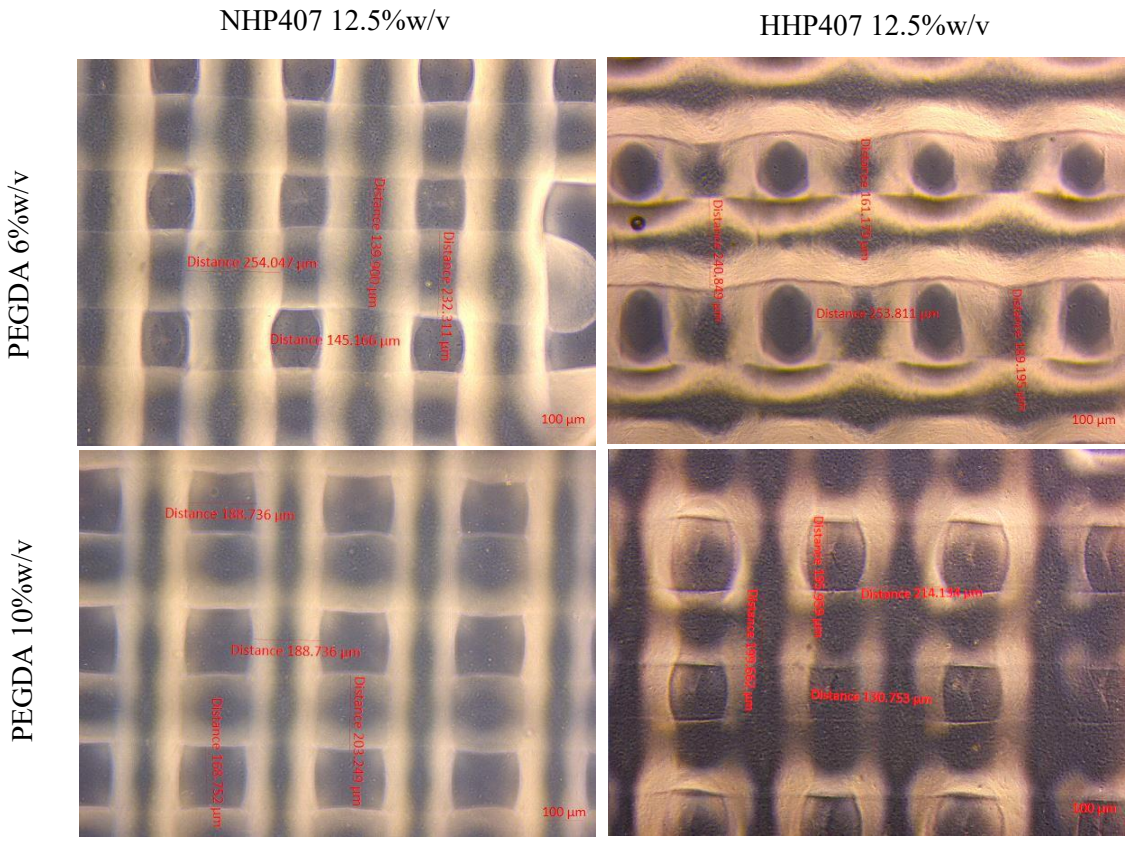

Figure 5.35 Inverted microscope images of the printed scaffolds.

5.1.5. Scaffold Swelling and Stability

3D printed scaffolds prepared starting from formulations containing the PUR (NHP407 or HHP407) at 12.5 %w/v concentration, PEGDA at 6 or 10 %w/v concentration and LAP (0.05 %w/v) were tested to assess their swelling and stability in water environment (according to **Equation 1** and **Equation 2**, respectively – Chapter 3 and 4). Moreover, two different irradiation time (30 and 60 sec) were tested in order to asses if this parameter can also affect scaffold stability.

Figure 5.36 and **Figure 5.37** show the swelling and stability results of NHP407- and HHP407-based bioinks blended with PEGDA.

For both NHP407- and HHP407-based bioinks, the formulations with the highest amount of PEGDA (i.e. 10 %w/v) showed higher PBS uptake, probably because of the higher degree of crosslinking within the hydrogels mesh (**Figure 5.36**). Moreover, at each analyzed time interval, PBS absorption was higher for HHP407-based formulations compared to NHP407-based ones with the same composition. This behavior is particularly visible on samples UV irradiated for 60 sec (**Figure 5.36 B**). In fact, although the trend of PBS absorption observed in both the 30s- and 60s-irradiated scaffolds was similar, the 60 sec irradiated samples showed higher PBS absorption compared to those photo-cured for 30 seconds (statistical differences at 7 and 28 days).

Hence, irradiation time turned out to affect the scaffold microstructure, resulting in an enhanced swelling potential of the constructs; similarly, the double degree of crosslinking within the HHP407/PEGDA-based formulations turned out to affect swelling and dissolution percentages compared to NHP407/PEGDA-based samples, with NHP407-based formulations showing a higher dissolution/degradation with respect to HHP407-based ones (approximately 100%, 80%,

70% and 40% for NHP407/PEGDA -12.5/6 %w/v-, NHP407/PEGDA -12.5/10 %w/v-, HHP407/PEGDA -12.5/6 %w/v- and HHP407/PEGDA -12.5/10 %w/v-, respectively).

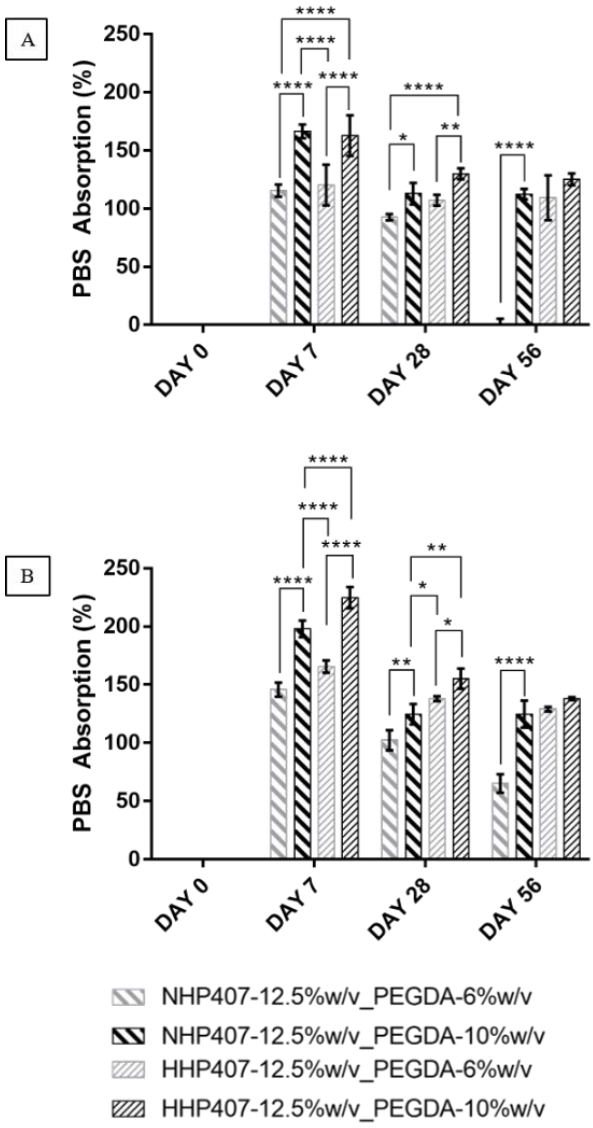

Figure 5.36 PBS absorption of NHP407/PEGDA- and HHP407/PEGDA-based scaffolds: **(A)** 30 sec and **(B)** 60 sec of UV irradiation.

For both NHP407- and HHP407-based bioinks, the formulations with the highest amount of PEGDA (i.e., 10 %w/v) showed slower dissolution/degradation, suggesting the possibility to modulate scaffold properties acting of PEGDA content in the designed sol-gel systems (**Figure 5.37**).

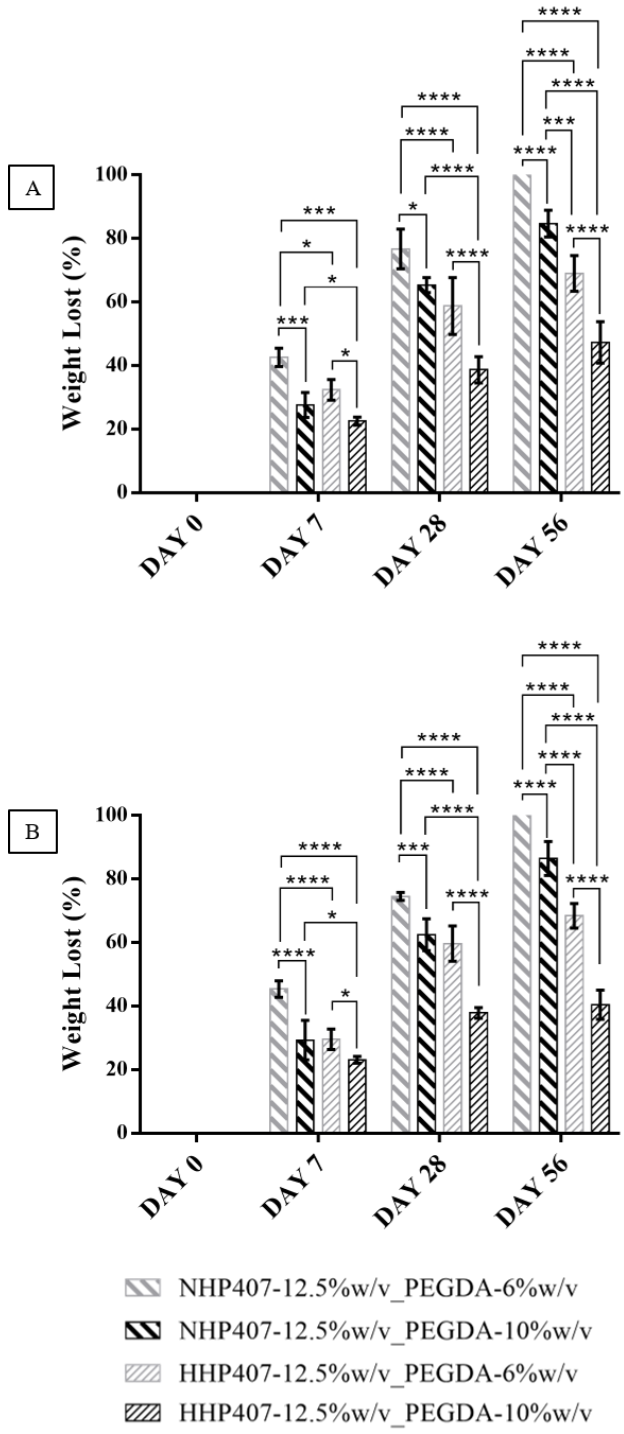

Figure 5.37 NHP407/PEGDA- and HHP407/PEGDA-based scaffolds weight loss: **(A)** 30 sec and **(B)** 60 sec of UV irradiation.

However, the previously mentioned differences between the 30 and 60 sec irradiated scaffolds were not evident in terms of scaffold stability in aqueous media. This result can be ascribed to

the accumulation of the UV light power energy on the lower layers of the scaffolds. In fact, the first layers, even if covered from the next ones and more distant from the UV source, are irradiated at each photo-curing step. This cumulative effect cancels the differences induced by irradiation time on scaffold residence time in aqueous environment.

Furthermore, scaffold geometry and microstructure were also analyzed by SEM imaging. **Figure 5.38** reports the SEM images of the analyzed scaffolds after different time of incubation in aqueous media.

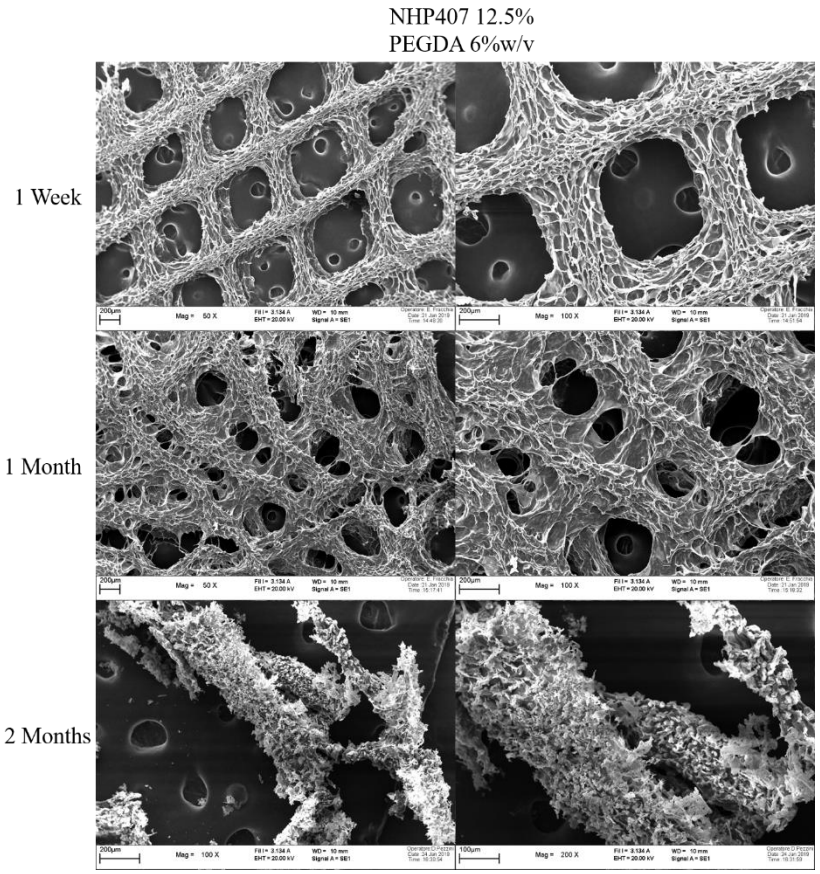

NHP407 12.5%
PEGDA 10%w/v

1 Week

1 Month

2 Months

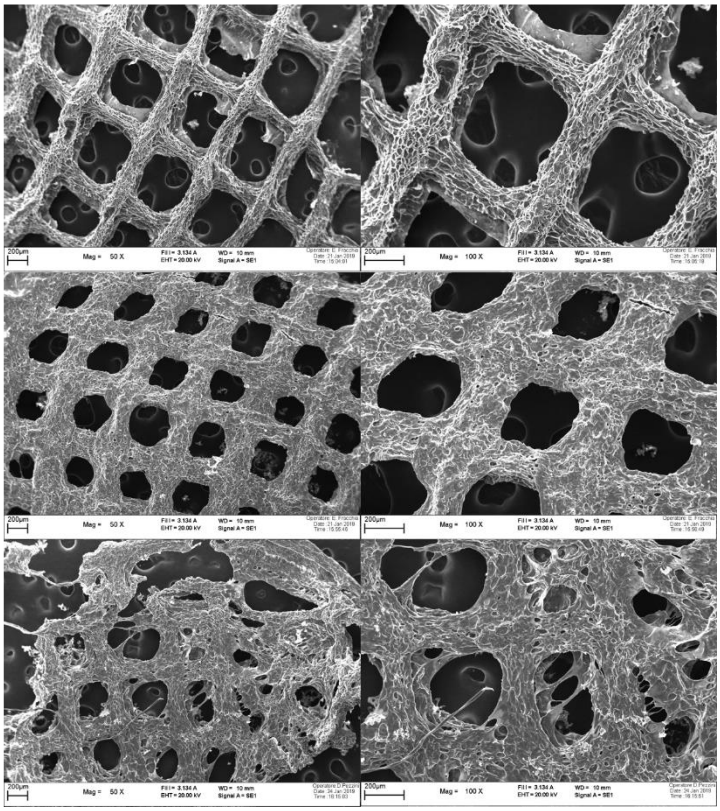

HHP407 12.5%
PEGDA 6%w/v

1 Week

1 Month

2 Months

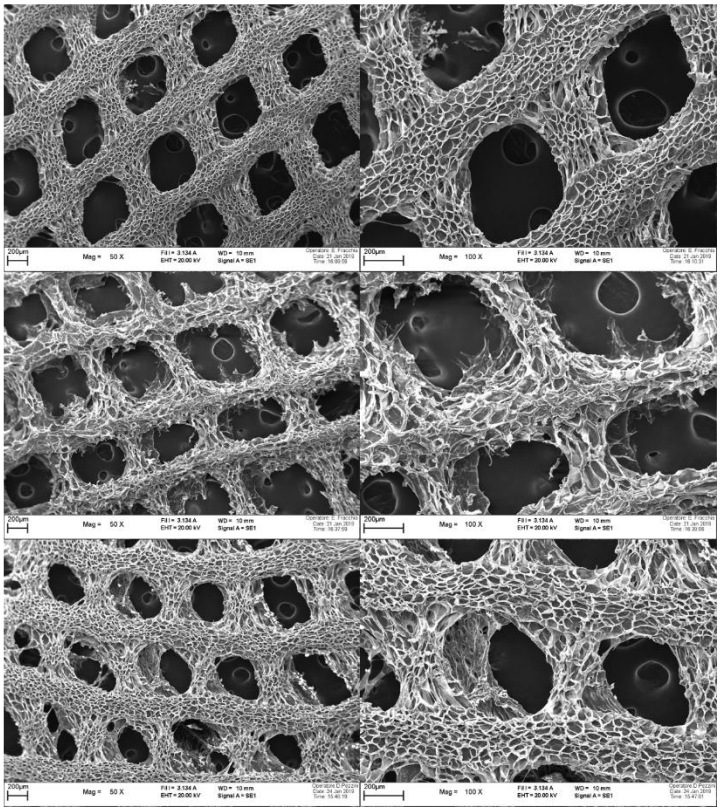

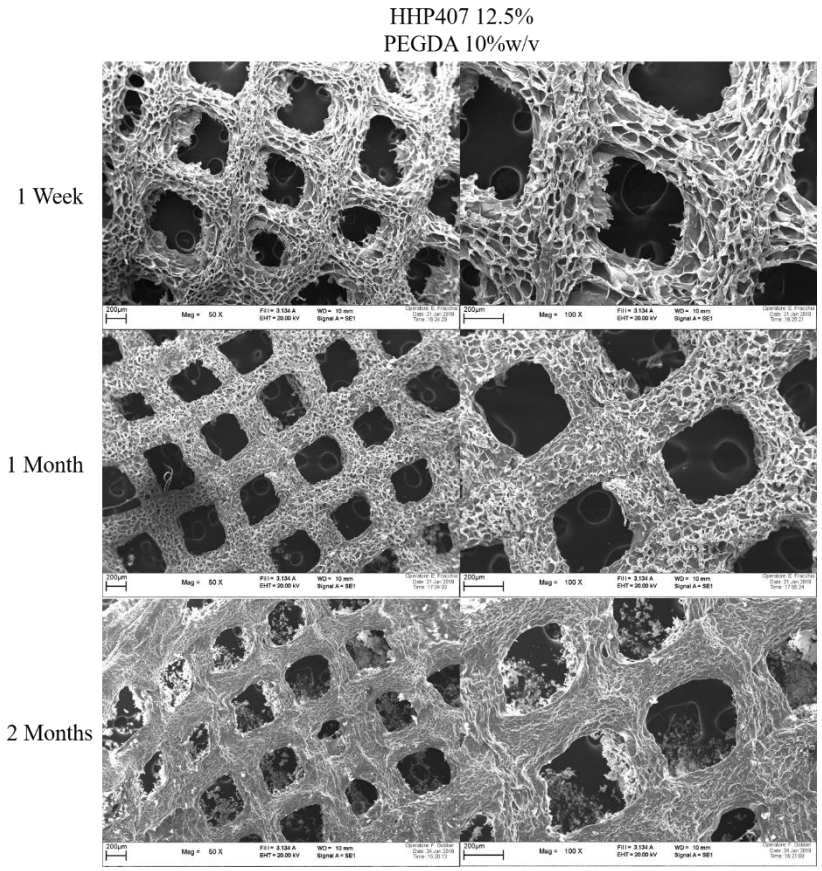

Figure 5.38 SEM images of the different formulation of the PUR/PEGDA-based scaffolds 3D printed with different UV irradiation time, dried through the freeze-drying process (the pictures on the left were taken at 50x magnitude, the ones on the right at 100x magnitude).

SEM imaging confirmed the hypothesis and considerations made on swelling and stability data: scaffold residence time increased with increasing PEGDA concentration within the printed formulation, with a significant improvement in NHP407-based compositions. Moreover, in agreement with the swelling and weight loss data, HHP407-based formulations showed higher stability with respect to the NHP407-based ones.

However, no considerations can be done about scaffold nanostructure. In fact, scaffolds immersion in liquid nitrogen before freeze-drying could have influenced pore orientation and size. Instead of freezing in liquid nitrogen followed by freeze-drying, a critical point dryer could be used to prepared samples for SEM. A preliminary test on this regard has been already

performed, however further optimization of the critical point drier protocol would be required to avoid sample shrinkage (**Figure 5.39**).

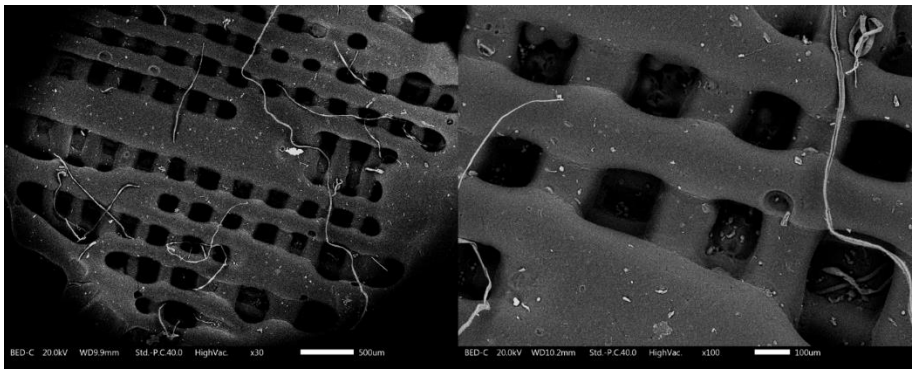

Figure 5.39 SEM images of a 3D printed scaffold (NHP407/PEGDA, 12.5/6%w/v) dried through the critical point drier process (the picture on the left was taken at 30x magnitude, the one on the right at 100x magnitude

5.1.6. Scaffold Mechanical Properties

The mechanical properties of 3D printed scaffolds were preliminary tested by means of AFM nanoindentation and compression tests, in order to asses if the differences between the designed bioink formulations and printing parameters are recognizable microscopically and macroscopically.

Figure 5.40 shows the force-distance curves obtained through the AFM nanoindentation, for different bioink formulations.

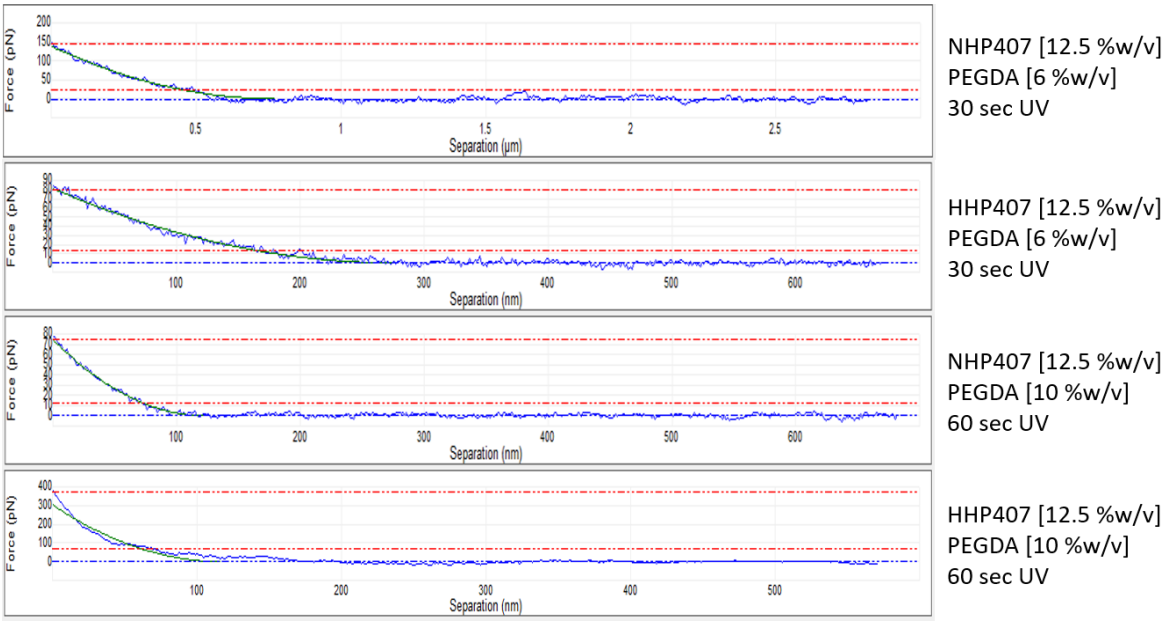

Figure 5.40 Force-distance curves obtained from AFM nanoindentation for different bioink formulation.

AFM nanoindentation demonstrated the possibility to effectively tune gel stiffness by changing the bioink formulation as well as the printing parameters, such as the irradiation time of the photo-crosslinking step.

In fact, different bioink formulation were tested showing the possibility to increase the final stiffness of the scaffolds by increasing PURs and PEGDA concentration as well as UV light exposure time. The obtainable scaffold stiffness was in the range between 1-100 kPa (**Table 5.1**), that match most of the soft tissue in the human body.[23-26]

Furthermore, the results obtained from AFM nanoindentation match with the one obtained from the photo-rheological characterization (Chapter 4).

Table 5.1 Elastic modulus evaluated for different bioink formulation from the AFM nanoindentation data.

Bioink Formulations	Local Young Modulus (kPa)
NHP407/PEGDA (12.5/6 %w/v)	1
HHP407/PEGDA (12.5/6 %w/v)	4.6
NHP407/PEGDA (12.5/10 %w/v)	21.5
HHP407/PEGDA (12.5/10 %w/v)	97.5

The force-volume analysis was also performed in order to estimate the mechanical properties over a 500nmx500nm area (**Figure 5.41**).

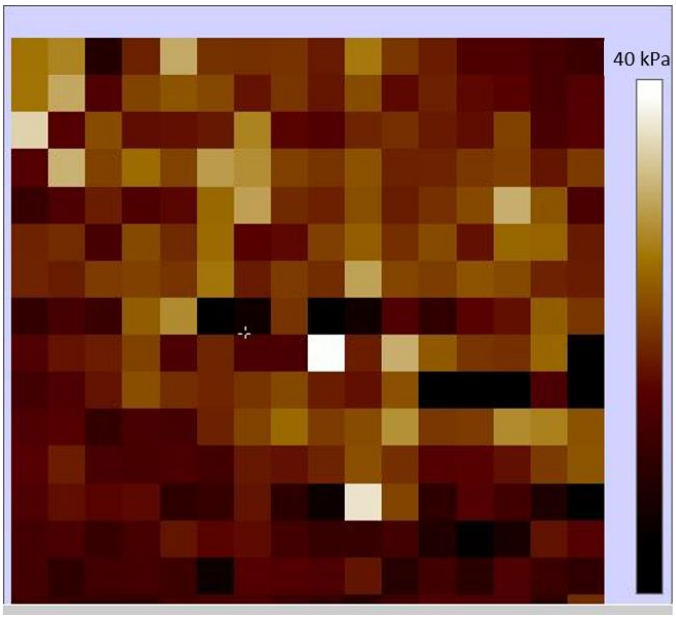

Figure 5.41 Volume-force curve of the NHP407/PEGDA-based formulation (12.5/10 %w/v) obtained from the AFM nanoindentation.

The volume-force curves highlight the difficulty encountered during the analysis in order to have a reliable measurement. In fact, the photo-crosslinking process occurs randomly (the formation of linkages between PEGDA chains as well as between HHP407 chains, is not controllable) and the formed mesh properties are not always homogeneous.

Concerning the overall mechanical properties of the 3D scaffolds, compression tests were performed with the scaffold immerged in PBS. The results are reported in **Figure 5.42.**

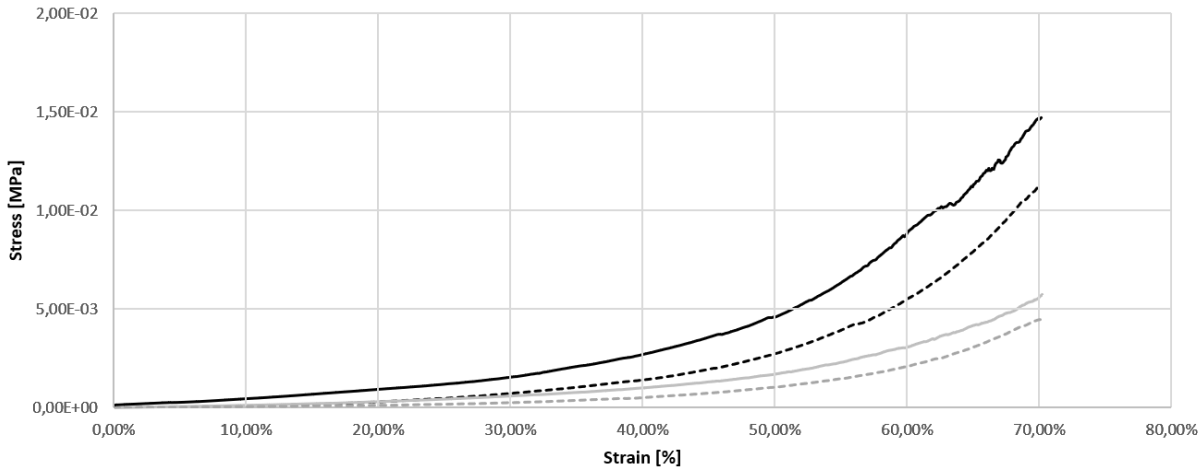

Figure 5.42 Compression tests results for different bioink formulations (grey dotted line: NHP407/PEGDA - 12.5/6 %w/v; grey solid line: HHP407/PEGDA - 12.5/6 %w/v; black dotted line: NHP407/PEGDA - 12.5/10 %w/v, black solid line: HHP407/PEGDA - 12.5/10 %w/v).

The influence of both bioink composition and UV irradiation time, already observed at the microscale through nanoindentation tests, was assessed also at the macroscale. However, the overall elastic modulus of the scaffolds was approx. one order of magnitude higher with respect to that measured through AFM nanoindentation (**Table 5.2**). In fact, whereas AFM nanoindentation characterizes the gel on the micro/nano scale with no effects coming from the overall scaffold structure, in macroscale compression test, scaffold geometry and structure play a key role in determining the final mechanical properties of the samples.

Table 5.2 Elastic modulus evaluated for different bioink formulation from the compression test data.

Bioink Formulations	Compressive Young Modulus (kPa)	Stress @ 70% of Strain (MPa)
NHP407/PEGDA (12.5/6 %w/v)	80±28	4.19E-03±0.31E-03
HHP407/PEGDA (12.5/6 %w/v)	210±42	5.23E-03±0.69E-03
NHP407/PEGDA (12.5/10 %w/v)	390±34	1.13E-02±0.26E-02
HHP407/PEGDA (12.5/10 %w/v)	470±55	1.47E-02±0.32E-0.2

5.1.7. Cellularized Scaffolds

The previously selected formulations (i.e., NHP407/PEGDA and HHP407/PEGDA, with PURs and PEGDA concentrations of 12.5 and 6-10 %w/v, respectively) were finally applied as cellularized bioinks and 3D printed through the modified bioprinter. The bioinks were prepared and sterilized as previously reported, and the MSCs, labeled with PKH26 red fluorescent membrane dye, were eventually added before the printing process.

Figure 5.43 shows the fluorescence microscope images of the cellularized scaffolds over different incubation times. The cells appeared stained in red due to the fluorescent dye: the fluorescent cells are viable meanwhile the dead ones lose the fluorescence.

All the cells looked well distributed within the 3D printed bioink. For all the tested formulations not significative differences in terms of cell number over time were observed. Hence, cells were viable (for up to 1 month) within both NHP407- and HHP407-based formulations, but they grew very slowly.

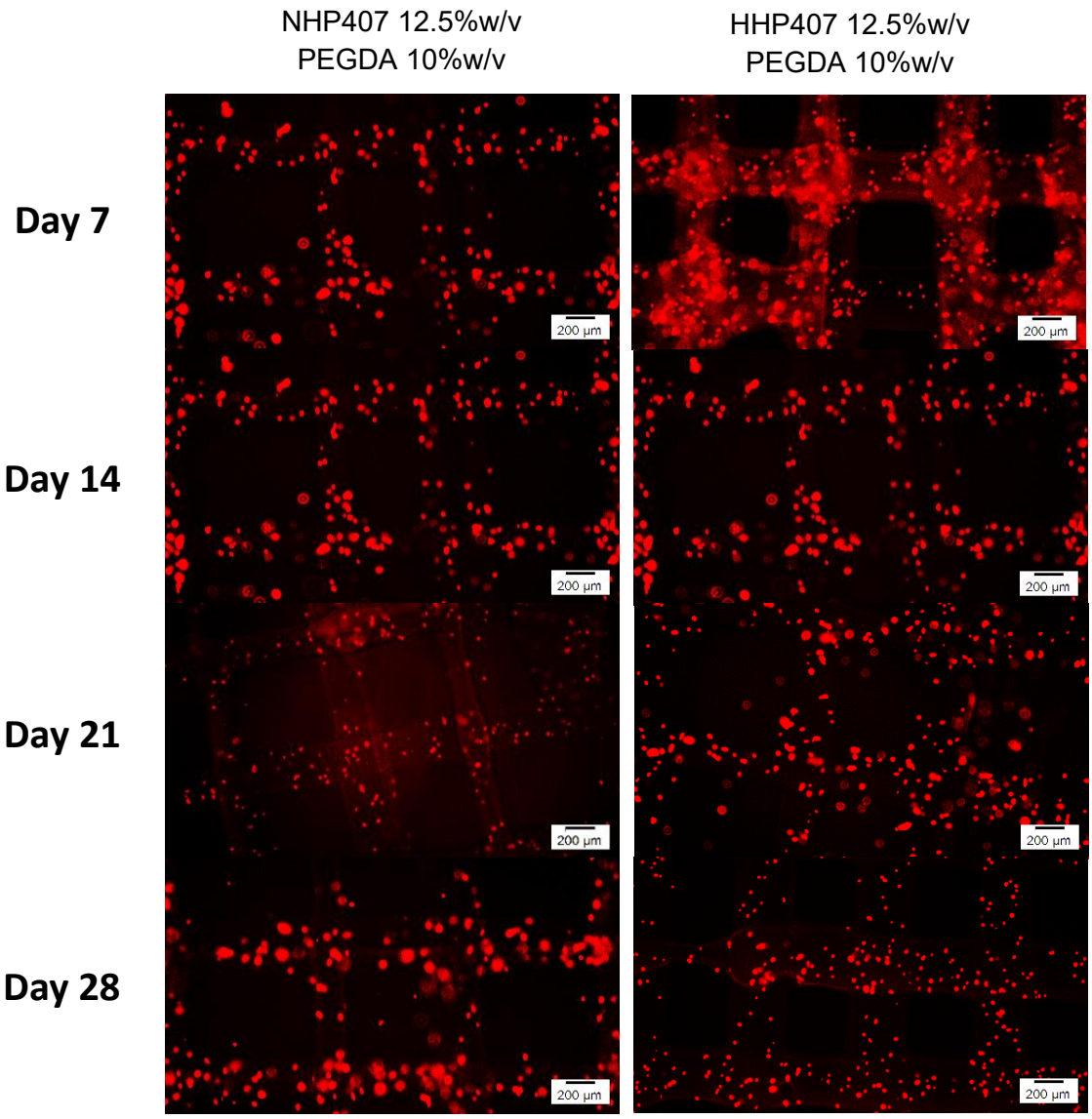

Figure 5.43 Fluorescence microscope images of the cellularized 3D printed scaffolds.

The fluorescence images sometimes appeared unfocused due to the 3D distribution of the cells, which made it difficult to focus all the cells at different z levels. For this reason, confocal imaging was also performed (**Figure 5.44**).

NHP407 12.5%w/v - PEGDA 10%w/v

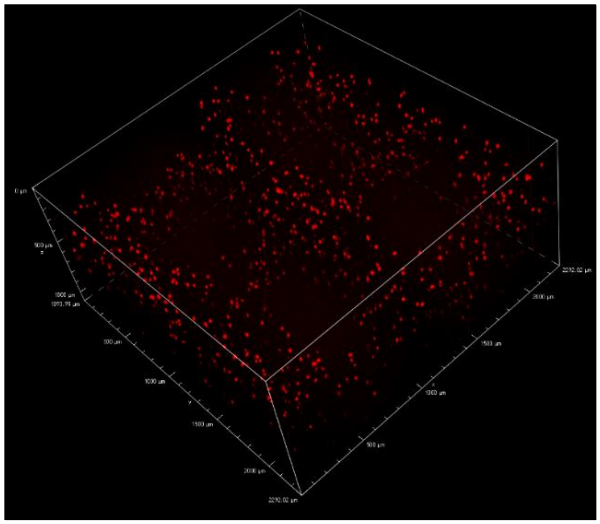

HHP407 12.5%w/v - PEGDA 10%w/v

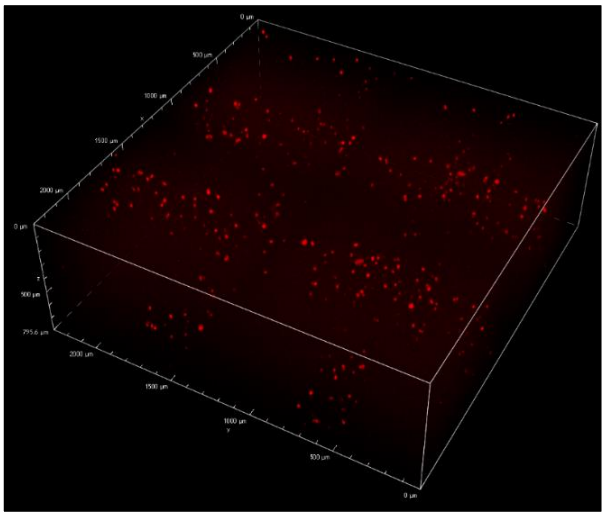

Figure 5.44 Confocal microscope images of the cellularized 3D printed scaffolds.

With the NHP407-based formulation the microscope laser was able to penetrate all the 4 layers of the scaffold showing the cells within the whole structure. On the other hand, with the HHP407-based formulation it was possible to detect only two of the four layers. The reason of this phenomenon probably lies in the higher crosslinking degree of the latter formulation that creates a denser mesh that does not allow the light to penetrate deeper.

In order to assess the progressive growth of the encapsulated cells, PrestoBlue assay (**Figure 5.45**) and MTT assay (**Figure 5.46**) were also performed on cellularized scaffolds prepared

starting from the selected bioink formulations and photo-cured for different irradiation times (30 and 60 s).

For both the experiments a calibration curve was first obtained by using different numbers of cells (MSCs) cultured on a multiwell in order to calibrate the assay outcomes (**Figure 5.45 A** and **Figure 5.46 A**).

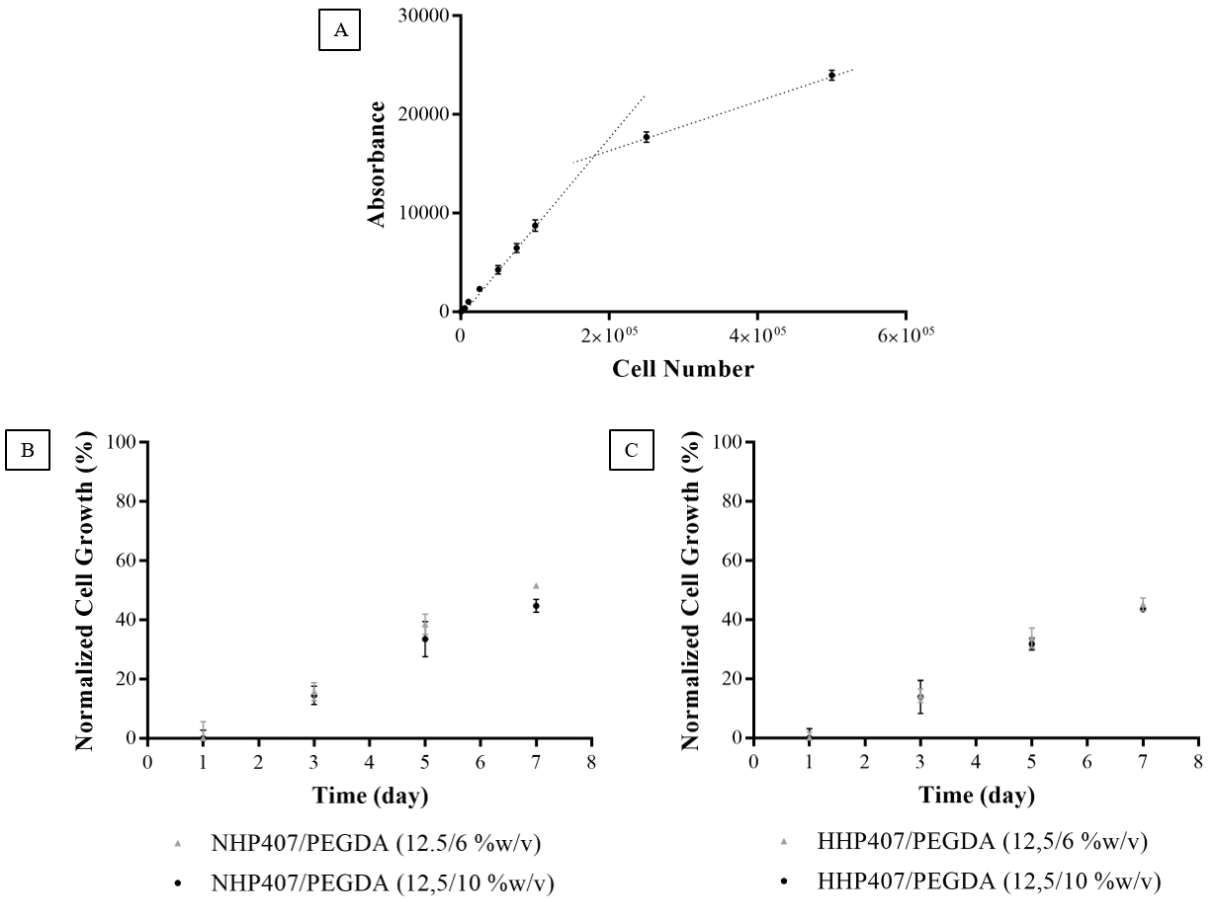

Figure 5.45 Cell Growth estimation assessed by PrestoBlue assay. **(A)** Calibration curve performed on MSCs. **(B, C)** normalized cell growth for 3D printed cellularized scaffolds based on NHP407/PEGDA and HHP407/PEGDA and 60 sec of UV irradiation.

As previously visually assessed, cell growth turned out to be slowed down within the scaffolds. Both NHP407- and HHP407-based formulations showed approximately a 45% of cell growth after 7 days incubation (with respect to day 0). Moreover, no significative differences were

observed between the formulations with 6 and 10 %w/v concentration of PEGDA and between scaffolds irradiated for 30 (results not reported) and 60 sec.

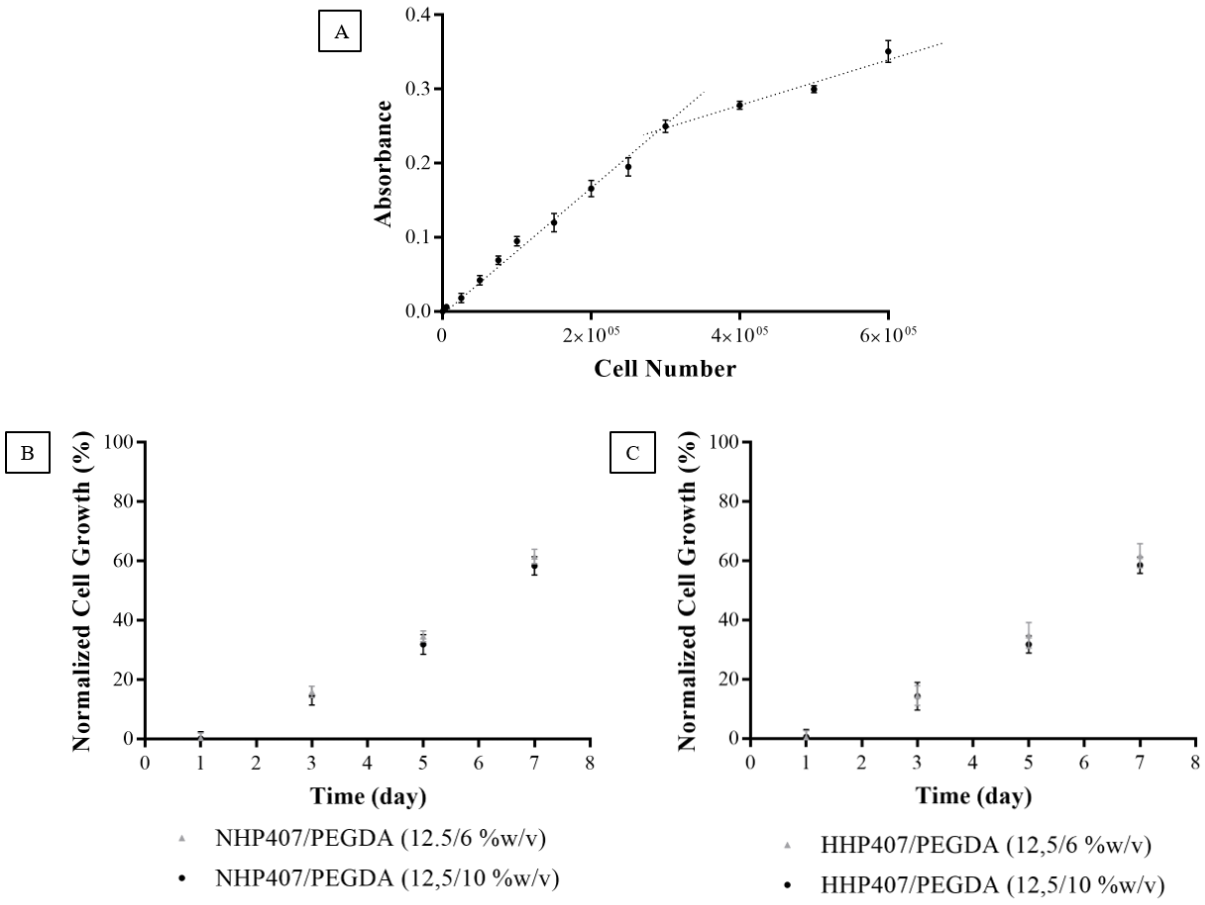

Figure 5.46 Cell Growth estimation assessed by MTT assay. **(A)** Calibration curve performed on MSCs. **(B, C)** normalized cell growth for 3D printed cellularized scaffolds based on NHP407/PEGDA and HHP407/PEGDA and 60 sec of UV irradiation.

The outcomes of the MTT assay showed a similar trend of cell growth. However, in this case the estimation of the cell growth at day 7 was statistically higher (approximately 65% with respect to day 0).

5.2. Conclusions

Thermo- and photo-sensitive bioinks formulation based on two different PURs (i.e. NHP407 and HHP407) were designed and previously characterized for their application in bioprinting.

The commercial bioprinter Inkredible + was equipped with a surface heater and a 365 nm LED with intensity control in order to 3D print the latter bioinks. In this way, the designed bioprinting setup allowed to control the temperatures over the cartridges and the printing platform, as well as to photo-crosslink the extruded structures. Thus, it was possible to modulate the temperature in order to reduce the viscosity and the shear stress applied to the encapsulated cells while maintaining a high printing resolution and fidelity.

The final concentration of the PUR was chosen from the biological validation of the printing process. In fact, 12.5 %w/v was the concentration that allows to maximize the printing resolution and cell viability by printing at room temperature on the platform kept at 37 °C.

Moreover, the photo-crosslinking step allowed to increase and modulate the scaffolds stability in water environment as well as their mechanical properties by changing bioinks constituent's concentration as well as the UV irradiation parameters.

Among the tested PEGDA concentration, the 6 and 10 %w/v were chosen because they represent the two extreme conditions of the photo-crosslinking process. In fact, the higher the concentration of PEGDA is the higher the crosslinking degree is expected.

The type of photo-initiator and its concentration were chosen in order to maximize the cell viability and accelerate the photo-crosslinking process. LAP was chosen because resulted less cytotoxic as well as more soluble in water. The 0.05 %w/v concentration was chosen, because among the tested one, it allows to maximize the cell viability and growth after its exposition to the cells.

The best printing conditions and formulations were combined in order to print 3D cellularized scaffold exploiting the modified bioprinter and a custom-made G-CODE.

The NHP407/PEGDA- and HHP407/PEGDA-based formulation were successfully 3D printed with high resolution (210±30 μm) and printing fidelity. The scaffold physico-chemical properties were studied in order to assess the possibility to tune their stability in water environment as well as their mechanical properties, by changing the bioink formulation and the irradiation parameters. The 3d printed scaffolds showed to be stable in water environment for up to 2 months with a degradation rate that depends on the bioink formulation. In particular, the formulations containing higher concentration of PEGDA and the ones containing HHP407, showed the higher stability over time. A similar trend was observed for the modulation of the scaffold mechanical properties. Moreover, it was possible also to demonstrate that the increase of the irradiation time enhances the final scaffold mechanical properties.

The 3D printed scaffolds were eventually biologically characterized showing a homogeneous distribution of the cells within the and a cells viability up to 1 month. Despite these promising preliminary results, the cells embedded within the scaffolds showed a slowed down and reduced growth. However this phenomenon is compatible with the synthetic nature of the designed bioinks.

The designed script in order to customize the G-CODE allowed to reduce the preprocessing time before the printing process, and the developed G-CODE allowed to control all the printing parameters.

References

[1] L.T.Ozbolat and M. Hospodiuk, *Biomaterials* **2016**: *76*.

[2] A. Panwar and L. Poh Tan, *Molecules* **2016**: *21*, 6.

[3] S. Ji and M. Guvendiren, *Front. Bioeng. Biotechnol.* **2017**.

[4] R. Chang, J. Nam and W. Sun, *Tissue Engineering Part A* **2008**: *14*, 1.

[5] N. Paxton, W. Smolan, T. Böck, F. Melchels, J. Groll and T. Jungst, *Biofabrication* **2017**: *9*.

[6] J.H.Y. Chung, S. Naficy, Z. Yue, R. Kapsa, A. Quigley, S.E. Moulton and G.G. Wallace, *Biomater. Sci*. **2013**: *1*.

[7] J. Cadet, S. Mouret, J.L. Ravanat and T. Douki, *Photochemistry and Photobiology* **2012**: 88.

[8] J. Cadet, T. Douki and J.L. Ravanat, *Photochemistry and Photobiology* **2015**, *91*.

[9] P. Karran and R. Brem, *DNA repair* **2016**: *44*.

[10] D.Y. Wong, T. Ranganath and A.M. Kasko, *PLoS ONE* **2015**: *10*, 9.

[11] N.Alessio, T. Squillaro, S. Özcan, G. Di Bernardo, M. Venditti, M. Melone, G. Peluso and U. Galderisi, *Oncotarget* **2018**: *9*, 27.

[12] D. Duscher, J. Barrera, V.W. Wong, Z.N. Maan, A.J. Whittam, M. Januszyk and G.C. Gurtner, *Gerontology* **2016**: *62*, 2.

[13] V. Tabar and L. Studer, *Nat. Rev. Genet.* **2014**: *15*, 2.

[14] A.A. Sánchez and S. Yamanaka, *Cell* **2014**, *157*, 1.

[15] P. Musialek, A. Mazurek, D. Jarocha, L. Tekieli, W. Szot, M. Kostkiewicz, R.P. Banys, M. Urbanczyk, A. Kadzielski, M. Trystula, J. Kijowski, K. Zmudk, P. Podolec and M. Majka, *Postep. Kardiol. Inter.* **2015**: *11*, 2.

[16] S.M. Richardson, G. Kalamegam, P.N. Pushparaj, C. Matta, A. Memic, A. Khademhosseini, R. Mobasheri, F.L. Poletti, J.A. Hoyland and A. Mobasheri, *Methods* **2016**: *99*.

[17] J. Kobolak, A. Dinnyes, A. Memic, A. Khademhosseini and A. Mobasheri. *Methods* **2016**: *99*.

[18] Z. Tong, A. Solanki, A. Hamilos, O. Levy, K. Wen, X. Yin and J.M. Karp, *EMBO J.* **2015**: *34*, 8.

[19] L. Ghasemi-Mobarakeh, M.P. Prabhakaran, L. Tian, E. Shamirzaei-Jeshvaghani, L. Dehghani and S. Ramakrishna, *World J Stem Cells* **2015**: *7*, 4.

[20] A.P. Roman, C. Seong-Jun, H. Cheol-Min, K. Jung-Ju, S. Hosup, W.L. Kam and K. Hae-Won, *Progress in Materials Science* **2016**: 82.

[21] F. Hsieh, H. Lin, S. Hsu, *Biomaterials* **2015**, *71*, 48.

[22] Y. Tsai, S. Li, S. Hu, W. Chang, U. Jeng, S. Hsu, *ACS Appl. Mater. Interfaces* **2015**, *7*.

[23] K. Arda, N. Ciledag, E. Aktas, B.K. Aribas and K. Köse, *Am. J. Roentgenol*. **2011**: *197*.

[24] V.F. Achterberg, L. Buscemi, H. Diekmann, J. Smith-Clerc, H. Schwengler, J.J. Meister, H. Wenck, S. Gallinat and B. Hinz, *J. Investig. Dermatol*. **2014**: *134*.

[25] E. Hoenig, U. Leicht, T. Winkler, G. Mielke, K. Beck, F. Peters, A.F. Schilling and M.M. Morlock, *Tissue Eng. A* **2013**: *19*.

[26] A.J. Engler, S. Sen, H.L. Sweeney and D.E. Discher, *Cell* **2006**, *126*.

Chapter 6
Conclusions and Future Works

Bio-fabrication technologies based on additive manufacturing are emerging as promising tools to design cellularized 3D scaffolds for tissue engineering/regenerative medicine approaches. The proper design of the bioink, used as building material, is crucial to ensure cell viability and the success of such approaches. Thermo-sensitive hydrogels are valuable candidates to design bioinks with tuned gelation properties without the need of crosslinking agents, organic solvents or photo-irradiation. They can be designed in order to gel around body temperature (37 °C) and their thermo-sensitive behavior can be exploited to easily encapsulate cells, biomolecules or drugs. Usually, the main drawbacks of such hydrogels are their low stability in water environment and their relatively poor mechanical properties, due to the non-covalent interactions between the chains (physical hydrogels).

Poloxamers are triblock copolymers of poly(ethylene oxide) (PEO) and poly(propylene oxide) (PPO) available in different molecular weights and PPO/PEO ratios. The presence of PEO and PPO blocks with an ABA-type triblock structure in a single polymer chain originates amphiphilic molecules that self-assemble undergoing a sol-to-gel transition with increasing temperature over the Lower Critical Gelation Temperature (LCGT), when polymer water solution concentration is above a minimum value, namely Critical Gelation Concentration (CGC). Poloxamer 407 (P407, PEO_{101}–PPO_{56}–PEO_{101}), in particular, has been showed to be

non-toxic and able form a soft gel around 25/37 °C at proper concentrations. However, its applications as bioink is greatly limited by its poor stability in aqueous media, limited mechanical properties and very high permeability, resulting from the physical crosslinking (i.e., hydrophobic interactions and hydrogen bonds) underpinning gel formation. In order to overcome these drawbacks, researchers have exploited different strategies, such as (i) increasing Poloxamer 407 molecular weight through chain extension reactions, (ii) blending with other polymers that can form chemical crosslinking, and (ii) chemically modifying its chains in order to add functionalities.

Among the available bio-fabrication technologies, extrusion-based bioprinting is emerging as a versatile low-cost approach to 3D print cellularized scaffolds. Compared to other techniques, its main drawbacks lie in the need of a bio-ink with suitable viscosity and its relative lower resolution and process duration. Thus, the proper design of the bioink as well as the optimization of the printing parameters represent some of the key aspects to maximize both printing speed and resolution as well as cell viability after printing.

In this work, amphiphilic Poloxamer-based polyurethanes have been synthesized and characterized for the design of injectable hydrogels. A first amphiphilic PUR with acronym NHP407 was designed starting from Poloxamer 407, an aliphatic diisocyanate and an amino acid-derived diol exposing BOC-protected amino groups that could be exploited for polymer bulk functionalization upon exposure in acidic conditions. NHP407 aqueous solutions have been studied in order to design thermo-sensitive hydrogels that can quickly gel within the range of temperatures between room temperature and body temperature (25-37 °C). For this purpose, hydrogel gelation (gelation time and temperature, rheological sol-gel properties) physico-chemical (degradation/dissolution, swelling, permeability, injectability) and biological properties (*in vitro* cytotoxicity) have been evaluated. NHP407-based hydrogels have been

showed to be suitable for applications that involves the injection of the hydrogels encapsulating cells or biomolecules (e.g., cells, biomolecules and/or drugs carrier), for short and mid-time (few days). However, although a significant improvement in gel physico-chemical and mechanical properties has been made compared to native P407-based hydrogels, NHP407-based gels still suffered of relatively short stability for long-term application. In particular, they turned out to be unsuitable bioinks for bioprinting applications, showing a drastic reduction in residence time in water environment when extruded in the shape of thin filaments. In fact, although the higher molecular weight of NHP407 allows PUR-based hydrogels to create more stable hydrophobic interactions and hydrogen bonds compared to P407-based ones, upon 3D printing in highly porous structures, the polymer-water ratio drastically drops and thus the micelles tend to dissolve due to the progressive absorption of water from the surrounding media and the consequent reduction in the polymer concentration. In order to overcome this drawback, different strategies have been tested, with the addition of photo-sensitivity to the hydrogel design showing the best results in terms of increasing gel long-term stability (weeks or months). In this way, the addition of toxic photo-initiators and the need of UV/Vis irradiation were balanced by the possibility to finely tune gel stability in water environment as well as the hydrogels mechanical properties. Hence, thermo- and photo-sensitive hydrogels were designed by designing new P407-based PURs with pendant acrylate moieties (HHP407 and PHP407), that, upon photo-initiator addition and UV/Vis irradiation, forms crosslinked micelles in water solutions.

Amphiphilic PURs with pendant acrylate moieties were designed by end-capping an isocyanate-terminated prepolymer synthesized from P407 and 1,6 hexamethylene diisocyanate with 1,6-hydroxyethyl methyl acrylate (HHP407) or pentaerythritol triacrylate (PHP407). Aqueous solutions of HHP407 and PHP407 showed similar, even if relatively lower, thermo-sensitive

properties compared to NHP407-based ones. However, the addition of terminal acrylate groups made HHP407 and PHP407 aqueous solutions also photo-sensitive, allowing an increase in hydrogel stability in aqueous environment as well as mechanical properties upon light-curing. However, although the increase in gel residence time provided by the photo-crosslinking process was significant, in particular in the case of HHP407-based gels, 3D printed structured prepared starting from these newly designed formulations still suffered for poor stability for long-term application. Hence, the design of bi-component blends of thermo-responsive and photo-curable polymers has been hypothesized to be the most versatile approach to finely modulate the properties of the resulting gels, in terms of both gelation and mechanical properties, as well as stability in watery environment, thus allowing the design of a wide plethora of new bioinks with the potential to match both bioprinting and specific tissues requirements. In order to fully exploit this approach two different blending strategies have been proposed: (i) blending NHP407 with a photo-sensitive polymer (i.e., PEGDA) that upon the addition of a photo-initiator and UV/Vis irradiation can form a mesh entrapping the PUR-based micelles; and (ii) blending the HHP407 with a photo-sensitive polymer (i.e., PEGDA), obtaining a double degree of crosslinking upon photo-crosslinking. Furthermore, the addition of the photo-sensitive polymer (i.e. PEGDA) has been demonstrated to further enhance the shear-thinning behavior of both NHP407 and HHP407 hydrogels allowing to increase the printing speed and reducing the printing pressure.

In order to apply such hydrogels as bioinks for 3D bioprinting, the optimization of their formulations and the printing protocol was necessary to maximize both printing resolution and cell viability. The designed polyurethane-based bioinks have been showed to own promising characteristics for bioprinting application (i.e., tunable viscosity and gelation time, fast gelation at 37 °C, improved and tunable stability and mechanical properties, cytocompatibility). The application of such bioinks in 3D bioprinting has been assessed by modifying a commercial

bioprinter (Inkredible +, CELLINK) and designing a custom-made printing-process. The overall process consisted of a constant pressure extrusion, in which the pressure valve was closed during all direction changes to avoid filament pulling by the printing nozzle, that has detrimental effects on both resolution and geometry fidelity. At the end of each layer, the UV led (365 nm, mounted on the second extruder of the bioprinter) was centered on the scaffold for the crosslinking step. The customized G-CODE, obtained from the custom-made script, have accelerated the overall process, allowing a fine control of all the printing steps parameters and owing the potential to be easily adapted to print even more complicated geometries.

Eventually, by combining the chemical versatility of polyurethanes and the technological versatility of 3D printing, polyurethane-based cellularized scaffolds have been printed showing high resolution and cell distribution, and maintaining the encapsulated cell viable for up to 1 month. Furthermore, the possibility to tune the scaffolds resident time as well as their mechanical properties, by modulating bioink formulation and printing parameters, was assessed. The PUR-based 3D printed scaffolds have showed promising properties for long-term applications, showing also the possibility to finely tune the final structure and the mechanical properties in order to match the ones of a specific tissue/organ, as schematized in **Figure 6.1**.

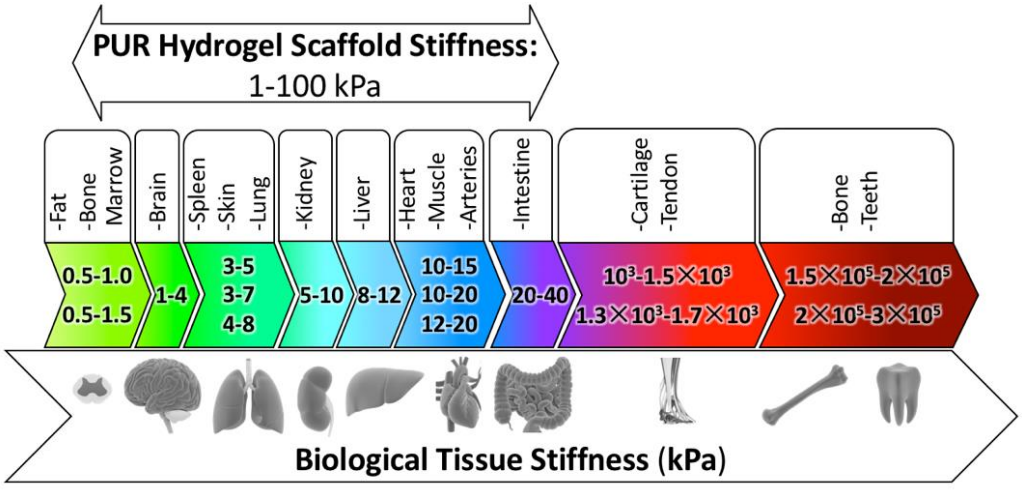

Figure 6.1 PUR-based bioink stiffness *versus* stiffness of soft biological tissues.

Although the data discussed in the previous chapters are promising, further biological investigation is required to better understand the encapsulated MSCs fate. In fact, despite the cells turned out to be viable for up to 1 month, they did not spread within the bioinks, probably due to the synthetic nature of the formulations and the soft nature of the hydrogels. Moreover, the cell growth resulted quite slowed down, probably due to the absence of attachment sites or maybe because the MSC started to differentiate.

Finally, the thorough investigation of cells differentiation potential upon encapsulation in scaffolds differing in stiffness and residence time in aqueous environment will complete the characterization of the designed construct, thus opening the way to their application in tissue engineering as *in vitro* engineered models or as regenerative therapeutics.

Appendix 1

C Script

```
#include "Circular-Scaffold.h"
#include <stdio.h>
#include <stdlib.h>
#include <string.h>
#include <math.h>

//---------------------- FUNCTION ----------------------//
void INFILL(FILE *fout, int flag_l, int flag_r, int diameter_s, float diameter_f, float gap, int n_layer, float y_m, float x, float y, int movement_speed, int printing_speed, int retraction, float n_fil, float z_well, float x_off, float y_off, int max);

int main()
{
  //-------------------- VARIABLES --------------------//
  FILE *fout;
  // number of layers
  int layer_tot = 4;
  // nozzle diameter
  float diameter_f = 0.210;
  // gap multiplier
  float m_gap = 2.5;
  // scaffold diameter
  int diameter_s = 10;
  // printing speed
  int printing_speed = 300;
  // movement speed without printing
  int movement_speed = 1800;
  // photo-crosslinking time
  int photo_time = 30;
  // x offset between extruder 1 and 2 (LED)
  float x_off = -33.5;
  // y offset between extruder 1 and 2 (LED)
  float y_off = 0;
  // pattern angle
  int alfa = 90;
  // layer thickness
  float layer_thickness = diameter_f - 0.01;
  // layer counter
  int n_layer = 1;
  // gap between the filaments
  float gap = (diameter_f * m_gap);
  // gap between the perimeter and the filaments
  float gap_perimetro;
  // number of filaments
  float n_fil;
  // scaffold thickness
  float tot_thickness;
  // x coordinate
  float x;
  // temporary x coordinate
  float x_tmp;
  // y coordinate (circumference)
  float y = sqrt(pow((diameter_s/2)-(diameter_f/2), 2)-(pow(x, 2)));
  // temporary y coordinate
  float y_tmp;
```

```
  // filament length
  float l;
  // y modulus
  float y_m= y;
  // E parameter
  float e = l
  float rest;
  int flag_l= 1;
  int flag_r= 1;
   // raw multiwell plate
  int r;
  // column multiwell plate
  int c;
  // x coordinate well
  float x_well;
  // y coordinate well
  float y_well;
  // z coordinate well
  float z_well = 20;
// z coordinate photo-crosslinking
  float z_ph = 19;
  // number of well to print in
  int n_well;
  int i;
  int max = 0;
  char file_name[25] = "Circular-Scaffold.gcode";

  //---------------------- WELLS ----------------------//
  // 24 well plate
  // printf("Number of wells (1-24):");
  // 12 well plate
  printf("Number of wells (1-12):");
  scanf ("%d",&n_well);
  for(i=1; i<=n_well; i++)
  {
    // printf("Row number (0-4, 0 if petri):");
    printf("Row number (0-3, 0 if petri):");
    scanf ("%d",&r);
    // printf("Column number (0-6, 0 if petri):");
    printf("Column number (0-4, 0 if petri):");
    scanf ("%d",&c);
    // Rows
    if(r==0)   // Petri dish
    {
      y_well=0;
    }
    if(r==1)   // A
    {
      // y_well=25.40;
      y_well=26.2;
    }
    if(r==2)   // B
    {
      // y_well=6.80;
      y_well=1;
    }
    if(r==3)   // C
    {
      // y_well=-12.80;
      y_well=-25.2;
    }
    // if(r==4)   // D
    // {
    //   y_well=-32.40;
    // }
    // Columns
    if(c==0)   // Petri dish
    {
      x_well=0;
    }
    if(c==1)   // 1
    {
      // x_well=-44.80;
      x_well=-38.2;
    }
    if(c==2)   // 2
```

```
{
  // x_well=-25.30;
  x_well=-12.2;
}
if(c==3)  // 3
{
  // x_well=-5.80;
  x_well=13.4;
}
if(c==4)  // 4
{
  // x_well=13.70;
  x_well=39.4;
}
// if(c==5)  // 5
// {
//   x_well=33.20;
// }
// if(c==6)
// {
//   x_well=52.70;
// }

//---------- NUMBER OF FILAMETS ----------//
if (n_fil == round(n_fil))  // n_fil integer
{
  n_fil =
  floor(((diameter_s)/(diameter_f+gap))-1);
}
else  // n_fil decimal
{
  n_fil =
  floor(((diameter_s)/(diameter_f+gap))-1.5);
}

//----------------- OPEN FILE -----------------//
fout=fopen(file_name, "w");  // file opening
(writing)
if(fout==NULL)  // check on file opening
{
  perror("Unable to open the file for
  writing\n");
  exit(1);
}

//---------------- START CODE ----------------//
fprintf(fout, "G21 ; set units to millimeters\n");
// mm
fprintf(fout, "G90 ; use absolute
coordinates\n");  // absolute coordinates
if (r==0)
{
  fprintf(fout,"\n;PETRI\n");
}
if (r==1)
{
  fprintf(fout,";WELL A%d\n", c);
}
if (r==2)
{
  fprintf(fout,";WELL B%d\n", c);
}
if (r==3)
{
  fprintf(fout,";WELL C%d\n", c);
}
if (r==4)
{
  fprintf(fout,";WELL D%d\n", c);
}
fprintf(fout,"G0 Z%f F1800\n", z_well);
// nozzle centering
fprintf(fout,"G0 X%f Y%f F1800\n", x_well,
y_well);
// save new origin
fprintf(fout,"G92 X0 Y0\n");
```

```
//---------------------- LAYERS ----------------------//
for(n_layer=1;                n_layer<=layer_tot;
n_layer=n_layer+1)
{
  // scaffold thickness
  tot_thickness = layer_thickness * n_layer;
  fprintf(fout, "\n\n;LAYER%d\n\n", n_layer);
  // extruder 1 (cartridge)
  fprintf(fout, "M751 ; active extruder 1\n");
 //  z adjusting
  fprintf(fout,"G0 Z%f F1800\n", z_well);
  if (retraction != 0)
  {
    fprintf(fout, "G0 E%d F%d\n", -retraction,
     movement_speed);
    fprintf(fout, "G92 E0\n");
  }

//------------------- PERIMETER -------------------//
  fprintf(fout, ";Perimeter\n");   // perimeter
  rest = fmodf(n_layer , 2);
  if(rest != 0)   // layer odd
  {
    x_tmp = -((diameter_s/2)-(diameter_f/2));
    y_tmp = 0;
  }
  else   // layer even
  {
    x_tmp = 0;
    y_tmp = -((diameter_s/2)-(diameter_f/2));
  }
  // circumference
  l=  (2  *  3.1415926  *  ((diameter_s/2)-
(diameter_f/2)));
  e = l;
  fprintf(fout,  "G0  X%.3f  Y%.3f  F%d\n",
    x_tmp , y_tmp ,movement_speed);
  fprintf(fout,      "G0      Z%.3f      F%d\n",
   tot_thickness, movement_speed);
  // start printing
  fprintf(fout, "M760 ; open valve 1\n");
  if (retraction != 0)
  {
    fprintf(fout, "G0 E%d F%d\n", retraction
     ,movement_speed);
  }
  fprintf(fout, "G2 X%.3f Y%.3f I%.3f J%.3f
   E%f  F%d\n",  x_tmp,  y_tmp,  -x_tmp,  -
   y_tmp, retraction+e, printing_speed);
  fprintf(fout, "M761 ; close valve 1\n");
  if (retraction != 0)
  {
    fprintf(fout,    "G0    E%f    F%d\n",    e
     ,movement_speed);
  }
  fprintf(fout, "G92 E0\n");

//---------------------- INFILL ----------------------//
  fprintf(fout, ";Infill\n");   // infill
  fprintf(fout,  "G0  E%d  F%d\n",  -retraction,
   movement_speed);
  // E parameter zeroing
  fprintf(fout, "G92 E0\n");
  rest = fmodf(n_fil , 2);
  if (rest != 0)   // number of filaments odd
  {
    flag_l= 1;
    flag_r= 1;
    max = 0;
    gap_perimetro=(diameter_s/2)-
     diameter_f-(((n_fil-1)/2)*diameter_f)-
     (diameter_f/2)-((((n_fil
     1)/2)*m_gap)*diameter_f);
    // if (gap_perimetro<gap)
    // {
```

```
//   gap_perimetro = gap_perimetro+gap;
// }
// x<=0
for(x=-((diameter_s/2)-diameter_f-
 gap_perimetro-(diameter_f/2));
 x<=diameter_f/2                    &&
 flag_l<=((n_fil/2)+0.5);
 x=(x+(diameter_f/2)+gap+(diameter_f/2)
 ))
 {
   // function
   INFILL(fout, flag_l, flag_r, diameter_s,
   diameter_f, gap, n_layer, y_m, x, y,
   movement_speed,        printing_speed,
   retraction, n_fil, z_well, x_off, y_off,
   max);
   if (flag_l != ((n_fil/2)+0.5))
   {
      flag_l=flag_l+1;
   }
 }
// x>0
for(x=        ((diameter_s/2)-diameter_f-
 gap_perimetro-(diameter_f/2)); x>0 &&
 flag_r<((n_fil/2)+0.5)      ;      x=(x-
 (diameter_f/2)-gap-(diameter_f/2)))
 {
   // function
   INFILL(fout, flag_l, flag_r, diameter_s,
   diameter_f, gap, n_layer, y_m, x, y,
   movement_speed,        printing_speed,
   retraction, n_fil, z_well, x_off, y_off,
   max);
   if (flag_r != ((n_fil/2)-0.5))
   {
      flag_r=flag_r+1;
      if (flag_r == ((n_fil/2)-0.5))
      {
         max = 1;
      }
   }
 }
}
else   // number of filaments even
{
   flag_l= 1;
   flag_r= 1;
   max = 0;
   gap_perimetro      =      (diameter_s/2)-
    diameter_f-((n_fil/2)*diameter_f)-
    ((((n_fil-2)/2)*m_gap)*diameter_f)-
    ((m_gap/2)*diameter_f);
   // if (gap_perimetro<gap)
   // {
   //   gap_perimetro = gap_perimetro+gap;
   // }
   // x<0
   for(x=      -((diameter_s/2)-diameter_f-
    gap_perimetro-(diameter_f/2)); x<0 &&
    flag_l<=((n_fil/2)+0.5);
    x=(x+(diameter_f/2)+gap+(diameter_f/2)
    ))
    {
      // function
      INFILL(fout, flag_l, flag_r, diameter_s,
      diameter_f, gap, n_layer, y_m, x, y,
      movement_speed,        printing_speed,
      retraction, n_fil, z_well, x_off, y_off,
      max);
      if (flag_l != (n_fil/2))
      {
         flag_l=flag_l+1;
      }
    }
   // x>0
```

```
        for(x=          ((diameter_s/2)-diameter_f-
        gap_perimetro-(diameter_f/2)); x>0 &&
        flag_r<((n_fil/2)+0.5);          x=(x-
        (diameter_f/2)-gap-(diameter_f/2)))
        {
          // function
          INFILL(fout, flag_l, flag_r, diameter_s,
          diameter_f, gap, n_layer, y_m, x, y,
          movement_speed,          printing_speed,
          retraction, n_fil, z_well, x_off, y_off,
          max);
          if (flag_r != (n_fil/2))
          {
            flag_r=flag_r+1;
            if (flag_r == (n_fil/2))
            {
              max = 1;
            }
          }
        }
      }

//---------- PHOTO-CROSSLINKING ---------- //
    // photo-crosslinking step
    fprintf(fout, ";Photo-crosslinking\n");
   // centering
    fprintf(fout, "G0 X%.3f Y%.3f F%d\n",
      x_off, y_off, movement_speed);
    // extruder 2 (LED)
    fprintf(fout, "M752 ; active extruder 2\n");
    // z adjusting
    fprintf(fout,"G0 Z%f F1800\n",
   (z_ph+(n_layer*layer_thickness)));
    // irradiation time
    fprintf(fout, "G4 S%d\n", photo_time);
    fprintf(fout,"G0 Z%f F1800\n", z_well);
}

    //---------- END CODE ----------//
    fprintf(fout, "G0 X0 Y0 F%d\n",
    movement_speed);
    fprintf(fout, "M761 ; active extruder 1\n");
    // fprintf(fout, "M84 ; disable motors\n");
    fprintf(fout,"G0 Z%f F1800\n", z_well);
    fprintf(fout,"G0 X%f Y%f F1800\n", -x_well, -
    y_well);
     // reset the origin
    fprintf(fout,"G92 X0 Y0\n");
    printf("layer_tot:%d\n", layer_tot);
    printf("diameter_f:%f\n", diameter_f);
    printf("n_fil:%f\n", n_fil);
    printf("gap:%f\n", gap);
    printf("gap_perimetro:%f\n", gap_perimetro);
    printf("filaments on the left:%d\n", flag_l);
    printf("filaments on the right:%d\n", flag_r);
    fclose(fout);
    return 0;
  }
}

//******* FUNCTION DECLARATIONS *******//
void INFILL(FILE *fout, int flag_l, int flag_r, int
diameter_s, float diameter_f, float gap, int n_layer,
float y_m, float x, float y, int movement_speed, int
printing_speed, int retraction, float n_fil, float
z_well, float x_off, float y_off, int max)
{
  float x_tmp;
  float x_tmp1;
  float y_tmp;
  float y_tmp1;
  float rest;
  float rest1;
  float l;
  float e;
  // filaments on the left/bottom side
```

```
if(x<=diameter_f/2)
{
  // first filament on the left/bottom side
  if (flag_l==1)
  {
    // perimeter
    x_tmp =  -((diameter_s/2)-(diameter_f/2));
    // circumference
    y = sqrt(pow((diameter_s/2)-diameter_f, 2)-
    (pow(x, 2)));
    rest = fmodf(n_layer , 2);
    // layer odd (first filament on the left side)
    if(rest != 0)
    {
      fprintf(fout, "G0 X%.3f Y%.3f F%d\n",
       x_tmp,                    y+(2*diameter_f),
       movement_speed);
      fprintf(fout, "G0 X%.3f Y%.3f F%d\n", x,
       y+(2*diameter_f), movement_speed);
      fprintf(fout, "G0 X%.3f Y%.3f F%d\n", x,
       y, movement_speed);
    }
    // layer even (first filament on the bottom
     side) --> invert x e y
    else
    {
      fprintf(fout, "G0 X%.3f Y%.3f F%d\n", -
       (y+(2*diameter_f)),              x_tmp,
       movement_speed);
      fprintf(fout, "G0 X%.3f Y%.3f F%d\n", -
       (y+(2*diameter_f)), x, movement_speed);
      fprintf(fout, "G0 X%.3f Y%.3f F%d\n", -
       y, x, movement_speed);
    }
  }
  // filaments on the left/bottom side except the
    first
  else
  {
    // previous filament
    x_tmp        =        x-(diameter_f/2)-gap-
  (diameter_f/2);
    // circumference
    y = sqrt(pow((diameter_s/2)-diameter_f, 2)-
  (pow(x, 2)));
    rest = fmodf(n_layer , 2);
    if(rest != 0) //  layer odd
    {
      rest = fmodf(flag_l , 2);
      // filament odd --> from the top to the
       bottom side
      if(rest != 0)
      {
        fprintf(fout, "G0 X%.3f Y%.3f F%d\n",
        x_tmp,                    y+(2*diameter_f),
        movement_speed);
        fprintf(fout, "G0 X%.3f Y%.3f F%d\n",
        x,                        y+(2*diameter_f),
        movement_speed);
        fprintf(fout, "G0 X%.3f Y%.3f F%d\n",
        x, y, movement_speed);
      }
      // filament even --> from the bottom to the
       top side
      else
      {
        fprintf(fout, "G0 X%.3f Y%.3f F%d\n",
        x_tmp,                    -(y+(2*diameter_f)),
        movement_speed);
        fprintf(fout, "G0 X%.3f Y%.3f F%d\n",
        x,                        -(y+(2*diameter_f)),
        movement_speed);
        fprintf(fout, "G0 X%.3f Y%.3f F%d\n",
        x, -y, movement_speed);
      }
    }
```

```
        // layer even --> invert x e y
        else
        {
          rest = fmodf(flag_l , 2);
          // filament odd --> from the left to the right
             side
          if(rest != 0)
          {
            fprintf(fout, "G0 X%.3f Y%.3f F%d\n",
            -(y+(2*diameter_f)),          x_tmp,
            movement_speed);
            fprintf(fout, "G0 X%.3f Y%.3f F%d\n",
            -(y+(2*diameter_f)),              x,
            movement_speed);
            fprintf(fout, "G0 X%.3f Y%.3f F%d\n",
            -y, x, movement_speed);
          }
          // filament even --> from the right to the
           left side
          else
          {
            fprintf(fout, "G0 X%.3f Y%.3f F%d\n",
              y+(2*diameter_f),           x_tmp,
              movement_speed);
            fprintf(fout, "G0 X%.3f Y%.3f F%d\n",
              y+(2*diameter_f),               x,
              movement_speed);
            fprintf(fout, "G0 X%.3f Y%.3f F%d\n",
              y, x, movement_speed);
          }
        }
      }
      fprintf(fout, "M760 ; open valve 1\n");
      if (retraction != 0)
      {
      fprintf(fout, "G0 E%d F%d\n", retraction
,movement_speed);
      }
      y_m = y;
      l= (2 * y_m);
      e = l;
      rest = fmodf(n_layer , 2);
      // layer odd
      if(rest != 0)
      {
        rest = fmodf(flag_l , 2);
        // filament odd
         if(rest != 0)
        {
          fprintf(fout, "G1 X%.3f Y%.3f E%f
           F%d\n",      x,      -y,      retraction+e,
           printing_speed);
        }
        else
        {
          fprintf(fout, "G1 X%.3f Y%.3f E%f
           F%d\n",      x,      y,      retraction+e,
           printing_speed);
        }
      }
      // layer even
      else
      {
        rest = fmodf(flag_l , 2);
        // filament odd
        if(rest != 0)
        {
          fprintf(fout, "G1 X%.3f Y%.3f E%f
           F%d\n",      y,      x,      retraction+e,
           printing_speed);
        }
        else
        {
          fprintf(fout, "G1 X%.3f Y%.3f E%f
           F%d\n",      -y,      x,      retraction+e,
           printing_speed);
```

```
        }
    }
    fprintf(fout, "M761 ; close valve 1\n");
    if (retraction != 0)
    {
        fprintf(fout,    "G0    E%f    F%d\n",    e
      ,movement_speed);
    }
    fprintf(fout, "G92 E0\n");
    x_tmp1 = x;
    y_tmp1 = y;
}
// filaments on the right/top side
else
{
    // first filament on the right/top side
    if (flag_r==1)
    {
        x_tmp = ((diameter_s/2)-(diameter_f/2));
        // circumference
        y = sqrt(pow((diameter_s/2)-diameter_f, 2)-
          (pow(x, 2)));
        rest = fmodf(n_layer , 2);
        // layer odd (first filament on the right side)
        if(rest != 0)
        {
            rest = fmodf(n_fil , 2);
            if(rest != 0)
            {
              rest1 = fmodf(((n_fil/2)+0.5) , 2);
            }
            else
            {
               rest1 = fmodf((n_fil/2) , 2);
            }
            // number of filaments odd and number of
            filament on the left even, or number of
            filaments even and number of filament on
            the left even
            if((rest != 0 && rest1 == 0) || (rest == 0
            && rest1 == 0))
            {
              fprintf(fout, "G0 X%.3f Y%.3f F%d\n",
              x_tmp1    ,    x_tmp+(2*diameter_f),
              movement_speed);
              fprintf(fout, "G0 X%.3f Y%.3f F%d\n",
              x         ,         x_tmp+(2*diameter_f),
              movement_speed);
              fprintf(fout, "G0 X%.3f Y%.3f F%d\n",
              x, y, movement_speed);
              y_tmp = -y;
            }
            ……..// number of filaments odd and number of
            filament on the left odd, or number of
            filaments even and number of filament on
            the left odd
            else if ((rest != 0 && rest1 != 0) || (rest ==
            0 && rest1 != 0))
            {
              fprintf(fout, "G0 X%.3f Y%.3f F%d\n",
                x_tmp1,     -(x_tmp+(2*diameter_f)),
                movement_speed);
              fprintf(fout, "G0 X%.3f Y%.3f F%d\n",
                x,              -(x_tmp+(2*diameter_f)),
                movement_speed);
              fprintf(fout, "G0 X%.3f Y%.3f F%d\n",
                x, -y, movement_speed);
              y_tmp = y;
            }
        }
        // layer even (first filament on the top) -->
          invert x e y
        else
        {
            rest = fmodf(n_fil , 2);
```

```
if(rest != 0)
{
   rest1 = fmodf(((n_fil/2)+0.5) , 2);
}
else
{
   rest1 = fmodf((n_fil/2) , 2);
}
// number of filaments odd and number of filament on the left even, or number of filaments even and number of filament on the left even
if((rest != 0 && rest1 == 0) || (rest == 0 && rest1 == 0))
{
   fprintf(fout, "G0 X%.3f Y%.3f F%d\n", -(x_tmp+(2*diameter_f)), x_tmp1, movement_speed);
   fprintf(fout, "G0 X%.3f Y%.3f F%d\n", -(x_tmp+(2*diameter_f)), x, movement_speed);
   fprintf(fout, "G0 X%.3f Y%.3f F%d\n", -y, x, movement_speed);
}
// number of filaments odd and number of filament on the left odd, or number of filaments even and number of filament on the left odd
else if ((rest != 0 && rest1 != 0) || (rest == 0 && rest1 != 0))
{
   fprintf(fout, "G0 X%.3f Y%.3f F%d\n", (x_tmp+(2*diameter_f)), x_tmp1, movement_speed);
   fprintf(fout, "G0 X%.3f Y%.3f F%d\n", (x_tmp+(2*diameter_f)), x, movement_speed);
   fprintf(fout, "G0 X%.3f Y%.3f F%d\n", y, x, movement_speed);
   }
  }
}
// filaments on the right/top side except the first
else
{
  x_tmp = x+(diameter_f/2)+gap+(diameter_f/2);
  // circumference
  y = sqrt(pow((diameter_s/2)-diameter_f, 2)-(pow(x, 2)));
  rest = fmodf(n_layer , 2);
  // layer odd (filaments on the right side except the first)
  if(rest != 0)
  {
    rest = fmodf(n_fil , 2);
    if(rest != 0)
    {
      rest1 = fmodf(((n_fil/2)+0.5) , 2);
    }
    else
    {
      rest1 = fmodf((n_fil/2) , 2);
    }
    // number of filaments odd and number of filament on the left even or number of filaments even and number of filament on the left even
    if((rest != 0 && rest1 == 0) || (rest == 0 && rest1 == 0))
    {
      rest = fmodf(flag_r , 2);
      // filament odd --> from the bottom to the top side
      if(rest != 0)
```

```
    {
      fprintf(fout, "G0 X%.3f Y%.3f F%d\n", x_tmp, y+(2*diameter_f), movement_speed);
      fprintf(fout, "G0 X%.3f Y%.3f F%d\n", x, y+(2*diameter_f), movement_speed);
      fprintf(fout, "G0 X%.3f Y%.3f F%d\n", x, y, movement_speed);
    }
    // filament even --> from the top to the bottom side
    else
    {
      fprintf(fout, "G0 X%.3f Y%.3f F%d\n", x_tmp, -(y+(2*diameter_f)), movement_speed);
      fprintf(fout, "G0 X%.3f Y%.3f F%d\n", x, -(y+(2*diameter_f)), movement_speed);
      fprintf(fout, "G0 X%.3f Y%.3f F%d\n", x, -y, movement_speed);
    }
  }
  // number of filaments odd and number of filament on the left odd, or number of filaments even and number of filament on the left odd
  else if ((rest != 0 && rest1 != 0) || (rest == 0 && rest1 != 0))
  {
    rest = fmodf(flag_r , 2);
    // filament odd --> from the top to the bottom side
    if(rest != 0)
    {
      fprintf(fout, "G0 X%.3f Y%.3f F%d\n", x_tmp, -(y+(2*diameter_f)), movement_speed);
      fprintf(fout, "G0 X%.3f Y%.3f F%d\n", x, -(y+(2*diameter_f)), movement_speed);
      fprintf(fout, "G0 X%.3f Y%.3f F%d\n", x, -y, movement_speed);
    }
    // filament even --> from the bottom to the top side
    else
    {
      fprintf(fout, "G0 X%.3f Y%.3f F%d\n", x_tmp, y+(2*diameter_f), movement_speed);
      fprintf(fout, "G0 X%.3f Y%.3f F%d\n", x, y+(2*diameter_f), movement_speed);
      fprintf(fout, "G0 X%.3f Y%.3f F%d\n", x, y, movement_speed);
    }
  }
  y_tmp = y;
}
// layer even (filaments on the top side except the first) --> invert x e y
else
{
  rest = fmodf(n_fil , 2);
  if(rest != 0)
  {
    rest1 = fmodf(((n_fil/2)+0.5) , 2);
  }
  else
  {
    rest1 = fmodf((n_fil/2) , 2);
```

```
}
// number of filaments odd and number of filament on the left even, or number of filaments even and number of filament on the left even
if((rest != 0 && rest1 == 0) || (rest == 0 && rest1 == 0))
{
  rest = fmodf(flag_r , 2);
  // filament odd --> from the left to the right side
  if(rest != 0)
  {
    fprintf(fout, "G0 X%.3f Y%.3f F%d\n", -(y+(2*diameter_f)), x_tmp, movement_speed);
    fprintf(fout, "G0 X%.3f Y%.3f F%d\n", -(y+(2*diameter_f)), x, movement_speed);
    fprintf(fout, "G0 X%.3f Y%.3f F%d\n", -y, x, movement_speed);
  }
  // filament even --> from the right to the left side
  else
  {
    fprintf(fout, "G0 X%.3f Y%.3f F%d\n", y+(2*diameter_f), x_tmp, movement_speed);
    fprintf(fout, "G0 X%.3f Y%.3f F%d\n", y+(2*diameter_f), x, movement_speed);
    fprintf(fout, "G0 X%.3f Y%.3f F%d\n", y, x, movement_speed);
  }
}
// number of filaments odd and number of filament on the left odd, or number of filaments even and number of filament on the left odd
else if ((rest != 0 && rest1 != 0) || (rest == 0 && rest1 != 0))
{
  rest = fmodf(flag_r , 2);
  // filament odd --> from the right to the left side
  if(rest != 0)
  {
    fprintf(fout, "G0 X%.3f Y%.3f F%d\n", y+(2*diameter_f), x_tmp, movement_speed);
    fprintf(fout, "G0 X%.3f Y%.3f F%d\n", y+(2*diameter_f), x, movement_speed);
    fprintf(fout, "G0 X%.3f Y%.3f F%d\n", y, x, movement_speed);
  }
  // filament even --> from the left to the right side
  else
  {
    fprintf(fout, "G0 X%.3f Y%.3f F%d\n", -(y+(2*diameter_f)), x_tmp, movement_speed);
    fprintf(fout, "G0 X%.3f Y%.3f F%d\n", -(y+(2*diameter_f)), x, movement_speed);
    fprintf(fout, "G0 X%.3f Y%.3f F%d\n", -y, x, movement_speed);
  }
 }
}
fprintf(fout, "M760 ; open valve 1\n");
if (retraction != 0)
{
```

```
    fprintf(fout, "G0 E%d F%d\n", retraction
    ,movement_speed);
  }
  y_m = y;
  l= (2 * y_m);
  e = l; // E parameter
  rest = fmodf(n_layer , 2);
  // layer odd
  if(rest != 0)
  {
    rest = fmodf(n_fil , 2);
    if(rest != 0)
    {
      rest1 = fmodf(((n_fil/2)+0.5) , 2);
    }
    else
    {
      rest1 = fmodf((n_fil/2) , 2);
    }
    // number of filaments odd and number of
     filament on the left even, or number of
     filaments even and number of filament on
     the left even
    if((rest != 0 && rest1 == 0) || (rest == 0 &&
     rest1 == 0))
    {
      rest = fmodf(flag_r , 2);
      if(rest != 0) //  filament odd
      {
        fprintf(fout, "G1 X%.3f Y%.3f E%f
          F%d\n", x, -y, retraction+e,
          printing_speed);
      }
      // filament even
      else
      {
        fprintf(fout, "G1 X%.3f Y%.3f E%f
        F%d\n", x, y, retraction+e,
        printing_speed);
      }
    }
    // number of filaments odd and number of
     filament on the left odd or number of
     filaments even and number of filament on
     the left odd
    else if ((rest != 0 && rest1 != 0) || (rest == 0
     && rest1 != 0))
    {
      rest = fmodf(flag_r , 2);
      // filament odd
      if(rest != 0)
      {
        fprintf(fout, "G1 X%.3f Y%.3f E%f
        F%d\n", x, y, retraction+e,
        printing_speed);
      }
      // filament even
      else
      {
        fprintf(fout, "G1 X%.3f Y%.3f E%f
        F%d\n", x, -y, retraction+e,
        printing_speed);
      }
    }
  }
  // layer even --> invert x and y
  else
  {
    rest = fmodf(n_fil , 2);
    if(rest != 0)
    {
      rest1 = fmodf(((n_fil/2)+0.5) , 2);
    }
    else
```

```
{
   rest1 = fmodf((n_fil/2) , 2);
}
// number of filaments odd and number of
 filament on the left even, or number of
 filaments even and number of filament on
 the left even
if((rest != 0 && rest1 == 0) || (rest == 0 &&
rest1 == 0))
{
   rest = fmodf(flag_r , 2);
   if(rest != 0) //  filament odd
   {
      fprintf(fout, "G1 X%.3f Y%.3f E%f
      F%d\n", y, x, retraction+e,
      printing_speed);
   }
   else
   {
      fprintf(fout, "G1 X%.3f Y%.3f E%f
      F%d\n", -y, x, retraction+e,
      printing_speed);
   }
}
// number of filaments odd and number of
 filament on the left odd, or number of
 filaments even and number of filament on
 the left odd
else if ((rest != 0 && rest1 != 0) || (rest == 0
&& rest1 != 0))
{
   rest = fmodf(flag_r , 2);
   // filament odd
   if(rest != 0)
   {
      fprintf(fout, "G1 X%.3f Y%.3f E%f
      F%d\n", -y, x, retraction+e,
      printing_speed);
   }
   // filament even
   else
   {
      fprintf(fout, "G1 X%.3f Y%.3f E%f
      F%d\n", y, x, retraction+e,
      printing_speed);
   }
  }
}
fprintf(fout, "M761 ; close valve 1\n");
if (retraction != 0)
{
  fprintf(fout, "G0 E%f F%d\n", e
 ,movement_speed);
}
fprintf(fout, "G92 E0\n");

if (max == 1)
{
  rest = fmodf(n_layer , 2);
  if(rest != 0) //  layer odd
  {
     rest = fmodf(n_fil , 2);
     if(rest != 0)
     {
        rest1 = fmodf(((n_fil/2)+0.5) , 2);
     }
     else
     {
        rest1 = fmodf((n_fil/2) , 2);
     }
     // number of filaments odd and number of
      filament on the left even, or number of
      filaments even and number of filament on
      the left even
     if((rest != 0 && rest1 == 0) || (rest == 0
      && rest1 == 0))
```

```
{
   rest = fmodf(flag_r , 2);
   // filament odd
   if(rest != 0)
   {
      fprintf(fout, "G0 X%.3f Y%.3f F%d\n", x, -(y+(2*diameter_f)), movement_speed);
      fprintf(fout,"G0 Z%f F1800\n", z_well);
                  fprintf(fout, "G0 X%.3f Y%.3f F%d\n", x_off, -y, movement_speed);
   }
   // filament even
   else
   {
      fprintf(fout, "G0 X%.3f Y%.3f F%d\n", x, y+(2*diameter_f), movement_speed);
      fprintf(fout,"G0 Z%f F1800\n", z_well);
      fprintf(fout, "G0 X%.3f Y%.3f F%d\n", x_off, y, movement_speed);
   }
}
// number of filaments odd and number of filament on the left odd or number of filaments even and number of filament on the left odd
else if ((rest != 0 && rest1 != 0) || (rest == 0 && rest1 != 0))
{
   rest = fmodf(flag_r , 2);
   // filament odd
   if(rest != 0)
   {
      fprintf(fout, "G0 X%.3f Y%.3f F%d\n", x, y+(2*diameter_f), movement_speed);
      fprintf(fout,"G0 Z%f F1800\n", z_well);
      fprintf(fout, "G0 X%.3f Y%.3f F%d\n", x_off, y, movement_speed);
   }
   // filament even
   else
   {
      fprintf(fout, "G0 X%.3f Y%.3f F%d\n", x, -(y+(2*diameter_f)), movement_speed);
      fprintf(fout,"G0 Z%f F1800\n", z_well);
      fprintf(fout, "G0 X%.3f Y%.3f F%d\n", x_off, -y, movement_speed);
   }
}
// layer even --> invert x and y
else
{
   rest = fmodf(n_fil , 2);
   if(rest != 0)
   {
      rest1 = fmodf(((n_fil/2)+0.5) , 2);
   }
   else
   {
      rest1 = fmodf((n_fil/2) , 2);
   }
   // number of filaments odd and number of filament on the left even or number of
```

```
    filaments even and number of filament on
    the left even
  if((rest != 0 && rest1 == 0) || (rest == 0
   && rest1 == 0))
  {
     rest = fmodf(flag_r , 2);
     // filament odd
     if(rest != 0)
     {
        fprintf(fout,  "G0  X%.3f  Y%.3f
         F%d\n",  y+(2*diameter_f),  x,
         movement_speed);
        fprintf(fout,"G0  Z%f  F1800\n",
         z_well);
        fprintf(fout,  "G0  X%.3f  Y%.3f
         F%d\n",  y,  y_off,
         movement_speed);
     }
     // filament even
     else
     {
        fprintf(fout,  "G0  X%.3f  Y%.3f
         F%d\n",  -(y+(2*diameter_f)),  x,
         movement_speed);
        fprintf(fout,"G0  Z%f  F1800\n",
         z_well);
        fprintf(fout,  "G0  X%.3f  Y%.3f
         F%d\n",  -y,  y_off,
         movement_speed);
     }
  }
  // number of filaments odd and number of
  filament on the left odd or number of
  filaments even and number of filament on
   the left odd
  else if ((rest != 0 && rest1 != 0) || (rest ==
   0 && rest1 != 0))
  {
     rest = fmodf(flag_r , 2);
     // filament odd
     if(rest != 0)
     {
        fprintf(fout,  "G0  X%.3f  Y%.3f
         F%d\n",  -(y+(2*diameter_f)),  x,
         movement_speed);
        fprintf(fout,"G0  Z%f  F1800\n",
         z_well);
        fprintf(fout,  "G0  X%.3f  Y%.3f
         F%d\n",  -y,  y_off,
         movement_speed);
     }
     // filament even
     else
     {
        fprintf(fout,  "G0  X%.3f  Y%.3f
         F%d\n",  y+(2*diameter_f),  x,
         movement_speed);
        fprintf(fout,"G0  Z%f  F1800\n",
         z_well);
        fprintf(fout,  "G0  X%.3f  Y%.3f
         F%d\n",  y,  y_off,
         movement_speed);
     }
  }
}
```

Resultant G-CODE

```
G21 ; set units to millimeters
G90 ; use absolute coordinates

; PETRI DISH
G0 Z20.000000 F1800
G0 X0.000000 Y0.000000 F1800
G92 X0 Y0

; LAYER 1
M751 ; active extruder 1
G0 Z20.000000 F1800
; Perimeter
G0 X-4.895 Y0.000 F1800
G0 Z0.200 F1800
M760 ; open valve 1
G2 X-4.895 Y0.000 I4.895 J-0.000 E0.014779 F300
M761 ; close valve 1
G92 E0
; Infill
G0 E0 F1800
G92 E0
G0 X-4.895 Y2.989 F1800
G0 X-4.043 Y2.989 F1800
G0 X-4.043 Y2.569 F1800
M760 ; open valve 1
G1 X-4.043 Y-2.569 E0.002469 F300
M761 ; close valve 1
G92 E0
G0 X-4.043 Y-3.885 F1800
G0 X-3.307 Y-3.885 F1800
G0 X-3.307 Y-3.465 F1800
M760 ; open valve 1
G1 X-3.307 Y3.465 E0.003330 F300
M761 ; close valve 1
G92 E0
G0 X-3.307 Y4.461 F1800
G0 X-2.572 Y4.461 F1800
G0 X-2.572 Y4.041 F1800
M760 ; open valve 1
G1 X-2.572 Y-4.041 E0.003883 F300
M761 ; close valve 1
G92 E0
G0 X-2.572 Y-4.844 F1800
G0 X-1.837 Y-4.844 F1800
G0 X-1.837 Y-4.424 F1800
M760 ; open valve 1
G1 X-1.837 Y4.424 E0.004251 F300
M761 ; close valve 1
G92 E0
G0 X-1.837 Y5.081 F1800
G0 X-1.102 Y5.081 F1800
G0 X-1.102 Y4.661 F1800
M760 ; open valve 1
G1 X-1.102 Y-4.661 E0.004480 F300
M761 ; close valve 1
G92 E0
G0 X-1.102 Y-5.196 F1800
G0 X-0.367 Y-5.196 F1800
G0 X-0.367 Y-4.776 F1800
M760 ; open valve 1
G1 X-0.367 Y4.776 E0.004590 F300
M761 ; close valve 1
G92 E0
G0 X-0.367 Y5.315 F1800
G0 X4.043 Y5.315 F1800
G0 X4.043 Y2.569 F1800
M760 ; open valve 1
G1 X4.043 Y-2.569 E0.002469 F300
M761 ; close valve 1
G92 E0
G0 X4.043 Y-3.885 F1800
G0 X3.307 Y-3.885 F1800
```

```
G0 X3.307 Y-3.465 F1800
M760 ; open valve 1
G1 X3.307 Y3.465 E0.003330 F300
M761 ; close valve 1
G92 E0
G0 X3.307 Y4.461 F1800
G0 X2.572 Y4.461 F1800
G0 X2.572 Y4.041 F1800
M760 ; open valve 1
G1 X2.572 Y-4.041 E0.003883 F300
M761 ; close valve 1
G92 E0
G0 X2.572 Y-4.844 F1800
G0 X1.837 Y-4.844 F1800
G0 X1.837 Y-4.424 F1800
M760 ; open valve 1
G1 X1.837 Y4.424 E0.004251 F300
M761 ; close valve 1
G92 E0
G0 X1.837 Y5.081 F1800
G0 X1.102 Y5.081 F1800
G0 X1.102 Y4.661 F1800
M760 ; open valve 1
G1 X1.102 Y-4.661 E0.004480 F300
M761 ; close valve 1
G92 E0
G0 X1.102 Y-5.196 F1800
G0 X0.367 Y-5.196 F1800
G0 X0.367 Y-4.776 F1800
M760 ; open valve 1
G1 X0.367 Y4.776 E0.004590 F300
M761 ; close valve 1
G92 E0
G0 X0.367 Y5.196 F1800
G0 Z20.000000 F1800
G0 X-33.500 Y4.776 F1800
; Photo-crosslinking
G0 X-33.500 Y0.000 F1800
M752 ; active extruder 2
G0 Z19.200001 F1800
G4 S30
G0 Z20.000000 F1800

; LAYER 2
M751 ; active extruder 1
G0 Z20.000000 F1800
; Perimeter
G0 X0.000 Y-4.895 F1800
G0 Z0.400 F1800
M760 ; open valve 1
G2 X0.000 Y-4.895 I-0.000 J4.895 E0.014779 F300
M761 ; close valve 1
G92 E0
; Infill
G0 E0 F1800
G92 E0
G0 X-2.989 Y-4.895 F1800
G0 X-2.989 Y-4.043 F1800
G0 X-2.569 Y-4.043 F1800
M760 ; open valve 1
G1 X2.569 Y-4.043 E0.002469 F300
M761 ; close valve 1
G92 E0
G0 X3.885 Y-4.043 F1800
G0 X3.885 Y-3.307 F1800
G0 X3.465 Y-3.307 F1800
M760 ; open valve 1
G1 X-3.465 Y-3.307 E0.003330 F300
M761 ; close valve 1
G92 E0
G0 X-4.461 Y-3.307 F1800
G0 X-4.461 Y-2.572 F1800
G0 X-4.041 Y-2.572 F1800
M760 ; open valve 1
G1 X4.041 Y-2.572 E0.003883 F300
M761 ; close valve 1
```

```
G92 E0
G0 X4.844 Y-2.572 F1800
G0 X4.844 Y-1.837 F1800
G0 X4.424 Y-1.837 F1800
M760 ; open valve 1
G1 X-4.424 Y-1.837 E0.004251 F300
M761 ; close valve 1
G92 E0
G0 X-5.081 Y-1.837 F1800
G0 X-5.081 Y-1.102 F1800
G0 X-4.661 Y-1.102 F1800
M760 ; open valve 1
G1 X4.661 Y-1.102 E0.004480 F300
M761 ; close valve 1
G92 E0
G0 X5.196 Y-1.102 F1800
G0 X5.196 Y-0.367 F1800
G0 X4.776 Y-0.367 F1800
M760 ; open valve 1
G1 X-4.776 Y-0.367 E0.004590 F300
M761 ; close valve 1
G92 E0
G0 X-5.315 Y-0.367 F1800
G0 X-5.315 Y4.043 F1800
G0 X-2.569 Y4.043 F1800
M760 ; open valve 1
G1 X2.569 Y4.043 E0.002469 F300
M761 ; close valve 1
G92 E0
G0 X3.885 Y4.043 F1800
G0 X3.885 Y3.307 F1800
G0 X3.465 Y3.307 F1800
M760 ; open valve 1
G1 X-3.465 Y3.307 E0.003330 F300
M761 ; close valve 1
G92 E0
G0 X-4.461 Y3.307 F1800
G0 X-4.461 Y2.572 F1800
G0 X-4.041 Y2.572 F1800
M760 ; open valve 1
G1 X4.041 Y2.572 E0.003883 F300
M761 ; close valve 1
G92 E0
G0 X4.844 Y2.572 F1800
G0 X4.844 Y1.837 F1800
G0 X4.424 Y1.837 F1800
M760 ; open valve 1
G1 X-4.424 Y1.837 E0.004251 F300
M761 ; close valve 1
G92 E0
G0 X-5.081 Y1.837 F1800
G0 X-5.081 Y1.102 F1800
G0 X-4.661 Y1.102 F1800
M760 ; open valve 1
G1 X4.661 Y1.102 E0.004480 F300
M761 ; close valve 1
G92 E0
G0 X5.196 Y1.102 F1800
G0 X5.196 Y0.367 F1800
G0 X4.776 Y0.367 F1800
M760 ; open valve 1
G1 X-4.776 Y0.367 E0.004590 F300
M761 ; close valve 1
G92 E0
G0 X-5.196 Y0.367 F1800
G0 Z20.000000 F1800
G0 X-4.776 Y0.000 F1800
; Photo-crosslinking
G0 X-33.500 Y0.000 F1800
M752 ; active extruder 2
G0 Z19.400000 F1800
G4 S30
G0 Z20.000000 F1800

; LAYER3
M751 ; active extruder 1
```

```
G0 Z20.000000 F1800
; Perimeter
G0 X-4.895 Y0.000 F1800
G0 Z0.600 F1800
M760 ; open valve 1
G2 X-4.895 Y0.000 I4.895 J-0.000 E0.014779 F300
M761 ; close valve 1
G92 E0
; Infill
G0 E0 F1800
G92 E0
G0 X-4.895 Y2.989 F1800
G0 X-4.043 Y2.989 F1800
G0 X-4.043 Y2.569 F1800
M760 ; open valve 1
G1 X-4.043 Y-2.569 E0.002469 F300
M761 ; close valve 1
G92 E0
G0 X-4.043 Y-3.885 F1800
G0 X-3.307 Y-3.885 F1800
G0 X-3.307 Y-3.465 F1800
M760 ; open valve 1
G1 X-3.307 Y3.465 E0.003330 F300
M761 ; close valve 1
G92 E0
G0 X-3.307 Y4.461 F1800
G0 X-2.572 Y4.461 F1800
G0 X-2.572 Y4.041 F1800
M760 ; open valve 1
G1 X-2.572 Y-4.041 E0.003883 F300
M761 ; close valve 1
G92 E0
G0 X-2.572 Y-4.844 F1800
G0 X-1.837 Y-4.844 F1800
G0 X-1.837 Y-4.424 F1800
M760 ; open valve 1
G1 X-1.837 Y4.424 E0.004251 F300
M761 ; close valve 1
G92 E0
G0 X-1.837 Y5.081 F1800
G0 X-1.102 Y5.081 F1800
G0 X-1.102 Y4.661 F1800
M760 ; open valve 1
G1 X-1.102 Y-4.661 E0.004480 F300
M761 ; close valve 1
G92 E0
G0 X-1.102 Y-5.196 F1800
G0 X-0.367 Y-5.196 F1800
G0 X-0.367 Y-4.776 F1800
M760 ; open valve 1
G1 X-0.367 Y4.776 E0.004590 F300
M761 ; close valve 1
G92 E0
G0 X-0.367 Y5.315 F1800
G0 X4.043 Y5.315 F1800
G0 X4.043 Y2.569 F1800
M760 ; open valve 1
G1 X4.043 Y-2.569 E0.002469 F300
M761 ; close valve 1
G92 E0
G0 X4.043 Y-3.885 F1800
G0 X3.307 Y-3.885 F1800
G0 X3.307 Y-3.465 F1800
M760 ; open valve 1
G1 X3.307 Y3.465 E0.003330 F300
M761 ; close valve 1
G92 E0
G0 X3.307 Y4.461 F1800
G0 X2.572 Y4.461 F1800
G0 X2.572 Y4.041 F1800
M760 ; open valve 1
G1 X2.572 Y-4.041 E0.003883 F300
M761 ; close valve 1
G92 E0
G0 X2.572 Y-4.844 F1800
G0 X1.837 Y-4.844 F1800
```

```
G0 X1.837 Y-4.424 F1800
M760 ; open valve 1
G1 X1.837 Y4.424 E0.004251 F300
M761 ; close valve 1
G92 E0
G0 X1.837 Y5.081 F1800
G0 X1.102 Y5.081 F1800
G0 X1.102 Y4.661 F1800
M760 ; open valve 1
G1 X1.102 Y-4.661 E0.004480 F300
M761 ; close valve 1
G92 E0
G0 X1.102 Y-5.196 F1800
G0 X0.367 Y-5.196 F1800
G0 X0.367 Y-4.776 F1800
M760 ; open valve 1
G1 X0.367 Y4.776 E0.004590 F300
M761 ; close valve 1
G92 E0
G0 X0.367 Y5.196 F1800
G0 Z20.000000 F1800
G0 X-33.500 Y4.776 F1800
; Photo-crosslinking
G0 X-33.500 Y0.000 F1800
M752 ; active extruder 2
G0 Z19.600000 F1800
G4 S30
G0 Z20.000000 F1800

; LAYER4
M751 ; active extruder 1
G0 Z20.000000 F1800
; Perimeter
G0 X0.000 Y-4.895 F1800
G0 Z0.800 F1800
M760 ; open valve 1
G2 X0.000 Y-4.895 I-0.000 J4.895 E0.014779 F300
M761 ; close valve 1
G92 E0
; Infill
G0 E0 F1800
G92 E0
G0 X-2.989 Y-4.895 F1800
G0 X-2.989 Y-4.043 F1800
G0 X-2.569 Y-4.043 F1800
M760 ; open valve 1
G1 X2.569 Y-4.043 E0.002469 F300
M761 ; close valve 1
G92 E0
G0 X3.885 Y-4.043 F1800
G0 X3.885 Y-3.307 F1800
G0 X3.465 Y-3.307 F1800
M760 ; open valve 1
G1 X-3.465 Y-3.307 E0.003330 F300
M761 ; close valve 1
G92 E0
G0 X-4.461 Y-3.307 F1800
G0 X-4.461 Y-2.572 F1800
G0 X-4.041 Y-2.572 F1800
M760 ; open valve 1
G1 X4.041 Y-2.572 E0.003883 F300
M761 ; close valve 1
G92 E0
G0 X4.844 Y-2.572 F1800
G0 X4.844 Y-1.837 F1800
G0 X4.424 Y-1.837 F1800
M760 ; open valve 1
G1 X-4.424 Y-1.837 E0.004251 F300
M761 ; close valve 1
G92 E0
G0 X-5.081 Y-1.837 F1800
G0 X-5.081 Y-1.102 F1800
G0 X-4.661 Y-1.102 F1800
M760 ; open valve 1
G1 X4.661 Y-1.102 E0.004480 F300
M761 ; close valve 1
```

```
G92 E0
G0 X5.196 Y-1.102 F1800
G0 X5.196 Y-0.367 F1800
G0 X4.776 Y-0.367 F1800
M760 ; open valve 1
G1 X-4.776 Y-0.367 E0.004590 F300
M761 ; close valve 1
G92 E0
G0 X-5.315 Y-0.367 F1800
G0 X-5.315 Y4.043 F1800
G0 X-2.569 Y4.043 F1800
M760 ; open valve 1
G1 X2.569 Y4.043 E0.002469 F300
M761 ; close valve 1
G92 E0
G0 X3.885 Y4.043 F1800
G0 X3.885 Y3.307 F1800
G0 X3.465 Y3.307 F1800
M760 ; open valve 1
G1 X-3.465 Y3.307 E0.003330 F300
M761 ; close valve 1
G92 E0
G0 X-4.461 Y3.307 F1800
G0 X-4.461 Y2.572 F1800
G0 X-4.041 Y2.572 F1800
M760 ; open valve 1
G1 X4.041 Y2.572 E0.003883 F300
M761 ; close valve 1
G92 E0
G0 X4.844 Y2.572 F1800
G0 X4.844 Y1.837 F1800
G0 X4.424 Y1.837 F1800
M760 ; open valve 1
G1 X-4.424 Y1.837 E0.004251 F300
M761 ; close valve 1
G92 E0
G0 X-5.081 Y1.837 F1800
G0 X-5.081 Y1.102 F1800
G0 X-4.661 Y1.102 F1800
M760 ; open valve 1
G1 X4.661 Y1.102 E0.004480 F300
M761 ; close valve 1
G92 E0
G0 X5.196 Y1.102 F1800
G0 X5.196 Y0.367 F1800
G0 X4.776 Y0.367 F1800
M760 ; open valve 1
G1 X-4.776 Y0.367 E0.004590 F300
M761 ; close valve 1
G92 E0
G0 X-5.196 Y0.367 F1800
G0 Z20.000000 F1800
G0 X-4.776 Y0.000 F1800
; Photo-crosslinking
G0 X-33.500 Y0.000 F1800
M752 ; active extruder 2
G0 Z19.799999 F1800
G4 S30
G0 Z20.000000 F1800
G0 X0 Y0 F1800
M761 ; active extruder 1
G0 Z20.000000 F1800
G0 X-0.000000 Y-0.000000 F1800
G92 X0 Y0
```